Towards Building a Screenable *In Vitro*Three-Dimensional Neuromuscular Junction to Study Neuromuscular Disorders

María José Castellanos Montiel



Department of Neurology & Neurosurgery McGill University

April 2025

A thesis submitted to McGill University in partial fulfillment of the requirements of the degree of

PhD of Neuroscience

© 2025 María José Castellanos Montiel

Table of Contents

Abstract	I
Résumé	3
Acknowledgments	6
Contribution to original knowledge	9
Contribution of authors	11
List of abbreviations	14
List of figures	17
Introduction	18
Literature review	20
1. The corticospinal tract	20
1.1 Upper motor neurons and lower motor neurons	20
1.2 Classification of lower motor neurons	22
2. The neuromuscular junction	23
2.1 Cellular components of the neuromuscular junction	23
2.2 Developmental origin of neuromuscular junction components	24
2.2.1 Development of α-motor neurons	25
2.2.2 Development of skeletal muscle	29
2.2.2.1 The sarcomere: the contractile unit of skeletal muscle	34
2.2.2.2 Slow-twitch and fast-twitch myofibers	36
2.2.3 Development of perisynaptic Schwann cells	37
2.3 Development of the neuromuscular junction	37
2.3.1 Postsynaptic differentiation	38

2.3.2 Presynaptic differentiation
2.3.3 Synapse elimination
2.3.4 Synapse maturation
2.4 Function of the neuromuscular junction
3. Neuromuscular disorders
3.1 Motor neuron diseases: Amyotrophic lateral sclerosis
3.2 Neuromuscular junction disorders: Myasthenia gravis
3.3 Myopathies: Duchenne muscular dystrophy
4. Stem cells
4.1 Induced pluripotent stem cells
4.1.1 iPSC-derived motor neurons
4.1.2 iPSC-derived skeletal muscle
4.1.3 iPSC-derived perisynaptic Schwann cells
5. iPSC-derived models of the neuromuscular junction
5.1 2D iPSC-derived models of the neuromuscular junction
5.2 Hybrid models of the neuromuscular junction
5.3 3D iPSC-derived models of the neuromuscular junction
Chapter 1 - Optimization of a protocol to generate and characterize 3D MN spheroids derived
from iPSCs of healthy donors
An optimized workflow to generate and characterize iPSC-derived motor neuron (MN)
spheroids
Abstract
Introduction

Materials and methods
Results
Discussion
References
Figures
Supplementary Materials
Chapter 2 - Using 3D iPSC-derived MN spheroids carrying mutations linked to fALS to
investigate disease-related phenotypes
Mutations in SOD1 induce ALS-related phenotypes in 3D iPSC-derived motor neuron (MN)
spheroids
Abstract
Introduction
Materials and methods
Results
Discussion
References
Figures
Supplementary Materials
Chapter 3 – Generation and characterization of 3D skeletal muscle structures for co-culture with
iPSC-derived MN spheroids within a microfluidic device to establish an in vitro 3D NMJ, along
with the development of high-content-compatible tools for analysis
Development of image-based analysis tools to assess in vitro 3D neuromuscular morphology
and function within a microfluidic device

Abstract	
Introduction	177
Materials and methods	180
Results	
Discussion	
References	196
Figures	
Supplementary Materials	
Discussion	
Conclusion	
References	224

Abstract

The neuromuscular junction (NMJ) is a highly specialized synapse where motor neuron (MN) neurotransmitter release generates the electrical stimulation of skeletal muscle, inducing its contraction. Neuromuscular disorders (NMDs) selectively affect MNs, the motor endplate, and/or myofibers, leading to NMJ dysfunction. To gain a deeper understanding of the mechanisms driving NMDs, various research groups have pursued the generation of human models of the NMJ in vitro. The generation of these models primarily relies on the use of induced pluripotent stem cells (iPSCs), which can generate all cell types of the human body, including MNs and muscle cells. In particular, three-dimensional (3D) iPSC-derived models using microfluidic devices have yielded meaningful results in NMD modeling, demonstrating increased physiological relevance by enhancing cell-to-cell and cell-to-matrix interactions and compartmentalizing the MN soma from skeletal muscle, as observed in vivo. However, a significant challenge in translating these systems to preclinical research is the lack of a truly scalable model for drug development, along with limited access to analysis tools compatible with current high-content approaches. We aimed to develop a human in vitro 3D NMJ model within a microfluidic device, with the potential to be scalable and suitable for high-content analysis.

We established a reproducible workflow to generate and characterize the 3D presynaptic component of the model: iPSC-derived MN spheroids. These spheroids can be produced in large quantities and express well-known MN markers at both transcriptional and protein levels. Additionally, they were able to protrude neurites when plated onto a scaffold and remained functional throughout the entire analysis period.

iPSC-derived MN spheroids generated through our optimized workflow proved to be a reliable model for studying NMDs. Using iPSC lines harboring mutations in *SOD1*, a gene linked to the onset of familial amyotrophic lateral sclerosis (ALS), we demonstrated that these spheroids recapitulate several disease phenotypes associated with ALS, such as altered *SOD1* expression, reduced cell viability, downregulation of neurofilament subunit expression, and disrupted activity.

The 3D postsynaptic component of our model, the skeletal muscle micro-tissue, was generated from primary and iPSC-derived myoblasts. We developed two image-based tools that effectively analyze intracellular calcium changes and contractility in both primary and iPSC-derived skeletal muscle micro-tissues, demonstrating their reproducibility. These tools are intended for future applications, specifically for assessing muscle function triggered by MN stimulation. Furthermore, both types of skeletal muscle micro-tissues successfully formed 3D NMJs when co-cultured with iPSC-derived MN spheroids within a microfluidic device, as confirmed by an additional image-based tool developed to analyze NMJ morphology.

In conclusion, we have successfully developed a human *in vitro* 3D NMJ within a customized microfluidic device, designed with dimensions suitable for scaling into a 96-well plate format. Additionally, we have developed image-based tools to analyze various aspects of the 3D NMJ, which can be adapted for high-content approaches, essential for advancing these models toward the preclinical setting.

Résumé

La jonction neuromusculaire (JNM) est une synapse hautement spécialisée où la libération de neurotransmetteurs par le motoneurone (MN) génère la stimulation électrique du muscle squelettique, induisant sa contraction. Les maladies neuromusculaires (MNM) affectent sélectivement les MN, les plaques motrices et/ou les myofibres, entraînant un dysfonctionnement de la JNM. Pour mieux comprendre les mécanismes à l'origine des MNM, des modèles humains de la JNM in vitro ont été générés. Ces modèles reposent principalement sur l'utilisation de cellules souches pluripotentes induites (CSPi), qui peuvent se différencier en n'importe quel type de cellules de l'organisme, y compris en MN et en cellules musculaires. Démontrant une pertinence physiologique accrue, les modèles tridimensionnels (3D) dérivés des CSPi utilisant des dispositifs microfluidiques ont donné en particulier des résultats significatifs dans la modélisation des MNM, en améliorant les interactions cellule-cellule et cellule-matrice, et en compartimentant le soma du MN du muscle squelettique, comme observé in vivo. Cependant, l'absence d'un modèle véritablement adapté au développement de médicaments et un accès limité aux outils d'analyse compatibles avec les études à haut contenu actuelles constituent un défi important dans l'utilisation de ces systèmes en recherche préclinique. Notre objectif était donc de développer un modèle 3D de JNM humaine in vitro évolutif et adapté à l'analyse à haut contenu dans un dispositif microfluidique.

Nous avons établi une méthode de travail reproductible pour la génération et la caractérisation de la composante présynaptique en 3D de notre modèle: les sphéroïdes de MN dérivés de CSPi. Ces sphéroïdes expriment des marqueurs spécifiques des MN au niveau transcriptionnel et protéique, et peuvent être produits en grande quantité. Ils sont également

capables de projeter des neurites lorsqu'ils sont placés dans une matrice et restent fonctionnels pendant toute la période d'analyse.

Les sphéroïdes de MN dérivés de CSPi générés grâce à notre méthode de travail optimisée se sont avérés être un modèle fiable pour l'étude des MNM. En utilisant des lignées de CSPi porteuses de mutations dans *SOD1*, un gène lié à l'apparition de la sclérose latérale amyotrophique (SLA) familiale, nous avons démontré que ces sphéroïdes récapitulent plusieurs phénotypes associés à la maladie, tels qu'une altération de l'expression de *SOD1*, une réduction de la viabilité cellulaire, une régulation à la baisse de l'expression de la sous-unité des neurofilaments et une perturbation de l'activité neuronale.

La composante postsynaptique en 3D de notre modèle, le microtissu musculaire squelettique, a été générée à partir de myoblastes primaires et de myoblastes dérivés de CSPi. Nous avons développé deux outils d'imagerie permettant l'analyse des changements de calcium intracellulaire et de la contractilité des microtissus musculaire squelettique primaires et dérivés de CSPi, démontrant leur reproductibilité. Ces outils sont destinés à des applications futures, en particulier à l'évaluation de la fonction musculaire déclenchée par la stimulation des MN. Par ailleurs, l'utilisation d'un outil supplémentaire d'imagerie développé pour l'analyse de la morphologie des JNM a confirmé la formation de JNM en 3D entre les deux types de microtissus musculaire squelettique et des sphéroïdes de MN dérivés de CSPi co-cultivés dans un dispositif microfluidique.

En conclusion, nous avons développé avec succès une JNM humaine *in vitro* en 3D à l'intérieur d'un dispositif microfluidique sur mesure, dont les dimensions permettent une mise à l'échelle dans un format de plaque 96 puits. En outre, nous avons développé des outils d'imagerie

pour l'analyse de la JNM en 3D, pouvant être adaptés à des approches à haut contenu, essentielles pour l'utilisation de ce modèle dans un cadre préclinique.

Acknowledgments

My deepest thanks to my supervisor, Thomas Durcan, who welcomed me as an intern in 2017 and gave me the opportunity to conduct science in Canada for the first time, later inviting me back as a graduate student. Thank you for listening to my crazy ideas and encouraging me to explore them. Your guidance has been essential in shaping the neuroscientist I am today. I am truly grateful for your approachability, unwavering support throughout my degree, and the meaningful relationship we have built over the years. Thank you for being an unconventional PI!

To my parents, I love you both deeply and am incredibly grateful for your constant support and for always prioritizing my education. Being away from home has been one of the most difficult things I have ever done. Your encouragement, even from afar, has been a guiding force throughout this journey. I miss you every day.

To my husband, Cochis, who cheered me on after long days of failed experiments, listened to my endless rants, and stayed up with me through late writing nights. Our "retozaciones" kept my writing spirit going. Thank you for pushing me through procrastination (by extensive mockery) and celebrating my small victories, like perfectly aligning the panels of a figure, and the big ones, like finishing my degree!

To my little brother Max, who is a driving force behind all the goals I set for myself. I will always strive to be the best version of myself so I can set a great example for you and make you proud.

To my grandmothers, Leticia and Rebeca, who are my greatest examples of women's empowerment.

To my aunt Gaby, whose inspiration led me to pursue a career in science and who has always been a role model.

To my uncles, Leonel and Ismael, and my aunts, Irais and Liliana, thank you for being a part of my education and growth as a person.

To my cousins, Lalo, Ismaelito, Frida, Abraham and Iker, thanks for keeping things fun and reminding me not to take life too seriously.

To my stepfather, Enrique, thank you for your constant support over the years and for helping me seize numerous valuable opportunities.

To my cats, Benito and Freyja, who graciously served as my personal stress relief bags, offering purrs and occasional naps during the chaos of my degree and thesis writing.

To my labmates in the Early Drug Discovery Unit (EDDU), I would not have been able to complete this work without you. A special shout-out to Anna Flowers, who has become a close friend and provided me with incredible support during very difficult times in my research project (I couldn't have done it without you!).

To Daniel and Mathilde, senior researchers who played a pivotal role in shaping my technical foundation as a scientist. I am grateful for the knowledge and expertise you have shared with me.

To Elise, Hugo, and Lena at eNUVIO Inc., who supported me scientifically and cheered me on every step of the way. A heartfelt thanks to Mark, who always cared about my well-being and was there to boost the progress of my project.

To Bunny, my dear friend, thank you for always being there during every existential crisis.

Our conversations never fail to bring both a smile and a laugh, regardless of the situation.

To all my friends, both in Mexico and here in Canada, for their incredible support in so many ways.

To my Advisory Committee, Dr. Benoit Gentil, Dr. Simon Wing, and Dr. Stefano Stifani, for their presence at the Committee Meetings and dedicating their time to providing me with scientific feedback throughout my entire degree.

To the internal and external examiners of my PhD Oral Defense Committee, Dr. Natasha C. Chang and Dr. Nicolas Dumont, thank you for dedicating your time to reviewing my PhD Thesis and contributing to the graduating process.

Finally, I extend my thanks to the institutions and organizations that provided financial support over the years: the Integrated Program in Neuroscience at McGill University, the Healthy Brains, Healthy Lives and NeuroSphere initiatives at McGill University, the Quebec Consortium for Drug Discovery (CQDM), Muscular Dystrophy Canada (MDC), Mitacs-Accelerate, and eNUVIO Inc. My sincere appreciation goes to the ALS Society of Canada, which, in addition to funding my work, also provided me with a community that inspired my daily research.

Contribution to original knowledge

In recent years, there has been growing interest in developing human three-dimensional (3D) *in vitro* neuromuscular junction (NMJ) models, as they more accurately mimic human physiology in both control and disease conditions compared to conventional two-dimensional (2D) models. However, the limited scalability of existing 3D systems, along with a limited number of instruments and analytical techniques capable of high-content analysis, has hindered their application in preclinical research. To address these challenges, I aimed to develop a human *in vitro* 3D NMJ with potential for scalability and suitability for high-content analysis.

In a paper published in the journal *Cells* in February 2023 (1), I optimized a protocol to generate and characterize 3D induced pluripotent stem cell (iPSC)-derived motor (MN) spheroids, the presynaptic component of the NMJ, at the morphological, transcriptional, protein and functional levels. This comprehensive characterization involved the development of a number of methods and software, some of which are compatible with high-content image acquisition and analysis. In addition to enhancing our understanding of this model's features, the tools described in this study will assist other researchers in assessing other 3D systems.

In a second paper following up on this work, uploaded onto BioRxiv and submitted to *Acta Neuropathologica Communications* to be considered for publication (2), I applied the characterization tools developed, along with additional techniques, to demonstrate that iPSC-derived MN spheroids provide valuable insight for modeling neuromuscular disorders (NMDs). iPSC-derived MN spheroids harboring *SOD1* mutations associated with familial amyotrophic lateral sclerosis (fALS), a condition that selectively affects MNs, effectively recapitulated several disease-related phenotypes. Moreover, we demonstrated that the long-term culture enabled by this

3D model is crucial for observing certain phenotypes that only emerge at time points inaccessible to 2D models.

Finally, in collaboration with eNUVIO Inc. through a Mitacs-Accelerate award, we developed a customized microfluidic device to co-culture iPSC-derived MN spheroids and skeletal muscle microtissues, representing the 3D postsynaptic component of the NMJ. This approach enables the replication of the spatial gap between the MN soma and skeletal muscle observed *in vivo*, thereby enhancing the physiological relevance of the model. Importantly, the device was designed with scalability in mind, allowing for future adaptation to a 96-well plate format. In a third manuscript, which we are preparing for publication, we successfully developed a timeline for generating 3D NMJs within our microfluidic device. Additionally, we developed three image-based techniques that can be adapted for high-content analysis of NMJ morphology and skeletal muscle responses to stimuli. Taken together, our findings contribute to the development of a model that could be employed in future preclinical settings.

Contribution of authors

Chapter 1

The following authors contributed to the manuscript presented in Chapter 1: María José

Castellanos-Montiel, Mathilde Chaineau, Anna Kristyna Franco-Flores, Ghazal Haghi, Dulce

Carrillo-Valenzuela, Wolfgang E Reintsch, Carol X.-Q. Chen, Thomas M. Durcan.

MJC-M: Conceptualization, methodology, validation, formal analysis, investigation, data curation,

writing-original draft preparation, writing-review and editing, visualization, project

administration, funding acquisition.

MC: Methodology, validation, writing-review and editing.

AKF-F: Software, investigation.

GH: Investigation.

DC-V: Data curation.

WER: Software.

CX-QC: Investigation,

TMD: Validation, writing-review and editing, supervision, project administration, funding

acquisition.

All authors have read and agreed to the published version of the manuscript.

Chapter 2

The following authors contributed to the manuscript presented in Chapter 2: María José

Castellanos-Montiel, Anna Kristyna Franco-Flores, Michael Nicouleau, Ghazal Haghi, Sarah

11

Lépine, María Baeza-Trallero, Carol X.-Q. Chen, Taylor M. Goldsmith, Nathalia Aprahamian, Doris Hua, Mathilde Chaineau, Lale Gursu, Eric Deneault, Narges Abdian, Thomas M. Durcan.

MJC-M: Conceptualization, study design, data collection, result analysis, and the writing, reviewing, and editing of the manuscript.

AKF-F: Data collection, result analysis, and the reviewing and editing of the manuscript.

MN: Generation and validation of the CRISPR/Cas9-edited iPSC lines.

GH: Generation and characterization of iPSC-derived MNPCs.

SL: Development of image analysis pipelines.

MB-T: Image analysis.

CX-QC: Performance of quality control analyses for all iPSC lines.

TG: Performance of quality control analyses for all iPSC lines.

NA: Performance of karyotyping of all iPSC lines.

DH: Image acquisition and analysis.

MC: Analysis of results, funding acquisition, and reviewing and editing of the manuscript.

LG: Generation and characterization of AIW002-02 iPSC-derived MNPCs.

NA: Performance of the quality control analyses for the AIW002-02 iPSC line.

ED: Generation of the CRISPR/Cas9-edited iPSC lines.

TMD: Study design, funding acquisition, and the reviewing and editing of the manuscript.

All authors have read and agreed to the published version of the manuscript.

Chapter 3

The following authors contributed to the manuscript presented in Chapter 3: María José Castellanos-Montiel, Anna Kristyna Franco-Flores, Mark Aurousseau, Mathilde Chaineau, Ghazal Haghi, Sarah Lépine, Carol X.-Q. Chen, Taylor M. Goldsmith, Narges Abdian, Wolfgang Reintsch, Andrea Krahn, Thomas M. Durcan.

MJC-M: Conceptualization, study design, data collection, result analysis, funding acquisition, and the writing, review, and editing of the manuscript.

AKF-F: Substantial collection of data.

MA: Study design, result analysis and the review and editing of the manuscript.

MC: Study design, and the review and editing of the manuscript.

GH: Generation and characterization of AIW002-02 iPSC-derived MNPCs.

SL: Generation and characterization of AIW002-02 iPSC-derived MNPCs.

CX-QC: Performance of quality control analyses for the AIW002-02 iPSC line.

TG: Performance of quality control analyses for the AIW002-02 iPSC line.

NA: Performance of quality control analyses for the AIW002-02 iPSC line.

WR: Image acquisition.

AK: Image acquisition.

TMD: Study design, funding acquisition, and the reviewing and editing of the manuscript.

List of abbreviations

AChE-Acetyl choline sterase

AChR – Acetylcholine receptor

ACh-Acetyl choline

ALS – Amyotrophic lateral sclerosis

AP – Action potential

BMP – Bone morphogenetic protein

Ca²⁺ - Calcium

CNS – Central nervous system

CST – Corticospinal tract

DHPR – Dihydropyridine receptors

DM-Dermomyotome

DMD – Duchenne muscular dystrophy

fALS – Familial amyotrophic lateral sclerosis

FGF – Fibroblast growth factor

HD-MEAs – High-density MEAs

ICM – Inner cell mass

IN-Interneuron

iPSC – Induced pluripotent stem cell

JF – Junctional fold

K⁺ – Potassium

LMN – Lower motor neuron

M1 – Primary motor cortex

MEA – Microelectrode array

MG – Myasthenia gravis

MN – Motor neuron

MND – Motor neuron disease

MNPC – Motor neuron progenitor cell

MRF – Myogenic regulatory factor

MyHC – Myosin heavy chain

Na⁺ – Sodium

NF – Neurofilament

NMDs – Neuromuscular disorders

NMJ – Neuromuscular junction

NMP – Neuromuscular progenitor

NPC – Neural progenitor cell

PBMC – Peripheral blood mononuclear cells

PMC – Premotor cortex

pMN – Motor neuron progenitor domain

PSC – Perisynaptic Schwann cell

PSM – Presomitic mesoderm

RA – Retinoic acid

RyR – Ryanodine receptors

S1 – Primary somatosensory cortex

sALS – Sporadic amyotrophic lateral sclerosis

SHH – Sonic Hedgehog

SMA – Supplementary motor area

SMAD – Small mothers against decapentaplegic proteins

SR – Sarcoplasmic reticulum

SV – Synaptic vesicle

TGF- β – Transforming growth factor β

UMNs – Upper motor neurons

VGCC – Voltage-gated calcium channels

VGSC – Voltage-gated sodium channels

List of figures

Figure 1. Main differences between UMNs and LMNs	21
Figure 2. Early stages of embryonic development	24
Figure 3. Origin of spinal MNs	28
Figure 4. Skeletal muscle development	33
Figure 5. Organization of the sarcomere	35
Figure 6. Main components and function of the NMJ	42
Figure 7. Scaled plate for 3D NMJ cultures	220

Introduction

Studying the human neuromuscular junction (NMJ) is particularly challenging, as it can only be accessed directly through biopsies, amputations, or post-mortem tissue (3, 4). Consequently, the development of human *in vitro* NMJ models enables a more detailed exploration of the cellular features and molecular mechanisms present in this synapse under both healthy and pathological conditions. Currently, the generation of human *in vitro* NMJ models primarily relies on induced pluripotent stem cell (iPSC) technology, as these cells can differentiate into all human cell types, including motor neurons (MNs) and skeletal muscle, which are the main components of the NMJ (5, 6). Moreover, iPSCs can be derived from patients with neuromuscular disorders (NMDs), enabling the study of NMJ dysfunction *in vitro* (7, 8).

In vitro NMJ models can be broadly categorized into two-dimensional (2D) and three-dimensional (3D) approaches (9). Notably, 3D approaches have been shown to support longer culture periods and promote enhanced synaptic maturation of the NMJ (10, 11). To increase the physiological relevance of 3D cultures, researchers have incorporated microfluidic devices that compartmentalize the MN soma from skeletal muscle, mimicking the spatial organization observed in vivo (8, 10, 12). However, these 3D models rely on transgene-based approaches, optogenetics and other complex techniques, which, although effective, are neither scalable nor suitable for high-content applications. Therefore, the primary objective of this project is to develop a human in vitro 3D NMJ model within a microfluidic device, with the potential to be scalable and suitable for high-content analysis. For this project our aims were to:

 Optimize a protocol to generate and characterize 3D MN spheroids derived from iPSCs of healthy donors.

- 2. Use 3D iPSC-derived MN spheroids carrying mutations linked to familial forms of amyotrophic lateral sclerosis (fALS) to investigate disease-related phenotypes.
- 3. Optimize a protocol to generate and characterize human 3D skeletal muscle structures.
- 4. Establish co-culture conditions to generate an *in vitro* 3D model of the NMJ within a microfluidic device.
- 5. Develop high-content suitable tools to analyze different aspects of the 3D NMJ components.

Literature review

1. The corticospinal tract

1.1 Upper motor neurons and lower motor neurons

Within the central nervous system (CNS), the pyramidal or corticospinal tract (CST) is a complex neuronal pathway whose primary function is the cortical control of spinal cord activity, which mediates voluntary distal movements (13). The CST starts at the brain cortex, where upper motor neurons (UMNs) located in layer V of the primary motor cortex (M1), the primary somatosensory cortex (S1), the supplementary motor area (SMA), and the premotor cortex (PMC) project their axons to specific nuclei in the brainstem and the ventral horn of the spinal cord, where they synapse with lower motor neurons (LMNs). The LMNs, in turn, project to the periphery to innervate their target muscles (13, 14).

In addition to differences in cell body location and targets within and outside the CNS, UMNs and LMNs exhibit other fundamental differences (**Figure 1**). UMNs use glutamate as their main neurotransmitter to communicate with target cells, while LMNs release acetylcholine (ACh) to trigger muscle contraction. Additionally, spasticity is the primary clinical hallmark of UMN degeneration, while paralysis is more characteristic of LMN degeneration (15).

It should be emphasized that while UMNs and LMNs are fundamentally different, their classification into two discrete categories is meant to simplify the understanding of a highly interconnected and complex neural network.

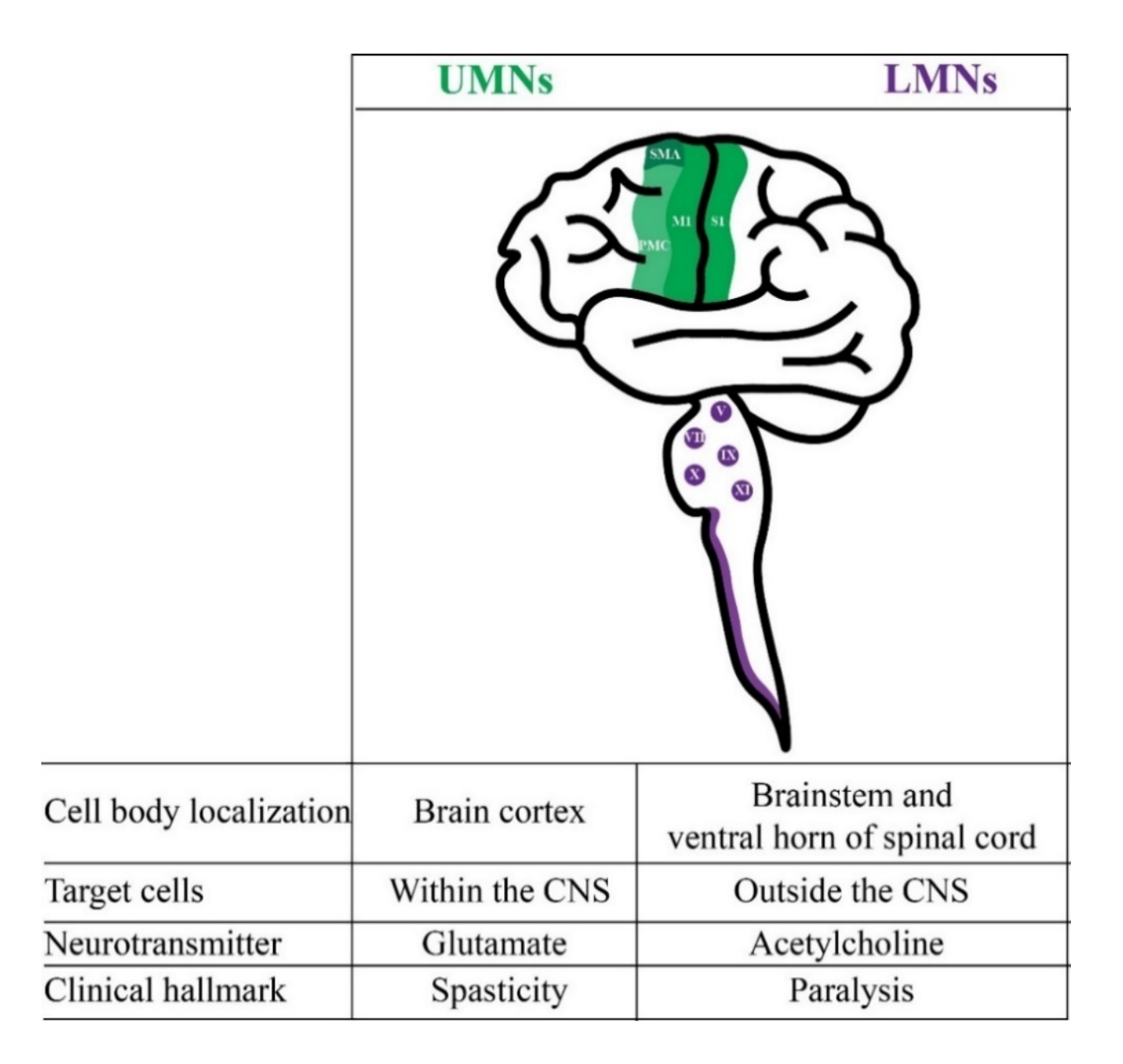


Figure 1. Main differences between UMNs and LMNs. Based on the location of the cell body, MNs can be broadly classified into UMNs and LMNs. UMNs are primarily located in the M1, S1, SMA and PMC of the brain cortex, while LMNs are in specific nuclei of the brainstem (V, VII, IX, X, XI) and the ventral horn of the spinal cord. Fundamental differences between these categories include the location of the target cell relative to the CNS, the primary neurotransmitter used, and the main clinical hallmark observed following lesion or degeneration. Figure created by María José Castellanos Montiel using Adobe Illustrator version 29.4.

1.2 Classification of lower motor neurons

LMNs are classified as somatic, brachial, or visceral based on the type of target they innervate (16). Somatic MNs, innervate skeletal muscles, the final effectors of the CST, enabling voluntary movements (17). Brachial MNs, a subtype of somatic MNs, control jaw movements, facial expressions, the larynx, and the pharynx via five cranial nerves: the trigeminal (V), facial (VII), glossopharyngeal (IX), vagus (X), and accessory (XI) (18). Visceral MNs, in contrast, are part of the autonomic nervous system and regulate cardiac muscles, smooth muscles, and glands (19). Although visceral MNs can be classified as LMNs due to their cell body localization within the CNS, they govern involuntary movements, and their activity is modulated by neuronal pathways distinct from the CST (15, 19).

Somatic MNs can be subdivided into α -MNs, γ -MNs, and β -MNs based on the type of muscle fibers (or myofibers) they innervate within a specific muscle target (15). α -MNs exhibit high expression of the DNA binding protein NeUN and innervate the force-generating extrafusal muscle fibers (20). γ -MNs, characterized by elevated expression of the orphan nuclear hormone receptor ERR3, target intrafusal muscle fibers found within muscle spindles, which relay proprioceptive information on the position and extension status of the muscle (15, 20). Compared to α -MNs and γ -MNs, β -MNs are less well-characterized; however, they are known to innervate both intrafusal and extrafusal muscle fibers, participating in muscle contraction and proprioception. (21).

2. The neuromuscular junction

2.1 Cellular components of the neuromuscular junction

 α -MNs innervate and activate their target skeletal muscles through highly specialized and organized synapses known as neuromuscular junctions (NMJs). The NMJ is considered a tripartite synapse, involving the interaction of the presynaptic MN, the postsynaptic myofiber and the terminal or perisynaptic Schwann cell (PSC) (22). A key feature of the NMJ is that the synaptic portions of all three cells contain high concentrations of organelles and molecules, which are typically found at lower concentrations in the extrasynaptic areas (23).

The presynaptic MN terminal is rich in 50-nm-diameter synaptic vesicles (SVs) containing ACh, along with a high density of mitochondria that supply the energy required for neurotransmitter synthesis and release (23, 24). SVs are clustered at the half-terminal facing the myofiber, with many concentrated in dense patches on the presynaptic membrane. These patches, known as active zones, are the sites where vesicles fuse with the membrane to release their contents into the synaptic cleft (4).

The postsynaptic membrane of the myofiber is sunken into gutters beneath the MN terminal, which then further invaginate to form approximately 1 μm-deep junctional folds (JFs) aligned with the active zones (23, 25). Acetylcholine receptors (AChRs) are densely concentrated at the crests (>10,000/μm²) and partially along the sides of the folds (23, 26). In turn, the deeper regions of the JFs contain a high concentration of voltage-gated sodium channels (VGSCs), which are responsible for initiating the action potential (AP) in the myofibers (27).

2.2 Developmental origin of neuromuscular junction components

The fertilized egg, or zygote, undergoes a series of cleavage divisions, which occur rapidly and without significant cell growth (Figure 2A). After several rounds of cleavage divisions (referred to as early cleavage stage) a structure known as the morula, consisting of 16-32 small cells called blastomeres, is formed. Continued cleavage divisions transform the morula into the blastula (Figure 2B). A fluid-filled cavity, the blastocoel, also forms within the blastula, facilitating cell movement for subsequent developmental stages. The blastomeres forming the outer layer of the blastula, known as the trophoblast, will give rise to the placenta, while a cluster of blastomeres within the blastula, referred to as the inner cell mass (ICM), will develop into the embryo (28). Subsequently, the blastula reorganizes into a multilayered structure called the gastrula through the process of gastrulation (Figure 2C). In mammals, gastrulation culminates in the formation of three primary germ layers: endoderm, mesoderm and ectoderm, each giving rise to progenies with restricted and distinct developmental fates. The endoderm is the innermost germ layer and gives rise to the gut tube, lungs, pancreas and liver. The mesoderm is the middle germ layer and forms connective tissues, muscle and most of the vascular system. The ectoderm is the outermost layer and develops into the skin and the neural plate, the precursor tissue of the peripheral and central nervous systems (29).

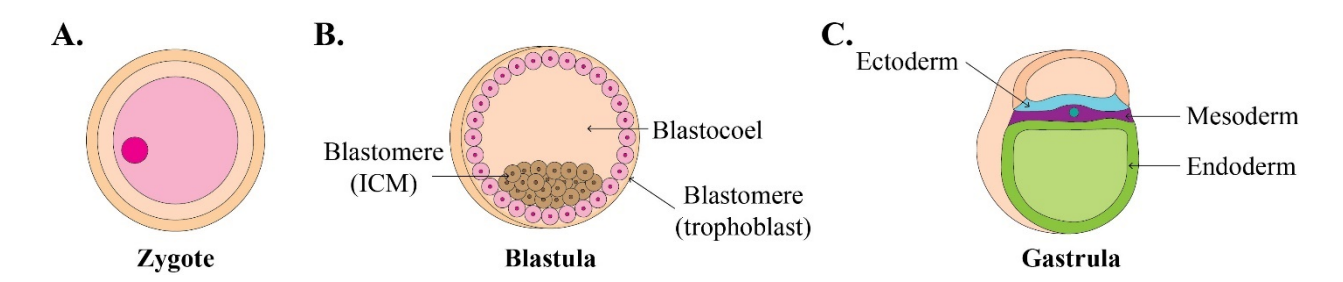


Figure 2. Early stages of embryonic development. A. Embryonic development starts with the fertilized egg or zygote, which undergoes rapid cleavage divisions to produce smaller cells called

blastomeres. At the end of the early cleavage stage, a structure called the morula, consisting of 16-32 blastomeres, is formed (not shown). **B.** Cleavage divisions continue, giving rise to the blastula, a structure composed of hundreds to thousands of blastomeres. The blastomeres of the trophoblast contribute to the formation of the placenta, while the blastomeres of ICM give rise to the embryo. Additionally, the blastocoel (fluid-filled cavity) forms to facilitate cell movement for subsequent developmental stages. **C.** Immediately after the formation of the blastula, cells migrate and rearrange to establish germ layers within a structure known as the gastrula. In mammals, three germ layers are identified: the endoderm, which gives rise to the gut tube, lungs, pancreas, and liver; the mesoderm, which forms connective tissue, vascular tissue, and skeletal muscle; and the ectoderm, which develops into the skin and nervous system. Figure created by María José Castellanos Montiel using Adobe Illustrator version 29.4.

2.2.1 Development of α-motor neurons

To trigger the formation of the neural plate (**Figure 3A**), the uncommitted ectoderm receives a signal from the organizer region (the notochord in mammals), which is composed of mesodermal cells. This signal consists of a mixture of multiple classes of proteins. Among them, bone morphogenetic protein (BMP) inhibitors play a critical role in neural plate formation. BMPs are members of the transforming growth factor β (TGF- β) superfamily, and they have been shown to prevent ectodermal cells from adopting a neuronal fate by promoting the acquisition of an epidermal fate (30). Thus, BMP inhibitors can induce ectodermal cells to differentiate into neural tissue.

Following its formation, the neural plate undergoes neurulation, a process in which it folds inward (**Figure 3B**) to form a tubular structure called the neural tube (**Figure 3C**). The spinal cord develops from the caudal region of the neural tube, while the brain arises from the rostral region. The rostrocaudal or anteroposterior axis of the neural tube is established by factors secreted by the neighboring mesoderm and endoderm (29). In particular, Wnt proteins are essential for guiding this process. The mesoderm flanking caudal regions of the neural plate secretes high levels of Wnt proteins, whereas the endoderm beneath the rostral region of the neural plate expresses Wnt signaling inhibitors (31). This differential secretion establishes a Wnt activity gradient that directs the rostrocaudal patterning. Once the neural tube has acquired its initial rostrocaudal organization, additional signals further refine this pattern. Notably, retinoic acid (RA) and fibroblast growth factor (FGF), secreted by the mesoderm at caudal levels of the neural axis, are essential for defining distinct subdomains within the hindbrain and spinal cord (29, 32).

Alongside rostrocaudal patterning, dorsoventral patterning also takes place within the neural tube. Here, we focus on the dorsoventral patterning of the caudal region of the neural tube, which gives rise to the spinal cord, where α -MNs are generated. In the spinal cord, neurons either relay sensory input to higher brain centers or are involved in the control of motor output (29). The neurons that perform these two functions are anatomically segregated, as they are generated at different positions along the dorsoventral axis. The neurons that control motor output, or MNs, are generated in the ventral half of the neural tube, while the neurons that process incoming sensory information are generated in the dorsal half of the neural tube (15, 29). The signaling required to establish the dorsoventral identity of spinal neurons is provided by the notochord and the epidermal ectoderm (**Figure 3C**).

The notochord, lying beneath the ventral neural tube, secretes high levels of Sonic Hedgehog (SHH) protein and induces the formation of floor plate cells, which also secrete SHH (33). This sequential secretion creates a ventral-to-dorsal gradient of SHH protein activity that directs progenitor cells in five cardinal ventral domains (pMN, p0, p1, p2, and p3) based on varying concentration thresholds (34). The pMN domain gives rise to spinal MNs which include α -MNs. In contrast, the p0, p1, p2, and p3 domains give rise to V0, V1, V2, and V3 ventral interneurons (INs), respectively (35). At the same time, the epidermal ectoderm, bordering the dorsal neural tube, emits BMP signals that induce the differentiation of the roof plate cells at the dorsal neural tube. Once the neural tube has completely closed, the roof plate cells begin to express BMPs, creating a dorsal-to-ventral gradient that promotes the establishment of six major dorsal progenitor domains (pd1, pd2, pd3, pd4, pd5, pd6) (36). These domains give rise to dI1, dI2, dI3, dI4, dI5 and dI6 INs, respectively (35). The progenitor domains formed along the dorsoventral axis are defined by distinct transcription factor profiles, which are well-described (35) (Figure 3D). In particular, motor neuron progenitor cells (MNPCs) from the pMN domain are characterized by the coexpression of PAX6 and OLIG2.

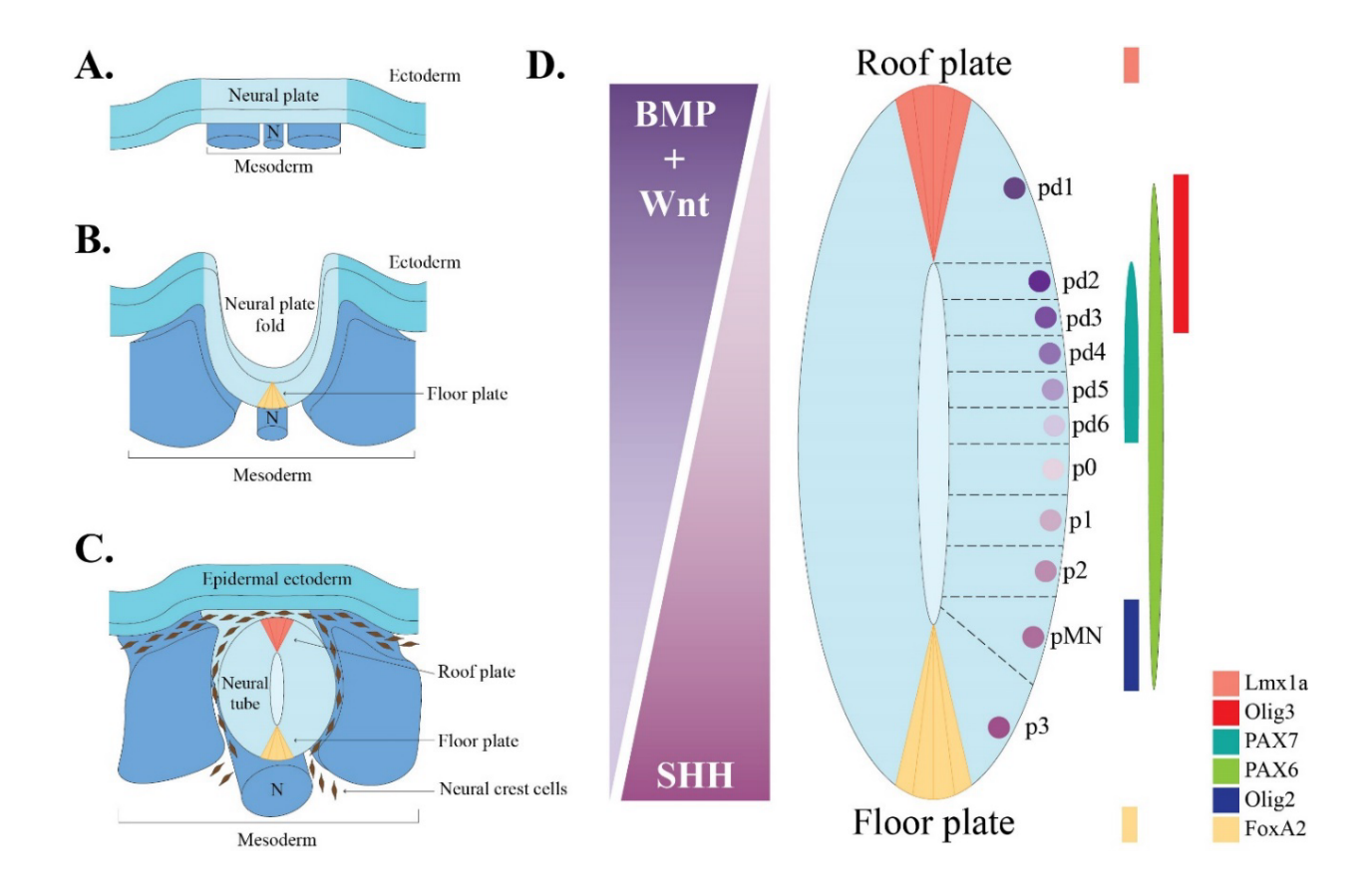


Figure 3. Origin of spinal MNs. A. The ectoderm gives rise to the skin and nervous system. A group of specialized cells in the mesoderm, the notochord (N), secretes high levels of BMP inhibitors, which prevent adjacent ectodermal cells from adopting an epidermal fate and instead promote the formation of neural tissue known as the neural plate. B. The neural plate folds inward during neurulation to form a tubular structure termed the neural tube. Chemical gradients along the neural plate pattern its rostroventral and dorsoventral axes. The mesoderm flanking the caudal neural plate secretes high levels of Wnt proteins, while the endoderm beneath the rostral neural plate expresses Wnt signaling inhibitors (not shown). This establishes a Wnt activity gradient that directs the rostrocaudal patterning of the neural tube. C. For dorsoventral patterning, the notochord induces the floor plate to secrete high levels of SHH, while the epidermal ectoderm induces the roof plate to secrete high levels of BMPs and Wnt proteins. D. These chemical gradients create five ventral domains and six dorsal domains with distinct transcriptional factor expression. Within

the ventral spinal cord, the MN progenitor domain (pMN) gives rise to spinal MNs, including α-MNs. Figure created by María José Castellanos Montiel using Adobe Illustrator version 29.4.

The differentiation of MNPCs into post-mitotic MNs is mediated by the transient coexpression of three LIM homeodomain transcription factors: 1) Insulin gene enhancer 1 (*ISL1*), 2)
LIM homeobox 3 (*LHX3*), and 3) MN and pancreas homeobox 1 (*MNX1*, also known as *HB9*)
(37). As MNs mature during development, LIM homeodomain transcription factors are
downregulated, while proteins involved in ACh synthesis and transport become increasingly
enriched. For instance, choline acetyltransferase (CHAT), which synthesizes ACh in the
cytoplasm, and vesicular acetylcholine transporter (VAChT), which loads ACh into synaptic
vesicles, are commonly used as markers of mature MNs (38, 39). Additionally, MNs are
characterized by high expression of non-phosphorylated neurofilament heavy (*NEFH*), a
neurofilament subunit protein expressed in mature neurons (40).

2.2.2 Development of skeletal muscle

In vertebrates, there are three types of muscle: smooth muscle, found in internal organs and surrounding blood vessels, facilitates peristalsis and regulates blood flow; cardiac muscle, restricted to the heart, is exclusively responsible for pumping blood; and skeletal muscle, attached to bones via tendons, enables voluntary movement (41). The focus here will be on the development of skeletal muscle, as it is the muscle type innervated by α -MNs to form NMJs.

The mesodermal germ layer gives rise to the paraxial mesoderm, a mesenchymal tissue that flanks both the neural tube and the notochord (**Figure 4A**). Initially formed as a continuous strip of tissue, the paraxial mesoderm undergoes sequential processes of presomitic mesoderm specification, somite formation, and somite specification (42).

First, during the presomitic mesoderm specification stage, the paraxial mesoderm develops into the presomitic mesoderm (PSM) in the posterior region of the embryo, induced by specific signaling molecules. In particular, chemical gradients of Wnt proteins, FGF proteins, and RA are essential to establish an anteroposterior axis along the PSM. Wnt and FGF proteins exhibit their highest expression in the posterior region of the PSM, while RA has its highest expression in the anterior region (43). As a result, the posterior region of the PSM remains unsegmented, whereas the anterior region undergoes somitogenesis, forming paired, repeating epithelial units called somites in an anterior-to-posterior direction (**Figure 4B**).

Notably, during somitogenesis, a subpopulation of cells called neuromesodermal progenitors (NMPs) has emerged as a crucial component of vertebrate development. NMPs are bipotent, possessing the capacity to differentiate into both neural tissue (specifically the spinal cord) and mesodermal tissue (such as the paraxial mesoderm), facilitating the generation of MNs or skeletal muscle (44). Although their exact developmental pathway remains undefined, NMPs are essential for the proper establishment of the body plan, playing a key role in body axis elongation.

Once formed, somite specification takes place. The ventral somite region undergoes an epithelial-to-mesenchymal transition to form the sclerotome, which will give rise to the axial skeleton and tendons. In contrast, the cells in the dorsal somite region remain epithelial and form the dermomyotome, which will develop into skeletal muscle, brown fat, and the dermis of the back

(45). Pax3, a transcriptional factor, is initially expressed in the forming somite, but its expression is reduced during sclerotome specification, whereas it continues to be expressed in the dermomyotome (46). Depending on the species, another transcriptional factor, Pax7, is also upregulated in the early steps of muscle development (47). Next, the dermomyotome subdivides into four distinct domains: the central domain, the dorsomedial lip, the anterior and posterior lips, and the ventrolateral lip. The central domain primarily contributes to the formation of the dermatome, which gives rise to the dermis and connective tissues of the back. In turn, cells from the four dermomyotomal lips delaminate as committed muscle progenitors (or myoblasts) and colonize the area beneath the dermomyotome to form the myotome, where myogenic differentiation begins to form the back muscles (Figure 4C). Also, committed myoblasts from the ventrolateral lip of the dermomyotome delaminate and migrate to the limb buds and only differentiate upon arrival to their target sites. Dermomyotome-derived myoblasts also migrate to form the diaphragm and tongue (41). All skeletal muscles (except the ones from the head) originate from the dermomyotome. Importantly, dermomyotomal progenitors commit to the myogenic lineage through the expression of Myf5 and/or MyoD—myogenic regulatory factors (MRFs) with partially redundant roles (48, 49).

Early myoblasts that form the myotome, as well as those migrating to the limbs, tongue, and diaphragm, are known as embryonic myoblasts. These cells undergo primary myogenesis to establish the basic muscle pattern. During this process, myogenin (or MyoG), an important MRF, contributes to the differentiation of embryonic myoblasts into myocytes, which are post-mitotic cells that fuse to form multinucleated myotubes (50). Myocyte fusion is a complex process primarily driven by myogenin, which directly regulates the expression of the fusogens *myomaker* and *myomerger* (51). *Myomaker* initiates fusion by enabling cells to become fusion-competent

(52), while *myomerger* drives the final stages of fusion by forming pores between cells, allowing their contents to combine and producing a single multinucleated cell known as a myotube (53). These primary myotubes, expressing structural proteins such as desmin and myosin heavy chain (MyHC) subunits, mature into primary myofibers, which extend from tendon to tendon and have complete contractile units (or sarcomeres) (Figure 4D). However, they are low in number and have small cross-sectional areas (41). Next, during secondary myogenesis, the myoblasts that did not differentiate in primary myogenesis undergo extensive proliferation. While some of these myoblasts, now designated as fetal myoblasts, remain in a proliferative state, others begin to differentiate. Once again, the expression of myogenin drives myoblasts to differentiate into myocytes that fuse to form secondary myotubes and, subsequently, secondary myofibers (50). Secondary myotubes align and extend along the primary myofibers in both directions until they span the full length of the muscle and insert into tendons. Unlike primary myofibers, secondary myotubes are numerous and will constitute the majority of adult myofibers. Importantly, transcriptional profiles differ between embryonic and fetal myoblasts. For instance, Pax3 is more expressed in embryonic myoblasts whereas Pax7, another transcriptional factor, is more abundant in fetal myoblasts (54). Another fundamental difference between primary and secondary myogenesis is the absence of a fully developed basal lamina (or basement membrane), a thin sheet that encases each myofiber and anchors it to the surrounding tissue. It has been hypothesized that basal lamina does not completely form during primary myogenesis to avoid interfering with α -MN innervation at this stage. Instead, the basal lamina begins to form more prominently during secondary myogenesis (55). Subsequently, during the postnatal period, a population of quiescent satellite cells, characterized by high Pax7 expression, becomes situated beneath this membrane. These satellite cells play a critical role in adult skeletal muscle tissue, as they can activate via the

expression of MRFs to proliferate and repair stress or injured tissue—a process known as adult myogenesis (56).

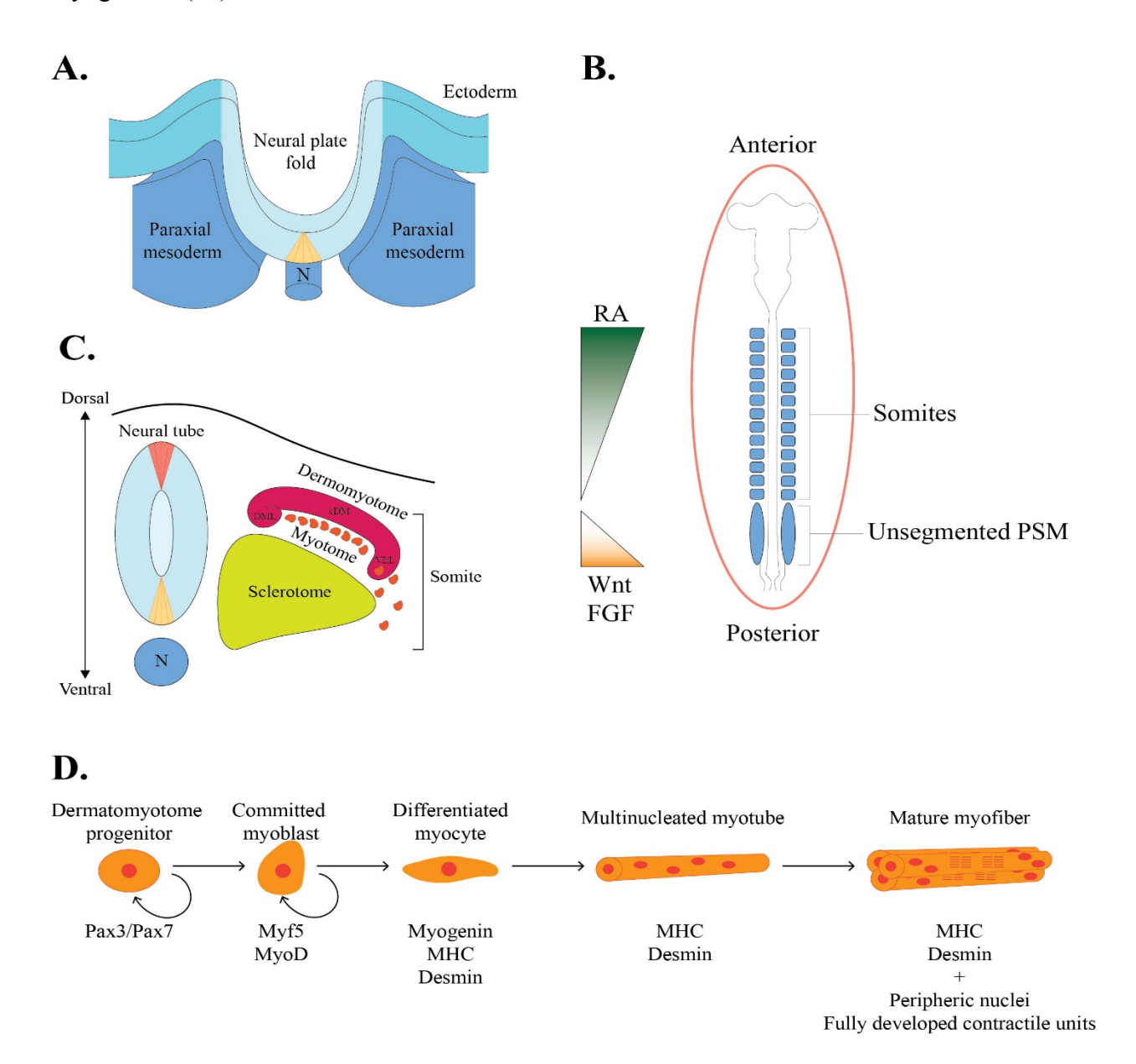


Figure 4. Skeletal muscle development. A. Skeletal muscle development begins with the specification of the paraxial mesoderm, which forms a continuous strip of tissue flanking the developing neural tube and notochord (N). **B.** Chemical gradients of RA, Wnt proteins and FGFs are required to establish the anteroposterior axis along the presomitic mesoderm (PSM). High

levels of Wnt proteins and FGFs prevent segmentation in the PSM, whereas high levels of RA are essential to induce somitogenesis in the embryo. **C.** Once formed, somites undergo a process of specification, wherein the dorsal region becomes the dermatomyotome (DM) and the ventral region becomes the sclerotome. Cells from the DM delaminate from the dorsomedial lip (DML) to form the myotome beneath it (which gives rise to trunk muscles) or delaminate from the ventrolateral lip (VLL) and migrate toward the limb buds (which give rise to limb muscles). **D.** Once at their target sites, committed myoblasts begin differentiating into myofibers, regulated by the expression of specific genes. Figure created by María José Castellanos Montiel using Adobe Illustrator version 29.4.

Towards the end of fetal development, the formation of new secondary myofibers slows down, as fetal myoblasts preferentially fuse with existing myofibers to increase their size. This growth pattern continues postnatally, as muscle mass undergoes intense expansion. However, up to a certain point after birth, myofiber growth does not rely entirely on the addition of new cells. Instead, adult myofibers also acquire their volume (process known as hypertrophy) by maintaining a balance between the synthesis and the degradation of proteins modulated by signaling molecules such as insulin growth-factor 1 (IGF-1) and growth hormone (57).

2.2.2.1 The sarcomere: the contractile unit of skeletal muscle

Myofibers are defined as a syncytium— multinucleated cells that shares a continuous cytoplasm (or sarcoplasm). Mature myofibers have their nuclei situated at the periphery, while their sarcoplasm contains fully assembled contractile units called sarcomeres. Ultrastructurally, a

sarcomere is divided into distinct zones (**Figure 5**): the isotropic band (I-band), which contains only actin (or thin) filaments; the anisotropic band (A-band), where actin and myosin (or thick) filaments overlap; the H-zone, located at the center and comprising only myosin filaments; the M-line, consisting of proteins that stabilize the thick filaments; and the Z-disk, which anchors actin filaments and delineates each sarcomere unit (58). The Z-disk is constituted by the ends of antiparallel actin filaments from adjacent sarcomeres, laterally cross-linked by α -actinin—a protein often used as a marker of mature skeletal muscle (59). Altogether, the components of the sarcomere promote muscle contraction by facilitating the sliding of actin filaments past the myosin filaments.

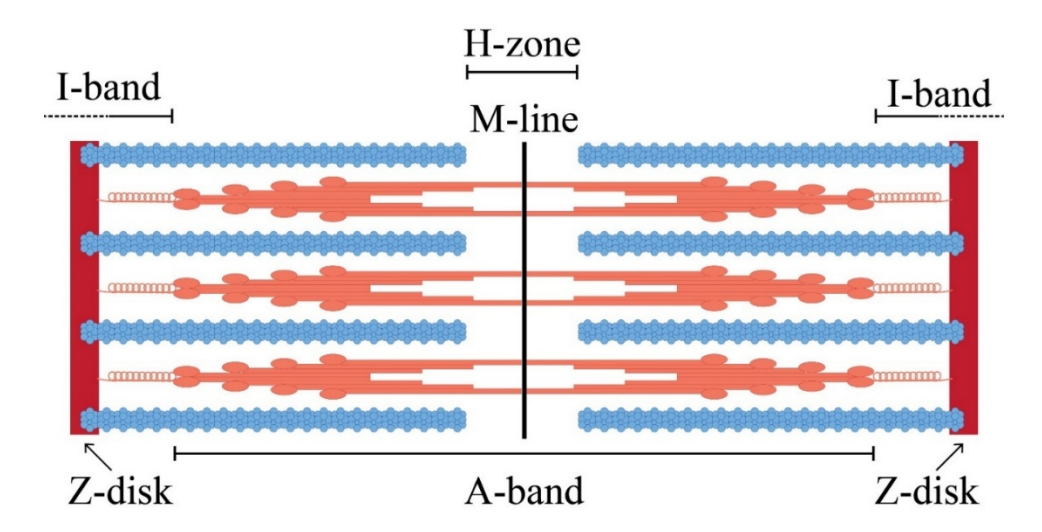


Figure 5. Organization of the sarcomere. The sarcomere is divided into distinct zones: the I-band contains only thin filaments, the H-zone contains only thick filaments, and the A-band represents the region of overlap between thin and thick filaments. Proteins at the Z-disk anchor the thin filaments, while proteins at the M-line stabilize the thick filaments. Figure created by María José Castellanos Montiel using Adobe Illustrator version 29.4.

2.2.2.2 Slow-twitch and fast-twitch myofibers

Over the years, myofibers have typically been classified as slow-twitch (Type I) or fast-twitch (Type II), with studies showing that their proportions vary across different skeletal muscles (60).

Slow-twitch fibers, known as Type-I fibers, are associated to MYH7 isoform expression. These fibers are linked to a greater reliance on aerobic metabolism, requiring oxygen to perform their functions. The steady ATP supply by aerobic metabolism promotes resistance to fatigue, making them ideal for endurance and long-duration activities (61).

In contrast, fast-twitch fibers, known as Type II, are associated to MYH2 (Type IIa) and MYH1 (Type IIx) isoform expression (45). Unlike Type I fibers, fast-twitch fibers are primarily linked to anaerobic metabolism, though Type IIa have been also reported to perform some aerobic functions. By providing a rapid source of energy without requiring oxygen, Type II fibers fatigue more quickly but are ideal for activities requiring rapid and intense movements. As they rely in less oxygen, they tend to appear pale or white due to their lower myoglobin content.

While this binary framework is useful for illustrating the presence of fibers with distinct characteristics, it can also be misleading, as it rests on broad assumptions—such as the notion that MyHC isoform expression directly reflects oxidative capacity, and force-generating potential (62). Moreover, recent transcriptomic and proteomic analyses have shown significant heterogeneity within traditional fiber types that extends beyond MyHC isoforms (63).

2.2.3 Development of perisynaptic Schwann cells

During neural tube dorsoventral patterning, roof plate cells begin secreting BMPs, which induce the differentiation of a population of stem cells known as neural crest cells. These cells delaminate from the neural rube and migrate into the periphery to generate the nerves and ganglia outside the brain and spinal cord, known as peripheral nervous system (**Figure 3C**). As neural crest cells migrate and encounter motor axons, they receive signals that specify them into Schwann precursor cells that later differentiate into PSCs at the NMJ (64).

2.3 Formation of the neuromuscular junction

Spinal α -MNs exit the ventral region of the neural tube and mix with sensory neurons to form the spinal nerves, which migrate together toward their skeletal muscle targets. Simultaneously, neural crest cells—the precursors of PSCs—migrate following motor axons to differentiate at their target sites. This coordinated process ensures the innervation of skeletal muscles, which occurs concurrently with the fusion of myoblasts into myotubes during primary myogenesis.

NMJ formation is a complex process that involves four critical events, all of which are dependent on the initial muscle-nerve contact: postsynaptic differentiation, presynaptic differentiation, synapse elimination, and synapse maturation.

2.3.1 Postsynaptic differentiation

The nerve mediates the differentiation of the postsynaptic membrane through three main mechanisms that localize AChRs to synapses: 1) agrin- and rapsyn-dependent clustering, synapsespecific transcription, and activity-dependent extrasynaptic repression.

AChR subunits are expressed by myofibers, assembled in the endoplasmic reticulum, and subsequently incorporated into the plasma membrane, where they to respond to neurotransmitter release from MNs. Initially, AChRs are diffusely distributed across the plasma membrane; however, following MN contact, they cluster in the postsynaptic membrane beneath the active zones of the presynaptic terminals. This process is orchestrated by the MN terminal through the secretion of agrin into the synaptic cleft, which interacts with proteins enriched at the postsynaptic membrane to mediate AChR clustering. Specifically, agrin interacts with MuSK, a transmembrane protein tyrosine kinase that is selectively expressed at skeletal muscle membrane (65). Downstream of MuSK, the cytoplasmic protein rapsyn plays a critical role in clustering by interacting with proteins that anchor and stabilize AChRs. In fact, once clusters form, AChRs and rapsyn co-localize at NMJs (66).

After muscle-nerve contact, a few myonuclei are repositioned beneath the presynaptic terminal, where they receive localized signals that drive synapse-specific transcription, including the high-rate transcription of AChR subunit genes. One important signal is agrin, while a trophic factor, neuregulin, has been identified as another key mediator of this process (67).

Soon after AChRs start to cluster at the synapse, the density of extrasynaptic AChRs starts to decline. This process results from the electrical impulse received by the myofiber during neurotransmission, which leads to the release of intracellular calcium. Calcium then binds to

protein kinase C (PKC), which phosphorylates and inactivates MRFs involved in the induction of AChR subunit genes along the entire myofiber (29). However, AChRs at the synapse are unaffected by this mechanism, as they are continuously stabilized and maintained through previously mentioned and other mechanisms (68).

2.3.2 Presynaptic differentiation

The differentiation of the presynaptic MN terminal primarily involves an increase in the number of SVs and their clustering at the active zones. These changes are only observed at the sites of contact with myofibers, implicating that target-derived factors drive presynaptic differentiation. For instance, FGFs (i.e., FGF7, FGF10, and FGF22), β2-laminins, and collagen IV—all components of the basal lamina—are known to be involved in the redistribution and local clustering of SVs at the presynaptic terminal (69).

2.3.3 Synapse elimination

A motor unit is defined as a single MN and the group of myofibers it innervates. Although a single MN can innervate multiple myofibers, each myofiber is innervated by only one MN (15). Initially, multiple immature presynaptic inputs converge at a myofiber; however, only one input remains as a result of a competitive process known as synapse elimination, which is mediated by both the nerve and the skeletal muscle. Anatomically, branches from all axons involved undergo atrophy, detachment, and withdrawal, until one axon loses the competition and retracts from the motor end plate (23). Synapse elimination is a complex process, whose multiple mechanisms are outlined in (70).

2.3.4 Synapse maturation

After synapse elimination, a subset of morphological and molecular changes occurs to achieve synapse maturation. For instance, the remaining presynaptic terminal largely modifies its arborization, JFs form at the postsynaptic membrane, and synaptic AChRs containing the embryonic gamma subunit ($\alpha 2\beta \gamma \delta$) are replaced by AChRs containing the adult epsilon subunit ($\alpha 2\beta \epsilon \delta$). Additionally, PSCs, which initially capped several axonal boutons, now cap individual terminal boutons (23).

2.4 Function of the neuromuscular junction

The unique arrangement of the JFs and their alignment with the active zones of the MN terminal enable the postsynaptic membrane to respond quickly and consistently to ACh release through the following sequence of events: The arrival of an AP induces the activation of voltage-gated calcium (Ca²⁺) channels (VGCCs) at the presynaptic terminal. The resulting influx of Ca²⁺, driven by its electrochemical gradient, triggers the exocytosis of SVs at the active zones, releasing ACh into the synaptic cleft. ACh then binds to AChRs on the postsynaptic membrane, opening the channels and facilitating the simultaneous inward movement of sodium (Na⁺) ions and outward movement of potassium (K⁺) ions, thereby generating a local depolarization known as the endplate potential. Typically, this depolarization reaches the threshold required to open VGSCs, which propagate the AP along the myofiber (71).

To transform the chemical signal into a mechanical response, the AP activates L-type VGCCs, also known as dihydropyridine receptors (DHPRs). These receptors, located in the postsynaptic membrane, allow the influx of Ca²⁺ into the cytosol. In skeletal muscle, these L-type

VGCC are mechanically coupled to ryanodine receptors (RyRs) in the sarcoplasmic reticulum (SR), which stores a significant amount of Ca²⁺. Consequently, the opening of L-type Ca²⁺ channels triggers the opening of RyRs further increasing intracellular Ca²⁺ levels. This elevated Ca²⁺ binds to troponin C, a component of the troponin complex, causing a conformational change that exposes myosin-binding sites on actin, previously blocked by tropomyosin. Myosin, previously unable to form cross-bridges, can now interact with actin through its globular heads, releasing adenosine diphosphate (ADP) and inorganic phosphate (Pi). This binding produces a power stroke, causing the thin actin filaments to slide past the thick myosin filaments, and resulting in muscle contraction. A new molecule of adenosine triphosphate (ATP) then binds to myosin, causing the cross-bridges to detach. The hydrolysis of ATP into ADP and Pi by myosin's ATP activity enables the cycle to repeat (72).

To halt neuromuscular synaptic transmission, ACh is enzymatically degraded by acetylcholinesterase (AChE) and cleared away from the synaptic cleft. Meanwhile, the presynaptic VGCCs close, and the membrane potential of the nerve terminal is reestablished through the opening of voltage-gated potassium channels (71).

Unlike myelin-forming Schwann cells, which are located in the preterminal portions of the axon and produce myelin sheaths, PSCs do not form myelin but instead cap the nerve terminal. In mammals, PSC processes are closely opposed to the terminal and its active zones, where they can sense neurotransmitter release and modulate synaptic activity (73). Notably, they are enriched with receptors that detect neurotransmission, such as L-type Ca²⁺ channels (74) and AChRs (75), as well as neuromodulators like nitric oxide (76). Additionally, PSCs have been implicated in synaptic formation, maintenance, plasticity, remodeling, and regeneration; a comprehensive review of these functions is available in (22).

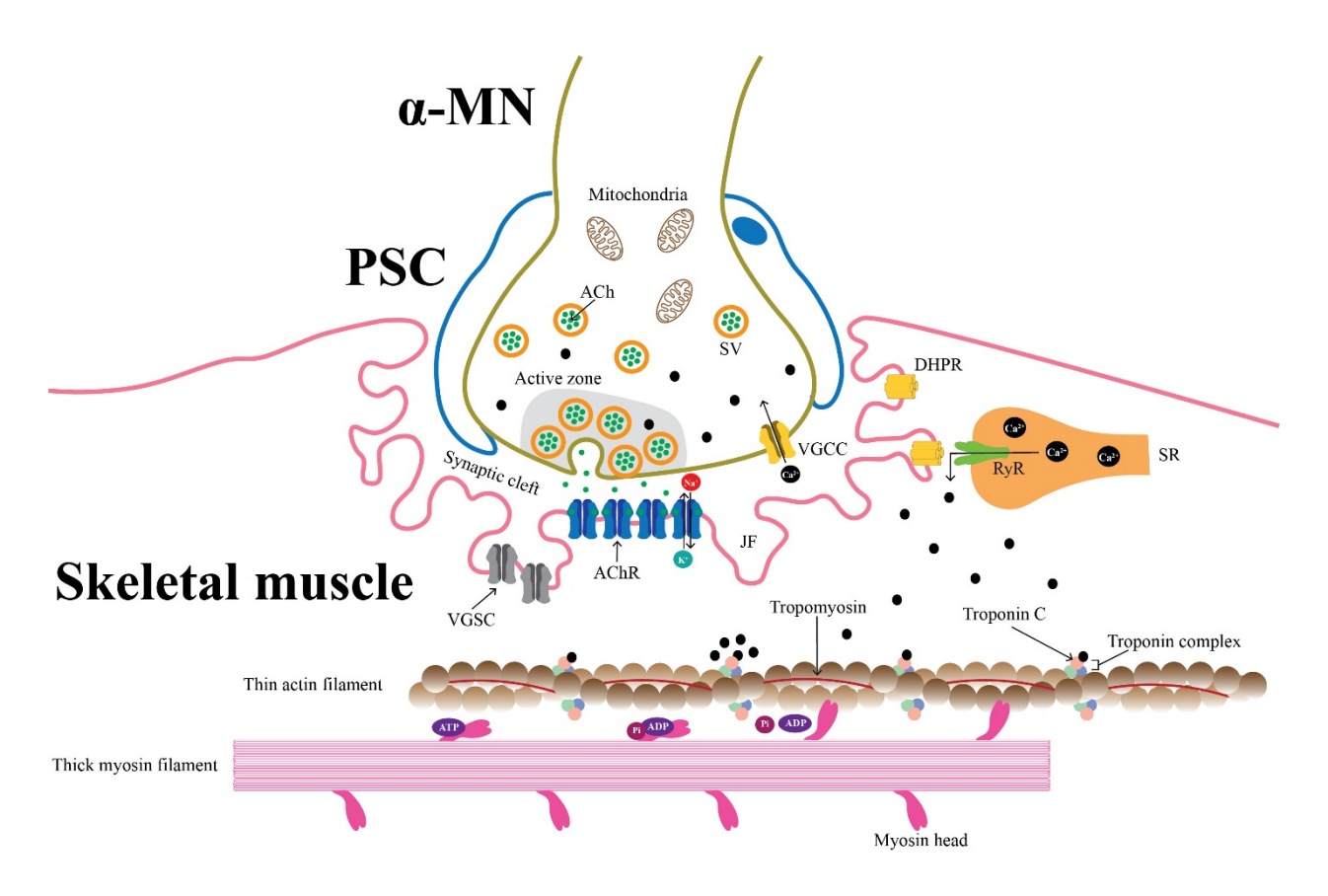


Figure 6. Main components and function of the NMJ. The NMJ is a tripartite synapse composed of the α -MN, the skeletal muscle and the PSC. These three cell types coordinate to transform the chemical signal into a mechanical response, starting with the arrival of the AP at the MN terminal. This depolarization event leads to an influx of Ca²⁺ into the terminal, triggering SV exocytosis and the release of ACh into the synaptic cleft. ACh binds to AChRs on the skeletal muscle membrane, promoting an inward flux of Na⁺ and an outward flux of K⁺. This ion exchange depolarizes the muscle membrane and activates VGSCs, propagating the AP along the muscle fiber. Subsequently, DPHRs allow Ca²⁺ influx into the skeletal muscle cytosol. At the same time, DPHRs mechanically activate RyRs on the sarcoplasmic reticulum, leading to a release of stored Ca²⁺ and a further increase in intracellular Ca²⁺ levels. The elevated Ca²⁺ concentration enables Ca²⁺ to bind to troponin C on the thin actin filaments, causing a conformational change that exposes myosin-binding sites. The binding of myosin heads to actin filaments releases ADP and Pi, and the resulting

power stroke slides the actin filaments past the myosin filaments, producing muscle contraction. ATP then binds to the myosin heads, detaching them from the actin filaments, and ATP hydrolysis by myosin's ATPase activity allows the cycle to repeat. Figure created by María José Castellanos Montiel using Adobe Illustrator version 29.4.

3. Neuromuscular disorders

Neuromuscular disorders (NMDs) are conditions that affect the motor unit at various levels, leading to impaired communication between MNs and skeletal muscle. In cases where dysfunction occurs within the cell body or axons of the MNs, it is classified as a motor neuron disease (MND). In turn, when pathology affects proteins directly involved in neuromuscular transmission, the condition is categorized as a NMJ disorder. Finally, if weakness and degeneration primarily affect myofibers themselves, the condition is referred to as a myopathy (71). Sections 3.1 to 3.3 will briefly describe the most common NMDs in each category, illustrating how NMJ disassembly triggered by diverse causes leads to the manifestation of a clinical phenotype.

3.1 Motor neuron diseases: Amyotrophic lateral sclerosis

Amyotrophic lateral sclerosis (ALS) is the most common MNDs, with an incidence of approximately 1-2.6 per 100,000 persons annually (77). It is a fatal adult-onset disease characterized by a selective progressive degeneration of both UMNs and LMNs, leading to muscle wasting and culminating in respiratory failure 3 to 4 years after diagnosis (78). Approximately 5-10% of cases follow a Mendelian pattern of inheritance and are classified as familial ALS (fALS).

Over the years, more than thirty genes have been linked to fALS, with the most common being *C9orf72*, *SOD1*, *FUS*, and *TARDBP* (79). The remaining ALS cases occur sporadically, meaning they lack a clear familial hereditary component, and are referred to as sporadic ALS (sALS). Currently, the major obstacle in treatment development is the disease's heterogeneity. In fact, the exact cause leading to MN death remains unclear and it has been suggested that multiple cellular pathways may be simultaneously affected to trigger disease onset (80). Also, environmental factors have been identified as potential triggers of the disease (81).

3.2 Neuromuscular junction disorders: Myasthenia gravis

Myasthenia gravis (MG) is a chronic autoimmune disease characterized by the production of autoantibodies against proteins that are important for maintaining NMJ structure. Most patients with MG produce autoantibodies against AChRs, while a minor proportion produces autoantibodies against other structural proteins such as agrin, MuSK, and rapysn (82, 83). The worldwide incidence of MG is 4.1–30 cases per million people annually (84). Although effective treatments are available for MG, patients may experience a reduced quality of life, and, in severe cases, the disease can be fatal (85).

3.3 Myopathies: Duchenne muscular dystrophy

Duchenne muscular dystrophy (DMD) is a severe and progressive disorder that causes muscle wasting. It results from mutations in the *DMD* gene, which encodes dystrophin, a protein enriched in skeletal muscle that links actin filaments to the extracellular matrix through membrane-

spanning glycoproteins, helping to prevent membrane damage during muscle contraction, among other functions (86). Symptoms typically appear between 2 and 3 years of age, and with optimal care, the median life expectancy is around 30 years, with patients most commonly succumbing to cardiac or respiratory failure (87). DMD is an X-linked recessive disorder, meaning it primarily affects males. The incidence of DMD is approximately 1 in 5,000 to 1 in 6,000 live male births, whereas it is extremely rare in females, with an estimated incidence of less than 1 in a million (88).

4. Stem cells

Stem cells are characterized by their unique ability to: 1) self-renew and 2) differentiate. Self-renewal refers to the capacity of stem cells to divide and produce identical copies of themselves, while differentiation refers to their potential to develop into specialized cell types. Based on their level of potency, stem cells can be classified as totipotent, pluripotent, multipotent, oligopotent or unipotent (89).

Totipotent stem cells, such as the zygote and early blastomeres, possess the ability to give rise to all cell types of an organism, including both embryonic and extra-embryonic tissues. Next, at the blastula stage, stem cells of the ICM restrict their potency and become pluripotent, capable of generating the three germ layers that constitute the entire embryo. Once the endoderm, mesoderm and ectoderm are established, cells within these layers further restrict their potency by becoming multipotent. For instance, cells of the neural plate, derived from the ectoderm, are considered multipotent, as they can differentiate into all neural and glial lineages (90). As development continues, stem cells become oligopotent, capable of differentiating into a narrower range of closely related cell types. A well-known example of this is myeloid progenitors, which

generate red blood cells, white blood cells, monocytes, and platelets. The final stage of potency is unipotency, where stem cells can only differentiate into a single cell type but retain their capacity for self-renewal. An example of this is muscle satellite cells, which, under normal physiological conditions, differentiate exclusively into myoblasts that mature into myocytes and fuse to form myofibers (89).

Totipotent and pluripotent stem cells are exclusive to embryonic development. However, tissues in the postnatal organism still contain multipotent, oligopotent, and unipotent stem cells, which play a key role in tissue repair and regeneration.

4.1 Induced pluripotent stem cells

In 2006, Yamanaka and his collaborators discovered a set of factors (Oct3/4, Sox2, c-Myc, and Klf4), whose induced expression in mouse adult fibroblasts could reprogram them into a pluripotent stem cell state that resembles ICM cells due to their ability to give rise to the three germ layers (91). These cells were referred to as induced pluripotent stem cells (iPSCs). In 2007, Yamanaka's group replicated their findings using human adult fibroblasts (92). Currently, it is possible to reprogram other somatic cells into iPSCs, including peripheral blood mononuclear cells (PBMCs), hair follicle keratinocytes, and renal tubular epithelial cells (93).

The discovery of iPSCs revolutionized cellular biology, and developmental biologists soon began optimizing protocols focused on modulating or inhibiting specific pathways to mimic the developmental processes that guide the differentiation of specific cell types. iPSCs can now be differentiated into cell types that are otherwise difficult to access, enabling their study *in vitro*. Moreover, they became crucial for disease research because they retain the donor's genetic

background, allowing researchers to create patient-specific disease models, including those for NMDs.

4.1.1 iPSC-derived spinal motor neurons

To date, several protocols exist for generating iPSC-derived spinal MNs (including α -MNs), which are typically the first to be affected in most NMDs (94). These protocols often incorporate small molecules along a defined timeline to mimic the developmental steps that guide MN differentiation, and they generally share three critical steps:

- 1. Neural induction is achieved through a process known as dual Small Mothers Against Decapentaplegic (SMAD) inhibition. SMADs are a family of intracellular signaling molecules that transduce the signals from the TGF-β superfamily, which includes Nodal, Activin and BMPs. Nodal and Activin are involved in mesodermal and endodermal specification through activation of SMAD2/3, while BMPs promote the acquisition of an epidermal fate via activation of SMAD1/5/8. Therefore, the addition of molecules that inhibit SMAD2/3 signaling, such as SB431542 and those that inhibit SMAD1/5/8, like dorsomorphin (known as DMH1), prevents iPSCs from acquiring endodermal, mesodermal or epidermal fates (6).
- 2. After neural induction, iPSCs are differentiated into neural progenitor cells (NPCs), which mimic the cells found in the neural plate. As discussed in Section 2.2.1, the establishment of a RA gradient is essential to refine the rostrocaudal organization of the neural tube. The rostral regions of the neural tube express low levels of RA, while the caudal regions express higher levels of RA. Thus, exposing NPCs to specific concentrations of RA drives their differentiation into progenitors with caudal neural fates, particularly those of spinal cord and parts of the hindbrain (95).

3. While NPCs are undergoing caudalization, it is also important to determine their dorsoventral identity. As described in Section 2.2.1, the formation of a ventral-to-dorsal gradient of SHH protein activity defines the ventral domains of the spinal cord. Thus, exposing NPCs to specific concentrations of molecules that activate the SHH signaling pathway, such as purmorphamine, can drive their differentiation into progenitors with ventral neural fates, including the pMN domain (96).

4.1.2 iPSC-derived skeletal muscle

In the same way as iPSC-derived MNs, systematic exposure to small molecules can generate iPSC-derived skeletal muscle from iPSCs. Multiple molecule-based protocols have been developed that are well described in (97, 98). Three essential steps are conserved across these protocols:

- 1. Wnt proteins are critical for both the formation and subsequent specification of the mesoderm. Notably, Wnt1 and Wnt3a play key roles in myogenic development by increasing the expression of Pax3 and Myf5 (99, 100). Consequently, activators of the Wnt signaling pathway, such as CHIR99021, are frequently employed to direct iPSCs toward the myogenic lineage.
- 2. Once committed myoblasts are achieved, inhibitors of differentiation are used to maintain the immature progenitor pool and stimulate their proliferation. In this context, FGF2 (also known as basic FGF or bFGF) has been shown to downregulate key MRFs required for differentiation, such as MyoD, myogenin, and MyHC (101).

3. Finally, terminal differentiation into skeletal muscle is achieved by allowing myoblasts to reach high confluence and introducing molecules that promote their differentiation into myocytes and subsequent fusion into myotubes. IGF-1 (102) is one of the most used molecules to enhance myotube formation, often in combination with other agents, such as glucocorticoids like dexamethasone and prednisolone (103).

Unlike MNs, the developmental cues driving skeletal muscle differentiation are not as well understood. Consequently, one of the biggest challenges in the iPSC skeletal muscle field remains the issue of low efficiency (97). However, continuous advancements in protocol optimization and the discovery of new developmental cues are gradually improving the efficiency of muscle differentiation.

4.1.3 iPSC-derived perisynaptic Schwann cells

Like iPSC-derived MN differentiation, iPSC-derived Schwann cell differentiation starts with neural induction. However, it also requires molecules that activate BMP signaling, such as BMP4, to induce a neural crest cell identity. Subsequently, the generation of Schwann cell precursors requires the addition of neuregulin, a signaling factor secreted by MNs *in vivo* (104). Regarding terminal differentiation of Schwann cells, available protocols primarily focus on generating myelin-producing Schwann cells. To date, there are no protocols specifically designed to generate iPSC-derived PSCs. A possible explanation for the lack of successful differentiation protocols is that the molecular and organizational interactions at the NMJ are essential for Schwann cell precursors to drive their specification toward PSCs (105). Supporting this idea, protocols generating iPSC-derived self-organizing neuromuscular cultures report the appearance of PSCs (7,

106). Also, the addition of iPSC-derived Schwann cell precursors into neuromuscular cultures promotes their specification toward PSCs (105). A deeper understanding of the developmental cues leading to the subspecification of PSCs is necessary to enable cell type-specific studies and manipulations.

5. iPSCs-derived models of the neuromuscular junction

Aiming to study the pathological mechanisms behind NMDs and perform drug testing in a human *in vitro* setting, several research groups have attempted to generate human iPSC-derived models of the NMJ. These models can be broadly divided into two dimensional (2D), hybrid, and three dimensional (3D) approaches.

5.1 2D iPSC-derived models of the neuromuscular junction

2D *in vitro* models of the NMJ were the first to appear. Initially, the 2D approach involved the creation of a monolayer of skeletal muscle, onto which MNs are subsequently layered, thus forming a 2D bilayer co-culture. Given the challenges associated with generating iPSC-derived skeletal muscle, early attempts to model the NMJ *in vitro* relied on iPSC-derived MNs and skeletal muscle from various animal sources. For example, a study showed that the co-culture of myotubes differentiated from an immortalized mouse myoblast line (C2C12) with iPSC-derived MNs from spinal muscular atrophy patients successfully recapitulated the early NMJ phenotype observed in this MND, which specifically affects LMNs (107). Aside from the limitation that one of the cell types does not originate from a human source, this model lacks the compartmentalization between the MN soma and skeletal muscle, as observed *in vivo*. Furthermore, it does not replicate the cell-

to-cell and cell-to-matrix interactions that cells acquire when cultured in 3D, which are known to influence their ability to form NMJs (11, 108).

To address challenges related to compartmentalization and cell source, later studies incorporated microfluidic devices that allow motor axons to contact skeletal muscle while spatially separating the MN somas. Additionally, researchers adopted primary myoblasts, obtained through biopsies, as the muscle cell source. Studies utilizing microfluidic devices to co-culture iPSC-derived MNs and primary myotubes demonstrated that this setup not only increased the physiological relevance of the model but also proved useful for localized drug testing (109, 110). This advantage arises because the spatial segregation of the two cell types enables independent treatment of the somatic and axonal compartments.

2D models of the NMJ were pioneers in NMD modeling. However, they still face a significant technical challenge: they cannot be cultured for prolonged periods. On one hand, iPSC-derived MNs are known to form clusters and detach from the surface over time (111). Similarly, muscle cells, regardless of their source, tend to detach quickly as they progress to final differentiation due to their high contractility (11).

5.2 Hybrid iPSC-derived models of the neuromuscular junction

Hybrid models refer to systems in which one cell type is cultured as a 2D monolayer, while the other is cultured as a 3D structure. For instance, in one study, iPSC-derived MNs were grown as 3D MN spheroids (or neurospheres) and co-cultured with 2D primary myotubes or iPSC-derived myotubes, successfully forming functional NMJs (112). In another study, a 3D structure composed

of iPSC-derived myotubes—either from control individuals or DMD patients—was co-cultured with 2D iPSC-derived MNs (113). This 3D muscle structure, commonly referred to as skeletal muscle micro-tissue (or engineered skeletal muscle), offers the advantage of parallel myoblast organization by utilizing a culture setup with two anchoring posts that mimic the function of tendons *in vivo*. This parallel alignment enhances fusion efficiency, resulting in the formation of more mature myotubes (11).

5.3 3D iPSC-derived models of the neuromuscular junction

3D models are products of the latest advances in bioengineering, biomaterials, and iPSC technology, representing the most innovative approaches for modeling the NMJ. For the presynaptic component, iPSC-derived MNs have been cultured as organoids (35) or MN spheroids (8, 10). Organoids are formed by seeding iPSCs in an environment that promotes their self-organization into 3D structures. These cells are then patterned into specific tissues, along with their associated cell types, by adding factors that mimic development. In contrast, spheroids are generated by directing cells toward a predetermined progenitor fate before promoting their 3D organization. While organoids achieve a higher level of maturation, their diverse and heterogeneous cell types introduce complexity that can complicate data interpretation and decrease reproducibility. Regarding the postsynaptic component, iPSC-derived skeletal muscle has been grown as skeletal muscle micro-tissues (11), spheroids (114) or organoids (115). While all promote a 3D maturation, skeletal muscle micro-tissues allow for a higher degree of alignment of the myotubes.

To achieve a high degree of physiological relevance, some research groups have developed human 3D NMJs composed of MN spheroids and skeletal muscle micro-tissues within microfluidic devices, which have been used to model MG (12) and ALS (8, 10). However, an important disadvantage of these protocols is their heavy reliance on genetic engineering to introduce the channelrhodopsin (ChR) cassette, which enables light-dependent stimulation of MNs (known as optogenetics). In addition to the technical and biological challenges of introducing external genetic material, optogenetics require a complex set up for data acquisition, making it incompatible with high-content approaches. Furthermore, the scalability of these co-culture systems has been limited to 24 co-cultures (116) in culture plates that are not compatible with high-content screening instruments.

Notably, protocols using iPSC-derived NMPs successfully generated functional neuromuscular organoids that recapitulated pathological aspects of spinal muscular atrophy (117) and MG (7). Furthermore, as organoid cultures can produce multiple cell types, these studies also reported the presence of PSCs, which are absent in many *in vitro* NMJ models. Another noteworthy study by Andersen et al. generated a model of the corticospinal tract, which had not yet been used to model disease (114). Although organoids are complex models, they lack the compartmentalization necessary to promote substantial MN axon elongation to innervate muscle cells, potentially masking phenotypes that affect these cells with very long axons. Additionally, as all cell types are merged within the same structure, genetic engineering is once again required to introduce cassettes containing fluorescent proteins for cell type identification.

In summary, the major challenges for advancing *in vitro* 3D NMJ models into preclinical research currently lie in developing a highly scalable system that is compatible with high-content screening. The introduction of genetic cassettes into cells involves complex, technically

demanding procedures, while existing methods for data acquisition and analysis are timeconsuming and unsuitable for high-content screening, which is essential for drug discovery and the advancement of personalized medicine.

In the following chapters, I present the development of an *in vitro* 3D iPSC-derived NMJ model that utilizes transgene-free approaches to differentiate cells. Additionally, this model was generated within a customized microfluidic device, which, if successful, has the potential to be scaled into a 96-well format. Finally, we developed various imaging tools to analyze different aspects of the NMJ components through a high-content approach.

Chapter 1 – Optimization of a protocol to generate and characterize 3D MN spheroids derived from iPSCs of healthy donors

The goal of this project was to establish a human *in vitro* 3D NMJ. To achieve this, the first objective was to generate a 3D structure containing the presynaptic component of the NMJ, namely the LMN. In a published study (1), we described the modification of a protocol previously adapted by our group for generating 2D iPSC-derived MNs (118, 119) to produce 3D structures composed of iPSC-derived MNs, referred to as iPSC-derived MN spheroids. To optimize this new 3D version of the protocol, we used two control iPSC cell lines, AIW002-02 and 3450 (120), which had been previously validated. Additionally, we provided a detailed description of the tools developed to profile these spheroids at morphological, expression, and functional levels.

Our results demonstrate that we successfully differentiated the AIW002-02 and 3450 iPSC lines into 3D MN spheroids in a reproducible manner. These iPSC-derived MN spheroids exhibited no morphological differences and expressed well-established MN markers (e.g., ISL1, HB9, and CHAT) at both the transcript and protein levels. Finally, we confirmed that these MN spheroids were capable of extending axons when seeded onto a coated surface and remained active up to the final analysis point at 28 days post-plating.

An optimized workflow to generate and characterize iPSC-derived

motor neuron (MN) spheroids

María José Castellanos-Montiel¹, Mathilde Chaineau¹, Anna Kristyna Franco-Flores¹, Ghazal

Haghi¹, Dulce Carrillo-Valenzuela¹, Wolfgang E. Reintsch¹, Carol X-Q Chen¹, Thomas M.

Durcan1*

* Correspondance: thomas.durcan@mcgill.ca

Author's affiliations:

¹The Neuro's Early Drug Discovery Unit (EDDU), McGill University, 3801 University Street,

Montreal, QC H3A 2B4, Canada.

Abstract

A multitude of in vitro models based on induced pluripotent stem cell (iPSC)-derived motor

neurons (MNs) have been developed to investigate the underlying causes of selective MN

degeneration in motor neuron diseases (MNDs). For instance, spheroids are simple 3D models that

have the potential to be generated in large numbers that can be used across different assays. In this

study, we generated MN spheroids and developed a workflow to analyze them. To start, the

morphological profiling of the spheroids was achieved by developing a pipeline to obtain

measurements of their size and shape. Next, we confirmed the expression of different MN markers

at the transcript and protein levels by qPCR and immunocytochemistry of tissue-cleared samples,

respectively. Finally, we assessed the capacity of the MN spheroids to display functional activity

in the form of action potentials and bursts using a microelectrode array approach. Although most

56

of the cells displayed an MN identity, we also characterized the presence of other cell types,

namely interneurons and oligodendrocytes, which share the same neural progenitor pool with

MNs. In summary, we successfully developed an MN 3D model, and we optimized a workflow

that can be applied to perform its morphological, gene expression, protein, and functional profiling

over time.

Keywords: iPSC; motor neurons; spheroids; 3D model; motor neuron disease; MEA; CUBIC

57

1. Introduction

Motor neurons (MNs) are a subset of efferent neurons within the nervous system responsible for innervating the muscles of the body, promoting their contraction through highly specialized and structurally organized synapses termed neuromuscular junctions (NMJs) (1). When the connection between MNs and skeletal muscle deteriorates or becomes interrupted as a result of MN degeneration, it leads to the development of a number of disorders known as motor neuron diseases (MNDs), which include amyotrophic lateral sclerosis (ALS), the most common disease in this category (2, 3). Recently, an epidemiologic study estimated ~260,000 individuals living with MNDs worldwide in 2019 (3). Additionally, the analyzed data revealed that the global burden of MNDs is continuously increasing (3), highlighting the urge to develop new therapies for these diseases, which currently have no cure.

Animal models have been widely used to elucidate the disease mechanisms behind MNDs. However, rising doubts about the translatability of animal models to human patients due to failures in clinical trials, ethical concerns, and other disadvantages (4, 5) have promoted the parallel development of in vitro models to increase our knowledge of MNDs and accelerate drug discovery (4). With the advent of induced pluripotent stem cell (iPSC) technology, new approaches have emerged to generate and culture different cell types of the human body in vitro, including MNs (6). Human iPSCs are generated by expressing the Yamanaka's factors in adult somatic cells such as skin fibroblasts (FBs) or peripheral blood mononuclear cells (PBMCs) (7, 8). Thus, iPSCs can be derived from healthy individuals or patients with MNDs. In a disease context, patient-specific iPSCs retain the genetic background of the patient and, when differentiated into MNs, they can display characteristics of the diseases in vitro (9, 10). Remarkably, in cases where a monogenic mutation is identified as the primary cause of the disease, CRISPR-Cas9 genome editing can be

used to correct the mutation, generating isogenic controls that facilitate precise genotype and phenotype correlations (11, 12, 13, 14). In addition to the latter advantage, iPSC-derived neurons allow researchers to study sporadic MND cases (9), which has never been achieved with other model systems. Taken together, these advantages open up new insights and therapeutic avenues to explore.

Most protocols available to generate iPSC-derived MNs are typically optimized to obtain two dimensional (2D) monolayer cultures (15, 16, 17, 18, 19, 20), which have allowed the study of pathogenic molecular mechanisms associated with MNDs such as cytoskeletal abnormalities, axonal transport deficits, and changes in excitability (21, 22). However, several lines of evidence suggest that the absence of three-dimensional (3D) cell-to-cell and cell-to-matrix interactions may be detrimental to the maturation (23, 24, 25), differentiation (26), and morphology (27, 28) of cells grown in vitro. In addition, technical challenges arise when culturing iPSC-derived MNs as 2D monolayers. For instance, the cell bodies of the MNs often form clusters, making them unsuitable for some assays (29, 30, 31) such as microelectrode array (MEA) analyses, which become challenging due to MNs randomly clustering away from the recording electrodes. Moreover, the clustering cells are prone to detachment from the surface (31), preventing their long-term culture and making the damaged floating monolayer of cells difficult to analyze by immunofluorescent staining or MEA. Maintaining cultures over several weeks is a critical aspect in MND modelling considering that disease phenotypes might only appear after a long period of culture. While some groups are optimizing 2D protocols to reduce the aggregation of iPSC-derived MNs (29, 32), other groups are developing techniques to generate 3D cultures that include spinal organoids (33, 34, 35, 36) and MN spheroids (25, 37, 38, 39) to address some of the technical issues that arise with 2D monolayers and to enhance MN maturation by exposing the cells to a 3D environment. In fact,

such 3D in vitro cultures have been proposed as an alternative to bridge the gap between current pre-clinical animal models and human studies given their greater physiological relevance compared to conventional monolayer cultures (5). Within 3D in vitro models, spheroids have the advantage of being scaffold-free systems, opposed to organoid cultures, whose formation relies on the use of natural or synthetic matrices (40). Typically, Matrigel is the preferred matrix for organoid generation, however, it is known to have high lot-to-lot variability that can impact culture results (40, 41). In addition, spheroids are smaller in size compared to organoids, making them less prone to some of the technical issues associated with 3D cultures such as the heterogenous distribution of components (i.e., oxygen and nutrients) (40). Finally, there is no need for expensive and highly specialized equipment to maintain spheroids in culture, making them more cost effective than organoid approaches (40).

MN spheroids can be generated by making modifications to previously established 2D protocols (25, 37, 38, 39, 42). Plating neural stem cells (NSCs) (25, 37, 43), motor neuron progenitor cells (MNPCs) (43), or MNs (38, 39) onto a low-attachment surface takes advantage of their ability to spontaneously assemble into clusters and form spheroids in which they can continue their differentiation towards MNs. Even though these MN spheroids show expression of well-known MN markers (i.e., pan-MN marker motor neuron and pancreas homeobox 1/ISL LIM homeobox 1 (HB9/ISL1) and choline acetyltransferase (CHAT)), a characterization at the gene expression and protein levels using different markers to identify the presence of other cell types such as interneurons (INs) and glial cells within MN spheroids is lacking. Additionally, the development and optimization of a defined workflow to analyze these 3D structures in more detail is a challenging task that needs to be addressed. With this in mind, we adapted a previously established 2D protocol (44) to generate 3D MN spheroids from iPSC-derived MNPCs that can be

grown and maintained for up to 28 days, and longer if needed. By applying tissue-clearing, 3D optical imaging, and quantitative real-time PCR (qPCR), we characterized the identity of the cells within the MN spheroids and found that the majority of the cells expressed MN markers. Moreover, by performing microelectrode array (MEA) activity recordings, we confirmed that these MN spheroids contain electrically-active neurons.

The differentiation process from iPSCs towards a desired cell type can be time-consuming. Thus, a technical advantage associated with the selected protocol for MNPC generation is that it allows for their storage and expansion (12, 16). Importantly, we showed that these MNPCs retain their capacity to proliferate and form MN spheroids across passage number, saving time for the end user and increasing the cost-effectiveness of the process. This work describes the optimization of several techniques that can help bridge the gap of information observed in similar studies. For instance, our protocol showed that optical opacity, often portrayed as a disadvantage of 3D models (40), can be easily overcome in this type of model by performing a tissue-clearing protocol that preserves the cytoarchitecture of the samples and enables the visualization of proteins by immunocytochemistry using conventional fluorescence microscopy. Moreover, we outline our workflow to obtain activity readouts from MN spheroids, which are not suitable for classic patchclamp analysis (40). All together, we develop a new, reliable, and efficient pipeline to characterize MN spheroids that has the potential to be applied to other types of neural spheroids. Easy to maintain and generated at high numbers, spheroids represent a simple model that has the potential to be applied to different assays and to be used as a cellular jigsaw, in which other cell types can be added to form more advanced co-culture spheroids.

2. Materials and methods

2.1. Generation and Maintenance of Human iPSCs

Two control iPSC lines were used to optimize the protocols constituting the workflow for this study: AIW002-02 and 3450. The complete profiles of the iPSCs, culture conditions, and quality control analysis have been published (12, 45, 46). The 3450 and AIW002-02 iPSCs were thawed and passaged in Matrigel-coated dishes. To choose the ideal culture medium, iPSCs were cultured in E8 and mTeSR1 media. The medium promoting the fastest growth rate of the cells without having an impact on their overall attachment, spontaneous differentiation, and morphology was selected to maintain each iPSC line. The 3450 iPSC line exhibited a faster growth rate when cultured in E8 medium, while the AIW002-02 iPSC line exhibited a faster growth rate when cultured in AIW002-02 medium (45). Both iPSC lines were between passage 8 and 12 after performing the reprogramming and quality control steps. For every independent differentiation, iPSCs were kept under passage 15. Genomic stability testing at different passages through karyotyping and qPCR has shown that exceeding 15 passages can lead to the appearance of genomic alterations (45). Prior to the experiments, the iPSCs were found to be free from mycoplasma, hepatitis B/C, and HIV 1/2 virus.

2.2. Generation of iPSC-Derived MN Spheroids

Starting from iPSCs, we adapted a previously described protocol (12, 16) to derive MNPCs (Supplementary Figure S1) that can be used to generate MN spheroids. The media and biochemicals used to generate MN spheroids are listed in Table 1. Consumables and equipment

are listed in Supplementary Table S1. The media compositions for the different differentiation steps are listed in Table 2.

Table 1. List of media and biochemicals.

Reagents	Supplier/Manufacturer	Working Concentration	Catalogue Number
Accutase *	Thermo Fisher Scientific, Waltham, MA, USA	1X	A1110501
Antibiotic-Antimycotic (Anti-Anti)	Thermo Fisher Scientific, Waltham, MA, USA	1X	15240-062
B-27 supplement * BDNF * CHIR-99021 Compound E Dimethyl sulfoxide	Thermo Fisher Scientific, Waltham, MA, USA PeproTech, Cranbury, NJ, USA Selleckchem, Houston, TX, USA STEMCELL Technologies, Vancouver, BC, Canada	0.5X 10 ng/mL 3 μM or 1 μM 0.1 μM	17504-044 450-02 \$2924 73954
(DMSO)	Thermo Fisher Scientific, Waltham, MA, USA	10%	BP231-1
DMEM/F-12 medium DMH1 E8 medium	Thermo Fisher Scientific, Waltham, MA, USA Selleckchem, Houston, TX, USA Thermo Fisher Scientific, Waltham, MA, USA	1Χ 2 μΜ 1Χ	10565018 S7146 A1517001
Fetal bovine serum (FBS)	Thermo Fisher Scientific, Waltham, MA, USA	1X	12484-028
Gentle cell dissociation reagent (GCDR)	STEMCELL Technologies, Vancouver, BC, Canada	1X	07174
GlutaMAX supplement	Thermo Fisher Scientific, Waltham, MA, USA	0.5X	35050-061
Laminin *	Sigma-Aldrich, St. Louis, MO, USA	5 μg/mL	L2020
L-Ascorbic acid (AA)	Sigma-Aldrich, St. Louis, MO, USA	100 μM	A5960
Matrigel *	Corning, New York, NY, USA	1X	354277
MTeSR1 medium	STEM CELL Technologies, Vancouver, BC, Canada		85850
N-2 supplement *	Thermo Fisher Scientific, Waltham, MA, USA	0.5X	17502-048
Neurobasal medium	Thermo Fisher Scientific, Waltham, MA, USA	1X	21103-049
Phosphate buffer saline (PBS)	Wisent Products, Saint-Jean-Baptiste, QC, Canada	1X	311-010-CL
Poly-L-ornithine (PLO)	Sigma-Aldrich, St. Louis, MO, USA	$10 \mu g/mL$	P3655
Purmorphamine (Pur)	Sigma-Aldrich, St. Louis, MO, USA	0.5 μM or 0.1 μM	SML-0868
Retinoic acid (RA)	Sigma-Aldrich, St. Louis, MO, USA	$0.1 \mu\text{M} \text{ or } 0.5 \mu\text{M}$	
SB431542	Selleckchem, Houston, TX, USA	2 μM	S1067
Valproic acid (VPA)	Sigma-Aldrich, St. Louis, MO, USA	0.5 μM	P4543
Y-27632 (ROCK inhibitor)	Selleckchem, Houston, TX, USA	10 μM	S1049

^{*} Note: Biochemicals with an asterisk are more susceptible to lot-to-lot variability. The main reason is the production source, either animal or human. It is therefore important to keep track of lot numbers. Regarding the Accutase solution, we noticed lot-to-lot variability in enzyme efficiency, as previously reported (46). To compensate for weaker enzyme activity, incubate for a longer time until the cells detach properly.

Table 2. Media composition.

Media	Components		
	• 1:1 Neurobasal: DMEM/F12		
	• 1X Anti-Anti		
	• 0.5X N-2		
	• 0.5X B-27		
Neural induction medium	 0.5X GlutaMAX supplement 		
	• 100 μM AA		
	• 3 μM CHIR-99021		
	• 2 μM SB431542		
	• 2 μM DMH1		
	• 1:1 Neurobasal: DMEM/F12		
	• 1X Anti-Anti		
	• 0.5X N-2		
	• 0.5X B-27		
	• 0.5X GlutaMAX supplement		
MNPC patterning medium	• 100 μM AA		
	• 1 μM CHIR-99021		
	• 2 μM DMH1		
	• 2 μM SB431542		
	• 0.1 μM RA		
	• 0.5 μM Pur		
	• 1:1 Neurobasal: DMEM/F12		
	• 1X Anti-Anti		
	• 0.5X N-2		
	• 0.5X B-27		
	• 0.5X GlutaMAX supplement		
ANIDO amanai an madimus	• 100 μM AA		
MNPC expansion medium	• 3 μM CHIR-99021		
	• 2 μM DMH1		
	• 2 μM SB431542		
	• 0.1 μM RA		
	• 0.5 μM Pur		
	• 0.5 μM VPA		
	1:1 Neurobasal: DMEM/F12		
	• 1X Anti-Anti		
	• 0.5X N-2		
MN induction and maturation medium *	• 0.5X B-27		
	• 0.5X GlutaMAX supplement		
	• 100 μM AA		
	• 0.5 μM RA		

- 0.1 μM Pur
- 0.1 μM Compound E
- 10 ng/mL BDNF

* The MN induction and maturation medium composition used in this study lacks two of the growth factors (CNTF and IGF-1) found in the original protocol (16). This decision was made to avoid technical challenges in future experiments, as (a) skeletal muscle, a cell type often co-cultured with MNs, undergoes hypertrophy in the presence of IGF-1 (47) and (b) a disease phenotype could be masked in MN spheroids generated from patient iPSC lines grown in the presence of CNTF, which promotes neurite formation and outgrowth (48).

2.2.1. Day 0 (D0): Seeding of iPSCs

Start from a 100 mm dish of human iPSCs with a confluence between 70 and 80%, containing less than 5% of spontaneously differentiated cells. Once cells are ready, aspirate the medium from the iPSC culture and wash with 5 mL of DMEM/F-12 containing 1X Antibiotic-Antimycotic (Anti-Anti). Add 5 mL of Gentle Cell Dissociation Reagent (GCDR) and incubate at room temperature (RT) for 4–5 min. Avoid incubating the iPSCs in GCDR for too long, as cells dissociated into single cells are not ideal for the induction process. Aspirate the GCDR and rinse the cells with 5 mL of DMEM/F-12 containing 1X Anti-Anti. Aspirate the medium and then add 5 mL of DMEM/F-12 containing 1X Anti-Anti. Gently detach the colonies with a cell scraper and transfer the cells to a 15 mL conical tube. Wash the dish with an additional 5 mL of DMEM/F-12 containing 1X Anti-Anti to collect the remaining detached cells. Determine the cell number using a cell counter. Transfer 2–3 million cells to a fresh 15 mL conical tube and pellet the cells by centrifugation at 1200 rpm for 3 min. Aspirate the supernatant. Gently resuspend the cells in 1 mL of neural induction medium containing ROCK inhibitor (10 µM). Transfer the cells to a Matrigel-

coated T-25 flask and add 4 mL of neural induction medium containing ROCK inhibitor (10 μ M). Distribute the cells uniformly and place the flask in a 37 °C/5%CO₂ incubator.

Note: The quality of the iPSCs (45) is crucial to the successful generation of MNPCs. Thus, mycoplasma tests should be performed routinely, ideally every other week, to confirm the absence of contamination before using the iPSCs. To verify the absence of mycoplasma from cultures, we used a mycoplasma detection assay (MycoAlertTM mycoplasma detection kit, Lonza) to measure the luminescence of 1.5 mL medium samples, according to manufacturer's instructions.

2.2.2. Day 1 (D1): Neural Induction

Within 24 h of plating the iPSCs, change the medium to 5 mL of neural induction medium without ROCK inhibitor. Continue to change the medium every other day until D6 to induce the cells towards a neural progenitor cell (NPC) identity.

Check the cell morphology and density of the cells 24 h after plating. The cells must be 30% confluent. If the cells are too confluent, causing the medium to turn yellow, change the medium every day until D6.

2.2.3. Day 6 (D6): MNPC Patterning

Six days after plating the iPSCs in neural induction medium, the cells should be 100% confluent and differentiated into NPCs. For the next step, cells will be plated on a T-25 and a T-75 PLO/laminin-coated flask. For PLO/laminin coating, PLO must be kept for at least 2 h, or overnight, then washed three times with 1X PBS and switched to laminin for a minimum of 2 h,

or overnight. Aspirate the neural induction medium and rinse the cells with 5 mL of DMEM/F-12 containing 1X Anti-Anti. Add 2 mL of GCDR and incubate at 37 °C for 5-7 min. After the incubation, cells will begin lifting from the dish. Gently tap the plate to allow for the complete detachment of the cells into the GCDR. Add 5 mL of DMEM/F-12 containing 1X Anti-Anti and transfer the cells to a 15 mL conical tube. Pellet the cells by centrifugation at 1200 rpm for 3 min. Aspirate the supernatant. Resuspend the cells in 4 mL of MNPC patterning medium containing ROCK inhibitor (10 µM) and gently pipette the cells up and down. Plate 3 mL of the cell suspension into the PLO/laminin-coated T-75 flask. Complete with 12 mL of MNPC patterning medium containing ROCK inhibitor (10 µM) to reach a final volume of 15 mL and distribute the cells uniformly. Plate the remaining mL of the cell suspension into the PLO/laminin-coated T-25 flask. Complete with 4 mL of MNPC patterning medium containing ROCK inhibitor (10 µM) to reach a final volume of 5 mL and distribute the cells uniformly. Place the flasks in a 37 °C/5%CO₂ incubator and, 24 h after plating the NPCs, change the medium to MNPC patterning medium without ROCK inhibitor. Continue to change the MNPC patterning medium every other day until D12.

Check the cell morphology and density of the cells 24 h after plating. The cells must be 50% confluent. If the cells are too confluent, causing the medium to turn yellow, change the medium every day until D12.

2.2.4. Day 12 (D12): MNPC Expansion

Six days after plating the NPCs in MNPC patterning medium, cells should be 70% to 100% confluent and patterned to MNPCs (Supplementary Figure S1). For the next step, cells will be

plated into four T-75 PLO/laminin-coated flasks. Split the cells following Section 2.2.3. Resuspend the cells in 4 mL of MNPC expansion medium containing ROCK inhibitor (10 μM) and gently pipette the cells up and down. Plate 1 mL of cell suspension into each of the four PLO/laminin-coated T-75 flasks. Complete with 14 mL of MNPC expansion medium containing ROCK inhibitor (10 μM) to reach a final volume of 15 mL and distribute the cells uniformly. Place the flasks in a 37 °C/5% CO₂ incubator. At 24 h after plating the MNPCs, change the medium to MNPC expansion medium without ROCK inhibitor. Continue to change the medium every other day until D18.

If the cells are too confluent, causing the medium to turn yellow, change the medium every day until D18.

2.2.5. Day 18 (D18): MNPC Storage, Split, or MN Spheroid Generation

MNPC storage: Six days after plating the MNPCs in MNPC expansion medium, cells should be 70% to 100% confluent. Proceed directly to freeze or split the cells. MNPCs can be frozen up to passage 3, depending on the cell morphology and density of the cells. MNPCs reduce their proliferation after 4 or more passages.

The 4 T-75 flasks in MNPC expansion medium can be frozen into 20 to 40 cryovials, with each vial containing ~3–5 million cells in 1 mL of FBS containing 10% DMSO.

MNPC thawing: Thaw the frozen cryovial of MNPCs in a 37 °C water bath by gently shaking the cryovial continuously until only a small, frozen cell pellet remains. Sterilize the outside of the cryovial with 70% ethanol. Transfer the cells to a 15 mL conical tube with 4 mL of DMEM/F-12

containing 1X Anti-Anti and pipette gently. Pellet the cells by centrifugation at 1200 rpm for 3 min. Aspirate the supernatant. Resuspend the cells in 5 mL of MNPC expansion medium containing ROCK inhibitor (10 μ M) and transfer them into a T-25 PLO/laminin-coated flask. Place the flask in a 37 °C/5% CO₂ incubator. At 24 h after plating the MNPCs, change the medium to MNPC expansion medium without ROCK inhibitor. Continue to change the MNPC expansion medium every other day for 6–7 days.

MNPC split: Before starting MN spheroid generation from a recently thawed MNPC cryovial, it is recommended to passage the cells at least once to allow their complete recovery. After each passage, plate two T-25 flasks. One flask will be used to keep the MNPC stock in culture (up to five passages) through GCDR dissociation, and the other flask will be used to initiate MN spheroid generation through Accutase dissociation. Split the cells following Section 2.2.3. Resuspend the cells in MNPC expansion medium containing ROCK inhibitor (10 μ M) and plate ~3–4 million cells into a PLO/laminin-coated T-25 flask. Complete with MNPC expansion medium containing ROCK inhibitor (10 μ M) to reach a final volume of 5 mL and distribute the cells uniformly and place the flask in a 37 °C/5% CO₂ incubator. Within 24 h of plating the MNPCs, change the medium to MNPC expansion medium without ROCK inhibitor. Continue to change the MNPC expansion medium every other day for 6–7 days.

MN spheroid generation: MNPCs are ready for differentiation when cells have been cultured in MNPC expansion medium for 6–7 days. Split the cells following Section 2.2.3, incubating with 2 mL of Accutase at 37 °C for 4–6 min instead of GCDR to achieve a single cell suspension. Monitor the cells so the dissociation can be stopped as soon as all cells have detached. Resuspend the cells in 1 mL of MN induction and maturation medium without ROCK inhibitor and pipette the cells up and down. Quantify cell number using a cell counter. Plate 5000 MNPCs in 100 μL

into each well of a 96 U-bottom ultra-low attachment plate in MN induction and maturation medium. Centrifuge the plate at 1200 rpm for 5 min using a centrifuge with adapters for cell culture plates. Place the culture plate in a 37 °C/5% CO₂ incubator. This centrifugation step will speed up the aggregation of the cells, thus speeding up the formation of the spheroids. However, the spheroids will also form (albeit at a slower rate) even if this step is not performed. To maintain the MN spheroids in culture over time, replenish each well of the 96 U-bottom ultra-low attachment plate with 50 µL of MN induction and maturation medium every 14 days.

Note: When plating the cells into the 96 U-bottom ultra-low attachment plate, avoid seeding cells in the outer wells of the plate. Evaporation of the medium is higher in these wells and it has a negative impact on spheroid formation. Instead, fill the outer wells with 200 µL of 1X PBS. Although rare, we have noticed random inappropriate formation of MN spheroids regardless of the iPSC line (Supplementary Figure S2). Instead of fusing into a single spheroid, MNPCs formed two or more spheroids. In this case, those spheroids were not considered for any further analysis.

2.3. Cell Profiler Macro for Size Profiling of MN Spheroids

The equipment used to profile the size of the MN spheroids is listed in Supplementary Table S1. Bright-field images of MN spheroids were acquired with a light microscope after culture for 14 and 28 days in MN induction and maturation medium. Importantly, the images acquired at the two different time points were always saved with their location within the plate (Ex. B2, B3, B4, B5...) in order to follow each MN spheroid growth over time. We performed measurements on 28–30 MN spheroids from each of five different batches for each cell line (AIW002-02 = 150 spheroids; 3450 = 145 spheroids). The images were analyzed by a modified version of a pipeline developed in our group using CellProfiler Analyst, www.cellprofiler.org (accessed on 1 August

2021) (46, 49), available online (https://doi.org/10.17605/OSF.IO/V84WS) (accessed on 27 September). Briefly, images of the spheroids obtained with a bright-field microscope are inverted, and speckles with a diameter smaller than 10 pixels are filtered out to eliminate cell debris and cells that were not incorporated into the spheroids. From this point, the primary object (named "Sphere") is identified using Otsu thresholding and its size and shape are measured (Supplementary Figure S3A). The primary objects identified as the final spheroids are overlaid with the original input image for visual control of the spheroid identification (Supplementary Figure S3B). As a result, the pipeline gives an CSV file with different measurements in pixels for each MN spheroid, including the min. Feret diameter (used as diameter) and the area. The measurements in pixels have to be manually transformed into µm (diameter) or µm² (area) according to the microscope scale if needed. The radius of each spheroid was calculated by dividing the min. Feret diameter by half and substituting it into the formula $(4/3 \prod r^3)$ to determine the volume of a sphere. In addition, to assess the circularity of the spheroids, the radius of each spheroid was substituted into the formula ($\prod r^2$) to determine the area of a circle, and a ratio between the calculated area and the area given by the software was performed. The efficiency of the CellProfiler pipeline to identify the primary objects (spheroids) highly depends on the pixel intensities through the entire bright-field image, meaning that sometimes cell debris or individual cells with a pixel intensity similar to the sphere lead to misinterpretation of the primary object (Supplementary Figure S3C). To establish a threshold that helped us define images in which the CellProfiler pipeline performed poorly, we used GraphPad Prism (created by Dotmatics, version 9.1.1, Boston, MA, USA) to identify outliers using the ROUT method with a Q = 1%. The images marked as potential outliers were checked to corroborate that they were not the actual size of the spheroid. A paired t-student was performed to compare the diameter, area, volume, and circularity

measurements of 14- and 28-day MN spheroids (AIW002-02 = 137 spheroids; 3450 = 142 spheroids).

2.4. qPCR Analysis of MN Spheroids

MN spheroids from one 96 U-bottom ultra-low attachment plate (60 spheroids) were pooled at 14 and 28 days for RNA extraction. The reagents to perform the qPCR from MN spheroid samples are listed in Table 3. The consumables and equipment are listed in Supplementary Table S1. The probes used for the qPCR analysis are listed in Table 4.

Table 3. List of reagents.

Reagents	Supplier/Manufacturer	Final Working Concentration per Reaction Tube	Volume (μL)	Catalogue Number
2X no UNG Taqman TM fast advanced master mix	Thermo Fisher Scientific, Waltham, MA, USA	N/A	N/A	A44360
miRNeasy micro kit	Qiagen, Hilden, Germany	N/A	N/A	217004
M1 mix				
Distilled water	N/A	N/A	12 μ1	N/A
dNTPs	New England BioLabs, Whitby, ON, Canada	0.5 Mm	2 μL of a 10 Mm stock	N0447L
Random primers	Thermo Fisher Scientific, Waltham, MA, USA	12.5 ng/Ml	$2~\mu L$ of a 250 ng/ μL stock	48190011
M2 mix				
DTT	Thermo Fisher Scientific, Waltham, MA, USA	0.01 M	$4~\mu L$ of 0.1 M stock	28025013
First strand buffer	Thermo Fisher Scientific, Waltham, MA, USA	1X	$8 \mu L \text{ of } 5X \text{ stock}$	28025013
M-MLV RT	Thermo Fisher Scientific, Waltham, MA, USA	400 U	$2~\mu L$ of 200 U/ μL M-MLV RT	28025013

Table 4. Probes/primers.

Gene Target	Reference	Supplier
$ACT\beta$	Hs01060665_g1	Thermo Fisher Scientific
ChAT	Hs00758143_m1	Thermo Fisher Scientific
GAPDH	Hs02786624_g1	Thermo Fisher Scientific
GFAP	Hs00909233_m1	Thermo Fisher Scientific
HB9	Hs00907365_m1	Thermo Fisher Scientific
ISL1	Hs00158126_m1	Thermo Fisher Scientific
MAP2	Hs00258900_m1	Thermo Fisher Scientific
MBP	Hs00921945_m1	Thermo Fisher Scientific
NANOG	Hs02387400_g1	Thermo Fisher Scientific

OCT4	Hs04260367_gH	Thermo Fisher Scientific
OLIG2	Hs00377820_m1	Thermo Fisher Scientific
PAX6	Hs01088114_m1	Thermo Fisher Scientific
SIM1	Hs00231914 m1	Thermo Fisher Scientific
VSX2	Hs01584046 m1	Thermo Fisher Scientific

Total RNA was isolated using the miRNeasy micro kit according to manufacturer's instructions. After RNA isolation, reverse transcriptions were performed to obtain cDNA. For each sample, 40 ng of total RNA was diluted in distilled water to reach a final volume of 10 µL. Next, 16 μL of M1 mix (distilled water, 0.5 mM dNTPs, and 12.5 ng/μL of random primers) was added to each reaction tube. A denaturation step was performed in the thermocycler at 65 °C for 5 min on the total RNA mixed with the M1 mix, constituting a volume of 26 μL. Finally, 14 μL of M2 mix (0.01 M DTT, 1X first strand buffer and 400 U M-MLV RT) was added to each reaction tube to make a total volume of 40 µL. The reverse transcriptions were performed with an incubation at 37 °C for 50 min followed by an incubation at 70 °C for 10 min in the thermocycler. qPCR reactions were performed in 384-well plates using the QuantStudio5 PCR machine. For each well, the PCR mix included 9 µL of 2X no UNG Tagman TM Fast Advanced Master, 0.5 µL of primers/probe mix, 1 μL of cDNA, and H₂O up to 10 μL. Serial dilutions of a mix of cDNA, consisting of cDNA from all the samples, ranging between 50 ng and 0.003052 ng, were used to generate a calibration curve for absolute quantification (12, 50, 51, 52). Expression levels were given as a ratio between the relative quantities of the gene of interest and the endogenous control. The mean between Actβ and GAPDH was used as the endogenous control for normalization.

2.5. Fixation, Tissue Clearing, and Immunofluorescent Staining of MN Spheroids

MN spheroids from 96 U-bottom ultra-low attachment plates (60 spheroids/plate) were fixed, cleared, and immunostained at 14 and 28 days (46, 53, 54). The reagents to perform the fixation and the immunofluorescent staining of the MN spheroids are listed in Table 5. The compositions to prepare the two solutions needed to perform the Clear Unobstructed Brain/Body Imaging Cocktail and Computational Analysis (CUBIC) protocol (53), CUBIC reagent 1 (R1) and CUBIC reagent 2 (R2), are listed in Table 6. The composition of the blocking solution used for the immunostaining process is listed in Table 7. The consumables and equipment are listed in Supplementary Table S1. The primary and secondary antibodies used for immunostaining are listed in Table 8.

Table 5. List of reagents.

Reagents	Supplier/Manufacturer	Working Concentration	Catalogue Number
16% formaldehyde (FA)	Thermo Fisher Scientific, Waltham, MA, USA	4%	28,908
Hoechst33342	Thermo Fisher Scientific, Waltham, MA, USA	1:1000	H3570
Phosphate buffer saline (PBS)	Wisent Bioproducts, Saint-Jean-Baptiste, QC, Canada	1X	311-010-CL

Table 6. CUBIC reagent 1 (R1) and CUBIC reagent 2 (R2) compositions.

Reagents	Supplier/Manufacturer	Working Concentration	Catalogue Number
R1			
dH ₂ O	N/A	35% by wt	N/A
Urea	Sigma-Aldrich, St. Louis, MO, USA	25% by wt	15604
Quadrol (N, N, N', N'-tetrakis			
(2-hydroxy-propyl)	Sigma-Aldrich, St. Louis, MO, USA	25% by wt	122262
ethylenediamine)			
Triton X-100	Bioshop, Burlington, ON, Canada	15% by wt	TRX506
R2			
dH ₂ O	N/A	15% by wt	N/A
Triethanolamine	Thermo Fisher Scientific, Waltham, MA, USA	10% by wt	T407-500
D-sucrose	Thermo Fisher Scientific, Waltham, MA, USA	50% by wt	BP220-1
Urea	Sigma-Aldrich, St. Louis, MO, USA	25% by wt	15604

Table 7. Blocking solution composition.

Reagents	Supplier/Manufacturer	Working Concentration	Catalogue Number
Bovine serum albumin (BSA)	Wisent Bioproducts, Saint-Jean-Baptiste, QC, Canada	0.05%	800-095-CG
Normal donkey serum (NDS)	Millipore, Burlington, MA, USA	5%	S30
Phosphate buffer saline (PBS)	Wisent Bioproducts, Saint-Jean-Baptiste, QC, Canada	1X	311-010-CL
Triton X-100	Bioshop, Burlington, ON, Canada	0.2%	TRX506

Table 8. Primary and secondary antibodies.

Primary Antibodies			
Antibody	Host Species	Working Dilution	Reference
ChAT	Goat	1:100	Millipore; Cat. No. MAB144P
Hb9 (81.5C10)	Mouse	1:50	DSHB
Isl1 (40.2D6)	Mouse	1:50	DSHB
Ki67	Mouse	1:200	BD Biosciences; Cat. No. 556003
MBP	Rat	1:200	Novusbio; Cat. No. NB600-717
Nestin	Mouse	1:250	Abcam; Cat. No. ab92391
Neurofilament-H	Chicken	1:1000	Abcam; Cat. No. ab4680
Nkx2.2	Mouse	1:100	DSHB
Nkx6.1	Mouse	1:100	DSHB
O4 *	Mouse	1:200	R&D System; Cat. No. MAB1326
Oct3/4	Goat	1:500	Santa Cruz; Cat. No. sc-8628
Olig2	Rabbit	1:100	Millipore; Cat No. AB 9610
Pax6	Mouse	1:100	DSHB
SMI-32	Mouse	1:100	Biolegend; Cat. No. 801701
Sox1	Goat	1:100	R&D System; Cat. No. AF3369
Unex	Rabbit	1:250	Novusbio; Cat. No. NBP2-56480
Vsx2 (Chx10)	Mouse	1:250	Santa-Cruz; Cat. No. sc-365519

Secondary Antib	odies		
Host Species	Target Species- Fluorophore	Working Dilution	Reference
Donkey	Goat IgG-DyLight 550	1:250	Abcam; Cat No. ab96932
Donkey	Goat IgG-AlexaFluor 647	1:250	Jackson Immunoresearch; Cat. No. 703-605-155
Donkey	Mouse IgG-DyLight 488	1:250	Abcam; Cat. No. ab96875
Donkey	Chicken IgG-AlexaFluor 647	1:250	Jackson Immunoresearch; Cat. No. 703-605-155
Donkey	Rabbit IgG-DyLight 550	1:250	Abcam; Cat. No. ab96892
Donkey	Rabbit-DyLight 488	1:250	Abcam; Cat. No. ab96891
Goat	Rat IgG-DyLight 488	1:250	Abcam; Cat. No. ab96887

st Note: To obtain optimal results with O4 primary antibody, perform a live staining for 30 min at

 $^{37\ ^{\}circ}\text{C}$ before formal dehyde fixation.

A maximum of six MN spheroids per 0.6 mL collection tube were transferred from the 96 Ubottom ultra-low attachment plates, fixed in 4% FA for 15-20 min at RT and washed three times with 1X PBS. To perform all the PBS washes of Section 2.5., the spheroids were allowed to reach the bottom of the collection tube through gravity (~5 min) before removing the supernatant. For each wash, 400 µL of 1X PBS was used and the tube was left in the nutating mixer for 10 min. After fixation, the CUBIC protocol was performed by replacing 1X PBS with 200 µL of CUBIC R1. Incubation of the samples with CUBIC R1 was performed at 37 °C with gentle shaking (~80 rpm) for 48–72 h. The removal of CUBIC R1 was achieved by performing three 1X PBS washes. MN spheroids were blocked in 200 µL of blocking solution overnight at 37 °C with gentle shaking (~80 rpm). Blocking solution was removed by allowing the spheroids to reach the bottom of the collection tube by gravity (~5 min). Primary antibodies were diluted in blocking solution and added to the MN spheroids for 24–72 h at 37 °C with gentle shaking (~80 rpm). A final volume of 150 μL was used per collection tube. Primary antibodies were washed out by performing three 1X PBS washes. Secondary antibodies and Hoechst33342 were diluted in blocking solution and added to the MN spheroids for 24–72 h at 37 °C with gentle shaking (~80 rpm). A final volume of 150 μL was used per collection tube. Secondary antibodies and Hoechst33342 were washed out by performing three 1X PBS washes.

For imaging, we optimized a protocol to image MN spheroids at large scale using black 96-well plates. Each spheroid was transferred into the center of a well using wide-orifice low-binding tips. Excess 1X PBS was removed and 100 μ L of CUBIC R2 was added per well as mounting medium. Images of the immunostained MN spheroids were acquired with the Opera Phenix High-Content Screening System using the PreScan function to find the spheres within the focal plane at 5X and then perform the imaging at 20X. System $5\times/0.16$ and $20\times/1.0$ objectives. Image size 512

 \times 512, voxel size $0.29 \times 0.29 \times 5~\mu m$. The data were extracted to be organized and analyzed by an in-house script developed in MATLAB. Images were analyzed as raw Z-stacks without altering brightness and contrast. Alternatively, MN spheroids can be mounted over a glass slide to be imaged with a conventional confocal microscope. For this, a hydrophobic pen is used to draw a circle in the middle of a glass slide and an MN spheroid is transferred in the center using wide-orifice low-binding tips. Excess 1X PBS was removed and a drop of CUBIC R2 (\sim 30 μ L) was added to the spheroids, followed by the placing of a glass coverslip on top.

Note: CUBIC R1 and R2 solutions must be filtered using a cell strainer to remove any solutes that did not incorporate into the solution. This will reduce undesired detritus at the imaging step. After the addition of CUBIC R1, the spheroids become transparent, and they are almost imperceptible to the eye. After the first 1X PBS wash, the spheroids recover their white color, and it is possible to visualize them again. For the mounting process inside black 96-well plates, it is essential to remove almost all the 1X PBS surrounding the spheroids before adding the CUBIC R2. This will prevent the spheroids from floating at different heights inside the well, thus making their tracing difficult at the microscope.

2.6. Microelectrode Array (MEA) Recordings of MN Spheroids

Each batch of MNPCs was used to generate one 96 U-bottom ultra-low attachment plate (60 spheroids). The reagents to perform MN spheroid MEA recordings are listed in Table 9. The consumables and equipment are listed in Supplementary Table S1. The composition of the artificial cerebrospinal fluid (aCSF) solution needed for MEA recordings is detailed in Table 10.

Table 9. List of reagents.

Reagents	Supplier/Manufacturer	Working Concentration	Catalogue Number
Laminin	Invitrogen, Waltham, MA, USA	5 μg/mL	23017015
Poly-L-ornithine (PLO)	Sigma-Aldrich, St. Louis, MO, USA	$10 \ \mu g/mL$	P3655
Tetrodotoxin (TTX)	Sigma-Aldrich, St. Louis, MO, USA	1 mM	T8024

Table 10. Composition of aCSF.

Reagents **	Supplier/Manufacturer	Working Concentration	Catalogue Number
CaCl ₂	Thermo Fisher Scientific, Waltham, MA, USA	1.6 mM	AC423525000
D-glucose *	Sigma-Aldrich, St. Louis, MO, USA	5.5 mM	G8270
KC1	Bioshop, Burlington, ON, Canada	4 mM	POC888.5
KH ₂ PO ₄	Thermo Fisher Scientific, Waltham, MA, USA	1.18 mM	AC424200250
MgSO ₄	Thermo Fisher Scientific, Waltham, MA, USA	1.17 mM	AC423905000
NaCl	BioShop, Burlington, ON, Canada	119 mM	SOD004.5
NaHCO ₃ *	Thermo Fisher Scientific, Waltham, MA, USA	24 mM	AC424270010

^{*} These reagents are not added to the 10X stock solution to prevent the growth of microorganisms. They are added to the 1X solution before every recording experiment. ** Add 2 g of NaCl to 10X solution stock for adjusting osmolality 305 mOsM.

Cytoview 24-well MEA plates with 16 electrodes per well were treated with PLO (10 μ g/mL) for 24 h, washed 3 times with 1X PBS, and coated with laminin (5 μ g/mL) for 24 h. MN spheroids were generated and cultured for 7 days into the 96 U-bottom ultra-low attachment well plates before being transferred to each well of the Cytoview 24-well MEA plate using wide-orifice low-binding tips. Six whole spheroids were deposited in the center of each well (55) in no more than 20 μ L of medium to prevent the spheroids from spreading to the edges of the well. The plate was returned to the incubator for 20–30 min to allow the spheroids to attach to the electrodes before addition of 500 μ L of fresh MN induction and maturation medium.

Before each recording, 50 mL of 1X aCSF solution was prepared from a 10X stock solution, adding D-glucose and NaHCO₃ at the working concentrations. The tube with the 1X aCSF solution was left with the lid loose inside the incubator for 1 h to equilibrate the solution with the same gaseous conditions found inside the incubator. Before the 1X aCSF solution was added to the cells, it was filtered to avoid any possible contamination. After removing the MN induction and maturation medium and adding 500 μ L of the 1X aCSF solution to each well, the MEA plate was returned to the incubator at 37 °C/5% CO₂ for 30–45 min.

MEA recordings were performed on days 7, 14, 21, and 28 after plating the MN spheroids. Data were collected for 5 min using the Axis Navigator software (provided by Axion Biosystems, version 1.5.1.12, Atlanta, GA, USA). A band-pass filter of 3 kHz (low-pass) to 200 Hz (high-pass) was applied. For the analysis, a "spike" was defined as a short extracellular electrical event with a peak voltage six times or greater than the standard deviation of the estimated "noise" signal. A "burst" was defined as ≥ 5 spikes with no more than 100 ms separating each spike. Network bursts were not measured, as the presence of spheres within the plate was random with very few spheres centered within an electrode for the entire recording period of 28 days. The MEA plate was placed into the Axion Maestro Edge with temperature and CO2 concentration set to 37 °C and 5%, respectively. The plate was allowed to equilibrate for 5 min inside the instrument prior to recording. After the recording, the MEA plate was removed from the instrument and the aCSF was replaced with MN induction and maturation medium to keep the cells in culture for the following recording time points. At day 28, after the basal recording of 5 min in aCSF was performed, the plate was removed from the instrument and dosed with vehicle (H₂O) or 1 mM tetrodotoxin (TTX). The plate was returned to the instrument and allowed to equilibrate for 5 min before performing a second recording of 5 min. This was the endpoint of the MEA recordings.

3. Results

We generated MN spheroids from two different healthy control iPSC lines (AIW002-02 and 3450), adapting a previously described protocol used to generate MNs as a 2D monolayer (Figure 1A) (16). For our experiments, 80% confluent iPSC cultures were differentiated into MNPCs. At the MNPC stage, we confirmed the expression of the neural precursor markers Sox1, Nestin, and Pax6 (56, 57), in addition to Ki67, an endogenous marker of active cell cycle, thus confirming the cells' proliferation capacity (58) (Supplementary Figure S1). MNPCs also co-expressed the markers Nkx6.1 and Olig2, confirming their identity as MNPCs (59) (Supplementary Figure S1). From these MNPCs, 5000 cells per well were used to generate iPSC-derived MN spheroids into 96-well U-bottom ultra-low attachment plates (Figure 1B). Diameter (3450, 14 days = 262.9 μm ± 1.976 , 28 days = 278.3 μ m ± 2.255 ; AIW002-02, 14 days = 305.4 μ m ± 2.225 , 28 days = 326.4 $\mu m \pm 1.752$), area (3450, 14 days = 5.92 × 10⁴ $\mu m^2 \pm 804.4$, 28 days = 6.61 × 10⁴ $\mu m^2 \pm 1065$; AIW002-02, 14 days = $8.13 \times 10^4 \, \mu m^2 \pm 1090$, 28 days = $9.40 \times 10^4 \, \mu m^2 \pm 1244$), and volume $(3450, 14 \text{ days} = 9.73 \times 10^6 \,\mu\text{m}^3 \pm 214,272, 28 \,\text{days} = 1.15 \times 10^7 \,\mu\text{m}^3 \pm 274,041; \,\text{AIW}002-02, 14)$ days = $1.52 \times 10^7 \ \mu m^3 \pm 346{,}330, \ 28 \ days = 1.84 \times 10^7 \ \mu m^3 \pm 303{,}753)$ measurements were obtained by analyzing bright-field images of the MN spheroids (Figure 1C) with a CellProfiler Analyst pipeline. We observed that the spheroids from both control lines grew in size from 14 to 28 days, as confirmed by increases in the measurements of their overall diameter (3450 = p < 0.0001; AIW002-02 = p < 0.0001), area (3450 = p < 0.0001; AIW002-02 = p < 0.0001), and volume (3450 = p < 0.0001; AIW002-02 = p < 0.0001) (Figure 2A,B). Importantly, since our protocol allows us to expand the MNPCs for up to five passages (16), we generated MN spheroids from MNPCs between passages two and four, and we observed that the spheroids were successfully generated and kept their capacity to grow over time regardless of the passage number.

In terms of morphology, the MN spheroids display a circular shape, however, an analysis of circularity (Figure 2C) showed that the spheroids are not perfectly round (or circularity ratio = 1). Taken together, we succeeded in the establishment of culture conditions to generate 3D iPSC-derived MN spheroids in a reproducible manner.

Next, we assessed the expression of MN markers in the MN spheroids derived from the two control lines (AIW002-02 and 3450) at the transcript and protein levels by qPCR (Figure 3) and immunofluorescent staining (Figure 4), respectively. For both 3450 (Figure 3A) and AIW002-02 (Figure 3B) lines, the expression of different genes at the transcript level was assessed at the iPSC (NANOG and OCT4), MNPC (OLIG2 and PAX6), and MN spheroid (HB9, ISL1, CHAT, and MAP2) stage. The expression levels were compared using a one-way ANOVA with a post Dunnett's test in which the control condition has been defined based on the mRNA transcript assessed. The complete results of the statistical analyses can be found in Supplementary Table S3. As expected, the pluripotency markers NANOG and OCT4 were found to be downregulated at the MNPC and MN spheroid stages compared to the iPSC stage. Significantly higher expression levels of the MNPC markers PAX6 and OLIG2 were found upregulated at the MNPC stage compared to the iPSC and MN spheroid stages. Finally, the expression level of the neural marker MAP2, as well as the expression levels of the MN markers HB9, ISL1, and CHAT were found to be upregulated at the MN spheroid stage, while being almost absent at the iPSC and MNPC stages. Additionally, we assessed the expression levels of interneuron (VSX2 and SIM1), oligodendrocyte (MBP), and astrocyte (GFAP) markers to address the presence of other cell types within the MN spheroids. For both cell lines, we confirmed the upregulation of MN markers at the transcript level, indicating a successful differentiation towards MN identity. GFAP expression remained undetected at the different differentiation stages, suggesting the absence of astrocytes. However,

we observed the expression of interneuron and oligodendrocyte markers, indicating the presence of these cell types within MN spheroids.

To determine the presence of the different markers at the protein level, we analyzed the images of the cleared immunostained MN spheroids at 14 and 28 days (Figure 4A) with our in-house MATLAB script. We confirmed the expression of the pan MN markers Hb9/Isl1 after 14 and 28 days of differentiation with no statistical difference observed at the different time points for either cell line (Figure 4B). The expression of CHAT, a marker associated with MN maturation, was also assessed, showing an increase of its expression at 28 days compared to 14 days for both cells lines (3450 = p < 0.0001; AIW002-02 = p < 0.01) (Figure 4B). The expression of neurofilament heavy (NF-H) subunit, a marker indicating neuronal identity, was also increased at 28 days in both cell lines, however, it only reached a statistical significance in one of the cells lines (3450 = p < 0.01) (Figure 4B). Finally, we assessed the expression of SMI-32, an antibody that recognizes the nonphosphorylated form of the neurofilament medium (NF-M) and NF-H subunits, which is known to be highly enriched in spinal motor neurons. The expression of SMI-32 was confirmed at the two time points for both cell lines. We observe a tendency of SMI-32 to increase its expression at 28 days; however, it did not reach the statistical significance for either of the cell lines (Figure 4B). MN spheroids were also stained for pluripotency (Oct3/4) and MNPC (Pax6 and Olig2) markers to confirm their downregulation (Supplementary Figure S4). The expression of Hb9, Isl1, CHAT, and NF-H confirmed that, at the protein level, the MN spheroids are composed primarily of neurons with an MN identity. Nevertheless, positive antibody staining for interneuron progenitor (NKX2.2), interneuron (Vsx2 and Uncx), and oligodendrocyte (O4 and MBP) markers (Supplementary Figure S4) confirms the presence of other cell types in the MN spheroids, as suggested by the qPCR analysis (Figure 3).

Finally, we used the MEA system to assess the electrical activity of the MN spheroids. Only the spheroids placed at the center of the electrode were considered for quantification, meaning that each spheroid was in contact with a single electrode within the well (Figure 5A). Action potentials ("spikes") and groups of action potentials ("bursts") were detected for the MN spheroids derived from the two control cell lines (3450 and AIW002-02) at different time points (7, 14, 21, and 28 days) (Supplementary Table S2). The mean firing rate (Hz), a ratio of the total number of spikes recorded over the duration of the recording, indicates that MN spheroids remain electrically active over time, as previously described for 2D monolayer iPSC-derived MN MEA recordings (60) (Figure 5B). Additionally, MN spheroids display burst firing over time (Figure 5C). Finally, treatment with TTX, a sodium channel blocker that inhibits the firing of action potential in neurons, confirmed the electrical activity of the MN spheroids, ruling out any potential artifacts coming from the system. Activity was not altered when a well was treated with vehicle (Figure 5D).

All graphs presented in the Results section were generated using GraphPad Prism (created by Dotmatics, version 9.1.1, Boston, MA, USA), www.graphpad.com, accessed 1 August 2022.

4. Discussion

Taken together, the results presented here demonstrate that we were able to develop a workflow to generate and characterize MN spheroids from iPSCs by modifying a protocol originally optimized to generate a 2D MN monolayer culture. A technical advantage associated with this protocol for the generation of iPSC-derived MNs is that it allows for the cryopreservation and expansion of MNPCs, making it time efficient. Importantly, we showed that thawed MNPCs used at different passages can produce MN spheroids in a reproducible manner and that culturing the cells in a 3D context did not interfere with the expression of MN identity markers, as shown by qPCR and immunofluorescent stainings. Remarkably, another technical advantage to growing the cells as 3D spheroids is that they can be grown and maintained for up to 28 days, and longer if needed, unlike 2D cultures that are often prone to clustering and detachment around 28 days in culture or earlier (31). This becomes relevant, as we see a significant upregulation of CHAT in 28day MN spheroids for both cell lines, which implies an increased maturation of the MNs over time, as shown by previous studies (61, 62). Interestingly, we observed different levels of significance between cell lines for some of the analyzed markers at both the gene expression and protein levels, which could be allusive to iPSC heterogeneity, a common obstacle in iPSC-based models (63). The latter highlights the importance of using isogenic controls when referring to iPSC disease modelling instead of lines derived from healthy individuals when there is a monogenic cause of disease.

Previous studies have described the generation of ESC- and iPSC-derived MN spheroids using 96-well plates that favor the aggregation of cells by gravity. Characterization of these MN spheroids by means of qPCR has demonstrated the expression of progenitor (i.e., *OLIG2*, *NGN2*, *NeuroD1*), oligodendrocyte (i.e., *CLDN11*, *SOX10*, *OSP*), and astrocyte markers (i.e., GFAP) in

aged spheroids (25). However, except for GFAP and O4, there is a lack of characterization of these markers at the protein level (25, 37, 39, 43). Additionally, these studies bypass the analysis of interneuron markers, which share a common progenitor pool with MNs and are known to modulate MN synaptic activity (16, 59). Thus, this workflow provides a broader characterization of different markers not only at the expression level but also at the protein level. In fact, we found the presence of interneuron and oligodendrocyte markers within the MN spheroids, which is consistent with observations made by single-cell RNA sequencing (64) when iPSC-derived MNs were cultured as a 2D monolayer following the original protocol (16). Therefore, this needs to be taken into consideration when assays are performed in these 3D models to avoid misinterpretations of results. Interestingly, opposed to similar work (25, 37, 39), we do not detect the expression of GFAP within our MN spheroids, raising the question as to whether an MNPC patterning step (43) is able to restrict more effectively the fate of the cells, giving rise only to cell types sharing a closest progenitor pool with MNs.

Even in small 3D samples such as spheroids, imaging is challenging due to the intrinsic opacity of biological tissues. Additionally, immunofluorescent staining of 3D structures was demonstrated to be difficult due to a low antibody penetrance, which can lead to the underestimation of specific staining for a given marker. Tissue clearing techniques are useful to reduce the water content of a sample and to remove lipids harbored within its cell membranes to (1) facilitate antibody penetrance and immunostaining and (2) reduce microscope light scattering to improve 3D image acquisition (46, 65). Among these, CUBIC is a rapid and inexpensive water-based clearing protocol that does not rely on the use of toxic reagents (46, 53, 66, 67). Recently, the CUBIC method was applied to clear spheroids coming from breasts cancer cell lines (68), however, to our knowledge, it has yet to be applied towards the clearing and imaging of neuronal

spheres of any kind. Here, we succeeded in adapting the CUBIC protocol to clear MN spheroids (Figure 4D; Supplementary Video S1). The performance of this technique improved the immunofluorescent staining and subsequent image acquisition of our samples, allowing their characterization at the protein level. In contrast, when the CUBIC protocol was not performed, antibody penetration was limited to the periphery of the spheroid, making its center perceived as a necrotic core (Figure 4C).

MEA recordings of the MN spheroids confirmed the presence of neuronal activity within these 3D structures, as demonstrated by their ability to fire action potentials as isolated spikes or in bursts. Burst pattern measurements obtained by performing MEA recordings have been used to assess longitudinal electrical changes in 2D monolayer cortical cultures (69), however, to our knowledge there are not equivalent studies using MN cultures. Thus, this assay opens the possibility of using an MEA approach to analyze differences in burst patterns longitudinally when MN spheroids are derived from control vs. patient iPSC lines. Nevertheless, considering the presence of other cell types within the MN spheroids, it would be important to identify the different types of synapses present in these 3D structures by applying ion channel-specific antagonists. From the technical perspective, placing the MN spheroids at the center of a single electrode is challenging. Therefore, for future functional characterization, we acknowledge that a better approach would be the use of high-density MEAs (HD-MEAs), which have been recently used to assess the electrical features of other 3D structures (70, 71). HD-MEAs are composed of thousands of electrodes with minimal space between them. Therefore, HD-MEA systems not only provide an increase of spatiotemporal resolution but they would also facilitate the seeding process of 3D structures. Another alternative is the dissociation of spheroids into a single cell suspension to

obtain MEA recordings of a 2D monolayer (55), however, this can raise concerns about the identity of the surviving population of cells after the dissociation process.

Even though there has been an increase in studies making use of MN spheroids, this is the first time a broader characterization has been made for such 3D structures with tools specifically developed with potential for large-scale studies. This is relevant because iPSC-derived spheroids/neurospheres have proven to be easy to generate 3D models that can be used for screening purposes (72), an important step towards drug discovery for MNDs. Moreover, this model can be used as a cellular jigsaw, in which other iPSC-derived cell types can be added to form more advanced co-culture spheroids, opening the possibility to study non-cell autonomous manifestation of the diseases.

Supplementary Materials: The following supporting information can be downloaded at: www.mdpi.com/xxx/s1, Figure S1: Motor neuron neural progenitor cell (MNPC) characterization by immunofluorescent staining; Figure S2: Inappropriate formation of MN spheroids; Figure S3: CellProfiler macro to perform the size profiling of the MN spheroids; Figure S4: Image profiling of iPSC-derived MN spheroids to identify different cell types; Figure S5: Graphic summary for the generation and characterizacion of iPSC-derived MN spheroids; Table S1: List of consumables and equipment; Table S2: Raw MEA data; Table S3: qPCR statistics; Video S1: Rotating 3D reconstruction of MN spheroid.

Author Contributions: Conceptualization, M.J.C.-M.; Methodology, M.J.C.-M. and M.C.; Software, A.K.F.-F. and W.E.R.; Validation, M.J.C.-M., M.C., and T.M.D.; Formal analysis, M.J.C.-M.; Investigation, M.J.C.-M., A.K.F.-F., G.H., and C.X.-Q.C.; Data curation, M.J.C.-M.

and D.C.-V.; Writing—original draft preparation, M.J.C.-M.; Writing—review and editing, M.J.C.-M., M.C., and T.M.D.; Visualization, M.J.C.-M.; Supervision, T.M.D.; Project administration, M.J.C.-M. and T.M.D.; Funding acquisition, M.J.C.-M. and T.M.D. All authors have read and agreed to the published version of the manuscript.

Funding: T.M.D. was supported by the Canada First Research Excellence Fund, awarded through the Healthy Brains, Healthy Lives initiative at McGill University, the CQDM FACs program, and Quantum Leaps program. M.J.C.-M. was supported by an ALS Society of Canada student fellowship. M.J.C.-M. was also supported by eNUVIO Inc. and Healthy Brains, Healthy Lives NeuroSphere at McGill University through a Mitacs Accelerate award.

Institutional Review Board Statement: The use of iPSCs in this research was approved by the McGill University Health Centre Research Ethics Board (DURCAN IPSC/2019-5374).

Informed Consent Statement: Not applicable.

Data Availability Statement: The data presented in this study are available on request from the corresponding author.

Acknowledgments: We acknowledge Veronica García-Vázquez for the design and coding of the in-house developed MATLAB script. We acknowledge Maria Lacalle-Aurioles for conceptualization and training in tissue clearing, 3D imaging and image processing. We acknowledge Ghislaine Deyab for her guidance with MEA data analysis. We acknowledge Gilles Maussion for his guidance with qPCR data analysis, and for editing and proofreading the manuscript. We thank Sarah Lépine, Lenore K. Beitel and Mark Aurousseau for editing and proofreading of the manuscript.

Conflicts of Interest: The funders had no role in the design of the study; in the collection, analyses, or interpretation of data; in the writing of the manuscript; or in the decision to publish the results.

References

- 1. Sanes, J.R.; Lichtman, J.W. Development of the vertebrate neuromuscular junction. *Annu. Rev. Neurosci.* **1999**, *22*, 389–442.
- 2. Tiryaki, E.; Horak, H.A. ALS and other motor neuron diseases. *Continuum* **2014**, *20*, 1185–1207.
- 3. Park, J.; Kim, J.E.; Song, T.J. The Global Burden of Motor Neuron Disease: An Analysis of the 2019 Global Burden of Disease Study. *Front. Neurol.* **2022**, *13*, 864339.
- 4. Gois, A.M.; Mendonça, D.M.F.; Freire, M.A.M.; Santos, J.R. In vitro and in vivo models of amyotrophic lateral sclerosis: An updated overview. *Brain Res. Bull.* **2020**, *159*, 32–43.
- 5. Slanzi, A.; Iannoto, G.; Rossi, B.; Zenaro, E.; Constantin, G. In vitro Models of Neurodegenerative Diseases. *Front. Cell Dev. Biol.* **2020**, *8*, 328.
- 6. Sances, S.; Bruijn, L.I.; Chandran, S.; Eggan, K.; Ho, R.; Klim, J.R.; Livesey, M.R.; Lowry, E.; Macklis, J.D.; Rushton, D.; et al. Modeling ALS with motor neurons derived from human induced pluripotent stem cells. *Nat. Neurosci.* **2016**, *19*, 542–553.
- 7. Takahashi, K.; Yamanaka, S. Induction of pluripotent stem cells from mouse embryonic and adult fibroblast cultures by defined factors. *Cell* **2006**, *126*, 663–676.
- 8. Takahashi, K.; Tanabe, K.; Ohnuki, M.; Narita, M.; Ichisaka, T.; Tomoda, K.; Yamanaka, S. Induction of pluripotent stem cells from adult human fibroblasts by defined factors. *Cell* **2007**, *131*, 861–872.
- 9. Fujimori, K.; Ishikawa, M.; Otomo, A.; Atsuta, N.; Nakamura, R.; Akiyama, T.; Hadano, S.; Aoki, M.; Saya, H.; Sobue, G.; et al. Modeling sporadic ALS in iPSC-derived motor neurons identifies a potential therapeutic agent. *Nat. Med.* **2018**, *24*, 1579–1589.
- 10. Ratti, A.; Gumina, V.; Lenzi, P.; Bossolasco, P.; Fulceri, F.; Volpe, C.; Bardelli, D.; Pregnolato, F.; Maraschi, A.; Fornai, F.; et al. Chronic stress induces formation of stress granules and pathological TDP-43 aggregates in human ALS fibroblasts and iPSC-motoneurons. *Neurobiol. Dis.* **2020**, *145*, 105051.
- 11. Kim, B.W.; Ryu, J.; Jeong, Y.E.; Kim, J.; Martin, L.J. Human motor neurons with SOD1-G93A mutation generated from CRISPR/Cas9 gene-edited iPSCs develop pathological features of amyotrophic lateral sclerosis. *Front. Cell Neurosci.* **2020**, *14*, 604171.
- 12. Deneault, E.; Chaineau, M.; Nicouleau, M.; Castellanos Montiel, M.J.; Franco Flores, A.K.; Haghi, G.; Chen, C.X.; Abdian, N.; Shlaifer, I.; Beitel, L.K.; et al. A streamlined CRISPR workflow to introduce mutations and generate isogenic iPSCs for modeling amyotrophic lateral sclerosis. *Methods* **2022**, *203*, 297–310.
- 13. Selvaraj, B.T.; Livesey, M.R.; Zhao, C.; Gregory, J.M.; James, O.T.; Cleary, E.M.; Chouhan, A.K.; Gane, A.B.; Perkins, E.M.; Dando, O.; et al. C9ORF72 repeat expansion causes vulnerability of motor neurons to Ca²⁺-permeable AMPA receptor-mediated excitotoxicity. *Nat. Commun.* **2018**, *9*, 347.
- 14. Guo, W.; Naujock, M.; Fumagalli, L.; Vandoorne, T.; Baatsen, P.; Boon, R.; Ordovás, L.; Patel, A.; Welters, M.; Vanwelden, T.; et al. HDAC6 inhibition reverses axonal transport defects in motor neurons derived from FUS-ALS patients. *Nat. Commun.* **2017**, *8*, 861.

- 15. Boulting, G.L.; Kiskinis, E.; Croft, G.F.; Amoroso, M.W.; Oakley, D.H.; Wainger, B.J.; Williams, D.J.; Kahler, D.J.; Yamaki, M.; Davidow, L.; et al. A functionally characterized test set of human induced pluripotent stem cells. *Nat. Biotechnol.* **2011**, *29*, 279–286.
- 16. Du, Z.W.; Chen, H.; Liu, H.; Lu, J.; Qian, K.; Huang, C.L.; Zhong, X.; Fan, F.; Zhang, S.C. Generation and expansion of highly pure motor neuron progenitors from human pluripotent stem cells. *Nat. Commun.* **2015**, *6*, 6626.
- 17. Qu, Q.; Li, D.; Louis, K.R.; Li, X.; Yang, H.; Sun, Q.; Crandall, S.R.; Tsang, S.; Zhou, J.; Cox, C.L.; et al. High-efficiency motor neuron differentiation from human pluripotent stem cells and the function of Islet-1. *Nat. Commun.* **2014**, *5*, 3449.
- 18. Amoroso, M.W.; Croft, G.F.; Williams, D.J.; O'Keeffe, S.; Carrasco, M.A.; Davis, A.R.; Roybon, L.; Oakley, D.H.; Maniatis, T.; Henderson, C.E.; et al. Accelerated high-yield generation of limb-innervating motor neurons from human stem cells. *J. Neurosci.* **2013**, *33*, 574–586.
- 19. Dimos, J.T.; Rodolfa, K.T.; Niakan, K.K.; Weisenthal, L.M.; Mitsumoto, H.; Chung, W.; Croft, G.F.; Saphier, G.; Leibel, R.; Goland, R.; et al. Induced pluripotent stem cells generated from patients with ALS can be differentiated into motor neurons. *Science* **2008**, *321*, 1218–1221.
- 20. Maury, Y.; Côme, J.; Piskorowski, R.A.; Salah-Mohellibi, N.; Chevaleyre, V.; Peschanski, M.; Martinat, C.; Nedelec, S. Combinatorial analysis of developmental cues efficiently converts human pluripotent stem cells into multiple neuronal subtypes. *Nat. Biotechnol.* **2015**, *33*, 89–96.
- 21. Karpe, Y.; Chen, Z.; Li, X.J. Stem cell models and gene targeting for human motor neuron diseases. *Pharmaceuticals* **2021**, *14*, 565.
- 22. Guo, W.; Fumagalli, L.; Prior, R.; Van Den Bosch, L. Current advances and limitations in modeling ALS/FTD in a dish using induced pluripotent stem cells. *Front. Neurosci.* **2017**, *11*, 671.
- 23. Afshar Bakooshli, M.; Lippmann, E.S.; Mulcahy, B.; Iyer, N.; Nguyen, C.T.; Tung, K.; Stewart, B.A.; van den Dorpel, H.; Fuehrmann, T.; Shoichet, M.; et al. A 3D culture model of innervated human skeletal muscle enables studies of the adult neuromuscular junction. *eLife* **2019**, *8*, e44530.
- 24. De Leeuw, S.M.; Davaz, S.; Wanner, D.; Milleret, V.; Ehrbar, M.; Gietl, A.; Tackenberg, C. Increased maturation of iPSC-derived neurons in a hydrogel-based 3D culture. *J. Neurosci. Methods* **2021**, *360*, 109254.
- 25. Osaki, T.; Uzel, S.G.M.; Kamm, R.D. Microphysiological 3D model of amyotrophic lateral sclerosis (ALS) from human iPS-derived muscle cells and optogenetic motor neurons. *Sci. Adv.* **2018**, *4*, eaat5847.
- 26. Brännvall, K.; Bergman, K.; Wallenquist, U.; Svahn, S.; Bowden, T.; Hilborn, J.; Forsberg-Nilsson, K. Enhanced neuronal differentiation in a three-dimensional collagen-hyaluronan matrix. *J. Neurosci. Res.* **2007**, *85*, 2138–2146.
- 27. Smith, I.; Haag, M.; Ugbode, C.; Tams, D.; Rattray, M.; Przyborski, S.; Bithell, A.; Whalley, B.J. Neuronal-glial populations form functional networks in a biocompatible 3D scaffold. *Neurosci. Lett.* **2015**, *609*, 198–202.
- 28. Vagaska, B.; Gillham, O.; Ferretti, P. Modelling human CNS injury with human neural stem cells in 2- and 3-Dimensional cultures. *Sci. Rep.* **2020**, *10*, 6785.
- 29. Thiry, L.; Clément, J.P.; Haag, R.; Kennedy, T.E.; Stifani, S. Optimization of long-term human iPSC-derived spinal motor neuron culture using a dendritic polyglycerol amine-based substrate. *ASN Neuro* **2022**, *14*, 17590914211073381.
- 30. Taga, A.; Dastgheyb, R.; Habela, C.; Joseph, J.; Richard, J.P.; Gross, S.K.; Lauria, G.; Lee, G.; Haughey, N.; Maragakis, N.J. Role of human-induced pluripotent stem cell-derived spinal cord astrocytes in the functional maturation of motor neurons in a multielectrode array system. *Stem Cells Transl. Med.* **2019**, *8*, 1272–1285.
- 31. Milky, B.; Zabolocki, M.; Al-Bataineh, S.A.; van den Hurk, M.; Greenberg, Z.; Turner, L.; Mazzachi, P.; Williams, A.; Illeperuma, I.; Adams, R.; et al. Long-term adherence of human brain

- cells in vitro is enhanced by charged amine-based plasma polymer coatings. *Stem Cell Rep.* **2022**, *17*, 489–506.
- 32. Toli, D.; Buttigieg, D.; Blanchard, S.; Lemonnier, T.; Lamotte d'Incamps, B.; Bellouze, S.; Baillat, G.; Bohl, D.; Haase, G. Modeling amyotrophic lateral sclerosis in pure human iPSc-derived motor neurons isolated by a novel FACS double selection technique. *Neurobiol. Dis.* **2015**, *82*, 269–280.
- 33. Faustino Martins, J.M.; Fischer, C.; Urzi, A.; Vidal, R.; Kunz, S.; Ruffault, P.L.; Kabuss, L.; Hube, I.; Gazzerro, E.; Birchmeier, C.; et al. Self-organizing 3D human trunk neuromuscular organoids. *Cell Stem Cell* **2020**, *26*, 172–186.e6.
- 34. Pereira, J.D.; DuBreuil, D.M.; Devlin, A.C.; Held, A.; Sapir, Y.; Berezovski, E.; Hawrot, J.; Dorfman, K.; Chander, V.; Wainger, B.J. Human sensorimotor organoids derived from healthy and amyotrophic lateral sclerosis stem cells form neuromuscular junctions. *Nat. Commun.* **2021**, *12*, 4744.
- 35. Hor, J.H.; Ng, S.Y. Generating ventral spinal organoids from human induced pluripotent stem cells. *Methods Cell Biol.* **2020**, *159*, 257–277.
- 36. Andersen, J.; Revah, O.; Miura, Y.; Thom, N.; Amin, N.D.; Kelley, K.W.; Singh, M.; Chen, X.; Thete, M.V.; Walczak, E.M.; et al. Generation of functional human 3D cortico-motor assembloids. *Cell* **2020**, *183*, 1913–1929.e26.
- 37. Osaki, T.; Uzel, S.G.M.; Kamm, R.D. On-chip 3D neuromuscular model for drug screening and precision medicine in neuromuscular disease. *Nat. Protoc.* **2020**, *15*, 421–449.
- 38. Machado, C.B.; Pluchon, P.; Harley, P.; Rigby, M.; Gonzalez Sabater, V.; Stevenson, D.C.; Hynes, S.; Lowe, A.; Burrone, J.; Viasnoff, V.; et al. In vitro modelling of nerve-muscle connectivity in a compartmentalised tissue culture device. *Adv. Biosyst.* **2019**, *3*, 1800307.
- 39. Kawada, J.; Kaneda, S.; Kirihara, T.; Maroof, A.; Levi, T.; Eggan, K.; Fujii, T.; Ikeuchi, Y. Generation of a motor nerve organoid with human stem cell-derived neurons. *Stem Cell Rep.* **2017**, *9*, 1441–1449.
- 40. Centeno, E.G.Z.; Cimarosti, H.; Bithell, A. 2D versus 3D human induced pluripotent stem cell-derived cultures for neurodegenerative disease modelling. *Mol. Neurodegener.* **2018**, *13*, 27.
- 41. Hughes, C.S.; Postovit, L.M.; Lajoie, G.A. Matrigel: A complex protein mixture required for optimal growth of cell culture. *Proteomics* **2010**, *10*, 1886–1890.
- 42. Yamamoto, K.; Yamaoka, N.; Imaizumi, Y.; Nagashima, T.; Furutani, T.; Ito, T.; Okada, Y.; Honda, H.; Shimizu, K. Development of a human neuromuscular tissue-on-a-chip model on a 24-well-plate-format compartmentalized microfluidic device. *Lab Chip* **2021**, *21*, 1897–1907.
- 43. Osaki, T.; Sivathanu, V.; Kamm, R.D. Engineered 3D vascular and neuronal networks in a microfluidic platform. *Sci. Rep.* **2018**, *8*, 5168.
- 44. Chen, X.; Rocha, C.; Rao, T.; Durcan, T.M. Motor neuron induction and differentiation (V2.0). *Zenodo* **2019**. https://doi.org/10.5281/zenodo.3738286
- 45. Chen, C.X.; Abdian, N.; Maussion, G.; Thomas, R.A.; Demirova, I.; Cai, E.; Tabatabaei, M.; Beitel, L.K.; Karamchandani, J.; Fon, E.A.; et al. A Multistep Workflow to Evaluate Newly Generated iPSCs and Their Ability to Generate Different Cell Types. *Methods Protoc.* **2021**, *4*, 50.
- 46. Mohamed, N.V.; Lépine, P.; Lacalle-Aurioles, M.; Sirois, J.; Mathur, M.; Reintsch, W.; Beitel, L.K.; Fon, E.A.; Durcan, T.M. Microfabricated disk technology: Rapid scale up in midbrain organoid generation. *Methods* **2022**, *203*, 465–477.
- 47. Yoshida, T.; Delafontaine, P. Mechanisms of IGF-1-mediated regulation of skeletal muscle hypertrophy and atrophy. *Cells* **2020**, *9*, 1970.
- 48. Oyesiku, N.M.; Wigston, D.J. Ciliary neurotrophic factor stimulates neurite outgrowth from spinal cord neurons. *J. Comp. Neurol.* **1996**, *364*, 68–77.
- 49. Jones, T.R.; Kang, I.H.; Wheeler, D.B.; Lindquist, R.A.; Papallo, A.; Sabatini, D.M.; Golland, P.; Carpenter, A.E. CellProfiler Analyst: Data exploration and analysis software for complex image-based screens. *BMC Bioinform.* **2008**, *9*, 482.

- 50. Maussion, G.; Moalic, J.M.; Simonneau, M.; Gorwood, P.; Ramoz, N. Increased expression of BDNF mRNA in the frontal cortex of autistic patients. *Behav. Brain Res.* **2019**, *359*, 903–909.
- 51. Bell, S.; Maussion, G.; Jefri, M.; Peng, H.; Theroux, J.F.; Silveira, H.; Soubannier, V.; Wu, H.; Hu, P.; Galat, E.; et al. Disruption of GRIN2B Impairs Differentiation in Human Neurons. *Stem Cell Rep.* **2018**, *11*, 183–196.
- 52. Maussion, G.; Thomas, R.A.; Demirova, I.; Gu, G.; Cai, E.; Chen, C.X.; Abdian, N.; Strauss, T.J.P.; Kelaï, S.; Nauleau-Javaudin, A.; et al. Auto-qPCR; a python-based web app for automated and reproducible analysis of qPCR data. *Sci. Rep.* **2021**, *11*, 21293.
- 53. Gómez-Gaviro, M.V.; Balaban, E.; Bocancea, D.; Lorrio, M.T.; Pompeiano, M.; Desco, M.; Ripoll, J.; Vaquero, J.J. Optimized CUBIC protocol for three-dimensional imaging of chicken embryos at single-cell resolution. *Development* **2017**, *144*, 2092–2097.
- 54. Mohamed, N.V.; Sirois, J.; Ramamurthy, J.; Mathur, M.; Lépine, P.; Deneault, E.; Maussion, G.; Nicouleau, M.; Chen, C.X.; Abdian, N.; et al. Midbrain organoids with an SNCA gene triplication model key features of synucleinopathy. *Brain Commun.* **2021**, *3*, fcab223.
- 55. Kahn-Krell, A.; Pretorius, D.; Guragain, B.; Lou, X.; Wei, Y.; Zhang, J.; Qiao, A.; Nakada, Y.; Kamp, T.J.; Ye, L.; et al. A three-dimensional culture system for generating cardiac spheroids composed of cardiomyocytes, endothelial cells, smooth-muscle cells, and cardiac fibroblasts derived from human induced-pluripotent stem cells. *Front. Bioeng. Biotechnol.* **2022**, *10*, 908848.
- 56. Lendahl, U.; Zimmerman, L.B.; McKay, R.D. CNS stem cells express a new class of intermediate filament protein. *Cell* **1990**, *60*, 585–595.
- 57. Neely, M.D.; Litt, M.J.; Tidball, A.M.; Li, G.G.; Aboud, A.A.; Hopkins, C.R.; Chamberlin, R.; Hong, C.C.; Ess, K.C.; Bowman, A.B. DMH1, a highly selective small molecule BMP inhibitor promotes neurogenesis of hiPSCs: Comparison of PAX6 and SOX1 expression during neural induction. *ACS Chem. Neurosci.* **2012**, *3*, 482–491.
- 58. Gerdes, J.; Lemke, H.; Baisch, H.; Wacker, H.H.; Schwab, U.; Stein, H. Cell cycle analysis of a cell proliferation-associated human nuclear antigen defined by the monoclonal antibody Ki-67. *J. Immunol.* **1984**, *133*, 1710–1715.
- 59. Ogura, T.; Sakaguchi, H.; Miyamoto, S.; Takahashi, J. Three-dimensional induction of dorsal, intermediate and ventral spinal cord tissues from human pluripotent stem cells. *Development* **2018**, *145*, dev162214.
- 60. Ronchi, S.; Buccino, A.P.; Prack, G.; Kumar, S.S.; Schröter, M.; Fiscella, M.; Hierlemann, A. Electrophysiological phenotype characterization of human iPSC-derived neuronal cell lines by means of high-density microelectrode arrays. *Adv. Biol.* **2021**, *5*, e2000223.
- 61. Phelps, P.E.; Barber, R.P.; Houser, C.R.; Crawford, G.D.; Salvaterra, P.M.; Vaughn, J.E. Postnatal development of neurons containing choline acetyltransferase in rat spinal cord: An immunocytochemical study. *J. Comp. Neurol.* **1984**, *229*, 347–361.
- 62. Sepehrimanesh, M.; Ding, B. Generation and optimization of highly pure motor neurons from human induced pluripotent stem cells via lentiviral delivery of transcription factors. *Am. J. Physiol. Cell Physiol.* **2020**, *319*, C771–C780.
- 63. Volpato, V.; Webber, C. Addressing variability in iPSC-derived models of human disease: Guidelines to promote reproducibility. *Dis. Model. Mech.* **2020**, *13*, dmm042317. 64.
- 65. Thiry, L.; Hamel, R.; Pluchino, S.; Durcan, T.; Stifani, S. Characterization of human iPSC-derived spinal motor neurons by single-cell RNA sequencing. *Neuroscience* **2020**, *450*, 57–70.
- 66. Zhao, J.; Lai, H.M.; Qi, Y.; He, D.; Sun, H. Current Status of Tissue Clearing and the Path Forward in Neuroscience. *ACS Chem. Neurosci.* **2021**, *12*, 5–29.
- 67. Susaki, E.A.; Tainaka, K.; Perrin, D.; Kishino, F.; Tawara, T.; Watanabe, T.M.; Yokoyama, C.; Onoe, H.; Eguchi, M.; Yamaguchi, S.; et al. Whole-brain imaging with single-cell resolution using chemical cocktails and computational analysis. *Cell* **2014**, *157*, 726–739.

- 68. Susaki, E.A.; Tainaka, K.; Perrin, D.; Yukinaga, H.; Kuno, A.; Ueda, H.R. Advanced CUBIC protocols for whole-brain and whole-body clearing and imaging. *Nat. Protoc.* **2015**, *10*, 1709–1727.
- 69. Diosdi, A.; Hirling, D.; Kovacs, M.; Toth, T.; Harmati, M.; Koos, K.; Buzas, K.; Piccinini, F.; Horvath, P. Cell lines and clearing approaches: A single-cell level 3D light-sheet fluorescence microscopy dataset of multicellular spheroids. *Data Brief* **2021**, *36*, 107090.
- 70. Wagenaar, D.A.; Pine, J.; Potter, S.M. An extremely rich repertoire of bursting patterns during the development of cortical cultures. *BMC Neurosci.* **2006**, *7*, 11.
- 71. Sharf, T.; van der Molen, T.; Glasauer, S.M.K.; Guzman, E.; Buccino, A.P.; Luna, G.; Cheng, Z.; Audouard, M.; Ranasinghe, K.G.; Kudo, K.; et al. Functional neuronal circuitry and oscillatory dynamics in human brain organoids. *Nat. Commun.* **2022**, *13*, 4403.
- 72. Passaro, A.P.; Stice, S.L. Electrophysiological analysis of brain organoids: Current approaches and advancements. *Front. Neurosci.* **2020**, *14*, 622137.
- 73. Kobolak, J.; Teglasi, A.; Bellak, T.; Janstova, Z.; Molnar, K.; Zana, M.; Bock, I.; Laszlo, L.; Dinnyes, A. Human induced pluripotent stem cell-derived 3D-neurospheres are suitable for neurotoxicity screening. *Cells* **2020**, *9*, 1122.

Figures

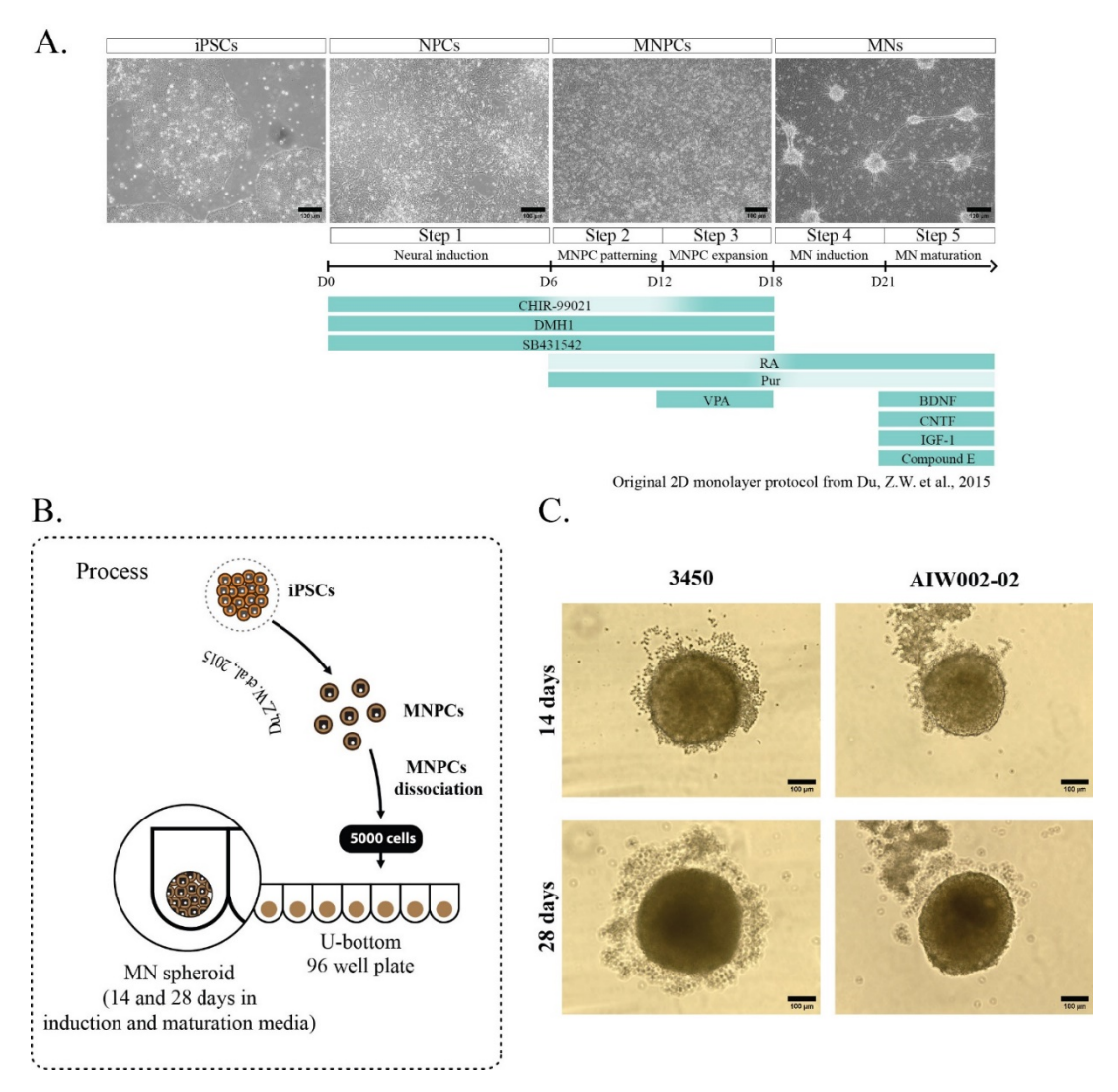


Figure 1. Generation of iPSC-derived MN spheroids. (A) Summary of the small-molecule protocol developed by (16) and optimized by our group to generate iPSC-derived MNs as a 2D monolayer. Briefly, iPSCs are differentiated towards neural progenitor cells (NPCs) that are patterned to motor neuron neural progenitor cells (MNPCs), which are finally differentiated into MNs. (B) At the MNPCs stage, two control cell lines (3450 and AIW002-02) were dissociated and plated into 96 U-bottom ultra-low attachment well plates in MN induction and maturation medium to generate MN spheroids that were kept in culture until their analysis. (C) Representative bright-field pictures of MN spheroids after 14 and 28 days of differentiation of both control cell lines.

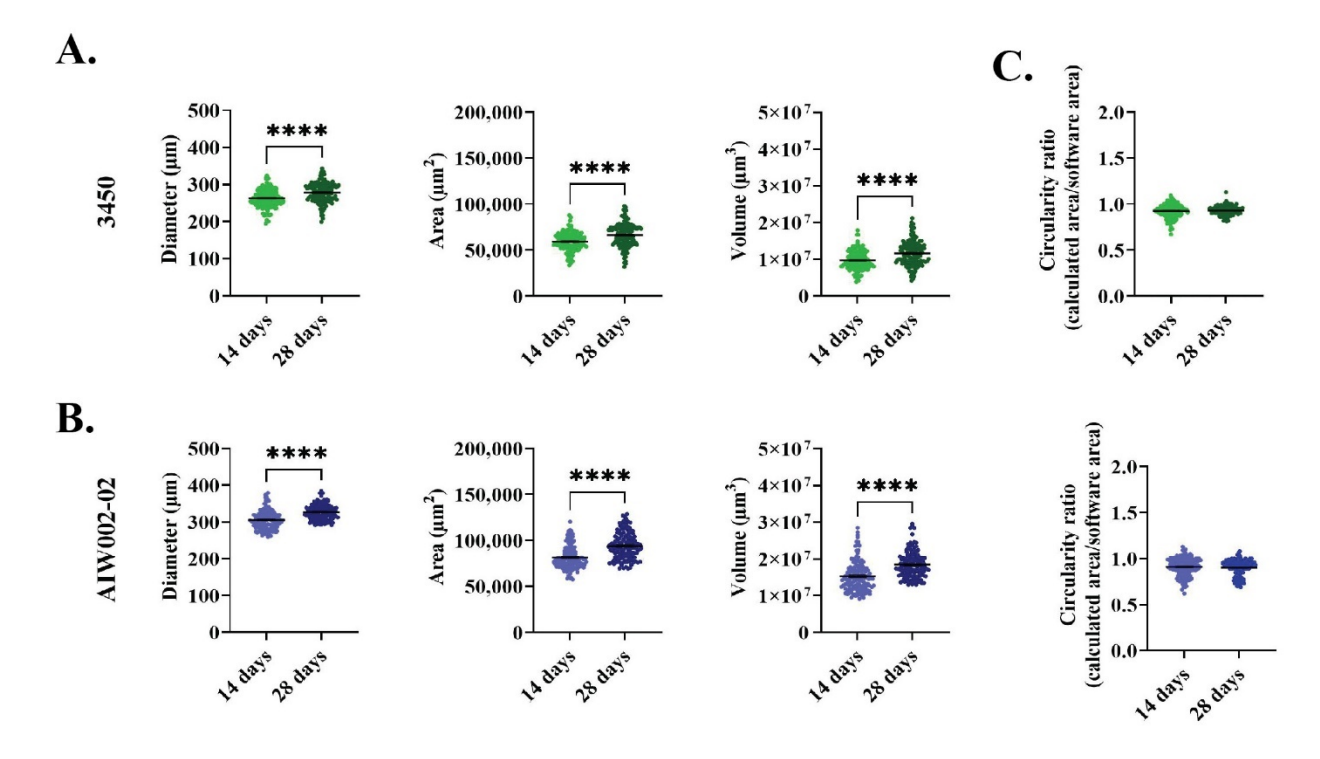


Figure 2. Size profile by a cell profiler pipeline. iPSC-derived MN spheroids from the (A) 3450 and (B) AIW002-02 control lines are consistently generated across different batches. They exhibit an increase in size over time as shown by diameter, area, and volume measurements. Scatter plots show the mean \pm SEM; for each cell line, five MN spheroid batches coming from at least two iPSC-derived MNPCs batches induced through independent differentiation processes (AIW002-02 = 137 spheroids; 3450 = 142 spheroids). To ensure that MNPC passage number was not having any effect on MN spheroid formation, we used the MNPCs at passage number 2 to 4. Significance was determined by a paired *t*-student. **** $p \le 0.0001$. (C) Additionally, MN spheroids display a circular shape with bulges appearing occasionally but without disturbing the circular morphology, as shown by the circularity ratio (0 = not circular; 1 = perfect circle).

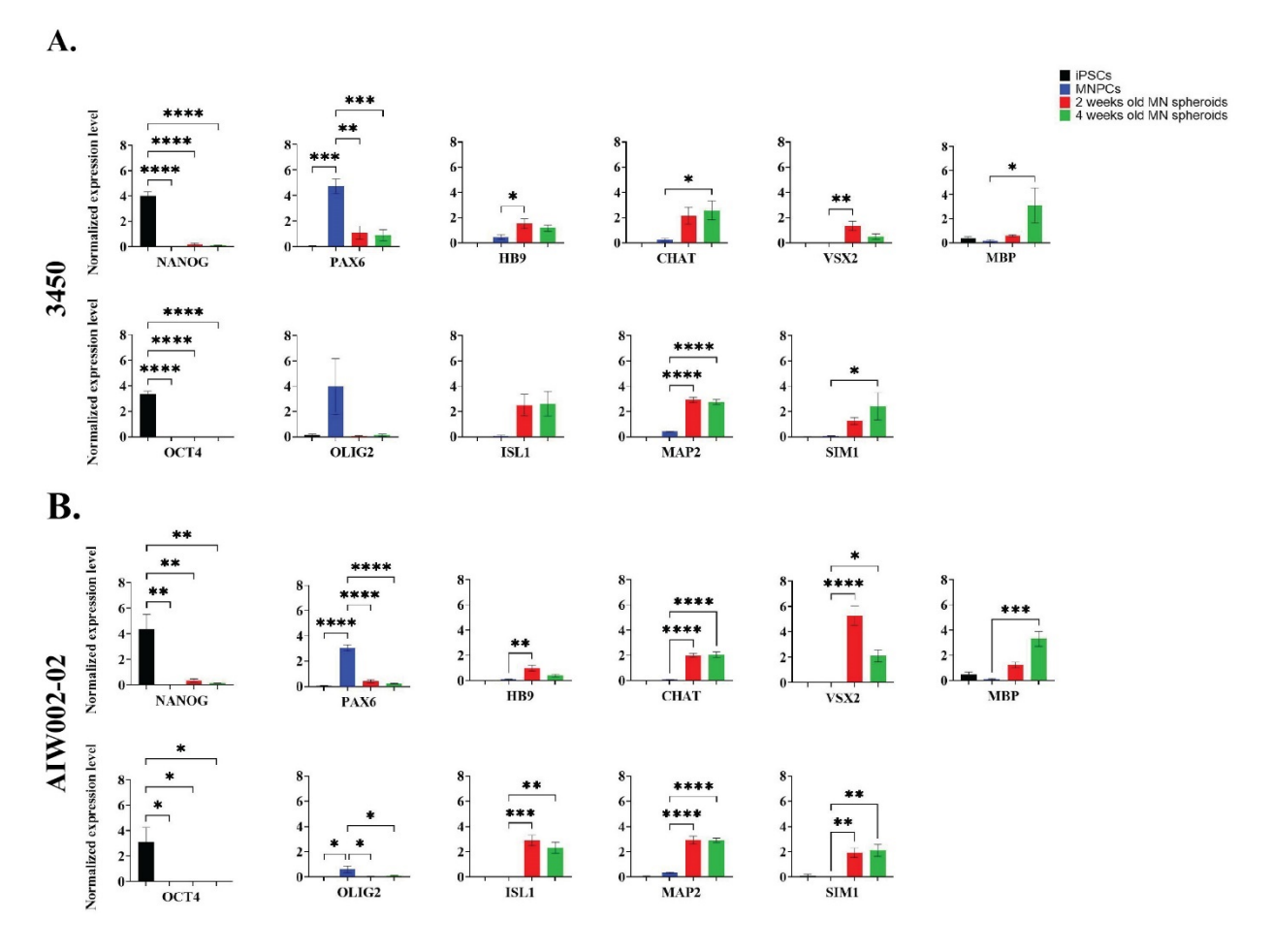


Figure 3. Transcript expression profile of iPSC-derived MN spheroids. Normalized expression levels of NANOG, OCT4, PAX6, OLIG2, HB9, ISL1, CHAT, MAP2, VSX2, SIM1, MBP, and GFAP in iPSCs, MNPCs, and iPSC-derived MN spheroids differentiated for 14 and 28 days from (A) 3450 and (B) AIW002-02 lines. Data normalized to Actβ-GAPDH expression. Bar graphs show the mean \pm SEM; three MN spheroid batches per time point (14 and 28 days). Each MN spheroid batch was obtained from iPSC-derived MNPC batches at passage 3 generated through independent differentiation processes. Significance was determined for each gene using a one-way ANOVA. Next, post Dunnett's tests using iPSCs (NANOG and OCT) or MNPCs (PAX6, OLIG2, HB9, ISL1, CHAT, MAP2, VSX2, SIM1, and MBP) as reference samples were performed. * $p \le 0.05$; *** $p \le 0.01$; **** $p \le 0.001$; **** $p \le 0.0001$.

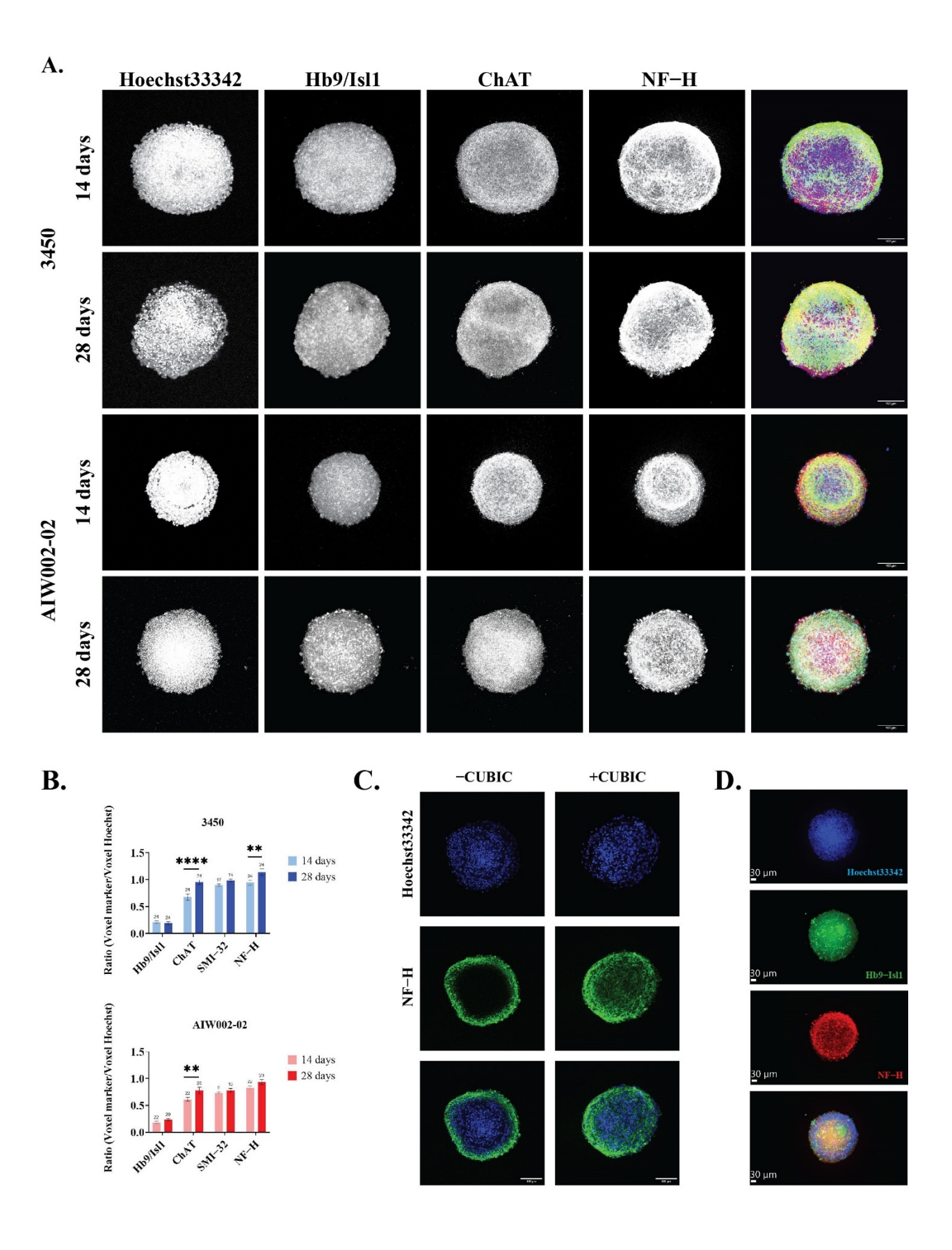


Figure 4. Image profiling of iPSC-derived MN spheroids. (A) Characterization of MN spheroids by immunostaining showed that MN spheroids generated from the 3450 and AIW002-02 iPSC lines express the specific MN markers Hb9, Isl1, CHAT, and SMI-32 (not shown), as well as the neuronal marker NF-H. Merge shows overlay of Hb9/Isl1 (blue), CHAT (red), and NF-H (green). (B) The presence of each MN marker was quantified using an in-house MATLAB pipeline. Graph bars show the mean ± SEM; for each cell line, each batch of three batches of iPSCderived MNPCs generated through independent differentiation processes were used to generate two MN spheroid batches. A minimum of 9 MN spheroids were required for quantification, and we ensured that at least 3 spheroids per MNPC batch were stained for each marker per cell line at each time point. The significance between the two different time points (14 days and 28 days) for each MN marker was determined by an unpaired t-student ** p < 0.01; **** p < 0.0001. (C) CUBIC, a tissue-clearing protocol, was developed to increase antibody penetrance and decrease optical opacity to perform the quantification of the different markers in a more precise manner. For each condition, a single image from the center of the Z-stack was selected to be presented. (**D**) Representative image of a MN spheroid reconstructed as a 3D structure using the IMARIS software from Oxford Instruments.

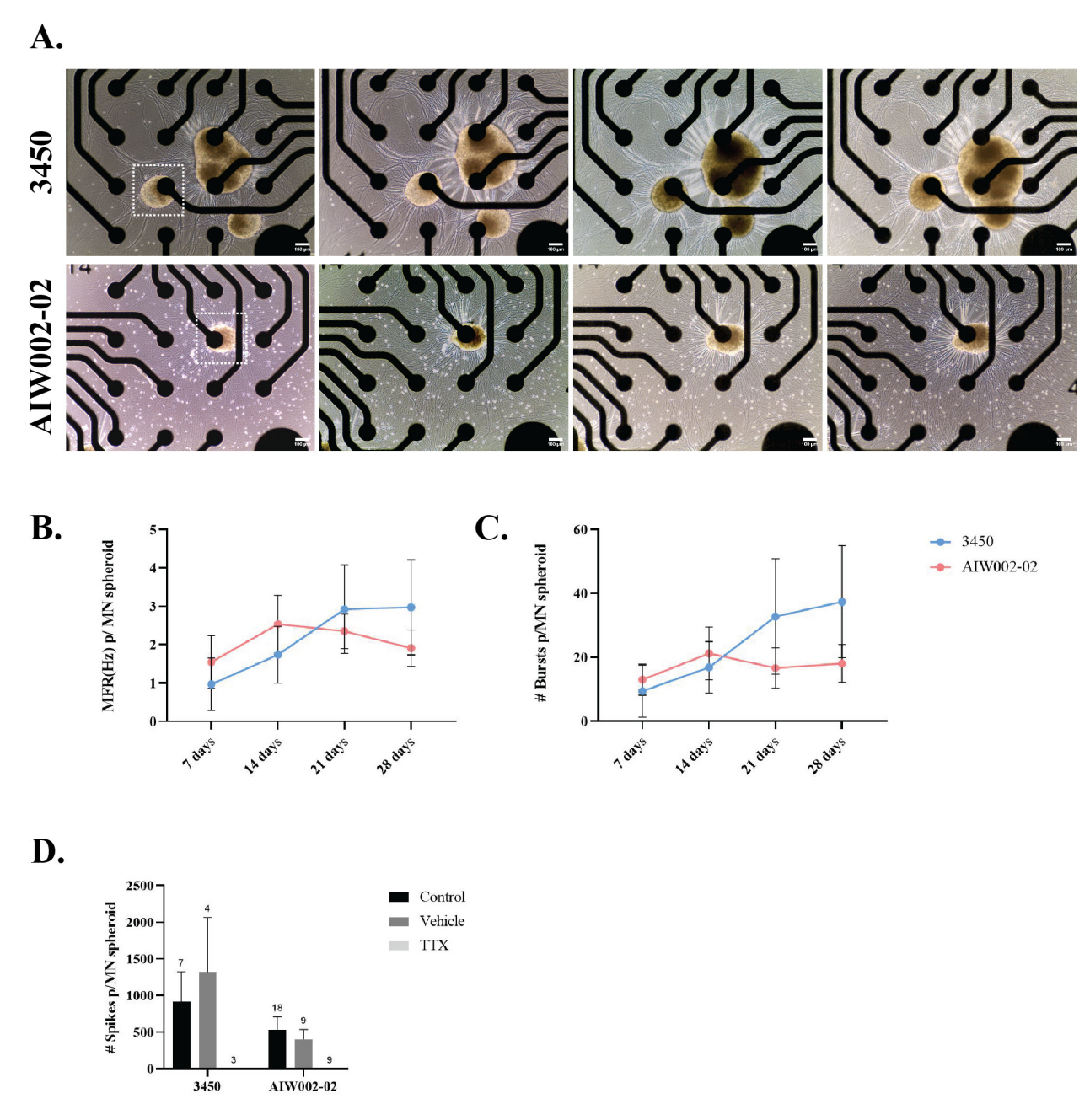


Figure 5. Spontaneous firing activity of iPSC-derived MN spheroids at different time points.

(A) iPSC-derived MN spheroids were plated on wells of Cytoview 24-well MEA plates and recorded every 7 days until 28 days. Only MN spheroids placed at the center of an electrode (squares) through the entire recording time were considered for quantification. (B) Mean firing rate (MFR) and (C) number of bursts were plotted per individual MN spheroid. The connected scatter plots show the mean ± SEM; for each cell line, each batch of three batches of iPSC-derived

MNPCs generated through independent differentiation processes were used to generate one MN spheroid batch. A minimum of nine MN spheroids were required for quantification to ensure that at least three spheroids per MNPC batch were quantified. (**D**) Tetrodotoxin (TTX) treatment blocked all firing in MN spheroids, ruling out system artifacts and confirming neural activity for both cell lines. H_2O was used as vehicle. Graph bars show mean \pm SEM.

Supplementary materials

An optimized workflow to generate and characterize iPSC-derived motor neuron (MN) spheroids

María José Castellanos-Montiel, Mathilde Chaineau, Anna Kristyna Franco-Flores, Ghazal Haghi, Dulce Carrillo-Valenzuela, Wolfgang E. Reintsch, Carol X-Q Chen, Thomas M. Durcan.

Corresponding author e-mail: thomas.durcan@mcgill.ca (T.M.D)

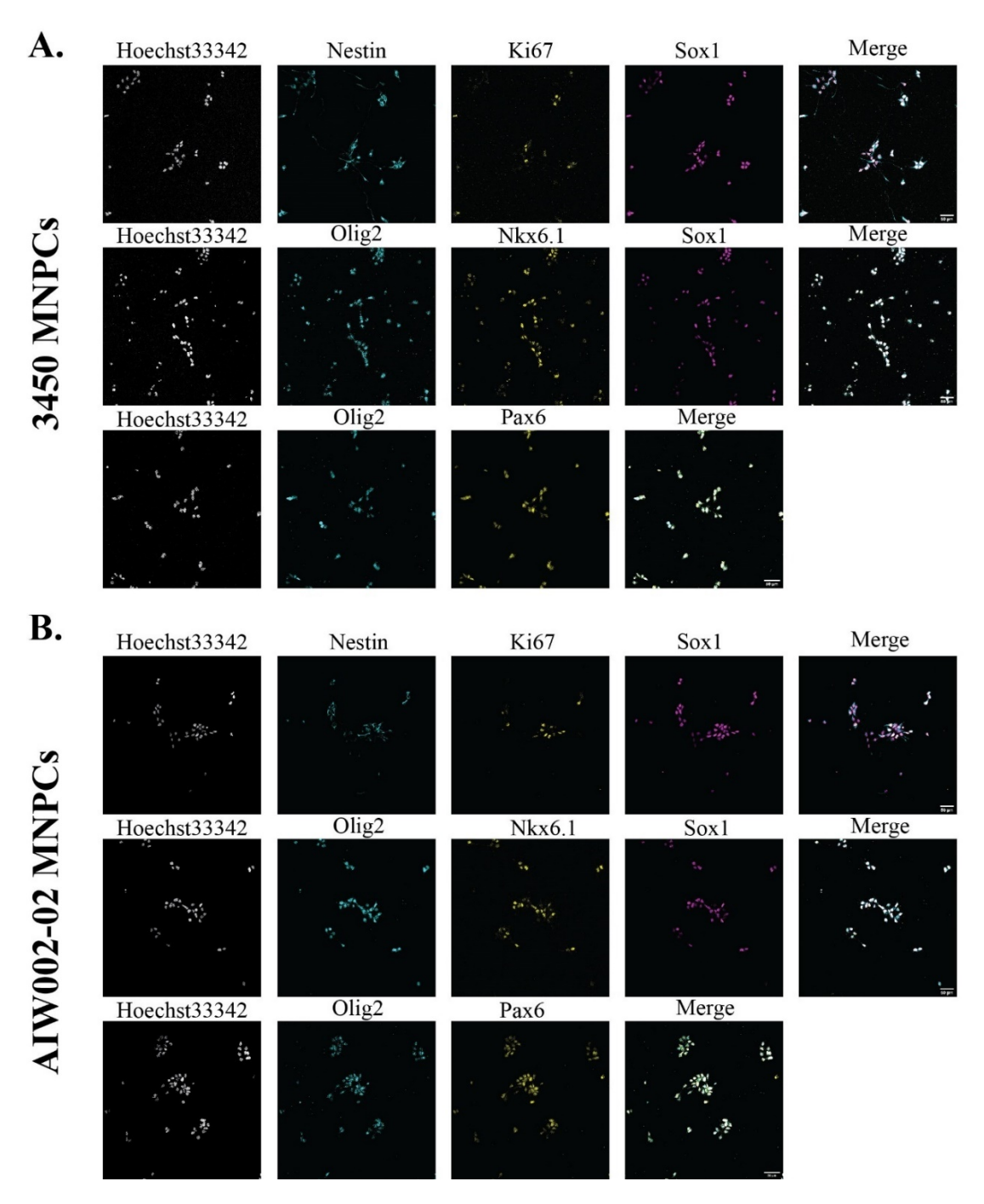
This PDF file includes:

Supplementary Table 1

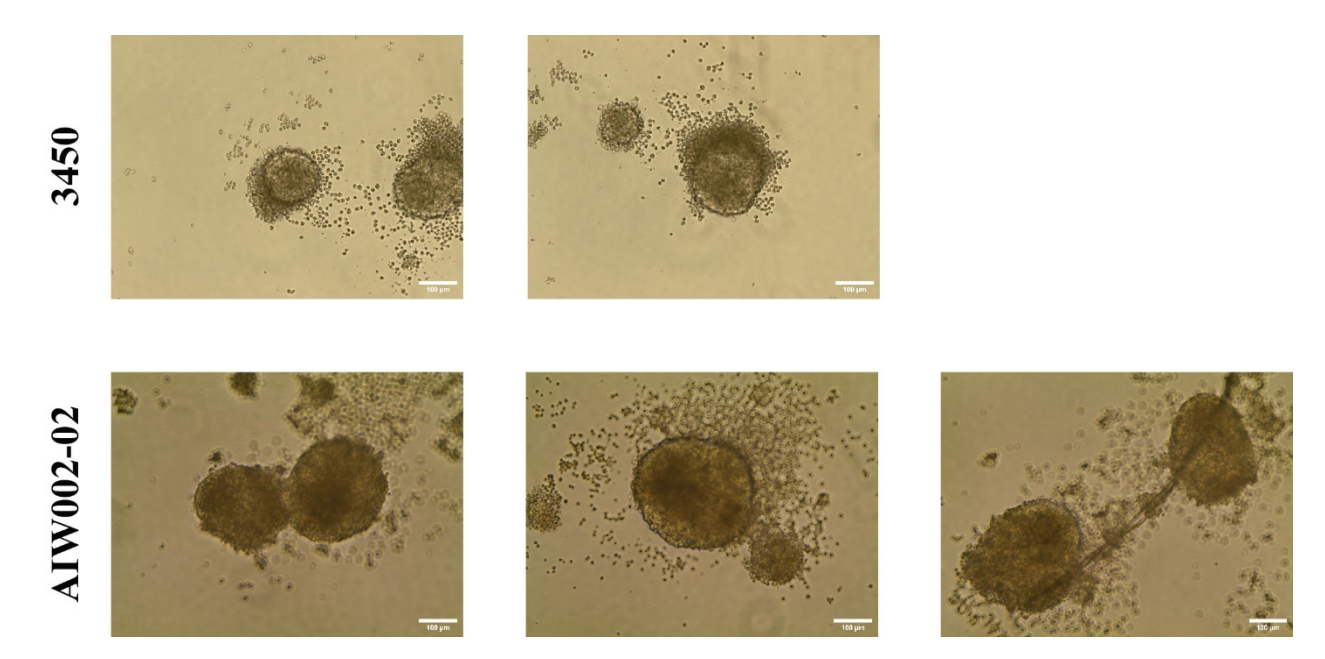
Supplementary Figures 1-4

Supplementary Table 1. List of consumables and equipment

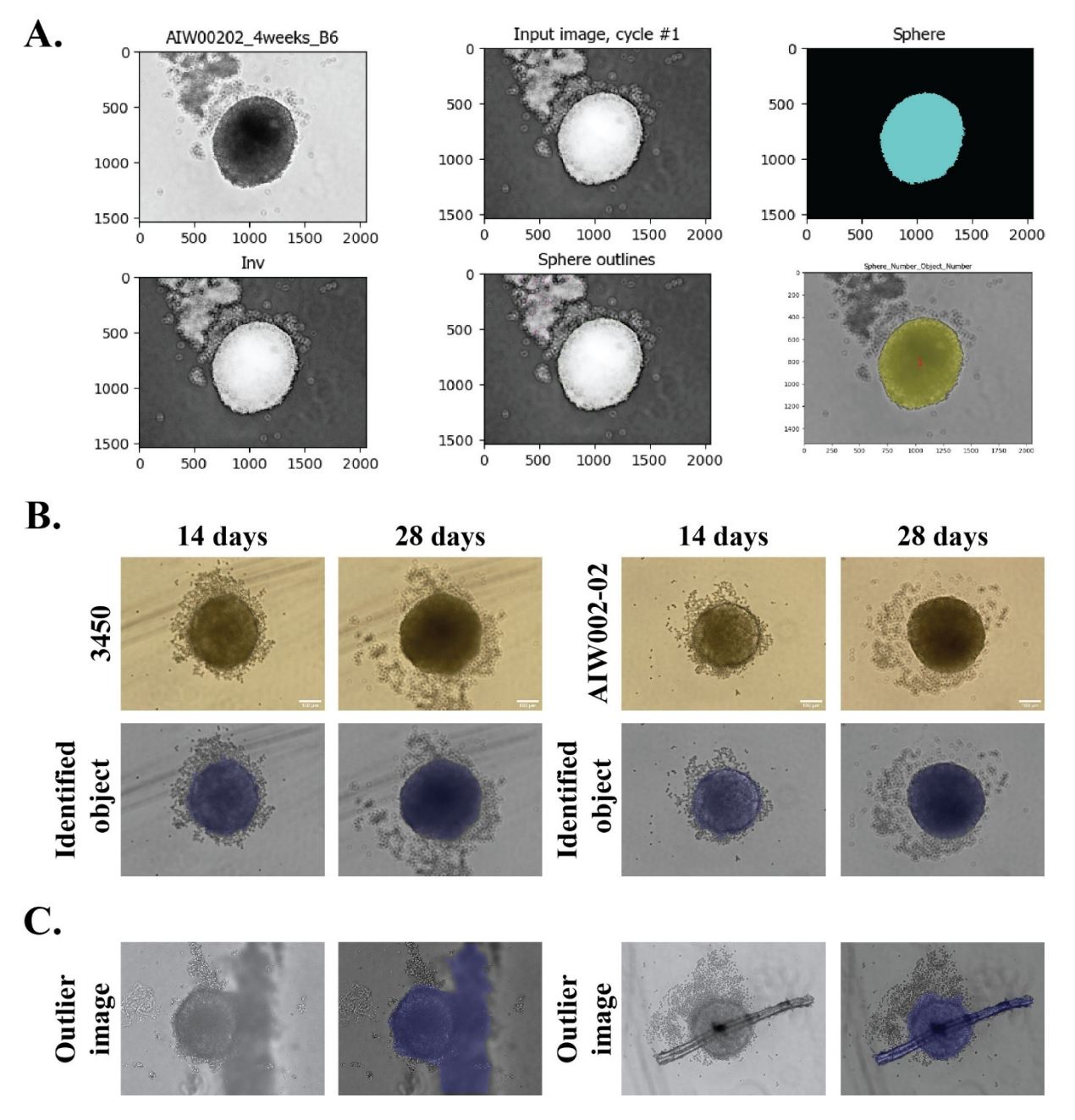
Supplier	Catalogue number
ls	
Corning	353003
Corning	CLS7007
Thermo Fisher Scientific	Steri-Cycle Model 370 Ref#20
Corning	CLS3010
Eppendorf	022626001
Eppendorf	5810R
Thermo Fisher Scientific	352097
Sarstedt	72.379
Logos biosystems	L40002
Thermo Fisher Scientific	13-678-11E
Thermo Fisher Scientific	13-678-11B
Thermo Fisher Scientific	13-678-11D
Thermo Fisher Scientific	12-556-009
Thermo Fisher Scientific	12-556-010
IN spheroids	
Thermo Fisher Scientific	AMEX1000
NanoEntek	NANOJS1000S
Thermo Fisher Scientific	N8010580
Thermo Fisher Scientific	4309849
Thermo Fisher Scientific	4323032
Thermo Fisher Scientific	4311971
Thermo Fisher Scientific	ND-ONE-W
Thermo Fisher Scientific	A28140
Thermo Fisher Scientific	A24811
rescent staining of MN spheroid	ds
Thermo Fisher Scientific	02-681-273
Corning	LSE TM 6790
Corning	353219
VWR	82007-202
PerkinElmer	N/A
Thermo Fisher Scientific	22363547
Labcon	1164-965-008-9
of MN spheroids	
Thermo Fisher Scientific	09-719C
VWR	76290-386
Progene	71-5000-В
Axion Biosystems	N/A
Axion Biosystems	M384-Tmea-24w
Labcon	1164-965-008-9
1	Corning Corning Thermo Fisher Scientific Corning Eppendorf Eppendorf Thermo Fisher Scientific Sarstedt Logos biosystems Thermo Fisher Scientific IN spheroids Thermo Fisher Scientific Corning Corning VWR PerkinElmer Thermo Fisher Scientific Labcon of MN spheroids Thermo Fisher Scientific VWR Progene Axion Biosystems Axion Biosystems



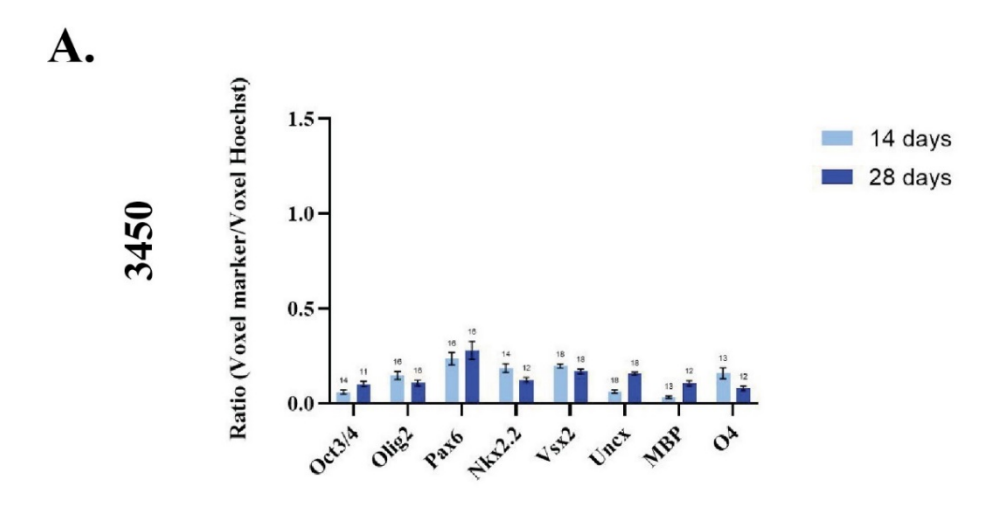
Supplementary Figure 1. Motor neuron neural progenitor cell (MNPC) characterization by immunofluorescent staining. A. 3450 and **B.** AIW002-02 MNPCs were positive for Sox1 and Nestin indicating their neural progenitor identity as well as Ki67, which demonstrates their proliferation capacity. Additionally, MNPCs are positive for the markers Pax6, Olig2 and NKx6.1 that indicate their successful specification towards motor neuron neural progenitor cells.

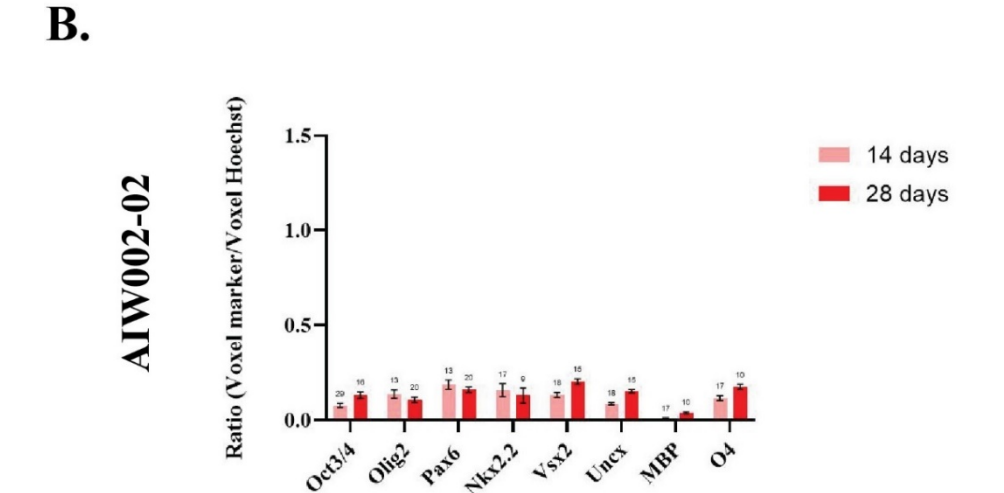


Supplementary Figure 2. Inappropriate formation of MN spheroids. Examples illustrating inappropriate formation of MN spheroids in random wells regardless of the iPSC line used.



Supplementary Figure 3. CellProfiler macro to perform the size profiling of the MN spheroids. A) A data set of pictures taken with a bright-field microscope is inserted into a Cell Profiler pipeline. B) The pipeline processes the image to identify a primary object that is overlaid with the original image. C) Images in which the macro performed poorly are considered outliers and removed from the analyses.





Supplementary Figure 4. Image profiling of iPSC-derived MN spheroids to identify different cell types. MN spheroids from **A)** 3450 and **B)** AIW002-02 control cell lines were stained for interneuron (Nkx2.2, Vsx2, Uncx) and oligodendrocyte markers (MBP, O4). The presence of these markers was quantified using an in-house MATLAB pipeline. Graph bars show the mean ± SEM; for each cell line, each batch of three batches of iPSC-derived MNPCs generated through independent differentiation processes was used to generate two MN spheroid batches. A minimum of 9 MN spheroids were required for quantification, and we ensured that at least 3 spheroids per MNPC batch where stained for each marker per cell line at each time point.

Chapter 2 – Using 3D iPSC-derived MN spheroids carrying mutations linked to fALS to investigate disease-related phenotypes

Once an optimized workflow was developed to generate and characterize iPSC-derived MN spheroids, we next explored whether this model could reproduce disease-related phenotypes associated with ALS, a NMD linked to MN degeneration.

The superoxide dismutase 1 gene (SOD1) encodes a 154-amino-acid protein that catalyzes the conversion of superoxide radicals (O_2) into hydrogen peroxide (H_2O_2) and molecular oxygen (O_2) (121). To date, over 200 pathogenic variants have been reported in SOD1 across all five exons encoding the protein (122), with varying disease prognoses observed among patients (123). The exact mechanism by which mutated SOD1 causes MN loss remains unclear; instead, it is hypothesized that a combination of mechanisms including aberrant protein aggregation, oxidative stress, excitotoxicity and mitochondrial dysfunction, triggers the onset and progression of the disease (124).

For Chapter 2, recently submitted to a journal as an original research paper (2), we generated MN spheroids from iPSC lines harboring homozygous knock-in mutations in *SOD1*, the second most common cause of fALS (77). These knock-in mutations were introduced into the AIW002-02 iPSC line which served as the isogenic control for accurate phenotypic comparisons.

Our results demonstrate that iPSCs with homozygous *SOD1* mutations at positions D90A, G93A, and the double mutant D90A/G93A can generate MN spheroids comparable to the isogenic control regarding cell identity. Using our 3D workflow instead of the conventional 2D monolayer approach allowed for a prolonged culture period and revealed distinct disease-related phenotypes.

Mutant SOD1 MN spheroids displayed differences in size, SOD1 expression, cell viability, neurofilament subunit (NF) expression, and MEA activity. However, not all genotypes exhibited every phenotype or showed the same degree of change, reflecting the heterogeneity of ALS, even among patients with mutations in the same gene.

Mutations in SOD1 induce ALS-related phenotypes in 3D iPSC-derived motor neuron (MN) spheroids

María José Castellanos-Montiel¹, Anna Kristyna Franco-Flores¹, Michael Nicouleau¹, Ghazal Haghi¹, Sarah Lépine², Belén Baeza¹, Carol X.-Q. Chen¹, Taylor M. Goldsmith¹, Nathalia Aprahamian¹, Doris Hua¹, Mathilde Chaineau¹, Lale Gursu¹, Narges Abdian¹, Eric Deneault³, Thomas M. Durcan¹*

Author's affiliations:

¹ Early Drug Discovery Unit (EDDU), The Neuro-Montreal Neurological Hospital and Institute, McGill University, Montreal, Quebec, Canada.

² Faculty of Medicine and Health Sciences, McGill University, Montreal, Quebec, Canada.

³ Centre for Oncology, Radiopharmaceuticals and Research; Biologic and Radiopharmaceutical Drugs Directorate, Health Products and Food Branch, Health Canada, Ottawa, Ontario, Canada.

* Correspondance : thomas.durcan@mcgill.ca

Abstract

A significant challenge in ALS research is the heterogeneity of the disease. Even mutations within the same gene can lead to different disease prognosis. For instance, *in silico* protein modeling predicts distinct properties for distinct SOD1 mutations. With this in mind, in this study, we generated and characterized 3D iPSC-derived MN spheroids carrying homozygous knock-in SOD1 mutations (D90A and G93A), as well as a double mutation (D90A/G93A), to evaluate potential synergistic effects. An isogenic control line with the same genetic background was used for phenotypic comparisons with the knock-in variants. Mutant SOD1 MN spheroids exhibited

	SOD1 ^{D90A-KI}	SOD1 ^{G93A-KI}	SOD1 ^{D90A/G93A-KI}
Size	Smaller	Bigger	Bigger
SOD1 expression	NW NW NW NW Higher	Lower	UB UB Lower
Cell viability (ATP levels)	Decreased 40%	Decreased 20%	Decreased 30%
Neurofilament subunit expression	NFL and NFH low	NFL low	NFL and NFH low
MEA activity	Irregular burst firing		Hypoactive

multiple ALS-related phenotypes including altered SOD1 expression, reduced cell viability, downregulation of neurofilament (NF) subunit expression, hypoactivity, and altered burst activity. Our results highlight the advantages of using 3D MN spheroids as a disease model and stress the importance of considering phenotype variability at the genetic level in ALS.

1. Introduction

Amyotrophic lateral sclerosis (ALS) is a heterogeneous, adult-onset neurodegenerative disease characterized by progressive motor neuron (MN) loss in the motor cortex, brainstem, and spinal cord, leading to skeletal muscle weakness and atrophy (1). Following an ALS diagnosis, the average survival is 3 – 4 years, with patients typically succumbing to respiratory failure (2). Sporadic ALS (sALS) accounts for 90% of cases, with the remaining 10%, referred to as familial ALS (fALS), following an inheritance pattern associated with identified gene mutations (3, 4). Mutations in superoxide dismutase 1 (*SOD1*) account for ~20% of fALS cases, making it the second most common genetic cause of the disease, surpassed only by C9orf72 mutations, which account for ~40% of fALS cases (4, 5).

SOD1 is a 32 kDa homodimeric enzyme whose primary function is to mitigate oxidative stress by converting free superoxide radicals into oxygen and hydrogen peroxide (6, 7). Early evidence from post-mortem brain tissue of sALS and fALS patients suggests that loss-of-function mechanisms resulting from SOD1 haploinsufficiency contribute to increased oxidative stress levels in neurons (8). However, later evidence has shown a limited correlation between enzyme activity and the onset or clinical forms of the disease (9). In turn, it was found that misfolded mutant SOD1 can aggregate and acquire toxic gain of function properties (8, 10). Nevertheless, *in silico* protein modeling and *in vitro* aggregation propensity studies have shown that these aggregation properties can differ between SOD1 variants (11, 12). Thus, a central question in the ALS field is whether SOD1 mutations result in a loss of function, a gain of toxic function, or both.

In 1994, Gurney and colleagues introduced the first transgenic mouse model for ALS, which overexpresses the human SOD1 gene with a glycine-to-alanine mutation at position 93

(SOD1^{G93A}) (13, 14). To date, the SOD1^{G93A} mouse model remains the gold standard for motor deficit assessment in preclinical studies (15). However, issues arising from overexpression, inconsistencies in disease progression, and other limitations cast doubt on the complete translatability of this model to the human context (15). Induced pluripotent stem cells (iPSCs) provide access to human neurons derived from patients with neurodegenerative diseases, including MNs, enabling the study of neurodegeneration *in vitro*. Currently, patient iPSC-derived MNs are used alongside animal models to study ALS (16, 17). Moreover, the advent of CRISPR/Cas9 genome editing technology enables the creation of isogenic controls for accurate phenotypic comparisons (18, 19).

Various protocols exist for differentiating iPSC-derived MNs, typically resulting in a 2D monolayer of neurons (20). However, this approach poses technical challenges, as MNs tend to aggregate and detach over time, limiting its suitability for long-term analysis. This is particularly important when modeling neurodegenerative diseases, where disease phenotypes may only emerge after extended culture periods. (21, 22). In a study from our group, we successfully differentiated 2D iPSC-derived MNs harboring ALS-related mutations and maintained them in culture for ~42 days under optimal conditions for analysis (18). Nevertheless, the lack of a significant reduction in MN viability in the ALS lines implies that the MNs may not have been mature enough to detect a disease phenotype at the examined time points, highlighting the challenges associated with long-term culture and emphasizing the need for strategies to overcome these limitations. Advancements in 3D *in vitro* systems, such as organoids and spheroids, provide environments that closely mimic cellular development, bringing us closer to replicating human physiology and pathology (23, 24, 25, 26). Furthermore, 3D cultures overcome the detachment issues seen in 2D cultures, enabling extended analysis.

In this study, we observed a number of ALS-related phenotypes in 3D iPSC-derived MN spheroids (23) generated from iPSCs carrying homozygous knock-in mutations at positions D90A and G93A, as well as in a double mutant SOD1^{D90A/G93A-KI} iPSC line developed previously (19). We have previously demonstrated that MNs can be cultured for up to 28 days while maintaining the expression of well-established MN markers (23). Here, we extended the culture period to 56 days to determine whether the observed phenotypes become more pronounced over longer durations. To ensure the accuracy of our findings, we compared the phenotypic changes in these mutant lines to MN spheroids derived from the isogenic control iPSC line (27), which shares the same genetic background except for the introduced *SOD1* mutations. This approach provides a 3D scalable model for investigating ALS distinct cellular pathologies associated with SOD1 mutations.

2. Materials and methods

Generation and maintenance of human iPSCs

Following a streamlined CRISPR/Cas9 workflow, the validated non-carrier AIW002-02 iPSC line (27) was used to engineer a homozygous double knock-in iPSC line carrying two SOD1 mutations known to encode fALS variants: D90A and G93A (SOD1^{D90A/G93A-KI}) (19). Here, we describe the correction of the SOD1^{D90A/G93A-KI} iPSC line to generate two new iPSC lines, each carrying a single homozygous mutation, either D90A (SOD1^{D90A-KI}) or G93A (SOD1^{G93A-KI}) (Additional file 1) (Additional files 2-4: Tables S1-3) (Additional file 8). For this study, the SOD1^{D90A-KI}, SOD1^{G93A-KI}, and SOD1^{D90A/G93A-KI} iPSC lines were used alongside the original AIW002-02 iPSC line as the isogenic control for precise phenotypic comparisons. Briefly, all iPSC lines were maintained on Matrigel (#354277, Corning)-coated dishes in mTeSR1TM medium (#85850, STEMCELL Technologies) and passaged at 80% confluence using Gentle Cell Dissociation Reagent (#100-0485, STEMCELL Technologies) (27). The complete profiles of the iPSCs, detailed culture procedures, and methods for quality control analyses-including immunocytochemistry for pluripotency associated markers, qPCR to assess chromosome copy numbers, karyotyping and virology testing—are available in (19, 27) (Additional file 1) (Additional file 9). Prior to starting the experiments, iPSCs were tested weekly and found to be free from mycoplasma. The use of iPSCs in this research was approved by the McGill Research Ethics Board (IRB Study Number A03-M19-22A).

Generation and characterization of iPSC-derived motor neuron (MN) spheroids

For each iPSC line (AIW002-02, SOD1^{D90A-KI}, SOD1^{G93A-KI}, and SOD1^{D90A/G93A-KI}), three independent differentiations were performed to obtain motor neuron progenitor cells as previously described (MNPCs) (**Supplementary Figure 3**) (18, 19, 23, 28). Next, MNPCs were used to generate and characterize MN spheroids following a published optimized workflow (23). Briefly, MNPCs were dissociated into a single cell suspension using Accutase (#07922, Thermo Fisher Scientific) and plated into round-bottom ultra-low-attachment 96-well plates (#707, Corning) to promote their aggregation as 5K or 10K MN spheroids that were assessed at different time points at the morphological, transcript, protein, and functional level.

Size profiling

Bright-field images of 5K or 10K MN spheroids were acquired with an EVOSTM XL Core (Thermo Fisher Scientific) light microscope after 14, 28, and 56 days in MN induction and maturation medium. System 20X/0.40 objective. Image size, 1024 x 768 pixels. Pixel size, 0.449 μm x 0.449 μm. The longitudinal growth of each MN spheroid was followed by saving their location within the plate. Next, a CellProfiler pipeline available online was used to measure the area of each MN spheroid in pixels (https://doi.org/10.17605/OSF.IO/V84WS) (accessed on 9 September 2024) (23). Finally, the area in pixels was manually transformed into μm² by multiplying x 0.449 μm x 0.449 μm. For each cell line, twenty MN spheroids from each of three different batches were analyzed.

Clearing and immunocytochemistry

5K MN spheroids were fixed, cleared, and immunostained at 14, 28 and 56 days, as previously described with minor modifications (23). During the Clear Unobstructed Brain/Body Imaging Cocktail and Computational Analysis (CUBIC) protocol (23, 29), 56-day-old MN spheroids required a 72 h treatment with CUBIC R1 due to their size. Images of the immunostained MN spheroids were acquired with the Opera Phenix High-Content Screening System using the PreScan function to find the spheres within the focal plane at 5X and then perform the imaging at 20X. System 5X/0.16 and 20Xwater/1.0 objectives. Image size 512×512 pixels. Voxel size, 0.29 μ m \times 0.29 μ m \times 5 μ m. Data was extracted to be organized and analyzed by an in-house script developed in MATLAB. Images were analyzed as raw Z-stacks without altering brightness and contrast. A list of all primary and secondary antibodies used is provided in **Additional file 5 and** 6: **Tables S4 and S5**.

RT-qPCR

For each condition, sixty 5K MN spheroids were pooled into a 1.7 mL collection tube (#87003-294, VWR) and total RNA was isolated using the miRNeasy Micro Kit (#217084, Qiagen) according to the manufacturer's instructions. Subsequently, reverse transcription reactions for cDNA synthesis, followed by qPCR reactions, were performed as previously described (23). The mean between Actβ and GAPDH was used as the endogenous control for normalization. A list of all the TaqMan probes used is provided in **Additional file 7: Table S6.**

Western Blotting

Sixty 10K MN spheroids were pooled into a single 1.7 mL collection tube for whole protein extraction. Briefly, samples were incubated with cold 1X RIPA buffer (#20-188, Millipore) containing a cocktail of protease (#11697498001, Roche) and phosphatase inhibitors (#04906837001, Roche) for 15 minutes at 4°C. Every 5 minutes, the samples were mechanically dissociated using a pipette. Finally, the samples were centrifuged at 10,000 g for 30 min at 4°C, and supernatants were collected for protein quantification.

Protein concentration in the supernatants was quantified using the DC Protein Assay (#5000116, Bio-Rad) according to the manufacturer's instructions. For blotting NFL, NFM, and NFH, 1 µg of protein was loaded onto a 7.5% SDS-PAGE gel and run at 70 V for 15 min, then at 120 V for ~1.5 h. Semi-dry transfer to nitrocellulose membranes was performed using the Trans-Blot Turbo Transfer System (Bio-Rad) for 10 min at 2.5 A, up to 25 V. For blotting βIII-tubulin, SOD1, and cleaved caspase-3, 1 µg (or 5 µg for cleaved caspase-3) of protein was loaded onto a 12% SDS-PAGE gel, run at 70 V for 15 min, then at 120 V for ~1 h. Semi-dry transfer to nitrocellulose membranes was performed for 30 min up to 1.0 A, at 25 V. After transfer, the membranes were blocked with 5% BSA (or 5% skimmed milk [#SKI400.1, Bioshop] for cleaved caspase-3) in 1X TBS buffer containing 0.1% Tween 20 (#TWN510, Bioshop) (blocking solution) for 1 h at room temperature (RT) with continuous shaking, followed by overnight incubation with primary antibodies, diluted in their respective blocking solutions, at 4°C with continuous shaking. After three 10-min washes with 1X TBS containing 0.1% Tween 20 (washing solution) and continuous shaking, membranes were incubated with horseradish peroxidase (HRP)-conjugated antibodies, diluted in their respective blocking solutions, for 2 h at RT with continuous shaking. After three 10-min washes with washing solution and continuous shaking, protein bands were

detected using the ClarityTM Western ECL (#<u>1705060</u>, Bio-Rad) (or ClarityTM Max Western ECL [#<u>1705062S</u>, Bio-Rad] for cleaved caspase-3) according to the manufacturer's instructions and visualized using a Chemidoc MP Imaging System (Bio-Rad). Quantification was performed with the Image Lab 6.0.1 software (Bio-Rad), using β -Actin and GAPDH as loading controls. A list of all antibodies used is provided in **Additional file 5 and 6: Tables S4 and S5**.

CellTiter-Glo® 3D Cell Viability Assay

10K MN spheroids were grown for 56 days in round-bottom ultra-low-attachment 96-well plates. At the endpoint and before starting the experiment, bright-field images of the MN spheroids were acquired with an EVOSTM XL Core light microscope for normalization of the luminescence measures against MN size. System 20X/0.40 objective. Image size, 1024 x 768 pixels. Pixel size, 0.449 μm x 0.449 μm. Each MN spheroid along with 100 μL of medium was transferred into a well of a white round-bottom 96-well plate (#3789A, Corning) using wide-orifice low-binding tips and the CellTiter-Glo® 3D Cell Viability Assay (#G9682, Promega) was performed following the manufacturer's instructions. Luminescence readings as random luminescence units (RLU) were acquired using a SpectraMax iD3 multi-mode microplate reader (Molecular Devices). After RLU acquisition, each measurement was normalized against the area in pixels of its corresponding MN spheroid to obtain a ratio (RLU/area in pixels). For comparisons across cell lines, ratios were converted to percentages, with the ratio of the isogenic control set as 100% survival.

Detection of NFL release in cell culture medium

10 K MN spheroids were cultured for 56 days in round-bottom ultra-low-attachment 96-well plates, with no medium changes throughout the entire culture period. Media from five MN spheroids (60 μL per spheroid) were pooled into a 1.7 mL collection tube for each condition, resulting in a final volume of 300 μL, and were snap-frozen in liquid nitrogen. For the experiment, all samples were thawed and centrifuged at 1000 g for 20 min at 4°C. The assay was then performed according to the manufacturer's instructions (#NBP2-81184, Novus Biologicals).

Microelectrode array (MEA) recordings

5K MN spheroids were generated into round-bottom ultra-low-attachment 96-well plates. After 7 days in culture, a maximum of six MN spheroids were pooled into a 0.6 mL collection tube and plated into an individual well of a Cytoview 24–well MEA plate (#M384-Tmea-24w, Axion Biosystems) using wide-orifice low-binding tips as previously described (23). Cytoview 24-well MEA plates were coated with a 10 μg/mL solution of poly-L-ornithine (PLO, #P3655, Sigma-Aldrich) diluted in 1X PBS. After 24 h at 37 °C, PLO was washed out by performing three washes with 1X PBS. Immediately afterward, MEA plates were coated with a 5 μg/mL solution of laminin (#L2020, Sigma-Aldrich) diluted in DMEM/F-12 (#10565018, Thermo Fisher Scientific) and incubated for 24 h at 37 °C.

MEA recordings were performed on days 14, 28, 42, and 56 post-plating (p-p) the MN spheroids. Before every recording, MN induction and maturation medium was replaced with 1X artificial cerebrospinal fluid (aCSF) prepared as previously described (23). Osmolarity (~305mOsm/L) and pH (~7.4) were monitored before adding the aCSF to the MN spheroids to

ensure physiological values. MEA plates with 1X aCSF were kept in the incubator for 1 h before being transferred to the Axion Maestro Edge (Axion Biosystems) and allowed to equilibrate at 37°C and 5% CO2 for 5 min before recording. Data was collected for 5 min using the Axis Navigator software (provided by Axion Biosystems, version 1.5.1.12, Atlanta, GA, USA). A bandpass filter of 3 kHz (low-pass) to 200 Hz (high-pass) was applied. After recording, the MEA plate was removed from the instrument and the 1X aCSF was replaced with MN induction and maturation medium to keep the cells in culture for the following recording points. At day 56 p-p, after the initial 5-min recording in 1X aCSF, the plates were removed from the instrument and dosed with either vehicle (H₂O) or 1 mM tetrodotoxin (TTX, # T8024, Sigma-Aldrich) before performing a second 5-min recording. This was the endpoint of the MEA recordings. For analysis, a "spike" was determined as a short extracellular electrical event with a peak voltage six times or greater than the standard deviation of the estimated "noise" signal. A "burst" was determined as ≥ 5 spikes with no more than 100 ms separating each spike. Only data from MN spheroids that covered 90–100% of the electrodes and had four consecutive recording time points were included in the analysis.

3. Results

iPSCs carrying the SOD1^{D90A-KI}, SOD1^{G93A-KI}, and SOD1^{D90A/G93A-KI} mutations were successfully differentiated into 2D motor neuron progenitor cells (MNPCs)

SOD1^{D90A-KI}, SOD1^{G93A-KI}, SOD1^{D90A/G93A-KI}, and AIW002-02 (isogenic control) iPSCs expressing the pluripotency-associated markers homeobox protein NANOG, podocalyxin-like protein 1 (Tra-1-60), stage-specific embryonic antigen 4 (SSEA-4), and octamer-binding transcription factor 4 (OCT4) (Additional file 9: Supplementary Figure 2A/B) were differentiated into iPSC-derived motor neuron progenitor cells (MNPCs). The cellular identity of the MNPCs from all the lines was characterized by immunocytochemistry and qPCR, at the same passage number. To determine the dorsoventral identity of the MNPCs, we quantified the expression levels of PAX6 and OLIG2, as these markers are expected to be elevated in the MN progenitor domain (pMN) of the spinal cord (30). OLIG2 was found at comparable levels between cell lines at the transcriptional level, while PAX6 was downregulated in SOD1^{D90A/G93A-KI} MNPCs (p = 0.023) but reached similar levels to the isogenic control at the MN stage (Additional file 10: Supplementary Figure 3A). In addition, the percentage of cells positive for the double immunostaining PAX6⁺/OLIG2⁺ confirmed a comparable expression between cell lines at the protein level (AIW002-02, 43.1 \pm 4.09; SOD1^{D90A-KI}, 55.97 \pm 6.87; SOD1^{G93A-KI}, 49.33 \pm 4.84; $SOD1^{D90A/G93A-KI}$, 47.3 \pm 14.38) (Additional file 10: Supplementary Figure 3B-G). Finally, the transcriptional expression of the marker NKX6.1 further confirmed the ventralization of the MNPCs from all cell lines (Additional file 11: Supplementary Figure 4A-D) (30).

The rostrocaudal identity of MNs is defined by the differential expression of several HOX genes in their progenitor cells along the neural tube during early embryonic development (31).

Thus, we analyzed the expressions of *HOXA5*, *HOXB8*, and *FOXG1* as markers of brachial, thoracic, and forebrain MNs, respectively. MNPCs from all the cell lines show almost no transcriptional expression of *FOXG1*, while expressing higher levels of *HOXB8* compared to *HOXA5*, suggesting that they possess a brachial-thoracic identity (**Additional file 11: Supplementary Figure 4A-D**).

MNPCs generated from three independent iPSC inductions per cell line exhibited comparable expression of key MNPC markers (PAX6 and OLIG2) at both the transcript and protein levels. Additionally, the enriched expression of HOXB8, relative to FOXG1, confirmed their spinal identity. Thus, after characterization, we concluded that all MNPCs were comparable, and we proceeded with the generation of MN spheroids from the four cell lines that were assessed at multiple levels at 14, 28, and 56 days in culture.

iPSC-derived MN spheroids from SOD1 mutants display size differences compared to the isogenic control

The morphology assessment of the MN spheroids generated from the four different lines (**Figure 1A**) showed that SOD^{G93A-KI} and SOD1^{D90A/G93A-KI} MN spheroids were greater in size than AIW002-02 MN spheroids at 14, 28, and 56 days (**Figure 1B-E**). In contrast, SOD1^{D90A-KI} MN spheroids were smaller in size than AIW002-02 MN spheroids across all time points (**Figure 1B-E**). To assess if the disparity in size was linked to differences in the number of proliferative cells within the MN spheroids, we performed qPCR and immunocytochemistry analyses to detect the expression of *SOX1*.

SOX1 (**Figure 1F**), encoding SOX-1 (**Figure 1G/H**), a marker associated with panneuronal proliferating precursors (32), was mostly absent in all cell lines at the iPSC stage. At the MNPC stage, *SOX1* expression was downregulated in the SOD1^{G93A-K1} and SOD1^{D90A/G93A-K1} cell lines. However, *SOX1* expression reached comparable levels to the isogenic control in SOD1^{G93A-K1} and SOD1^{D90A/G93A-K1} MN spheroids after 14 and 28 days. In line with this, SOD1^{G93A-K1} MN spheroids matched the isogenic control at the protein level (SOX-1) at 28 days. Interestingly, while SOD1^{D90A/G93A-K1} MN spheroids do not exhibit significant changes in *SOX1* after 14 and 28 days, there is an upregulation of SOX-1 after 14 days that remains until 28 days. Similarly, SOD1^{D90A-K1} MN spheroids showed an increased expression of *SOX1* that was also significant at the protein level (SOX-1) after 14 and 28 days.

These results suggest that the larger size of SOD1^{D90A/G93A-KI} MN spheroids could be attributed to a slower decline in the population of proliferative neural precursors expressing SOX-1. However, SOD1^{D90A-KI} MN spheroids showed the highest levels of SOX-1 but were smaller than the isogenic control, while SOD1^{G93A-KI} MN spheroids were larger than the isogenic control despite having similar SOX-1 decline patterns. Taken together, these results indicate that the size difference observed for the different MN spheroids is not driven by the rate of neural precursor population decline.

SOD1 MN spheroids retain a cellular identity comparable to their isogenic control

To determine if the proportion of differentiated cells was similar within MN spheroids regardless of their size, we assessed the transcriptional and protein profiles of AIW002-02,

SOD1^{D90A-KI}, SOD1^{G93A-KI}, and SOD1^{D90A-KI/G93A-KI} MN spheroids by qPCR and immunocytochemistry respectively.

The transient co-expression of insulin gene enhancer 1 (ISL1) and MN and pancreas homeobox 1 (MNX1, better known as HB9) can be used to identify nascent lower motor neurons (LMNs) from the brainstem and spinal cord (20, 33). However, medial and lateral LMNs belonging to the lateral motor column, which innervates limb muscles, are expected to downregulate both ISL1 and HB9 as they mature (34, 35). Thus, the expression of choline acetyltransferase (ChAT) is also analyzed to identify more mature LMNs (20, 34). With this in mind, the expressions of ISL1, HB9 and CHAT were assessed in 28 and 56-day-old MN spheroids at both the transcript and protein levels (Additional file 12: Supplementary Figure 5A) (Figure 2).

At the transcriptional level, *ISL1* and *HB9* are completely absent at the iPSC stage. As the cells are induced to MNPCs and later differentiated into MNs, both genes upregulate their expression at comparable levels between cell lines (**Additional file 12: Supplementary Figure 5A**). Similarly, *CHAT* expression is only upregulated after differentiation into MNs (**Additional file 12: Supplementary Figure 5A**). Nevertheless, SOD1^{D90A-KI} showed significant downregulation of *CHAT* at 28 days that persisted up to 56 days. Additionally, SOD1^{D90A-KI} (General exhibited a significant downregulation of *CHAT* at 56 days. Further analyses at the protein level by immunocytochemistry (**Figure 2A**) did not show statistical differences in the levels of ISL1 (**Figure 2B**), HB9 (**Figure 2C**), or CHAT (**Figure 2D**) between cell lines at 56 days. While slight differences were observed at the transcript level, the expression of MN markers at the protein level within MN spheroids was comparable across cell lines. Together, these findings confirmed that the number of MNs generated within the MN spheroids was comparable between cell lines at 56 days, the end point for these studies.

iPSC differentiation protocols into MNs typically do not yield pure cultures containing only MNs. Previous work has shown the presence of other cell types, including interneurons and glial cells (28, 31, 36). Thus, to investigate the cell identities present in our cultures, we assessed the presence of transcriptional markers associated to interneurons (INs) from the V2 and V3 progenitor domains which flank the MN domain (30), oligodendrocytes and astrocytes (Additional file 12: Supplementary Figure 5B-E).

Interneurons (INs) from the V2a domain are identified by the expression of *VSX2* (37). At the iPSC and MNPC stages, *VSX2* expression was nearly absent, and was upregulated at later stages of differentiation. On day 28, there was a trend toward a downregulation of *VSX2* in SOD1^{D90A-KI} MN spheroids, although it did not reach statistical significance. The expression of *NKX2.2*, a marker associated with IN progenitors of the V3 domain, was expressed at the MNPC stage at similar levels between cell lines, and it was subsequently downregulated in MN spheroids at 14 and 28 days. As V3 domain progenitors exited the cell cycle, they differentiated into V3 INs as indicated by *SIM1* expression in MN spheroids. At day 28, although non-significant, there was a trend toward higher levels of *SIM1* in SOD1^{D90A-KI} and SOD1^{G93A-KI} MN spheroids (**Additional file 12: Supplementary Figure 5B**).

Since OLIG2 is also considered a pan-oligodendrocyte gene, we characterized the expression of *OLIG2* (**Supplementary Figure 3**) along with *SOX10* and *MBP* to investigate the presence of oligodendrocyte precursor cells (OPCs) and mature oligodendrocytes (38), respectively. At the iPSC stage, we detected the expression of *SOX10*, however, it was rapidly downregulated to negligible levels at the MNPC and MN stages. In contrast, *MBP* expression reached its peak in MN spheroids at 28 days, with no significant differences observed between the cell lines (**Additional file 12: Supplementary Figure 5C**).

Finally, to assess the presence of astrocytes within our MN spheroids, we checked the expression of established astrocyte markers, *ALDH1L1* (39) and *GFAP* (40). These markers were undetectable in MN spheroids from any cell line at 28 days (**Additional file 12: Supplementary Figure 5D).** Similarly, the pluripotency-associated markers *NANOG* and *OCT4*, which are used to characterize the cells at the iPSC stage (41), were absent in both MNPCs and MN spheroids independent of the cell line (**Additional file 12: Supplementary Figure 5E).**

Altogether, our results confirm the presence of other cellular types within the MN spheroids, namely INs from V2 and V3 domains, and oligodendrocytes. Although some trends were observed, the overall results indicate that there are no significant differences in the proportion of cell types present within MN spheroids across the different cell lines.

SOD1 expression is altered in SOD1 MN spheroids

As part of the end stage characterization, we assessed the expression of SOD1 in 56-dayold MN spheroids at the transcript and protein level through qPCR, immunostaining, and Western Blot, respectively.

As expected, *SOD1* was expressed at all differentiation stages due to its critical role as ROS scavenger (**Figure 3A**). Given that SOD1 functions in most subcellular compartments (42), it was anticipated that its transcription levels would be higher in differentiated neurons, correlating with the increased cell volume. Only SOD1^{G93A-KI} MN spheroids had a significant upregulation of *SOD1* at 28 days; however, its levels returned to comparable levels with the isogenic control at 56 days. Strikingly, analysis of SOD1 at the protein level revealed distinct expression patterns across cell lines. Immunoblotting against the C-terminal domain of SOD1 showed that SOD1^{D90A-KI} MN

spheroids have a strong upregulation of SOD1 (**Figure 3B/C**). In contrast, SOD1^{G93A-KI} and SOD1^{D90A/G93A-KI} MN spheroids displayed a significant downregulation in SOD1 (**Figure 3B/C**). Of note, SOD1^{D90A-KI} and SOD1^{D90A/G93A-KI} monomers displayed a higher motility which is expected given the predicted reduction in molecular mass that results from the Asp-to-Ala change (43, 44). Finally, an immunocytochemistry analysis showed similar results to those observed by Western Blot analysis in 56-day-old MN spheroids (**Figure 3D/E**). Importantly, the antibodies used in this study to detect SOD1 expression by Western Blot and immunocytochemistry were selected based on a recent publication validating numerous commercial SOD1 antibodies with SOD1-KO lines (45).

Taken together, our results show that SOD1 expression is dysregulated at the protein level in SOD1 MN spheroids. However, as mutated SOD1 is upregulated in SOD1^{D90A-KI} and downregulated in SOD1^{G93A-KI} and SOD1^{D90A/G93A-KI} MN spheroids, the mechanism through which SOD1 exerts its deleterious effects may differ among cell lines.

Dysregulation of neurofilament (NF) subunits in SOD1 MN spheroids

Neurofilaments (NF) are composed of three protein subunits that are the most abundant cytoskeletal component of neuronal cells: NF light (NFL), NF medium (NFM), and NF heavy (NFH) (46). Given the growing evidence that NF abnormalities may be an early pathological feature of ALS (47, 48), we characterized the transcriptional expression of the three genes encoding neurofilament subunits—*NEFL*, *NEFM*, and *NEFH*—in iPSCs, MNPCs, and MN spheroids derived from the three SOD1 lines and the isogenic control after 14, 28, and 56 days in culture. As expected, iPSCs from all cell lines lack expression of any NF subunit. Subsequently,

MNPCs begin to express NF subunits, albeit in lesser proportions compared to *NES*, which encodes for Nestin, an intermediate filament characteristic of immature neurons (**Additional file 13: Supplementary Figure 5A**). Finally, the expression of NF subunits was increased upon differentiation into MN spheroids.

NEFL expression did not show significant differences between cell lines at 28 and 56 days (Additional file 13: Supplementary Figure 5B). In contrast, *NEFM* expression showed a significant downregulation in SOD1^{D90A-KI} and SOD1^{G93A-KI} MN spheroids at 28 days (Additional file 13: Supplementary Figure 5C). Interestingly, the levels of *NEFM* in SOD1^{D90A-KI} MN spheroids were comparable to the isogenic control at 56 days, while those of SOD1^{G93A-KI} MN spheroids became significantly upregulated. As well, *NEFH* expression was significantly downregulated in SOD1^{D90A-KI} and SOD1^{D90A-KI} MN spheroids at 28 days (Additional file 13: Supplementary Figure 5D). At 56 days, *NEFH* was downregulated in all SOD1 mutants.

To assess if the differences in expression at the transcriptional level were also present at the protein level, we performed Western Blots on total protein extractions of 56-day-old MN spheroids (**Figure 4A**). To perform this assay, we pooled multiple 56-day-old MN spheroids per sample. We observed the downregulation of NFL across all SOD1 mutants, with SOD1^{D90A-KI} MN spheroids reaching statistical significance (**Figure 4B**). Among the three NF protein subunits, NFM exhibited the least variation, showing no significant differences between cell lines (**Figure 4C**). Conversely, NFH displayed a comparable pattern to NFL in SOD1^{D90A-KI} MN and SOD1^{D90A-KI} MN spheroids, also reaching statistical significance in SOD1^{D90A-KI} MN spheroids (**Figure 4D**). To further investigate if the observed changes were a result of a generalized cytoskeleton disruption, we quantified the expression of βIII-tubulin but no significant changes were found between cell lines (**Figure 4E**).

To investigate NF subunit protein expression within individual MN spheroids, we conducted immunocytochemistry analyses in 56-day-old MN spheroids (Figure 4F). Additionally, we immunostained the MN spheroids against SMI-32, which targets non-phosphorylated NFH enriched in MNs (Figure 4G). As expected, the protein expression levels of NF subunits, as measured by immunocytochemistry, mirrored the trends observed in the Western Blot analyses. NFL was downregulated in MN spheroids from all SOD1 mutants (Figure 4H), with statistically significant reductions observed in SOD1^{D90A/G93A-KI} MN spheroids at 28 days and in SOD1^{D90A-KI} MN spheroids at 28 and 56 days. NFM remained the least affected NF subunit, maintaining comparable levels across all cell lines (Figure 4I). Lastly, NEFH showed significant downregulation in $SOD1^{D90A\text{-}KI}\,MN$ spheroids at 28 and 56 days, as well as in $SOD1^{D90A/G93A\text{-}KI}$ MN spheroids at 56 days (Figure 4J). SMI-32 levels remained consistent across cell lines at 56 days (Figure 4K), indicating a similar number of MNs within the MN spheroids. Collectively, these findings suggest that SOD1 mutations are associated with dysregulation of NF subunits, which could lead to NF aggregation and neuronal degeneration as previously reported by another group (49).

SOD1 MN spheroids exhibited reduced viability and neuronal degeneration at 56 days

We next investigated whether the different SOD1 mutations lead to a decrease in viability (including metabolic activity and survival), and/or an increase in neuronal degeneration in 56-day-old MN spheroids.

To assess cell viability, a CellTiter-Glo® 3D cell viability assay and a Western blot for the apoptosis marker cleaved caspase 3 (CC3) were performed. The CellTiter-Glo® 3D cell viability

assay (**Figure 5A**) showed a decrease in ATP levels for the three SOD1 cell lines (SOD1^{D90A-KI}, 63.5 ± 6.84 %; SOD1^{G93A-KI}, 83.31 ± 8.16 %; SOD1^{D90A-KI/G93A-KI}, 77.56 ± 7.31 %). However, immunoblotting for CC3 (**Figure 5B/C**), revealed a trend toward increased levels of CC3 in SOD1^{G93A-KI} and SOD1^{D90A-KI/G93A-KI} MN spheroids.

In ALS, MN death results in the release of NFL protein into the CSF. Currently, the amount of NFL protein released into CSF, serum, or plasma is often used as a fluid biomarker to indicate disease severity and progression (50, 51, 52). Hence, to further assess the occurrence of neuronal degeneration in our model, we conducted an ELISA assay to measure NFL release in media that had been in contact with the MN spheroids for 56 days. To validate the ELISA assay, we assessed NFL release in the plasma samples from two healthy donors (one female and one male) and two sporadic ALS patients (one female and one male). The ages of the donors ranged from 55 to 70 years (Additional file 14: Supplementary Figure 7A). Consistent with findings in ALS patients, extracellular NFL levels were higher in the plasma of sporadic ALS patients compared to control donors (Additional file 14: Supplementary Figure 7B) in our assay. Extending this assay into MN spheroids, we observed an increase in NFL levels in the media for all three SOD1 cell lines (AIW002-02, 9000 ± 1144 pg/mL; SOD1^{D90A-KI}, 11121 ± 660 pg/mL; SOD1^{G93A-KI}, 10667 ± 2263 pg/mL; SOD1^{D90A/G93A-KI}, 11121 ± 1183 pg/mL) (Figure 5D).

The findings across all three assays indicate that SOD1 mutations are linked to decreased cell viability and increased neuronal degeneration in iPSC-derived MN spheroids.

Hypoactivity and irregular burst activity are linked to SOD1 mutations

Disrupted neuronal activity has been linked to ALS using iPSC-derived MNs (18, 53, 54). Given that our MN spheroids exhibited reduced viability, increased neuronal degeneration, and downregulation of NF subunits—recently identified as integral components of synapses—we sought to evaluate the functional activity of our MN spheroids using an MEA approach. For this, 7 day old MN spheroids were plated onto electrodes into MEA plates to perform longitudinal recordings until day 56 post-plating (p-p) (**Figure 6A**). The mean firing rate (MFR), representing the average number of spikes per second (Hz), decreased in all SOD1 mutants from 28 days p-p onward. Notably, SOD1^{G93A-KI} MN spheroids were significantly affected after 42 and 56 days p-p (**Figure 6B**).

Next, we assessed burst frequency per MN spheroid and various detailed properties of burst activity (**Figure 6C-G**). Burst frequency, defined as the average number of bursts per second (Hz), showed a slight reduction in SOD1 MN spheroids at 56 days p-p; however, no statistically significant differences were detected (**Figure 6C**). Starting at 28 days, SOD1^{G93A-KI} and SOD1^{D90A/G93A-KI} MN spheroids showed reduced average burst duration (**Figure 6D**) and a lower average number of spikes per burst (**Figure 6E**). Considering the reduced number of bursts observed in SOD1 MN spheroids, an increase in the average inter-burst-interval (s) was anticipated. This increase reached statistical significance for SOD1^{D90A-KI} at 56 days, whereas no significant changes were observed for SOD1^{G93A-KI} and SOD1^{D90A/G93A-KI} MN spheroids (**Figure 6F**). The inter-burst interval (IBI) coefficient of variation quantifies the variability in burst timing. An IBI coefficient of variation near zero indicates regular, consistent bursting, while higher values typically reflect irregular or disrupted neuronal activity. Throughout our longitudinal recordings, the IBI coefficient of variation was significantly elevated in SOD1^{D90A-KI} MN spheroids at 56 days,

indicating irregular burst activity compared to the isogenic control (**Figure 6G**). Importantly, acute treatment with tetrodotoxin (TTX) completely abolished the activity of MN spheroids across cell lines, confirming that our observations were not artifacts of the recording system (**Figure 6H**).

Overall, we observed a phenotype of hypoactivity in MN spheroids with SOD1 mutations, becoming apparent after 28 days p-p, with SOD1^{G93A-KI} MN spheroids being the most severely affected. Interestingly, although SOD1^{D90A-KI} MN spheroids did not show the most pronounced changes in overall activity compared to the isogenic control, they exhibited significant alterations in burst properties. Collectively, our findings suggest that SOD1 mutations are associated with hypoactivity and irregular burst activity.

4. Discussion

In this study, we used a protocol previously optimized by our group (23) to generate and characterize iPSC-derived MN spheroids from iPSC lines harboring homozygous mutations in *SOD1* and their corresponding isogenic control (AIW002-02). Notably, our model is highly scalable, allowing for the processing and analysis of multiple spheroids simultaneously, while also supporting long-term cultures for up to 56 days.

First, we performed the size profiling of our MN spheroids to assess potential morphological changes. SOD1^{D90A-K1} MN spheroids were smaller, while SOD1^{G93A-K1} and SOD1^{D90A/G93A-K1} were larger relative to the isogenic control. We hypothesized that size disparities arise from differences in the rate at which neural precursors exit the mitotic phase and commit to differentiation into neurons. To investigate this, we analyzed the downregulation of SOX1, a marker of pan-neuronal proliferative precursors. Surprisingly, SOD1^{D90A-K1} MN spheroids exhibited the highest expression of SOX-1, despite their smaller size, while SOD1^{G93A-K1} MN spheroids showed the lowest expression of SOX-1, regardless of their larger size. Only in the case of SOD1^{D90A/G93A-K1} MN spheroids could we conclude that the larger size was attributable to a slower rate of SOX1 downregulation. Although this result is intriguing, understanding the mechanisms driving the subtle size differences in MN spheroids falls outside the scope of this work. It is important to note, however, that the overall morphology of the MN spheroids and the expression of MN markers remain consistent across cell lines.

Studies using iPSC-derived MNs as a model have reported either increased or unchanged SOD1 expression, depending on the specific mutation analyzed (49, 53, 55). Here, we observed an upward trend toward higher levels of SOD1 in SOD1^{D90A-KI} MN spheroids, although no

statistical differences were detected. Similarly, the assessment of SOD1 expression in post-mortem tissue of the central nervous system and peripheral organs of ALS patients with a homozygous D90A mutation did not report significant differences compared to controls (43). In contrast, the use of reliable antibodies for SOD1 detection (45) allowed us to report significantly reduced SOD1 levels in SOD1^{G93A-KI} and SOD1^{D90A/G93A-KI} MN spheroids. A separate study on iPSC-derived MNs with a heterozygous G93A knock-in mutation reported unchanged SOD1 levels in the RIPAsoluble fraction compared to the isogenic control (53), prompting the question of whether differences in zygosity explain the conflicting results. Overall, ALS patients with SOD1 mutations have significantly reduced SOD1 protein levels, with varying degrees of protein expression changes associated with different SOD1 variants (10). Additionally, it is worth noting that the large validation study conducted by Ayoubi et al. (2023), enabled us to use reliable antibodies for SOD1 detection (45). Notably, the study conducted by Ayoubi et al. (2023) revealed that several SOD1 antibodies produce false-positive results, potentially confounding earlier findings, and underscores the value of Open Science initiatives that conduct such validations for the scientific community (45).

Cell viability and neuronal degeneration are commonly used as indicators of ALS pathology in iPSC-derived cells. In this study, we performed three assays to assess these indicators within 56-day-old MN spheroids. Initially, a 3D CellTiter-Glo assay was performed to measure ATP levels in MN spheroids, as higher ATP levels indicate active metabolism and viable cells. We observed reduced ATP levels in all SOD1 lines compared to the isogenic control, confirming that SOD1 mutations lead to a reduction in metabolic activity, thereby impacting cell viability. Next, we conducted a Western blot analysis for cleaved caspase-3, a downstream protein fragment in the apoptotic pathway that has been previously reported to be upregulated in iPSC-derived motor

neurons with SOD1 mutations (56). As anticipated, we observed upregulation of ~15 and ~17 kDa protein fragments but only in SOD1^{G93A-KI} and SOD1^{D90A/G93A-KI} MN spheroids. Surprisingly, SOD1^{D90A-KI} MN spheroids showed cleaved caspase-3 levels comparable to the isogenic control, despite exhibiting the lowest ATP levels in the CellTiter-Glo assay. A plausible explanation is that, while SOD1^{D90A-KI} MN spheroids are presented with reduced metabolic activity, they have not yet entered apoptosis. Cell viability remains a debated topic in ALS studies using iPSC-derived motor neurons, with some studies reporting a decrease in cell viability and activation of the apoptotic pathway (56, 57, 58), while others find no significant change (18, 59). It has been suggested that the failure to observe changes in viability is due to the technical challenge of maintaining 2D cultures in optimal conditions for long-term analysis, an important factor for studying age-associated progressive diseases (18, 60). Our study confirms that using a 3D culture system can sustain cells for longer periods, thereby revealing delayed phenotypes.

To assess neuronal degeneration, we investigated NFL subunit release into the media of MN spheroids, as elevated levels of NFL in blood, serum, plasma, and CSF are established biomarkers of ALS, indicative of axonal damage associated with the disease (51, 61). This approach has undergone limited optimization for cultured cells, particularly iPSC-derived cells, which presented a challenge for this assay. Therefore, to validate our method, NFL levels were also measured in plasma samples from healthy donors and ALS patients. All SOD1 lines trended toward an increase in NFL subunit levels in the media, although this was outside of statistical significance. We attribute this to NFL subunit release being measured from the pooled media of six MN spheroids, each composed of 10K cells, which may produce NFL levels that are only marginally above the detection limit of the measuring kit. Increasing the size of the MN spheroids,

pooling media from additional samples and/or increasing the culture time can potentially lead to a significant increase in NFL release, given how ALS is a progressive disease.

Studies investigating NF subunit expression in post-mortem tissues from sporadic ALS patients (62, 63) and iPSC-derived MNs with SOD1 mutations (49) have reported reduced NFL expression at both transcript and protein levels. Supporting these findings, evidence indicates that mutant SOD1 directly binds to NEFL mRNA, disrupting its stability (49, 64). In contrast, inconsistent results were reported when analyzing the expression of NFM and NFH in diseased MNs. While NFM and NFH protein expressions are downregulated in SOD1 iPSC-derived MNs (49), they are either upregulated at the protein level (65) or unaffected at the transcriptional level (63) in post-mortem tissue from sporadic ALS patients. More recently, a study analyzing the transcriptome in post-mortem spinal cord tissue of SOD1 ALS patients via bulk RNA-seq revealed significant downregulation of NEFL, NEFM, and NEFH (66). In our study, SOD1^{D90A-KI} MN spheroids exhibited significant reductions in NFL at the protein level, in NEFM at the transcriptional level, and in NFH at both the transcriptional and protein levels. Similarly, SOD1^{D90A/G93A-KI} MN spheroids showed a trend toward downregulation of NFL and a significant reduction in NFH at the protein level. Interestingly, SOD1^{G93A-KI} MN spheroids were the least affected, showing only a trend toward downregulation of NFL at the protein level. Overall, NFL appears to be the most downregulated NF subunit, showing consistent patterns across all SOD1 lines. Taken together, our results align with those reported by Chen et al. (2014), who observed a downregulation of NFL, NFM, and NFH at the protein level in iPSC-derived MNs carrying the A4V and D90A mutations in SOD1. We found it surprising that SOD1^{D90A/G93A-KI} MN spheroids did not exhibit the lowest levels of NF subunits, as we had anticipated a synergistic effect from the presence of both mutations. It appears that the G93A mutation may lead to a distinct interaction

between mutated SOD1 and NF subunits, as this cell line was the least affected. Future studies should examine the impact of a broader range of SOD1 mutations on NF subunit regulation.

Finally, as previous studies with iPSC-derived MNs suggest that synaptic dysfunction may precede MN degeneration (18, 59), we conducted a functional analysis using MEA recordings. For all functional properties measured, differences between cell lines emerged after 28 days p-p, emphasizing the importance of using a model that supports long-term culture for phenotypic comparisons. SOD1^{G93A-KI} MN and SOD1^{D90A/G93A-KI} MN spheroids exhibited a hypoactive phenotype while SOD1^{D90A-KI} MN spheroids displayed notable changes in burst properties. Similarly, previous work reported hypoactivity and disrupted burst activity in 2D iPSC-derived MNs with heterozygous SOD1 G93A and A4V mutations when seeded on a monolayer of primary astrocytes (53). In contrast, another study reported hyperexcitability in 2D iPSC-derived MNs carrying the heterozygous SOD1 A4V mutation (54); however, in this study, MNs were differentiated and recorded as a pure 2D culture. In our model, we cannot exclude the possibility that the 3D environment may alter the functional profile of the MNs. Additionally, while INs and oligodendrocytes are present in similar proportions across cell lines, their potential role in modulating MN activity cannot be disregarded as growing evidence suggests their involvement in ALS (67, 68).

The D90A and G93A mutations, both linked to fALS, occur near the β-barrel motif of SOD1 (7). Notably, these mutations are considered WT-like fALS mutations as they maintain crucial structural interactions required for metal-induced stabilization (69). Given these characteristics, we hypothesized that single homozygous mutations would induce similar pathological alterations, with the double mutation possibly exhibiting synergistic effects. Generating a model with enhanced deleterious phenotypes could help to provide deeper insights

into the mechanisms of disease. However, only a reduction in cell viability and downregulation of NFL were consistently observed across all three phenotypes, and these changes were not worsened by the double SOD1 mutation. This suggests that the conformational change created by the two mutations may have resulted in a structure similar to that of either of the single SOD1 mutants.

One of the primary challenges in ALS research is its intrinsic heterogeneity. Mutated SOD1 demonstrates variable behavior depending on the specific mutation (11, 12), and patients with fALS caused by SOD1 mutations exhibit diverse clinical manifestations and prognoses (10). This highlights the necessity of analyzing ALS at the genetic level, as even mutations in close proximity or with conserved structural interactions can result in distinct disease mechanisms.

Conclusion

In summary, we developed a 3D iPSC-derived MN spheroid model that recapitulates key ALS pathology features when SOD1 mutations are present. Our results revealed consistent reductions in cell viability and NFL downregulation across all phenotypes. While MN activity was also affected, hypoactivity was observed in SOD1 G93A and D90A/G93A genotypes, whereas a disrupted bursting pattern was more characteristic of the SOD1 D90A genotype. Notably, for the first time, we demonstrated that two SOD1 mutations linked to disease onset do not exhibit synergistic effects. These findings provide valuable insights into mutation-specific phenotypes and help contribute to our understanding of ALS heterogeneity.

Declarations

Ethics approval

The use of iPSCs in this research was approved by the McGill Research Ethics Board (IRB Study Number A03-M19-22A).

Consent for publication

Not applicable.

Availability of data and materials

All data generated or analyzed during this study are included in this published article.

Competing interests

The authors declare that they have no competing interests.

Funding

This study was supported by the ALS Society of Canada, and the Quebec Consortium for Drug Discovery (CQDM) for project funding support.

Authors' contributions

MJC-M contributed to the conceptualization, study design, data collection, result analysis, and the writing, reviewing, and editing of the manuscript. AKF-F contributed significantly to data collection, result analysis, and the reviewing and editing of the manuscript. MN generated and validated the CRISPR/Cas9-edited iPSC lines. GH generated and characterized iPSC-derived MNPCs. SL developed image analysis pipelines. MB-T contributed with image analysis. CX-QC and TMG performed quality control analyses for all iPSC lines. NA performed the karyotyping of all iPSC lines. DH contributed to image acquisition and analysis. MC contributed to the analysis

of results, funding acquisition, as well as the reviewing and editing of the manuscript. LG generated and characterized AIW002-02 iPSC-derived MNPCs. NA conducted quality control analyses for the AIW002-02 iPSC line. ED participated in generating the CRISPR/Cas9-edited iPSC lines. TMD contributed to the study design, funding acquisition, and the reviewing and editing of the manuscript. All authors have read and agreed to the published version of the manuscript.

Acknowledgements

We thank the donors for their generous donations of samples. Their contributions are invaluable in advancing our understanding of ALS. We thank The Neuro's Open Biobank (or Clinical Biospecimen Imaging and Genetic Repository, C-BIG), directed by Dr. Karamchandani, for providing us with access to the plasma samples from control and patient donors used for this study. We thank YCharOS for their expertise in antibody validation and the donation of different SOD1 antibodies for troubleshooting. We thank Martin H. Berryer and Mark Aurousseau for their valuable input in the drafting of this manuscript.

References

- 1. Brown RH, Al-Chalabi A. Amyotrophic Lateral Sclerosis. *N Engl J Med.* **2017**;377(2):162-72.
- 2. Younger DS, Brown RH, Jr. Amyotrophic lateral sclerosis. *Handb Clin Neurol*. **2023**;196:203-29.
- 3. Chen S, Sayana P, Zhang X, Le W. Genetics of amyotrophic lateral sclerosis: an update. *Mol Neurodegener.* **2013**;8:28.
- 4. Talbott EO, Malek AM, Lacomis D. The epidemiology of amyotrophic lateral sclerosis. *Handb Clin Neurol.* **2016**;138:225-38.
- 5. Bernard E, Pegat A, Svahn J, Bouhour F, Leblanc P, Millecamps S, Thobois S, Guissart C, Lumbroso S, Mouzat K. Clinical and Molecular Landscape of ALS Patients with SOD1 Mutations: Novel Pathogenic Variants and Novel Phenotypes. A Single ALS Center Study. *Int J Mol Sci.* **2020**;21(18).

- 6. Bunton-Stasyshyn RK, Saccon RA, Fratta P, Fisher EM. SOD1 Function and Its Implications for Amyotrophic Lateral Sclerosis Pathology: New and Renascent Themes. *Neuroscientist.* **2015**;21(5):519-29.
- 7. Hayward LJ, Rodriguez JA, Kim JW, Tiwari A, Goto JJ, Cabelli DE, Valentine JS, Brown RH, Jr. Decreased metallation and activity in subsets of mutant superoxide dismutases associated with familial amyotrophic lateral sclerosis. *J Biol Chem.* **2002**;277(18):15923-31.
- 8. Bowling AC, Schulz JB, Brown RH, Jr., Beal MF. Superoxide dismutase activity, oxidative damage, and mitochondrial energy metabolism in familial and sporadic amyotrophic lateral sclerosis. *J Neurochem.* **1993**;61(6):2322-5.
- 9. Fiszman ML, Borodinsky LN, Ricart KC, Sanz OP, Sica RE. Cu/Zn superoxide dismutase activity at different ages in sporadic amyotrophic lateral sclerosis. *J Neurol Sci.* **1999**;162(1):34-7.
- 10. Huang M, Liu YU, Yao X, Qin D, Su H. Variability in SOD1-associated amyotrophic lateral sclerosis: geographic patterns, clinical heterogeneity, molecular alterations, and therapeutic implications. *Transl Neurodegener.* **2024**;13(1):28.
- 11. Chen LX, Xu HF, Lin HX, Yang XX, Li HF, Wu ZY. Pathogenicity classification of SOD1 variants of uncertain significance by in vitro aggregation propensity. *Neurobiol Aging*. **2023**;123:182-90.
- 12. Berdyński M, Miszta P, Safranow K, Andersen PM, Morita M, Filipek S, Żekanowski C, Kuźma-Kozakiewicz M. SOD1 mutations associated with amyotrophic lateral sclerosis analysis of variant severity. *Sci Rep.* **2022**;12(1):103.
- 13. Gurney ME, Pu H, Chiu AY, Dal Canto MC, Polchow CY, Alexander DD, Caliendo J, Hentati A, Kwon YW, Deng HX, et al. Motor neuron degeneration in mice that express a human Cu,Zn superoxide dismutase mutation. *Science*. **1994**;264(5166):1772-5.
- 14. Rosen DR, Siddique T, Patterson D, Figlewicz DA, Sapp P, Hentati A, Donaldson D, Goto J, O'Regan JP, Deng HX, et al. Mutations in Cu/Zn superoxide dismutase gene are associated with familial amyotrophic lateral sclerosis. *Nature*. **1993**;362(6415):59-62.
- 15. Bonifacino T, Zerbo RA, Balbi M, Torazza C, Frumento G, Fedele E, Bonanno G, Milanese M. Nearly 30 Years of Animal Models to Study Amyotrophic Lateral Sclerosis: A Historical Overview and Future Perspectives. *Int J Mol Sci.* **2021**;22(22).
- 16. La Cognata V, Golini E, Iemmolo R, Balletta S, Morello G, De Rosa C, Villari A, Marinelli S, Vacca V, Bonaventura G, Dell'Albani P, Aronica E, Mammano F, Mandillo S, Cavallaro S. CXCR2 increases in ALS cortical neurons and its inhibition prevents motor neuron degeneration in vitro and improves neuromuscular function in SOD1G93A mice. *Neurobiol Dis*. **2021**;160:105538.
- 17. Muzio L, Sirtori R, Gornati D, Eleuteri S, Fossaghi A, Brancaccio D, Manzoni L, Ottoboni L, Feo L, Quattrini A, Mastrangelo E, Sorrentino L, Scalone E, Comi G, Marinelli L, Riva N, Milani M, Seneci P, Martino G. Retromer stabilization results in neuroprotection in a model of Amyotrophic Lateral Sclerosis. *Nat Commun.* **2020**;11(1):3848.
- 18. Lépine S, Nauleau-Javaudin A, Deneault E, Chen CX, Abdian N, Franco-Flores AK, Haghi G, Castellanos-Montiel MJ, Maussion G, Chaineau M, Durcan TM. Homozygous ALS-linked mutations in TARDBP/TDP-43 lead to hypoactivity and synaptic abnormalities in human iPSC-derived motor neurons. *iScience*. **2024**;27(3):109166.
- 19. Deneault E, Chaineau M, Nicouleau M, Castellanos Montiel MJ, Franco Flores AK, Haghi G, Chen CX, Abdian N, Shlaifer I, Beitel LK, Durcan TM. A streamlined CRISPR workflow to

- introduce mutations and generate isogenic iPSCs for modeling amyotrophic lateral sclerosis. *Methods*. **2022**;203:297-310.
- 20. Sances S, Bruijn LI, Chandran S, Eggan K, Ho R, Klim JR, Livesey MR, Lowry E, Macklis JD, Rushton D, Sadegh C, Sareen D, Wichterle H, Zhang SC, Svendsen CN. Modeling ALS with motor neurons derived from human induced pluripotent stem cells. *Nat Neurosci.* **2016**;19(4):542-53.
- 21. Thiry L, Clément JP, Haag R, Kennedy TE, Stifani S. Optimization of long-term human iPSC-derived spinal motor neuron culture using a dendritic polyglycerol amine-based substrate. *ASN Neuro*. **2022**;14:17590914211073381.
- 22. Milky B, Zabolocki M, Al-Bataineh SA, van den Hurk M, Greenberg Z, Turner L, Mazzachi P, Williams A, Illeperuma I, Adams R, Stringer BW, Ormsby R, Poonnoose S, Smith LE, Krasowska M, Whittle JD, Simula A, Bardy C. Long-term adherence of human brain cells in vitro is enhanced by charged amine-based plasma polymer coatings. *Stem Cell Reports*. **2022**;17(3):489-506.
- 23. Castellanos-Montiel MJ, Chaineau M, Franco-Flores AK, Haghi G, Carrillo-Valenzuela D, Reintsch WE, Chen CX-Q, Durcan TM. An optimized workflow to generate and characterize iPSC-derived motor neuron (MN) spheroids. *Cells*. **2023**;12, 545.
- 24. Andersen J, Revah O, Miura Y, Thom N, Amin ND, Kelley KW, Singh M, Chen X, Thete MV, Walczak EM, Vogel H, Fan HC, Paşca SP. Generation of functional human 3D cortico-motor assembloids. *Cell.* **2020**;183(7):1913-29.e26.
- 25. Faustino Martins JM, Fischer C, Urzi A, Vidal R, Kunz S, Ruffault PL, Kabuss L, Hube I, Gazzerro E, Birchmeier C, Spuler S, Sauer S, Gouti M. Self-organizing 3D human trunk neuromuscular organoids. *Cell Stem Cell*. **2020**;26(2):172-86.e6.
- 26. Pereira JD, DuBreuil DM, Devlin AC, Held A, Sapir Y, Berezovski E, Hawrot J, Dorfman K, Chander V, Wainger BJ. Human sensorimotor organoids derived from healthy and amyotrophic lateral sclerosis stem cells form neuromuscular junctions. *Nat Commun.* **2021**;12(1):4744.
- 27. Chen CX, Abdian N, Maussion G, Thomas RA, Demirova I, Cai E, Tabatabaei M, Beitel LK, Karamchandani J, Fon EA, Durcan TM. A Multistep Workflow to Evaluate Newly Generated iPSCs and Their Ability to Generate Different Cell Types. *Methods Protoc.* **2021**;4(3).
- 28. Du ZW, Chen H, Liu H, Lu J, Qian K, Huang CL, Zhong X, Fan F, Zhang SC. Generation and expansion of highly pure motor neuron progenitors from human pluripotent stem cells. *Nat Commun.* **2015**;6:6626.
- 29. Gómez-Gaviro MV, Balaban E, Bocancea D, Lorrio MT, Pompeiano M, Desco M, Ripoll J, Vaquero JJ. Optimized CUBIC protocol for three-dimensional imaging of chicken embryos at single-cell resolution. *Development*. **2017**;144(11):2092-7.
- 30. Ogura T, Sakaguchi H, Miyamoto S, Takahashi J. Three-dimensional induction of dorsal, intermediate and ventral spinal cord tissues from human pluripotent stem cells. *Development*. **2018**;145(16).
- 31. Namboori SC, Thomas P, Ames R, Hawkins S, Garrett LO, Willis CRG, Rosa A, Stanton LW, Bhinge A. Single-cell transcriptomics identifies master regulators of neurodegeneration in SOD1 ALS iPSC-derived motor neurons. *Stem Cell Reports.* **2021**;16(12):3020-35.
- 32. Aubert J, Stavridis MP, Tweedie S, O'Reilly M, Vierlinger K, Li M, Ghazal P, Pratt T, Mason JO, Roy D, Smith A. Screening for mammalian neural genes via fluorescence-activated cell sorter purification of neural precursors from Sox1-gfp knock-in mice. *Proc Natl Acad Sci U S A.* **2003**;100 Suppl 1(Suppl 1):11836-41.

- 33. Thaler JP, Koo SJ, Kania A, Lettieri K, Andrews S, Cox C, Jessell TM, Pfaff SL. A postmitotic role for Isl-class LIM homeodomain proteins in the assignment of visceral spinal motor neuron identity. *Neuron.* **2004**;41(3):337-50.
- 34. Shimojo D, Onodera K, Doi-Torii Y, Ishihara Y, Hattori C, Miwa Y, Tanaka S, Okada R, Ohyama M, Shoji M, Nakanishi A, Doyu M, Okano H, Okada Y. Rapid, efficient, and simple motor neuron differentiation from human pluripotent stem cells. *Mol Brain*. **2015**;8(1):79.
- 35. Solomon E, Davis-Anderson K, Hovde B, Micheva-Viteva S, Harris JF, Twary S, Iyer R. Global transcriptome profile of the developmental principles of in vitro iPSC-to-motor neuron differentiation. *BMC Mol Cell Biol.* **2021**;22(1):13.
- 36. Thiry L, Hamel R, Pluchino S, Durcan T, Stifani S. Characterization of human iPSC-derived spinal motor neurons by single-cell RNA sequencing. *Neuroscience*. **2020**;450:57-70.
- 37. Clovis YM, Seo SY, Kwon JS, Rhee JC, Yeo S, Lee JW, Lee S, Lee SK. Chx10 Consolidates V2a Interneuron Identity through Two Distinct Gene Repression Modes. *Cell Rep.* **2016**;16(6):1642-52.
- 38. Piscopo VEC, Chapleau A, Blaszczyk GJ, Sirois J, You Z, Soubannier V, Chen CX, Bernard G, Antel JP, Durcan TM. The use of a SOX10 reporter toward ameliorating oligodendrocyte lineage differentiation from human induced pluripotent stem cells. *Glia.* **2024**.
- 39. Cahoy JD, Emery B, Kaushal A, Foo LC, Zamanian JL, Christopherson KS, Xing Y, Lubischer JL, Krieg PA, Krupenko SA, Thompson WJ, Barres BA. A transcriptome database for astrocytes, neurons, and oligodendrocytes: a new resource for understanding brain development and function. *J Neurosci.* **2008**;28(1):264-78.
- 40. Soubannier V, Chaineau M, Gursu L, Haghi G, Franco Flores AK, Rouleau G, Durcan TM, Stifani S. Rapid Generation of Ventral Spinal Cord-like Astrocytes from Human iPSCs for Modeling Non-Cell Autonomous Mechanisms of Lower Motor Neuron Disease. *Cells.* **2022**;11(3).
- 41. Takahashi K, Tanabe K, Ohnuki M, Narita M, Ichisaka T, Tomoda K, Yamanaka S. Induction of pluripotent stem cells from adult human fibroblasts by defined factors. *Cell*. **2007**;131(5):861-72.
- 42. Zlatković J, Filipović D. Stress-induced alternations in CuZnSOD and MnSOD activity in cellular compartments of rat liver. *Mol Cell Biochem.* **2011**;357(1-2):143-50.
- 43. Jonsson PA, Graffmo KS, Andersen PM, Marklund SL, Brännström T. Superoxide dismutase in amyotrophic lateral sclerosis patients homozygous for the D90A mutation. *Neurobiol Dis.* **2009**;36(3):421-4.
- 44. Marklund SL, Andersen PM, Forsgren L, Nilsson P, Ohlsson PI, Wikander G, Oberg A. Normal binding and reactivity of copper in mutant superoxide dismutase isolated from amyotrophic lateral sclerosis patients. *J Neurochem.* **1997**;69(2):675-81.
- 45. Ayoubi R, Alshafie W, You Z, Southern K, McPherson PS, Laflamme C. Identification of high-performing antibodies for Superoxide dismutase [Cu-Zn] 1 (SOD1) for use in Western blot, immunoprecipitation, and immunofluorescence. *F1000Res*. **2023**;12:391.
- 46. Kotaich F, Caillol D, Bomont P. Neurofilaments in health and Charcot-Marie-Tooth disease. *Front Cell Dev Biol.* **2023**;11:1275155.
- 47. Castellanos-Montiel MJ, Chaineau M, Durcan TM. The Neglected Genes of ALS: Cytoskeletal Dynamics Impact Synaptic Degeneration in ALS. *Frontiers in Cellular Neuroscience*. **2020**;14(380).
- 48. Devarakonda SS, Basha S, Pithakumar A, L BT, Mukunda DC, Rodrigues J, K A, Biswas S, Pai AR, Belurkar S, Mahato KK. Molecular mechanisms of neurofilament alterations and its application in assessing neurodegenerative disorders. *Ageing Res Rev.* **2024**;102:102566.

- 49. Chen H, Qian K, Du Z, Cao J, Petersen A, Liu H, Blackbourn LWt, Huang CL, Errigo A, Yin Y, Lu J, Ayala M, Zhang SC. Modeling ALS with iPSCs reveals that mutant SOD1 misregulates neurofilament balance in motor neurons. *Cell Stem Cell.* **2014**;14(6):796-809.
- 50. Tortelli R, Ruggieri M, Cortese R, D'Errico E, Capozzo R, Leo A, Mastrapasqua M, Zoccolella S, Leante R, Livrea P, Logroscino G, Simone IL. Elevated cerebrospinal fluid neurofilament light levels in patients with amyotrophic lateral sclerosis: a possible marker of disease severity and progression. *Eur J Neurol*. **2012**;19(12):1561-7.
- 51. Lu CH, Macdonald-Wallis C, Gray E, Pearce N, Petzold A, Norgren N, Giovannoni G, Fratta P, Sidle K, Fish M, Orrell R, Howard R, Talbot K, Greensmith L, Kuhle J, Turner MR, Malaspina A. Neurofilament light chain: A prognostic biomarker in amyotrophic lateral sclerosis. *Neurology.* **2015**;84(22):2247-57.
- 52. Alagaratnam J, von Widekind S, De Francesco D, Underwood J, Edison P, Winston A, Zetterberg H, Fidler S. Correlation between CSF and blood neurofilament light chain protein: a systematic review and meta-analysis. *BMJ Neurol Open.* **2021**;3(1):e000143.
- 53. Kim BW, Ryu J, Jeong YE, Kim J, Martin LJ. Human motor neurons with SOD1-G93A mutation generated from CRISPR/Cas9 gene-edited iPSCs develop pathological features of amyotrophic lateral sclerosis. *Front Cell Neurosci.* **2020**;14:604171.
- 54. Wainger BJ, Kiskinis E, Mellin C, Wiskow O, Han SS, Sandoe J, Perez NP, Williams LA, Lee S, Boulting G, Berry JD, Brown RH, Jr., Cudkowicz ME, Bean BP, Eggan K, Woolf CJ. Intrinsic membrane hyperexcitability of amyotrophic lateral sclerosis patient-derived motor neurons. *Cell Rep.* **2014**;7(1):1-11.
- 55. Liu WC, Liu N, Wang Y, Huang C, Li YF, Wang H, Li XG, Deng M. Induced pluripotent stem cell-derived motor neurons from amyotrophic lateral sclerosis (ALS) patients carrying different superoxide dismutase 1 mutations recapitulate pathological features of ALS. *Chin Med J* (*Engl*). **2021**;134(20):2457-64.
- 56. Deng YC, Liu JW, Ting HC, Kuo TC, Chiang CH, Lin EY, Harn HJ, Lin SZ, Chang CY, Chiou TW. n-Butylidenephthalide recovered calcium homeostasis to ameliorate neurodegeneration of motor neurons derived from amyotrophic lateral sclerosis iPSCs. *PLoS One*. **2024**;19(11):e0311573.
- 57. Imamura K, Izumi Y, Watanabe A, Tsukita K, Woltjen K, Yamamoto T, Hotta A, Kondo T, Kitaoka S, Ohta A, Tanaka A, Watanabe D, Morita M, Takuma H, Tamaoka A, Kunath T, Wray S, Furuya H, Era T, Makioka K, Okamoto K, Fujisawa T, Nishitoh H, Homma K, Ichijo H, Julien JP, Obata N, Hosokawa M, Akiyama H, Kaneko S, Ayaki T, Ito H, Kaji R, Takahashi R, Yamanaka S, Inoue H. The Src/c-Abl pathway is a potential therapeutic target in amyotrophic lateral sclerosis. *Sci Transl Med.* **2017**;9(391).
- 58. Catanese A, Rajkumar S, Sommer D, Masrori P, Hersmus N, Van Damme P, Witzel S, Ludolph A, Ho R, Boeckers TM, Mulaw M. Multiomics and machine-learning identify novel transcriptional and mutational signatures in amyotrophic lateral sclerosis. *Brain*. **2023**;146(9):3770-82.
- 59. Devlin AC, Burr K, Borooah S, Foster JD, Cleary EM, Geti I, Vallier L, Shaw CE, Chandran S, Miles GB. Human iPSC-derived motoneurons harbouring TARDBP or C9ORF72 ALS mutations are dysfunctional despite maintaining viability. *Nat Commun.* **2015**;6:5999.
- 60. Thiry L, Clément J-P, Haag R, Kennedy TE, Stifani S. Optimization of long-term human iPSC-derived spinal motor neuron culture using a dendritic polyglycerol amine-based substrate. *bioRxiv*. **2021**.

- 61. Shi J, Qin X, Chang X, Wang H, Guo J, Zhang W. Neurofilament markers in serum and cerebrospinal fluid of patients with amyotrophic lateral sclerosis. *J Cell Mol Med.* **2022**;26(2):583-7.
- 62. Bergeron C, Beric-Maskarel K, Muntasser S, Weyer L, Somerville MJ, Percy ME. Neurofilament light and polyadenylated mRNA levels are decreased in amyotrophic lateral sclerosis motor neurons. *J Neuropathol Exp Neurol*. **1994**;53(3):221-30.
- 63. Wong NK, He BP, Strong MJ. Characterization of neuronal intermediate filament protein expression in cervical spinal motor neurons in sporadic amyotrophic lateral sclerosis (ALS). *J Neuropathol Exp Neurol.* **2000**;59(11):972-82.
- 64. Ge WW, Wen W, Strong W, Leystra-Lantz C, Strong MJ. Mutant copper-zinc superoxide dismutase binds to and destabilizes human low molecular weight neurofilament mRNA. *J Biol Chem.* **2005**;280(1):118-24.
- 65. Campos-Melo D, Hawley ZCE, Strong MJ. Dysregulation of human NEFM and NEFH mRNA stability by ALS-linked miRNAs. *Mol Brain*. **2018**;11(1):43.
- 66. Ziff OJ, Neeves J, Mitchell J, Tyzack G, Martinez-Ruiz C, Luisier R, Chakrabarti AM, McGranahan N, Litchfield K, Boulton SJ, Al-Chalabi A, Kelly G, Humphrey J, Patani R. Integrated transcriptome landscape of ALS identifies genome instability linked to TDP-43 pathology. *Nat Commun.* **2023**;14(1):2176.
- 67. Goffin L, Lemoine D, Clotman F. Potential contribution of spinal interneurons to the etiopathogenesis of amyotrophic lateral sclerosis. *Front Neurosci.* **2024**;18:1434404.
- 68. Gong Z, Ba L, Zhang M. Dysfunction of the oligodendrocytes in amyotrophic lateral sclerosis. *J Biomed Res.* **2022**;36(5):336-42.
- 69. Rodriguez JA, Valentine JS, Eggers DK, Roe JA, Tiwari A, Brown RH, Jr., Hayward LJ. Familial amyotrophic lateral sclerosis-associated mutations decrease the thermal stability of distinctly metallated species of human copper/zinc superoxide dismutase. *J Biol Chem.* **2002**;277(18):15932-7.

Figures

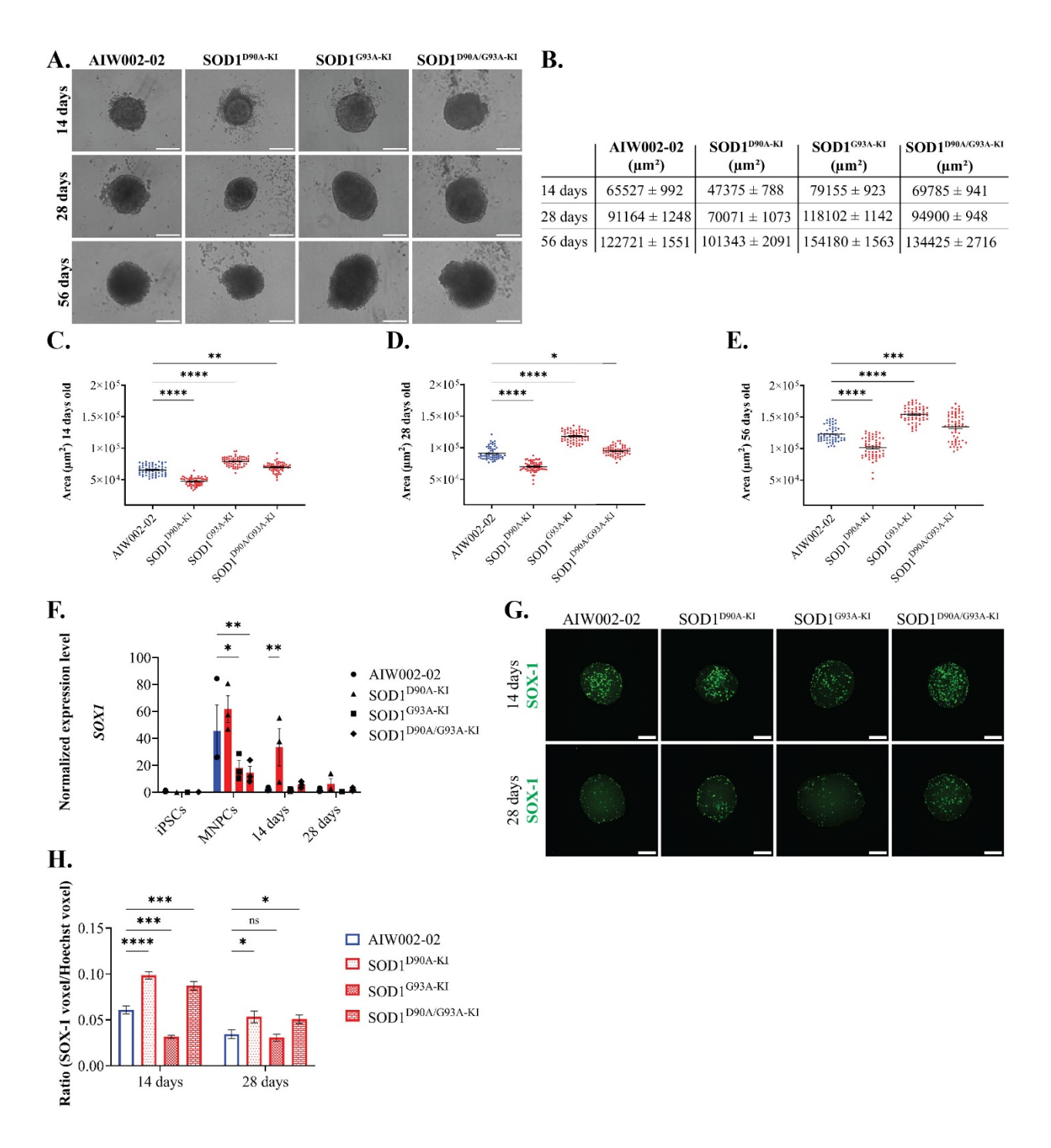


Figure 1. Size profiling using a CellProfiler pipeline reveals size variations in SOD1 MN spheroids. A. Bright-field images of AIW002-02 (isogenic control), SOD1^{D90A-KI}, SOD1^{G93A-KI}, and SOD1^{D90A-KI/G93A-KI} MN spheroids were acquired after 14, 28 and 56 days in culture. Scale

bar, 200 µm. **B.** Summary of the mean MN spheroid size for each cell line at 14, 28, and 56 days. The size of the MN spheroids was determined from the bright-field images using a CellProfiler pipeline. **C-E.** Scatter plots showing the distribution of ninety MN spheroids analyzed per cell line at 14, 28, and 56 days. Data shown as mean \pm SEM, N=3, n=30. **F.** A RT-qPCR targeting *SOX1* was performed to assess whether the size differences of the MN spheroids were linked to changes in the number of proliferative cells. Data shown as mean \pm SEM, N=3, n=3. **G-H.** In addition, SOX-1 (green) expression was analyzed by immunocytochemistry to examine its correlation to *SOX1* mRNA levels. Images represent the maximal projection of 50 optical slices acquired through confocal imaging. Scale bar, 100 µm. Data shown as mean \pm SEM, N=3, n=4. Significance was determined using a two-way ANOVA, followed by a post hoc Dunnett's test using AIW002-02 as the reference sample. *, p \leq 0.05; **, p \leq 0.01; ***, p \leq 0.001; ****, p \leq 0.0001; ns, non-significant (p > 0.05).

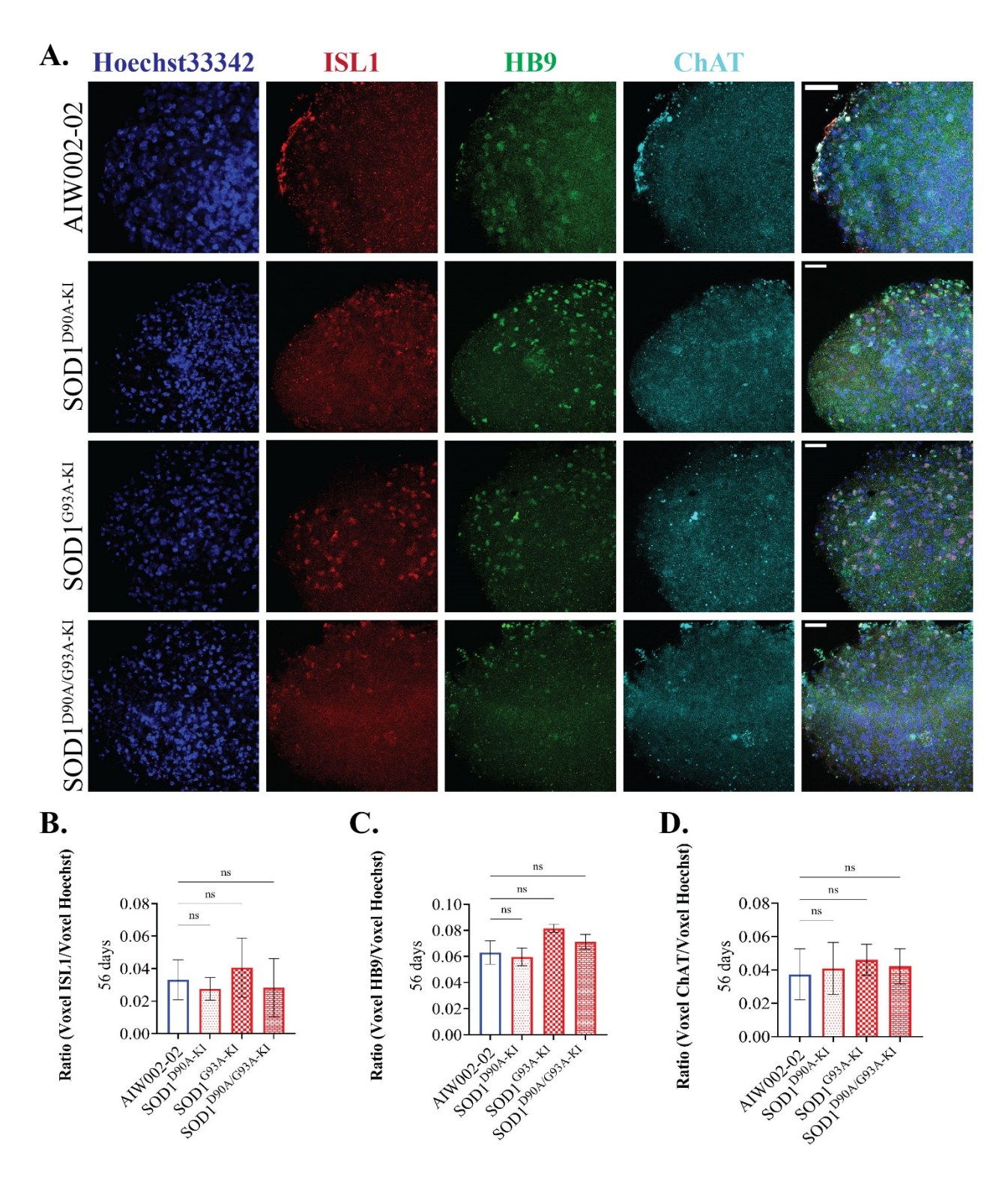


Figure 2. MN markers are consistently expressed at the transcript and protein levels in MN spheroids from the different lines. A. Immunocytochemistry analyses on 56-day-old MN spheroids were conducted to assess whether the protein levels of ISL1 (red), HB9 (green) and,

ChAT (cyan) correlated to their mRNA expression levels. Images show a zoom-in of the maximal intensity projection derived from 12 optical slices acquired through confocal imaging. Scale bar, 50 μ m. **B-D.** Quantification revealed no significant differences in the protein levels of ISL1, HB9, and ChAT across the different cell lines. Data shown as mean \pm SEM, N=3, n=4. Significance was determined using a two-way ANOVA, followed by a post hoc Dunnett's test using AIW002-02 as the reference sample. *, p \leq 0.05; ****, p \leq 0.0001; ns, non-significant (p > 0.05).

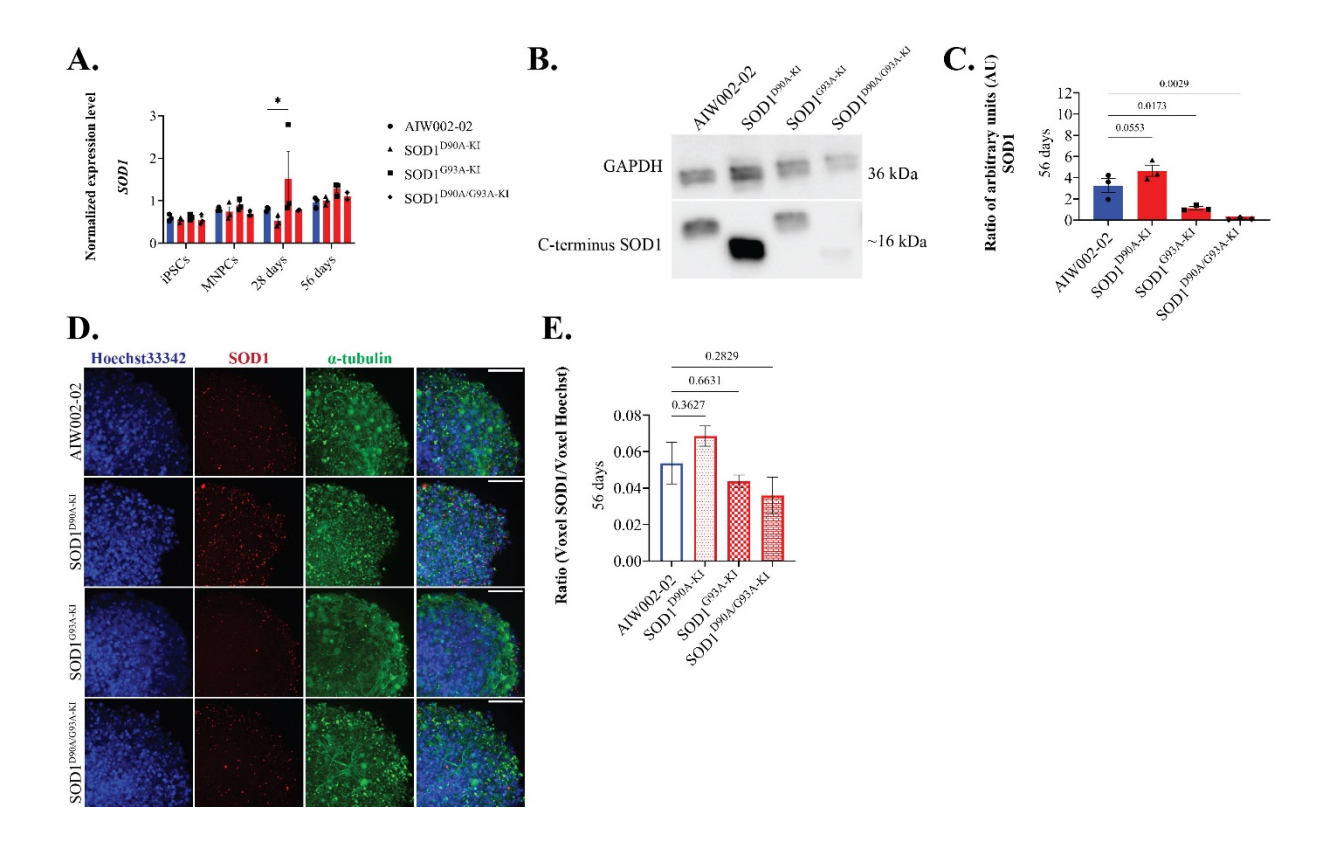


Figure 3. Transcript and protein levels of SOD1 in MN spheroids. A. A RT-qPCR was performed to assess the levels of SOD1 in iPSCs, MNPCs, 28-day-old and 56-day-old MN spheroids. At 56 days in culture, SOD1 was found at comparable levels in MN spheroids from all lines. Data shown as mean \pm SEM, N=3, n=3. Significance was determined using a two-way ANOVA, followed by a post hoc Dunnett's test using AIW002-02 as the reference sample. *, p \leq 0.05. B/C. Protein quantification of SOD1 through Western Blot analysis showed a strong trend toward upregulation of SOD1 in SOD1^{D90A-KI} MN spheroids. In contrast, SOD1^{G93A-KI} and SOD1^{D90A/G93A-KI} lines showed a mild trend toward downregulation of SOD1. Data shown as mean \pm SEM, N=3. D/E. Similarly, quantification through immunocytochemistry showed similar SOD1 (red) trends to those observed by Western Blot. Data shown as mean \pm SEM, N=3, n=3.

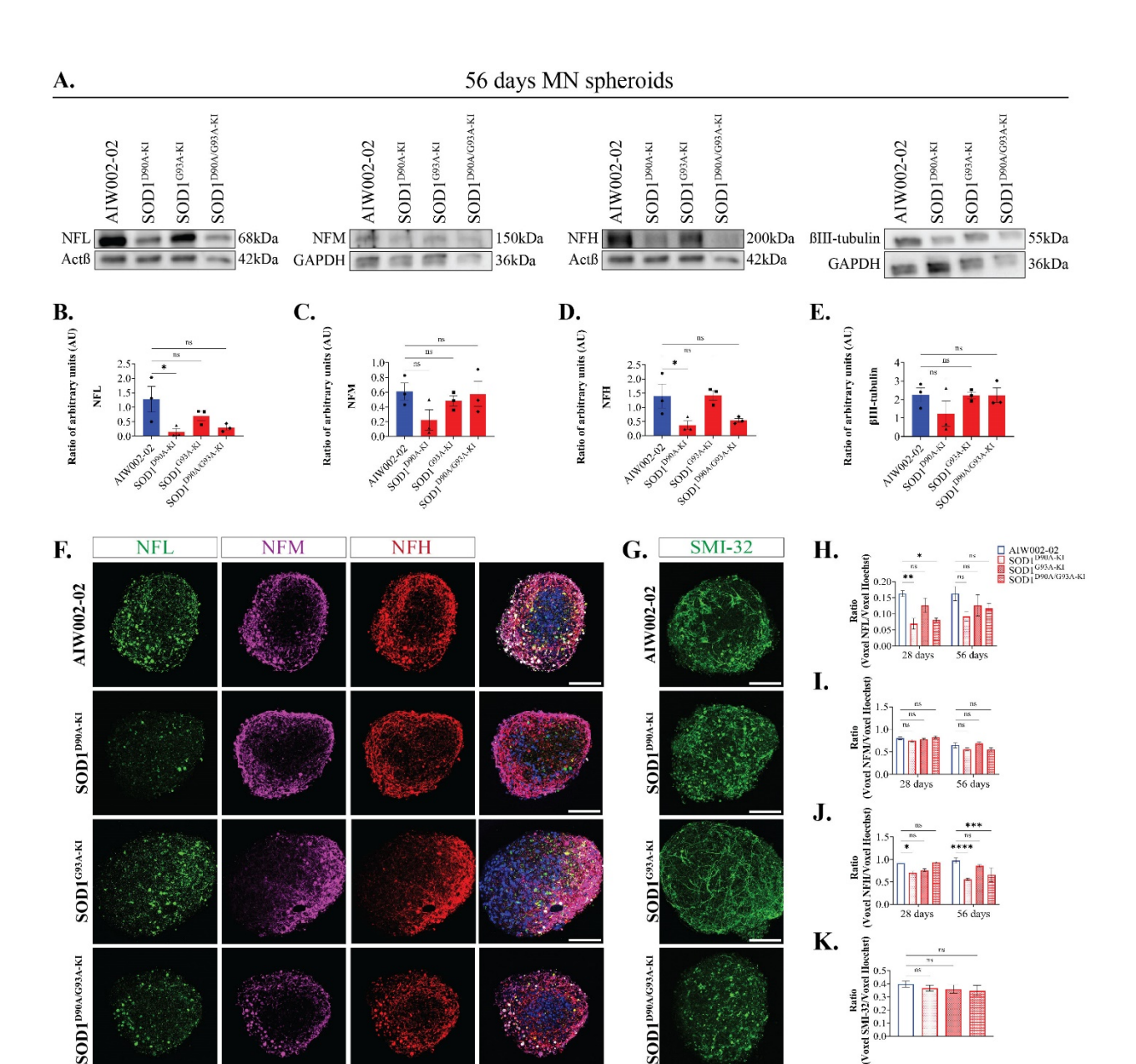


Figure 4. SOD1 MN spheroids showed reduced protein expression of neurofilament (NF)

subunits. Western Blot and immunocytochemistry analyses were performed to assess the expression of NF subunits at the protein level. **A.** For Western Blot, sixty spheroids were pooled per sample to quantify the levels of NFL, NFM, NFH, and βIII-tubulin **B.** NFL showed a trend toward downregulation in all SOD1 mutants, with a statistically significant reduction observed in SOD1^{D90A-KI} MN spheroids. **C.** In contrast, NEFM expression remained unchanged across cell lines. **D.** Finally, NEFH exhibited a trend similar to NFL in both SOD1^{D90A-KI} and SOD1^{D90A/G93A-KI}

KI MN spheroids, though significance was reached only in the SOD1^{D90A-KI} line. **E.** βIII-tubulin was used as a control for generalized cytoplasm alterations. Data shown as mean \pm SEM, N=3, n=3. Full-length blots are presented in Additional file 15: Supplementary Figure 8. F. Immunocytochemistry was performed on individual MN spheroids using antibodies against NFL (green), NFM (magenta), NFH (red), and Hoechst33342 (blue). Images represent a single slice from the middle of the Z-stack, acquired through confocal imaging. Scale bar, 100 µm. G. A second immunostaining against SMI-32 was conducted to control for the number of MN within MN spheroids. Images represent the maximal projection of 12 optical slices acquired through confocal imaging. Scale bar, 100 µm. H-K. Quantification of the immunostainings revealed trends consistent with those observed in Western Blot analyses, where NFL and NEFH were primarily downregulated in SOD1^{D90A-KI} and SOD1^{D90A/G93A-KI} MN spheroids. In contrast, NFM and SMI-32 levels remained stable across all cell lines. Data shown as mean \pm SEM, N=3, n=4. Significance was determined using a two-way ANOVA, followed by a post hoc Dunnett's test using AIW002-02 as the reference sample. *, $p \le 0.05$; **, $p \le 0.01$; ***, $p \le 0.001$; ****, $p \le 0.0001$; ns, nonsignificant (p > 0.05).

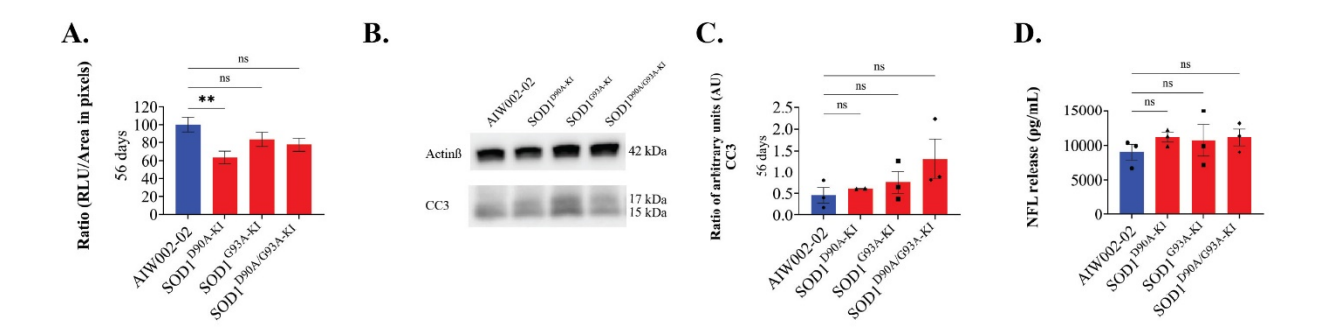


Figure 5. Assessment of cell death and neuronal degeneration indicators in SOD1 MN spheroids. A. A CellTiter-Glo® 3D cell viability assay performed in 56-day-old MN spheroids indicated a trend toward decreased cell viability in SOD1 lines with SOD1^{D90A-KI} line reaching statistical significance. Data shown as mean \pm SEM, N=3, n=2. B/C. Quantification of cleaved-caspase-3 through Western Blot indicated a trend toward increased apoptosis in SOD1^{G93A-KI} and SOD1^{D90A/G93A-KI} lines. Data shown as mean \pm SEM, N=3, n=2/3. Full-length blot is presented in Additional file 15: Supplementary Figure 8. D. Quantification of NFL protein released in the culture media showed a trend toward increased neuronal degeneration in SOD1 lines. Data shown as mean \pm SEM, N=3, n=2. Significance was determined using a one-way ANOVA, followed by a post hoc Dunnett's test using AIW002-02 as the reference sample. **, p \leq 0.01. ns, non-significant.

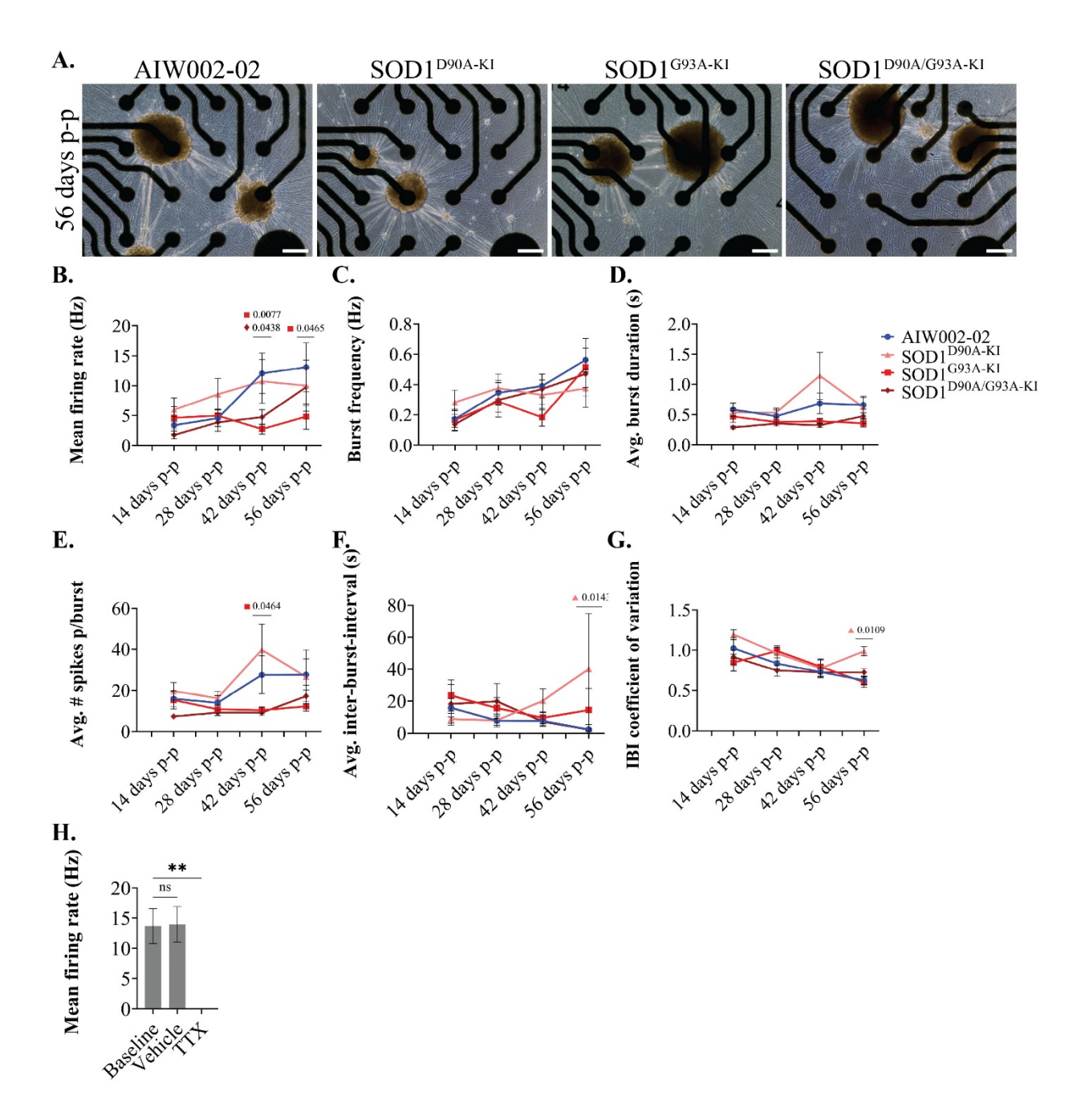


Figure 6. MEA recordings revealed hypoactivity and irregular burst properties in SOD1 MN spheroids. **A.** Representative bright-field images of iPSC-derived MN spheroids at 56 days p-p in Cytoview 24–well MEA plates. Scale bar, 200 μm. **B**. The MFR (Hz) was significantly reduced in SOD1^{D90A/G93A-KI} MN spheroids at 42 days p-p, and in SOD1^{G93A-KI} MN spheroids at both 42 and 56 days p-p. **C.** Burst frequency (Hz) showed a slight reduction in SOD1 MN spheroids at 56 days

p-p, although no statistically significant differences were observed. **D.** Starting at 28 days, SOD1^{G93A-KI} and SOD1^{D90A/G93A-KI} MN spheroids displayed reduced average burst duration. **E.** Also, a reduced number of spikes per burst was recorded in SOD1^{G93A-KI} and SOD1^{D90A/G93A-KI} MN spheroids from 28 days onward. **F.** Consistent with the reduced number of bursts observed in SOD1 MN spheroids, the SOD1^{D90A-KI} line showed a significant increase in the average inter-burst interval at 56 days. **G.** Additionally, the IBI coefficient of variation was significantly elevated in SOD1^{D90A-KI} MN spheroids a 56 days, indicating irregular burst activity compared to the isogenic control. Data shown as mean \pm SEM, N=3, n=3–10. Significance was determined using a two-way ANOVA, followed by a post hoc Dunnett's test using AIW002-02 as the reference sample. **H.** Acute treatment with vehicle or TTX was administered to all cell lines to verify the absence of recording artifacts. Data pooled from all cell lines and shown as mean \pm SEM, n=3–9. Significance was determined using a one-way ANOVA, followed by a post hoc Dunnett's test using Baseline as the reference sample. *, p \leq 0.05; **, p \leq 0.01; ns, non-significant (p > 0.05).

Supplementary materials

Mutations in SOD1 induce ALS-related phenotypes in 3D iPSC-derived motor neuron (MN)

spheroids

María José Castellanos-Montiel, Anna Kristyna Franco-Flores, Michael Nicouleau, Ghazal Haghi,

Sarah Lépine, Belén Baeza, Carol X.-Q. Chen, Taylor M. Goldsmith, Nathalia Aprahamian, Doris

Hua, Mathilde Chaineau, Lale Gursu, Narges Abdian, Eric Deneault, Thomas M. Durcan.

Corresponding author e-mail: thomas.durcan@mcgill.ca (T.M.D)

156

CRISPR/Cas9 genome editing and validation

Following a streamlined CRISPR workflow (1, 2), the P3 Primary Cell-4D NucleofectorTM X Kit S (#V4XP-3032, Lonza) was used to correct either p.D90A or p.G93A in the SOD1^{D90A/G93A-KI} iPSC line, thereby generating two iPSC lines with a single *SOD1* mutation. The sequences of the sgRNAs and ssODNs used are provided in **Table S2**.

After isolation, gene-edited clones were identified by ddPCR with a QX200TM Droplet Reader (Bio-Rad). The detection of the modified nucleotides by ddPCR was based on a TaqMan® assay including two PCR primers: one DNA probe fused to a fluorophore specific to the corrected/WT allele (FAM), and one DNA probe fused to a fluorophore specific to the edited allele (HEX). Locked Nucleic Acid (LNA®) probes were designed following the manufacturer's criteria. Sanger sequencing was used to validate the sequence integrity of successful clones. The sequences of the primers and probes used for ddPCR, and Sanger sequencing are provided in **Table S3**.

Karyotyping

For G-band karyotyping, AIW002-02 and SOD1^{D90A/G93A-KI} iPSCs were cultured for 72 h until they reached 50–60% confluency. iPSCs were split, pellet, and shipped live to the Wicell Cytogenetics Core (instructions provided by WiCell, Madison, WI, USA).

SOD1^{D90A-KI} and SOD1^{G93A-KI} iPSCs were cultured for 72 h until they reached 50–60 % confluency, and karyotyping was conducted as previously described (3).

Genomic abnormalities analyses

Genomic DNA was extracted with the Genomic DNA Mini Kit (Geneaid) according to the manufacturer's instructions. Genomic stability was detected using the hPSC Genetic Analysis Kit (#07550, STEMCELL Technologies). Briefly, 5 ng of genomic DNA was mixed with a ROX reference dye, and double-quenched probes tagged with 5-FAM that represent the eight most common karyotypic abnormalities reported in hiPSC: chr 1q, chr 8q, chr 10p, chr 12p, chr 17q, chr 18q, chr 20q or chr Xp. Reactions were run on a QuantStudio 5 Real-Time PCR System (Thermo Fisher Scientific). Copy numbers were analyzed using the ΔΔCT method and the copy number of a control region in chr4 was used for normalization (4, 5).

Virology test

Blood samples were cleared from Hepatitis A/B and HIV at the clinic. After reprogramming, iPSCs are assessed for mycoplasma using the MycoAlert® Mycoplasma Detection Kit (#LT07-318, Lonza) following manufacturer's instructions.

Immunocytochemistry of cell monolayers grown on glass coverslips

Immunocytochemistry of cell monolayers (i.e. iPSCs and MNPCs) grown on glass coverslips (#41001112, Fisher Scientific) was performed as previously described (4). Briefly, cells were fixed in 4% FA diluted in 1X PBS for 15–20 min at room temperature (RT) and washed three times for 5 min with 1X PBS. Cells were permeabilized with 0.2% Triton X-100 (#TRX506, Bioshop) diluted in 1X PBS for 10 min at RT, and were then blocked for 1 h at RT in a blocking

solution containing 5% normal donkey serum (NDS; #S30 Normal donkey, Millipore), 1% bovine serum albumin (BSA; #800-095-CG, Wisent Bioproducts), and 0.05% Triton X-100 diluted in 1X PBS (blocking solution). After blocking, cells were incubated with primary antibodies diluted in blocking solution overnight at 4°C. Primary antibodies were washed out by performing three 5 min washes with 1X PBS and cells were subsequently incubated with secondary antibodies diluted in blocking solution for 2 h at RT. Secondary antibodies were washed out by performing three 5 min washes with 1X PBS followed by a Hoechst33342 nucleic acid counterstain for 5 min. Coverslips were mounted with Fluoromount-GTM (00-4958-02, Thermo Fisher Scientific). Immunocytochemistry images were acquired using the automated Evos FL-Auto2 imaging system (Thermo Fisher Scientific) using 20X magnification (N.A 0.4) or the Zeiss Axio Observer Z1 Inverted Microscope using 20X magnification (N.A 0.8).

MNPC quantification

For each cell line, three images per batch were acquired with a Zeiss Axio Observer Z1 Inverted Microscope using 20X magnification (N.A 0.8). A CellProfiler pipeline (version 4.2.5) was used to quantify the number of Olig2⁺, Pax6⁺, and Olig2⁺/Pax6⁺ cells. Briefly, nuclei immunolabelled with Hoechst33342 were identified as primary objects called "Nuclei" based on the global threshold strategy, the Otsu thresholding method, and the diameter in pixels. The pixel intensity within each primary object was measured in the Pax6 channel and a threshold was applied to determine Pax6⁺ cells. The newly generated objects were called "Pax6positive". A similar approach was used to identify Olig2⁺ cells using the Olig2 channel, and the generated objects were called "Olig2positive". Finally, the pixel intensity of each "Pax6positive" object was measured in the Olig2 channel, and a threshold was applied to identify double-positive cells. AIW002-02: B1

(125 cells), B2 (400 cells), B3 (237 cells); SOD1^{D90A-KI}: B1 (487 cells), B2 (352 cells), B3 (484 cells); SOD1^{G93A-KI}; B1 (209 cells), B2 (292 cells), B3 (405 cells); SOD1^{D90A/G93A-KI}: B1 (129 cells), B2 (267 cells), B3 (155 cells).

Supplementary references

- 1. Lépine S, Nauleau-Javaudin A, Deneault E, Chen CX, Abdian N, Franco-Flores AK, Haghi G, Castellanos-Montiel MJ, Maussion G, Chaineau M, Durcan TM. Homozygous ALS-linked mutations in TARDBP/TDP-43 lead to hypoactivity and synaptic abnormalities in human iPSC-derived motor neurons. *iScience*. **2024**;27(3):109166.
- 2. Deneault E, Chaineau M, Nicouleau M, Castellanos Montiel MJ, Franco Flores AK, Haghi G, Chen CX, Abdian N, Shlaifer I, Beitel LK, Durcan TM. A streamlined CRISPR workflow to introduce mutations and generate isogenic iPSCs for modeling amyotrophic lateral sclerosis. *Methods.* **2022**;203:297-310.
- 3. Gandy A, Maussion G, Al-Habyan S, Nicouleau M, You Z, Chen CX, Abdian N, Aprahamian N, Krahn AI, Larocque L, Durcan TM, Deneault E. An Inducible Luminescent System to Explore Parkinson's Disease-Associated Genes. *Int J Mol Sci.* **2024**;25(17).
- 4. Chen CX, Abdian N, Maussion G, Thomas RA, Demirova I, Cai E, Tabatabaei M, Beitel LK, Karamchandani J, Fon EA, Durcan TM. A Multistep Workflow to Evaluate Newly Generated iPSCs and Their Ability to Generate Different Cell Types. *Methods Protoc.* **2021**;4(3).
- 5. Baker D, Hirst AJ, Gokhale PJ, Juarez MA, Williams S, Wheeler M, Bean K, Allison TF, Moore HD, Andrews PW, Barbaric I. Detecting Genetic Mosaicism in Cultures of Human Pluripotent Stem Cells. *Stem Cell Reports*. **2016**;7(5):998-1012.

Supplementary Table 1. Overview of iPSC lines

Cell line ID	ALS mutation	Sex	Age	Ethnicity	Primary cell line	Reprogramming method	Ref.
AIW002-02	None	Male	37	Caucasian	PBMCs	Sendai virus	(1)
SOD1 ^{D90A/G93A-KI}	p. D90A and p. G93A	Male	37	Caucasian	AIW002-02	n/a	(2)
SOD1 ^{D90A-KI}	p. D90A	Male	37	Caucasian	SOD1 ^{D90A/G93A-KI} , G93A correction	n/a	
SOD1 ^{G93A-KI}	p. G93A	Male	37	Caucasian	SOD1 ^{D90A/G93A-KI} , D90A correction	n/a	

- 1. Chen CX, Abdian N, Maussion G, Thomas RA, Demirova I, Cai E, Tabatabaei M, Beitel LK, Karamchandani J, Fon EA, Durcan TM. A Multistep Workflow to Evaluate Newly Generated iPSCs and Their Ability to Generate Different Cell Types. *Methods Protoc.* **2021**;4(3).
- 2. Deneault E, Chaineau M, Nicouleau M, Castellanos Montiel MJ, Franco Flores AK, Haghi G, Chen CX, Abdian N, Shlaifer I, Beitel LK, Durcan TM. A streamlined CRISPR workflow to introduce mutations and generate isogenic iPSCs for modeling amyotrophic lateral sclerosis. *Methods.* **2022**;203:297-310.

Supplementary Table 2. List of sgRNAs and ssODNS used to make SOD1 single mutation lines

Cell line ID	gRNAs	ssODN template
SOD1 ^{D90A-KI}		ATCTGATGCTTTTTCATTATTAGGCATGTTGG
		AGACTTGGGCAATGTGACTGCTGCCAAAGAT
		GGTGTGGCCGATGTGTCTATTGAAGATTCTG
	CACAUCGGCCACAGC	TGATCTCACTCTCAGGAGAC
SOD1 ^{G93A-KI}	AUCUU	ATCTGATGCTTTTTCATTATTAGGCATGTTGG
		AGACTTGGGCAATGTGACTGCTGACAAAGAT
		GCTGTGGCCGATGTGTCTATTGAAGATTCTGT
		GATCTCACTCTCAGGAGAC

Supplementary Table 3. List of primers and affinity probes used for ddPCR or Sanger sequencing

	$SOD1^{\mathrm{D90A-KI}}$	SOD1 ^{G93A-KI}
Probe-HEX (mutant)*	/5HEX/AG+AT+G+C+TG+T+	/5HEX/ACT+GCT+G+C+CAAA
1100e-11EX (mutant)	GG/3IABkFQ/	GA/3IABkFQ/
	/56-	/5HEX/ACT+GCT+G+A+CAAA
Probe-FAM (corrected/WT) *	FAM/AGAT+G+G+TG+T+GG	+GA/3IABkFQ/
	/3IABkFQ/	
ddPCR primer – F TTAGTGGCATCAGCCCTAATC		TC
ddPCR primer – R	AGTGTGCGGCCAATGAT	
Sanger sequencing primer – F	TCTGAAATCAGGTGCAGCC	
Sanger sequencing primer - R	ACCGCGACTAACAATCAAA	GTG

^{* &}quot;+" signs in front of nucleotides indicate the location of Locked Nucleic Acids (LNA®).

Supplementary Table 4. List of primary antibodies

Antibody	Host	Company	Clone or Cat. #	Dilution (Application)	
Actin	Mouse	Millipore	MAB1501	1:40000 (WB)	
βIII-tubulin	Mouse	Millipore	MAB5564	1:20000 (WB)	
ChAT	Goat	Millipore	MAB144P	1:50 (ICC)	
Cleaved-caspase 3	Rabbit	Cell signaling	9661	1:500 (WB)	
GAPDH	Mouse	Proteintech	60004-1-lg	1:40000 (WB)	
Hb9	Mouse	DSHB	81.5C10	1:50 (ICC)	
Isl-1	Mouse	DSHB	40.2D6	1:50 (ICC)	
Ki67	Mouse	BD Bioscience	556003	1:200 (ICC)	
Nanog	Rabbit	Abcam	ab21624	1:200 (ICC)	
NEH	Chialan	Abcam	4600	1:1000 (ICC),	
NFH	Chicken		4680	1:5000 (WB)	
NEL	Mouse	Siama	N5120	1:1000 (ICC),	
NFL	Mouse	e Sigma N5139	N3139	1:5000 (WB)	
NFM	Rabbit	Millipore	AB1987	1:1000 (ICC),	
111.111	Rabbit	wimpore	AD1967	1:5000 (WB)	
Oct3/4	Goat	Santa Cruz	Sc-8628	1:500 (ICC)	
Olig2	Rabbit	Millipore	AB9610	1:100 (ICC)	
Pax6	Mouse	DSHB	AB_528427	1:100 (ICC)	
SMI-32	Mouse	Biolegend	801701	1:100 (ICC)	
SOD1	D -1.1.24	Thermo Fisher	702783	1:500 (ICC)	
	Kabbit	Rabbit Scientific			
SOD1 (C-	Rabbit	ConoTou	CTV100650	1.500 (WD)	
terminal)	Kauun	GeneTex	GTX100659	1:500 (WB)	
SSEA-4	Mouse	Santa Cruz	sc-21704	1:200 (ICC)	
Tro 1 60	Mona	STEMCELL	TD A 1 60D	1.200 (ICC)	
Tra-1-60	Mouse	Technologies	TRA1-60R	1:200 (ICC)	

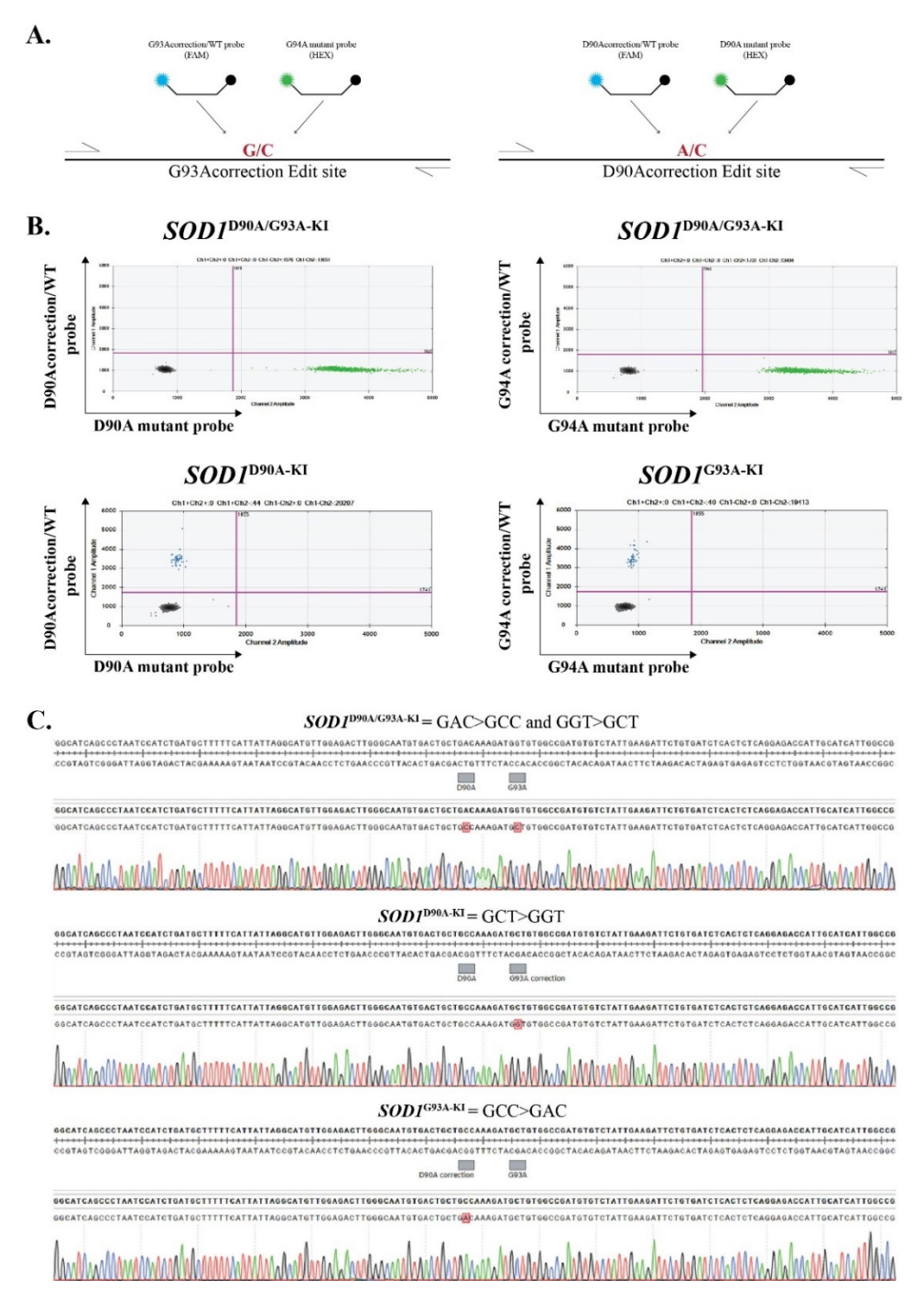
Supplementary Table 5. List of secondary antibodies

Antibody	Species Reactivity	Company	Cat.#	Dilution (Application)	
Hoechst33342	n/a	Invitrogen	H3570	1:1000 or 1:5000 (ICC)	
Dylight488	Rabbit IgG	Abcam	ab96891	1:500 (ICC)	
Dylight650	Chicken IgY	Abcam	ab96950	1:500 (ICC)	
Dylight488	Mouse IgG	Abcam	ab96875	1:500 (ICC)	
AlexaFluor647	Goat IgG	Invitrogen	A21447	1:500 (ICC)	
Dylight550	Goat IgG	Abcam	ab96936	1:500 (ICC)	
Dylight650	Mouse IgG	Abcam	Ab96878	1:500 (ICC)	
HRP	Mouse	Jackosn	115 025 002 1	1:10000 (WB)	
пкг	Wiouse	Immunoresearch	115-035-003 1:10000 (WB)		
HRP	Rabbit	Jackosn	111 005 144	111-035-144 1:10000 (WB)	
TIKI	Raooit	Immunoresearch	111-035-144		
HRP	Chicken	Jackosn		1.10000 (WD)	
пкг	CHICKCH	Immunoresearch	703-035-155	1:10000 (WB)	

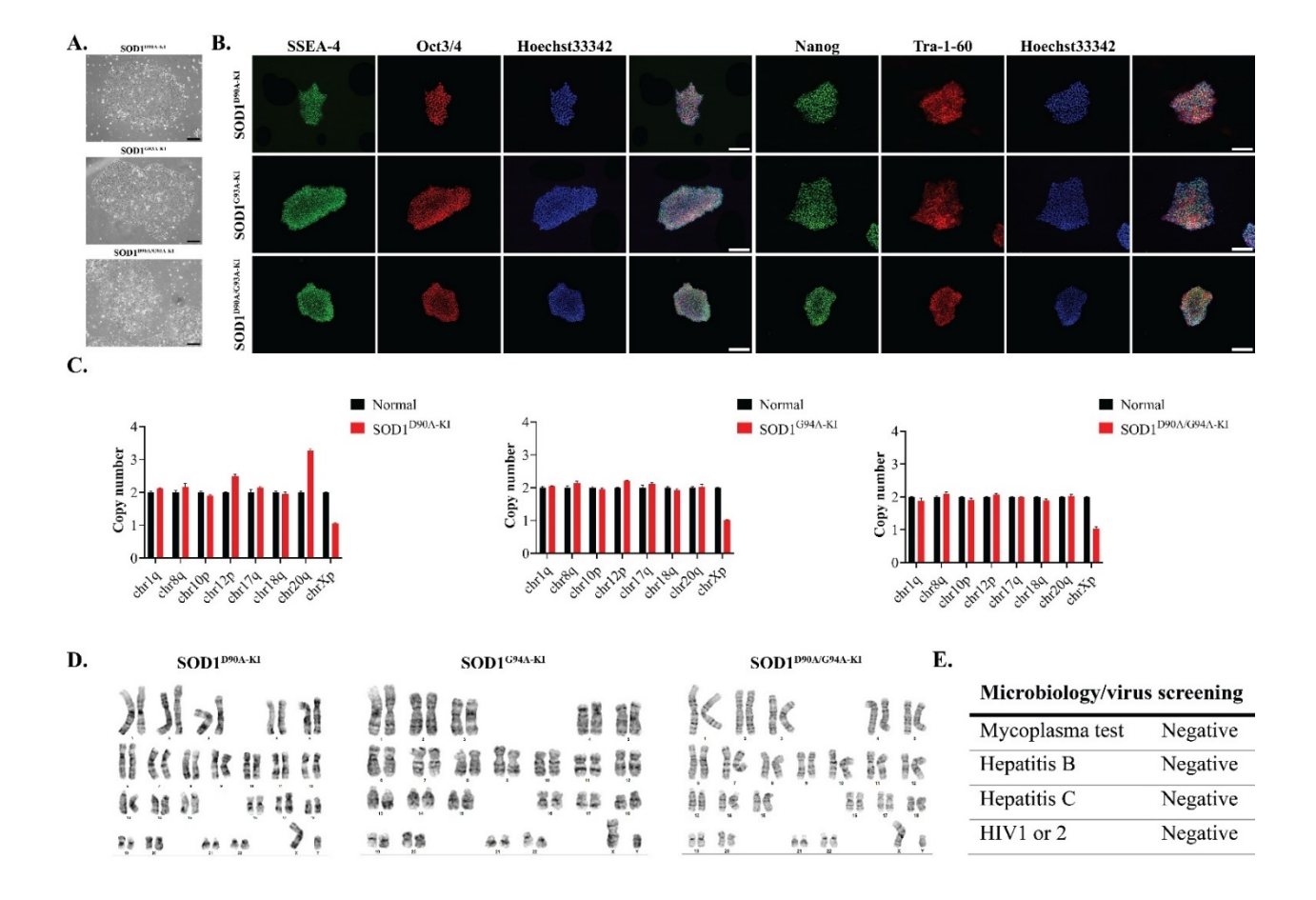
Supplementary Table 6. List of TaqMan qPCR probes

GENE	Reference
GAPDH	Hs02786624_g1
ACTB	Hs01060665_g1
HOXA5	Hs00430330_m1
HOXB8	Hs00256885_m1
FOXG1	Hs01850784_s1
NKX6.1	Hs00232355_m1
KI67	Hs010327443_m1
PAX6	Hs01088114_m1
OLIG2	Hs00377820_m1
NESTIN	Hs04187831_g1
НВ9	Hs00907365_m1
ISL1	Hs00158126_m1
CHAT	Hs00758143_ml

SOD1	Hs00533490_m1
NEFH	Hs00606024_m1
NEFM	Hs00193572_m1
NEFL	Hs00196245_m1

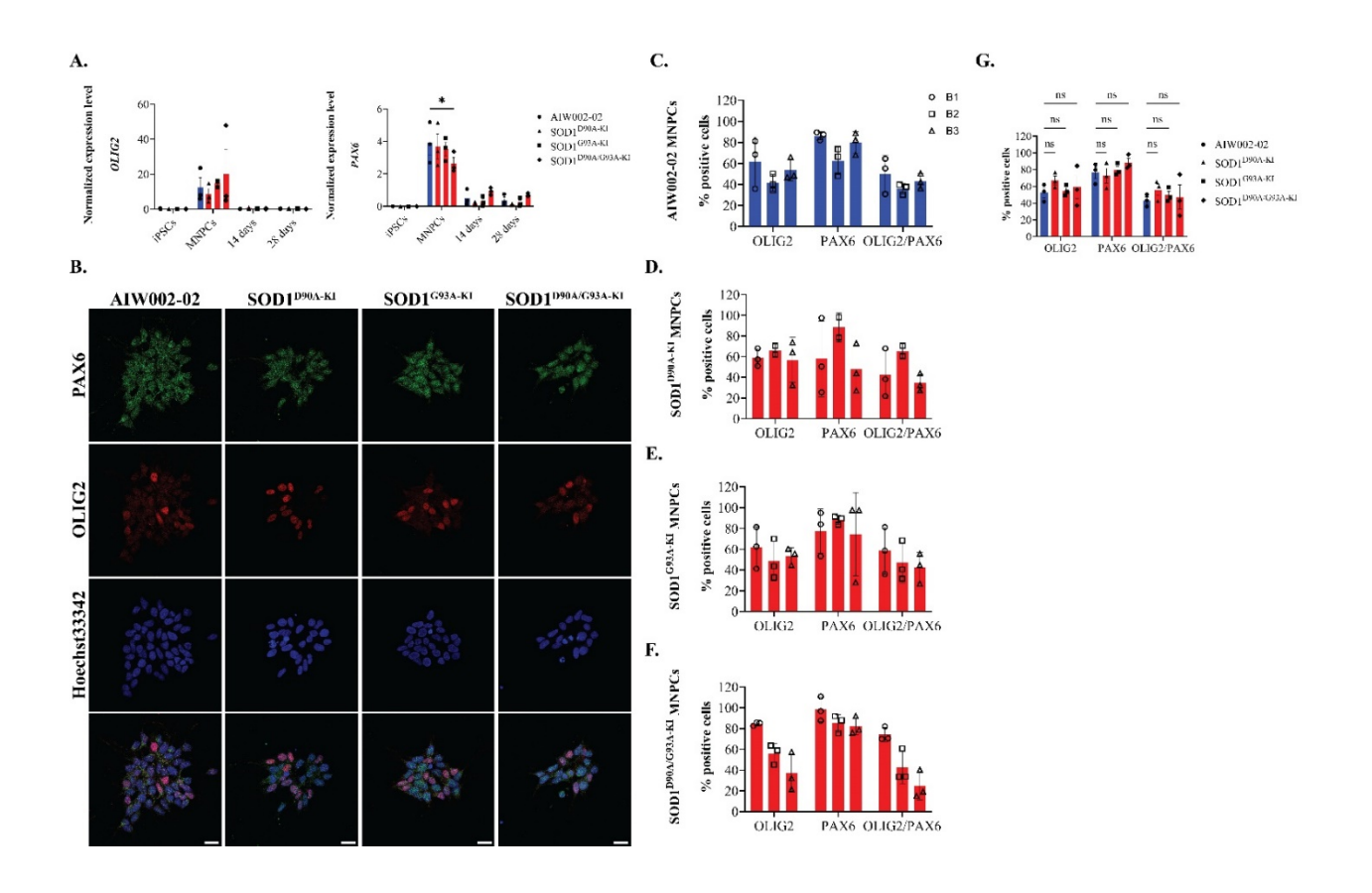


Supplementary Figure 1. Validation of CRISPR/Cas9 gene editing by ddPCR and Sanger sequencing. A. Pairs of corrected/WT (FAM, blue) and mutant (HEX, green) probes designed to target the wild-type (WT) or edited alleles, respectively. **B.** ddPCR scatter plots confirming correct gene editing and homozygosity of iPSC lines. **C.** Sanger sequence chromatograms from selected iPSC clones; red box shows complete correction of target nucleotide.

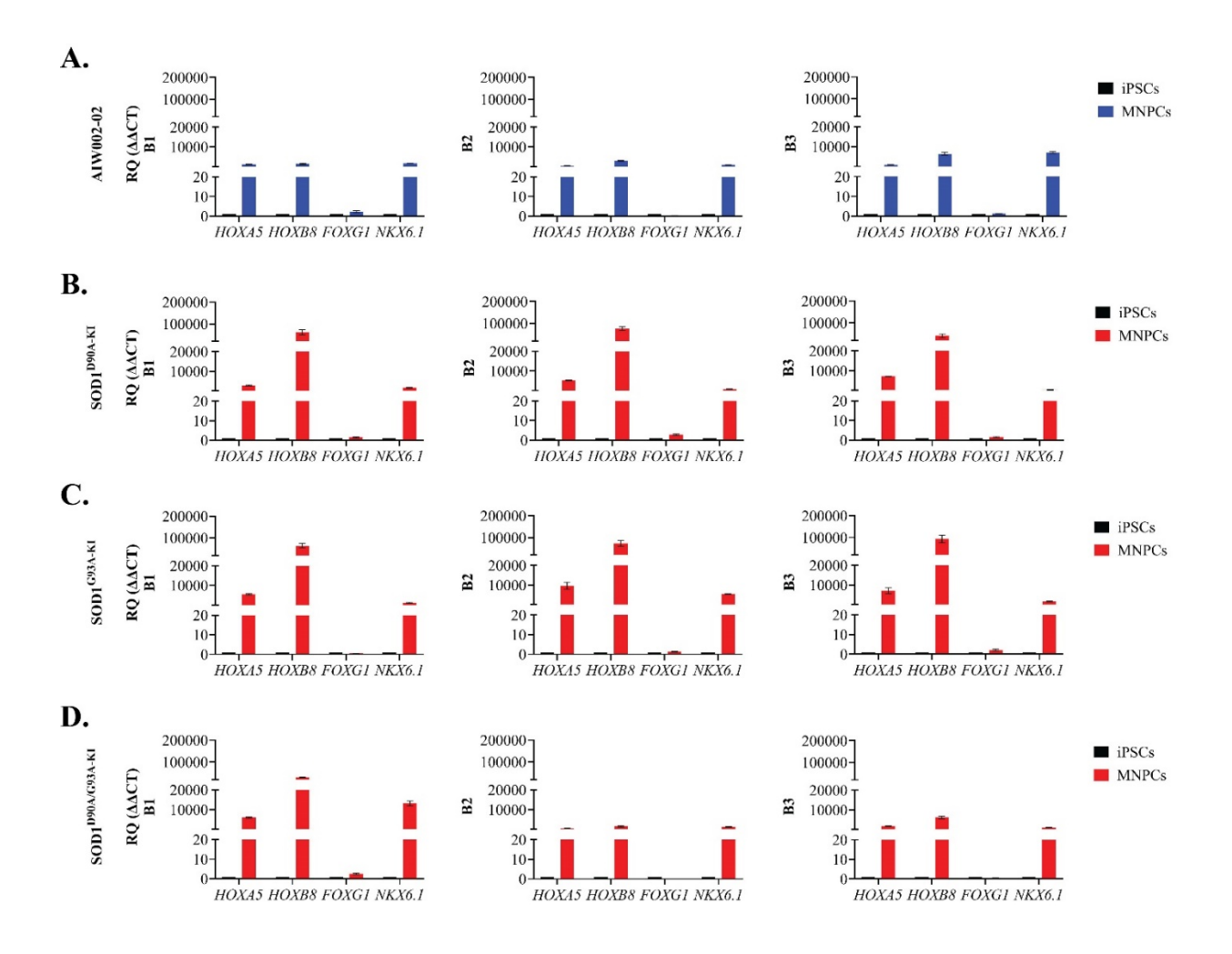


Supplementary Figure 2. Characterization and quality control of mutant SOD1 iPSC lines.

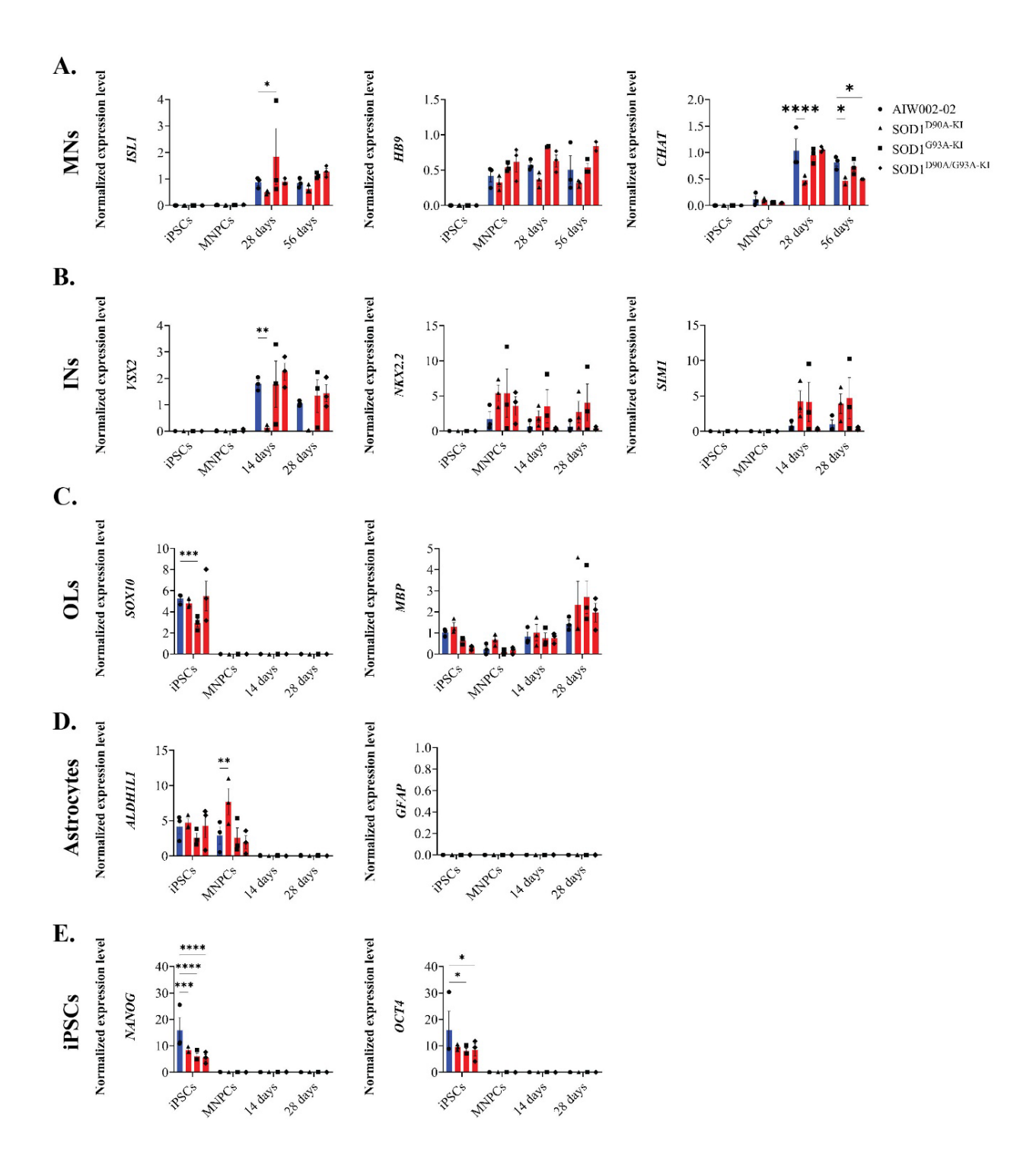
A. Representative phase-contrast image of SOD1^{D90A-KI}, SOD1^{G93A-KI}, and SOD1^{D90A/G93A-KI} iPSCs. Scale bar, 100 μm. **B.** Representative images of immunocytochemistry against pluripotency-associated markers Nanog, Tra-1-60, SSEA-4 and Oct3/4. Scale bar, 200 μm. **C.** All iPSC lines have normal chromosome copy number, as assessed by qPCR. Data shown as mean ± SEM, N=3, n=3. **D.** Mutant SOD1 iPSC lines display a normal G-band karyotype. **E.** Mutant SOD1 iPSCs are free from mycoplasma, hepatitis B/C and HIV 1/2 virus.



Supplementary Figure 3. Expression of PAX6 and OLIG2 by MNPCs. AIW002-02 SOD1^{D90A/G93A-KI}, SOD1^{G93A-KI}, and SOD1^{D90A/G93A-KI} were differentiated into MNPCs as previously described (18, 19, 23, 27). For each cell line, independent differentiation processes were performed to generate three batches of MNPCs, which were stored in liquid nitrogen and later thawed to generate MN spheroids. **A.** At the transcript level, MNPCs expressed OLIG2 and PAX6 as assessed by qPCR. Data shown as mean \pm SEM, N=3, n=3. **B-F.** At the protein level, MNPCs were immunostained for Olig2 and Pax6, and the number of Olig2⁺, Pax6⁺, and Olig2⁺/Pax6⁺ cells was quantified. Scale bar, 100µm. Data shown as mean \pm SD, n=3. **G.** Statistical analysis performed on the biological triplicates per cell line showed no statistical differences amongst Olig2⁺, Pax6⁺, and Olig2⁺/Pax6⁺ cells. Data shown as mean \pm SEM, N=3, n=3. Significance was determined using a one-way ANOVA, followed by a post hoc Dunnett's test using AIW002-02 as the reference sample. *, p \leq 0.05; ns, non-significant.



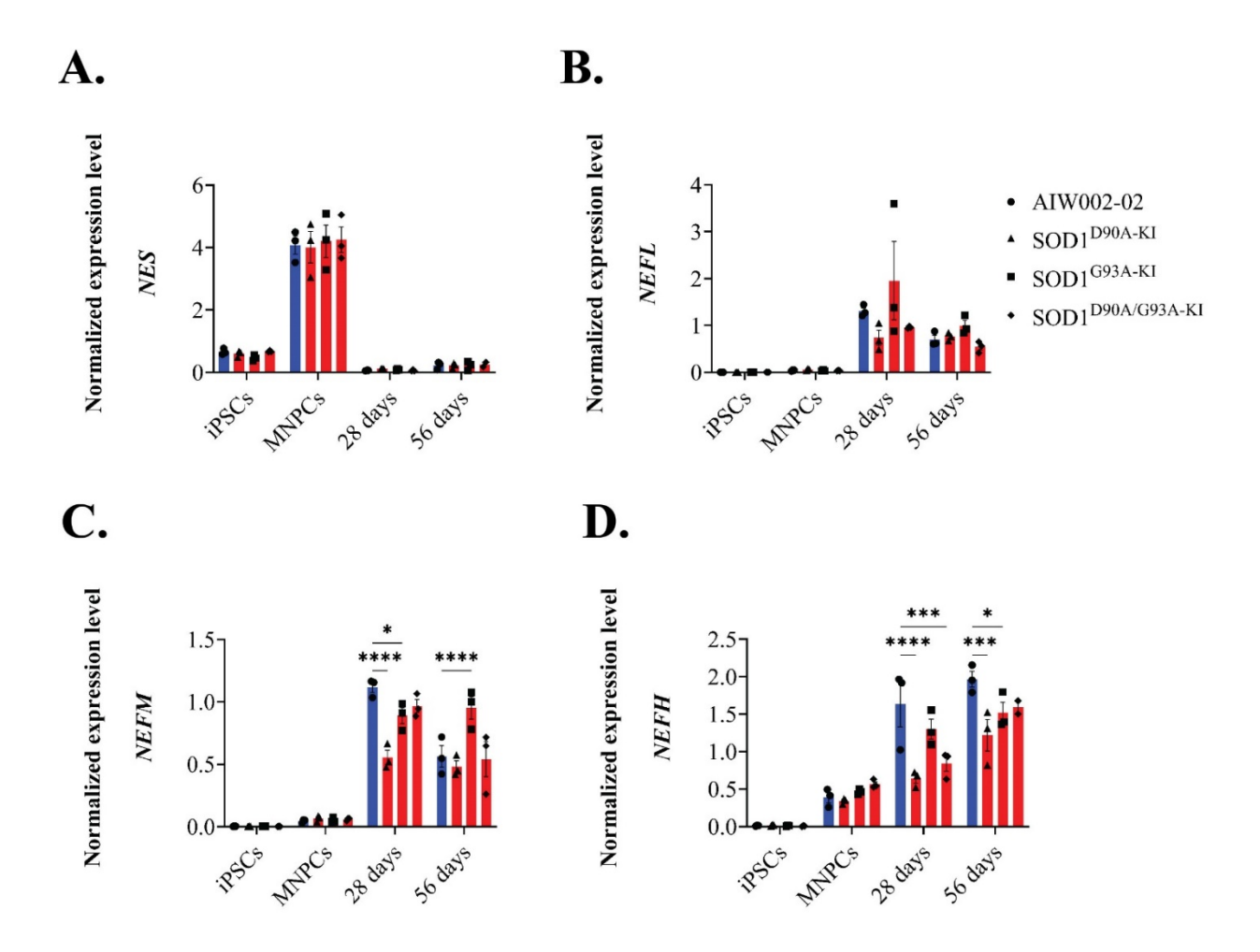
Supplementary Figure 4. Spatial identity of MNPCs in the spinal cord. The assessment of HOXA5 and HOXB8 confirmed the spinal lineage of the different MNPC batches induced from the **A.** AIW002-02, **B.** SOD1^{D90A-KI}, **C.** SOD1^{G93A-KI}, and **D.** SOD1^{D90A/G93A-KI} iPSC lines. FOXG1, a marker of cortical lineage, was used as a negative control. Additionally, the expression of NKX6.1 ascertained the ventral identity of the MNPCs. Bar graphs represent $\Delta\Delta$ CT values, normalized to endogenous controls and compared to iPSCs as the reference sample. Data shown as mean \pm SD, n=3.



Supplementary Figure 5. Expression profiling of different cell types within MN spheroids.

The transcriptional expression of markers associated with MNs, interneurons (INs), oligodendrocytes (OLs), astrocytes and iPSCs was analyzed via RT-qPCR across developmental

stages, including iPSCs, MNPCs, and MN spheroids at 14, 28, and 56 days. A. ISL1 and HB9 expression began at the MNPC stage and peaked during the MN spheroid stage, with no significant differences observed between cell lines after 56 days. CHAT, a marker of MN maturation, was predominantly expressed in MN spheroids; however, its expression was significantly downregulated in SOD1^{D90A-KI}, and SOD1^{D90A-KI/G93A-KI} after 56 days. **B.** Within the dorsoventral axis of the spinal cord, V2 and V3 INs flank the pMN domain. V2 INs were identified by VSX2 expression, while V3 INs were associated with NKX2.2 and SIM1 expression. None of these markers-VSX2, NKX2.X, or SIM1-showed significant differences across cell lines in MN spheroids after 28 days. C. Oligodendrocyte progenitor cells (OPCs) and mature oligodendrocytes were identified through the expression of SOX10 and MBP, respectively. SOX10 was absent in MN spheroids after 28 days, whereas MBP expression was upregulated to comparable levels between cell lines. **D.** Astrocyte detection was based on ADLH1L1 and GFAP expression. The downregulation of ALDH1L1 in MN spheroids and the absence of GFAP expression indicate a lack of astrocytes. E. As a negative control, the downregulation of the pluripotency-associated markers, *NANOG* and *OCT4*, was evaluated within MN spheroids. Data shown as mean \pm SEM, N=3, n=3. Significance was determined using a two-way ANOVA, followed by a post hoc Dunnett's test using AIW002-02 as the reference sample. *, $p \le 0.05$; **, $p \le 0.01$; ***, $p \le 0.001$; ****, $p \le 0.001$; 0.0001.

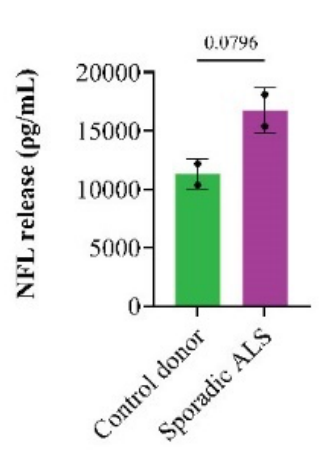


Supplementary Figure 6. Transcriptional expression of intermediate filaments in MN spheroids. The expression of A. NES, B. NEFL, C. NEFM, and D. NEFH, intermediate filaments essential for neuronal function and maturation, was measured through RT-qPCR. Data shown as mean \pm SEM, N=3, n=3. Significance was determined using a two-way ANOVA, followed by a post hoc Dunnett's test using AIW002-02 as the reference sample. *, p \leq 0.05; ***, p \leq 0.001; ****, p \leq 0.0001.

A.

Donor	Sex	Age
Control 1	F	70 y/o
Control 2	M	55 y/o
Sporadic ALS 1	F	65 y/o
Sporadic ALS 2	М	66 y/o

B.



Supplementary Figure 7. Quantification of NFL release in plasma of control donors and sporadic ALS patients. A. Plasma samples from two control donors and two sporadic ALS donors were used to validate the ELISA technique used to quantify NFL protein release in the culture media of MN spheroids. **B.** As expected, sporadic ALS donors displayed a trend toward higher levels of NFL protein in plasma than control donors. Data shown as mean ± SD, N=2, n=2. Significance was determined using a t-student.

Chapter 3 – Generation and characterization of 3D skeletal muscle structures for co-culture with iPSC-derived MN spheroids within a microfluidic device to establish an *in vitro* 3D NMJ, along with the development of high-content-compatible tools for analysis

In Chapter 1, we described the development of 3D iPSC-derived MN spheroids, and in Chapter 2, we demonstrated their advantages for modeling NMDs. In this chapter, we present a manuscript in progress where we describe the generation of skeletal muscle micro-tissues and their co-culture with iPSC-derived MN spheroids to form an *in vitro* 3D NMJ model, along with high-content compatible tools for analysis.

Following a similar approach to that used for the generating iPSC-derived MN spheroids, we optimized a protocol originally designed to obtain 2D iPSC-derived myotubes (125) for producing iPSC-derived skeletal muscle micro-tissues using the AIW002-02 line. Moreover, we developed two image-based tools that assess changes in intracellular calcium and cell contractility as indicators of muscle function. Future applications of these tools will focus on assessing muscle function in a disease context, either independently, stimulated by a pulse generator, or in coculture, triggered by MN activation. To demonstrate a broader applicability of these tools, we also tested them on human primary skeletal muscle micro-tissues differentiated using a different protocol.

The co-culture of skeletal muscle micro-tissues with iPSC-derived MNs was performed in a customized microfluidic device, which, in conjunction with the 3D environment, enhances the

physiological relevance of the model by replicating the spatial gap between the MN soma and skeletal muscle. Our results showed that after 14 days of co-culture, iPSC-derived MN spheroids and skeletal muscle micro-tissues successfully formed 3D NMJs, where we observed colocalization of presynaptic MN terminals with AChRs on the muscle membrane after developing a pipeline to analyze 3D-reconstructed images.

Altogether, our co-culture system and the tools developed to analyze it were designed to be scalable and compatible with high-content approaches, with the aim of enabling their future use in preclinical research.

Development of image-based analysis tools to assess *in vitro* 3D neuromuscular junction (NMJ) morphology and function in a compartmentalized microfluidic device

María José Castellanos-Montiel¹, Anna Kristyna Franco-Flores¹, Mark Aurousseau², Mathilde Chaineau¹, Ghazal Haghi¹, Sarah Lépine^{1,3}, Carol X.-Q. Chen¹, Taylor M. Goldsmith¹, Narges Abdian¹, Wolfgang Reintsch¹, Andrea Krahn¹, Thomas M. Durcan^{1*}.

Author's affiliations:

¹ Early Drug Discovery Unit (EDDU), The Neuro-Montreal Neurological Hospital and Institute, McGill University, Montreal, Quebec, Canada

² eNUVIO Inc., Montreal, QC, Canada

³ Faculty of Medicine and Health Sciences, McGill University, Montreal, Quebec, Canada

* Correspondance: thomas.durcan@mcgill.ca

Abstract

Compared with animal systems, direct access to the human neuromuscular junction (NMJ) with the aim of studying disease is not possible given ethical constraints. To address the lack of information related to the human NMJ, various groups have developed experimental culture systems to study the human NMJ *in vitro*. Among these, 3D cell culture models that incorporate microfluidic devices are employed to recreate some key physiological aspects of the NMJ by promoting cell-cell and cell-matrix interactions and by replicating the physical gap between the MN soma and skeletal muscle. Despite the success, a limitation to the implementation of human *in vitro* 3D NMJ models in non-clinical research is the scalability of the models and the

development of analysis tools suitable for high-content approaches. Here, we describe the

development of a transgene-free human 3D NMJ model using a compartmentalization device. This

culture device accommodates the unitary dimensions required for scaling into a 96-well microplate

for future higher throughput applications. Additionally, as most contemporary high-content

approaches rely on image analysis, we describe the development of image-based tools to analyze

various aspects of the NMJ components.

Keywords

iPSCs; motor neuron; spheroids; skeletal muscle; micro-tissue; NMJ.

176

1. Introduction

The neuromuscular junction (NMJ) is a highly organized and specialized synapse located in the peripheral nervous system that mediates the communication between motor neurons (MNs) and myofibers to initiate and maintain skeletal muscle contraction (1). A group of conditions known as neuromuscular disorders (NMDs) disrupt this communication by selectively inducing deleterious effects on MNs, motor endplates, and/or myofibers (2). To elucidate the mechanisms underlying the onset and progression of NMDs, and to develop systems that can be used in non-clinical research for drug discovery and development, research groups have sought to recreate physiologically-relevant models of the human NMJ *in vitro*.

The development of these *in vitro* models heavily relies on the use of human induced pluripotent stem cells (iPSCs), which can be differentiated into any cell type of the human body, enabling the production of unlimited supplies of MNs and muscle cells (3, 4, 5, 6). Available models include transgene-based and transgene-free protocols to differentiate iPSCs, as well as both two-dimensional (2D) and three-dimensional (3D) approaches for culturing them (7). 2D approaches typically refer to growing cells in monolayers on the surface of a culture vessel, whereas 3D approaches generally incorporate extracellular matrices and a more complex culture setup. Regarding the presynaptic component of the NMJ, iPSC-derived MNs can be cultured as MN spheroids (or neurospheres) enriched in a single cell type (8, 9, 10, 11) or as organoids containing a broader variety of cells (12, 13, 14). Concerning the post-synaptic component of the NMJ, a 3D culture is achieved by culturing cells as muscle organoids (15), spheroids (12) or skeletal muscle micro-tissues, the latter relying on devices containing reference structures that mimic tendon function *in vivo* (8, 9, 10, 16, 17, 18).

Compared to monolayer cultures, 3D co-culture methods aim to mimic native cell-cell and cell-matrix interactions, which demonstrate several biological and technical advantages. For instance, muscle cells cultured using a 3D method are critical for the acetylcholine receptor (AChR) subunit switch, where the embryonic gamma subunit ($\alpha 2\beta \gamma \delta$) is replaced by the adult epsilon subunit ($\alpha 2\beta \epsilon \delta$) to form mature synapses (17). Also, the long-term culture of MNs and skeletal muscle has proven technically challenging in a 2D setting, compared to 3D. iPSC-derived MNs cultures in monolayers tend to cluster and then detach from the culture vessel over extended culture periods (19). Similarly, muscle cells, which expectedly become highly contractile, are prone to detachment as they undergo final differentiation (16, 17).

To further increase the physiological relevance of 3D approaches, several groups have incorporated compartmentalized microfluidic devices into their cultures to recapitulate the physical gap that exists between the MN soma located in the ventral horn of the spinal cord, and skeletal muscle located in the periphery (2, 8, 9, 20). Recapitulation of this aspect is crucial given that MNs are the largest cells in the nervous system and are more susceptible to stress compared to other neuronal cell types. Existing culture protocols depend on genetic engineering to introduce the channelrhodopsin (ChR) cassette, enabling light-dependent stimulation of MNs for downstream functional analysis of the resulting NMJ. Taking this approach is problematic from a scalability perspective, since performing the necessary genetic changes on several different cell lines is a laborious and time-consuming process. Additionally, harnessing optogenetic approaches also requires complex equipment for data acquisition, which is currently incompatible for high-throughput approaches. In this work, we use a transgene-free approach to differentiate iPSCs into both MNs and skeletal muscle, and used these to establish a human *in vitro* 3D NMJ within a compartmentalized microfluidic device. Furthermore, we developed various image-based tools

that can be adapted for high-content approaches to analyze different aspects of the NMJ components.

2. Materials and methods

iPSC culture

The noncarrier AIW002-02 iPSC line, reprogrammed from a 37-year-old Caucasian male as previously described (21) was used for this study. Briefly, AIW002-02 iPSCs were maintained on 100 mm dishes (#353003, Corning) coated with Matrigel (#354277, Corning) in mTeSR1TM medium (#85850, STEMCELL Technologies) and passaged at 80% confluence using Gentle Cell Dissociation Reagent (#100-0485, STEMCELL Technologies). Prior to starting the experiments, iPSCs were tested weekly and found to be free from mycoplasma (#LT07-318, Lonza). The use of iPSCs in this research was approved by the McGill Research Ethics Board (IRB Study Number A03-M19-22A).

RT-qPCR

For each condition, a ~1M cells or a single skeletal muscle micro-tissue were pellet in a 1.7 mL collection (#87003-294, VWR) tube and total RNA was isolated using the miRNeasy Micro Kit (#217084, Qiagen) according to manufacturer's instructions. Subsequently, reverse transcription reactions for cDNA synthesis, followed by qPCR reactions were performed as previously described (22). The mean between Act β and GAPDH was used as the endogenous control for normalization. A list of TaqMan probes used in this can be found in **Supplementary Table 1**. For analysis, the relative quantification (RQ) values (Δ CT and Δ Δ CT) were calculated according to the method outlined in (23).

Generation of iPSC-derived MN spheroids

AIW002-02 iPSCs were differentiated into motor neuron progenitor cells (MNPCs) following a small-molecule approach (22, 24, 25). Next, MNPCs were dissociated into a single-cell suspension using Accutase (#07922, Thermo Fisher Scientific) and plated into round-bottom ultra-low-attachment 96-well plates (#707, Corning) to promote their aggregation as 20K spheroids as previously described (22).

Generation of iPSC-derived iMyoblasts

AIW00-02 iPSCs were differentiated into iPSC-derived iMyoblasts following a published protocol (26). Briefly, AIW002-02 iPSCs at 60–80% confluence were dissociated using TrypLETM Express enzyme (#12604013, Thermo Fisher Scientific):0.5 mM EDTA (3:1), and plated on thin-collagen I-coated (#A1048301, Thermo Fisher Scientific) 6-well plates (#353046, Corning) at a density of 2,500 cells/cm² in Skeletal Muscle Induction Medium (#SKM-01, Genea Biocells). After 10 days in Skeletal Muscle Induction Medium (S1 stage), cells were dissociated using TrypLETM Express enzyme and plated on thin-collagen-coated 6-well plates at a density of 2,500 cells/cm² in Myoblast Medium (#SKM-02, Genea Biocells). After 8 days in Myoblast Medium (S2 stage), and after the cells were 100% confluent, Myoblast Medium was switched to Myotube Medium (#SKM-03, Genea Biocells). After 8 days in Myotube Medium (S3 stage), cells were dissociated using TrypLETM Express enzyme, and plated at a density of 150,000–200,000 cells onto 0.1% gelatin (#7903, STEMCELL Technologies)-coated 100 mm dishes in HMP medium containing Ham's F-10 medium (#11550043, Thermo Fisher Scientific), 20% fetal bovine serum (#12484-028, Thermo Fisher Scientific), 1.2 mM CaCl₂ (#233506, Sigma), 1X Antibiotic-

Antiycotic (#15240-062, Thermo Fisher Scientific), and 1% chick embryo extract (#092850145, MP Biomedicals).

After expansion, cells were split, counted and frozen at passage 4 in cryovials (#72.379, Sarstedt), each containing 150,000–200,000 cells in 1 mL of FBS:HMP (1:1) containing 10% DMSO (#BP231-1, Thermo Fisher Scientific).

Human primary myoblasts culture

Commercially available human primary skeletal myoblasts (#SKB-F, Zenbio) at passage 3 were thawed in a T-75 flask (#12-556-010, Thermo Fisher Scientific) in SKM-M medium (#SKM-M, Zenbio) according to manufacturer's instructions. To increase cell attachment, the flask was pre-coated with Matrigel for at least 2 h. Medium was changed every other day. Upon reaching 70–80 % confluence in approximately 6–7 days, cells were split using Trypsin/EDTA (#325-045-EL, Wisent Bioproducts) and expanded into ~ 4–5 Matrigel-coated T-75 flasks (~ 400,000 cells per flask).

After expansion, cells were split, counted and frozen at passage 5 into 10 to 15 cryovials, each containing ~500,000 cells in 1 mL of FBS containing 10% DMSO.

Generation of skeletal muscle micro-tissues

To generate skeletal muscle micro-tissues, a vial of SKB-F cells at passage 5 was thawed in a Matrigel-coated T-75 flask in SKM-M medium. Alternatively, a vial of AIW002-02 iMyoblasts

at passage 4 was thawed in a 0.1% gelatin-coated 100 mm dish. Both SKB-F primary myoblasts and AIW002-02 iMyoblasts were maintained in proliferation medium (SKM-M or HMP) until they reached 70-80% confluence. On Day -1, cells were split and counted. Between 250,000-300,000 cells per skeletal muscle micro-tissue were transferred to a 1.7 mL collection tube (#87003-294, VWR) and centrifuged at 300 g. The supernatant was discarded, and the cells were resuspended in 25 μ L of a 1:4 Matrigel-collagen hydrogel to make a final volume of ~ 30–35 μ L that were seeded in polydimethylsiloxane (PDMS) devices that enable the organization of myoblasts as 3D structures (#OMEGA-MP, eNUVIO Inc.). To prepare the 1:4 Matrigel-collagen hydrogel, 4.7 µl of 0.5 % phenol red solution (#P0290, Sigma-Aldrich) were mixed in 995.3 µL of 1X PBS (#311-010-CL, Wisent Bioproducts) to make a phenol red solution with a concentration of 24 µg/mL. In a different collection tube, 340 µL of the 24 µg/mL phenol red solution were mixed with 660 µL of 3 mg/mL collagen I, resulting in final concentrations of 8 µg/mL and 1.98 mg/mL, respectively. To neutralize the collagen, a few drops ($\sim 12-15 \mu L$) of a sterilized 0.5% NaOH (#SHY500, Bioshop) solution were added. Once the collagen solution turned pink, 400 μL were transferred in a different collection tube and 100 µL of Matrigel were added. The final concentration of collagen was ~ 1.5 mg/mL.

The myoblasts embedded in the hydrogel were maintained in 2 mL of proliferation medium to enable their rearrangement around the anchoring structures of the device. After 24 hours, cells were rinsed once with 1X PBS, and the medium was switched to differentiation medium. For SKB-F myoblasts, SKM-M medium was switched to SKM-D (#SKM-D, Zenbio). For AIW002-02 iMyoblasts, HMP medium was switched to prednisolone differentiation medium modified from (26, 27) containing: DMEM/F-12 (#10565042, Thermo Fisher Scientific), 1X N-2 supplement (#17502048, Thermo Fisher Scientific), 1X insulin-transferrin-selenium (#41400045, Thermo

Fisher Scientific), 1X L-glutamine (#35050061, Thermo Fisher Scientific), 1 μM CHIR-99021 (#S2924, Selleckchem), 10μM SB431542 (#S1067, Selleckchem), and 10μM prednisolone (#P6004, Sigma). Lists of the primary and secondary antibodies used for characterization of skeletal muscle micro-tissues are in **Supplementary Tables 2/3.**

Of note, to prevent the cells from attaching as a monolayer to the PDMS, the skeletal muscle micro-tissue chamber must be pre-coated with 40 μ l of a 5% solution of Pluronic F-127 (#P2443, Sigma-Aldrich) prepared in 1X PBS at 4°C overnight or at 37°C for 15–20 min. Before use, the Pluronic F-127 solution was sterile-filtered using a 0.2 μ m filter (#09-719C, Thermo Fisher Scientific).

Calcium imaging of skeletal muscle micro-tissues

Fluo-4 AM (#F14201, Thermo Fisher Scientific) was reconstituted in DMSO to prepare a 5 mM stock solution. Before dilution into the loading medium (NMJ medium), the 5 mM Fluo-4 AM stock solution was mixed with an equal volume of 20% (w/v) Pluronic F-127 in DMSO, resulting in a solution containing 2.5 mM Fluo-4 AM and 10% Pluronic F-127. After 21 days in culture, skeletal muscle micro-tissues were incubated in 50 μL of NMJ medium containing a final concentration of 5 μM Fluo-4 AM and 0.02% Pluronic F-127 for 1 h at 37°C. Excess dye was removed by rinsing with fresh NMJ medium. Subsequently, the tissues were switched to 50 μL of Live Cell Imaging Solution (#A59688DJ, Thermo Fisher Scientific), buffered with HEPES at pH 7.4, which maintains cell viability for up to 4 h at RT. Imaging was conducted on a Zeiss Axiovert 200M fluorescence microscope equipped with a 470 nm LED for excitation and a 535/25 nm emission filter. Images were acquired with a 10X/0.3 objective at a frame rate of 30 frames per

second (fps) for 90 s at RT (30 s pre-stimulus, 30 s stimulus, 30 s post-stimulus). Fluorescence intensity changes were analyzed using ImageJ (version 1.54f). Regions of interest (ROIs) were defined for 3–5 cells within each skeletal muscle micro-tissue, and fluorescence intensity for each ROI was normalized to baseline fluorescence ($\Delta F/F$) for each frame.

Fluorescent bead movement within skeletal muscle micro-tissues

Fluorescent beads (3 µm diameter, Phosphorex LLC) were added to the 1:4 hydrogel mix prior to embedding the myoblasts. As the myoblasts rearrange around the anchoring structures of the device, they pull the fluorescent beads, which remain evenly distributed throughout the 3D structure. Prior to recording, the tissues were transferred to 50 µL of Live Cell Imaging Solution. Imaging was conducted on a Zeiss Axiovert 200M fluorescence microscope equipped with a 567.5 nm LED for excitation and a 610/75 emission filter. Images were acquired with a 10X/0.3 objective at a frame rate of 30 fps for 90 s at RT (30 s pre-stimulus, 30 s stimulus, 30 s post-stimulus). For analysis, the TrackMate plugin in ImageJ (version 1.54f) was used to identify single fluorescent beads as ROIs and evaluate their displacement.

Electrical stimulation of skeletal muscle micro-tissues

Two platinum electrodes were placed on either side of a skeletal muscle micro-tissue, and a stimulator (#PulsePal v2, Sanworks) was used to electrically stimulate the tissue at different frequencies. A sub-tetanic response was induced with 1 Hz stimulation, while tetanic responses were elucidated >20 Hz stimulation.

Microfluidic devices for NMJ^{3D} co-culture

The customized microfluidic devices developed for this study are made of PDMS and were manufactured and supplied by eNUVIO Inc. using a proprietary manufacturing process. The device consists of two adjacent chambers, each designed to harbor a MN spheroid or skeletal muscle micro-tissue, which are interconnected by a 180 µm wide by 750 µm long microchannel that permits the passage of axons (**Supplementary Figure 1**).

Co-culture of iPSC-derived MNs and skeletal muscle in 3D

After 7 days in culture, a single MN spheroid was transferred into the MN spheroid chamber while keeping the dish angled at 45° to direct the placement of the MN spheroid closest to the microchannel entrance (Day -7). A drop of Matrigel ($\sim 5~\mu L$) was added on top of the MN spheroid to seal it in place. After 5 min inside the incubator, a second drop of Matrigel ($\sim 5~\mu L$) was dropped on the other side of the microchannel to prevent myoblasts from invading the microchannel during their seeding. After 5 min inside the incubator, the MN spheroid chamber was filled with 150 μL of MN induction and maturation medium. The empty skeletal muscle micro-tissue chamber was filled with NMJ medium. For SKB-F myoblasts, NMJ medium consisted of MN induction and maturation medium:SKM-D (3:1). For AIW002-02 iMyoblasts, NMJ medium consisted in MN induction and maturation medium supplemented with 1X N-2 supplement, 1X insulin-transferrin-selenium, 1X L-glutamine, 1 μ M CHIR-99021, 10μ M SB431542, and 10μ M prednisolone.

Seven days after the MN spheroid was plated in the device, the medium from the skeletal muscle micro-tissue chamber was removed, and the chamber was filled with 40 μ L of 5% solution

of Pluronic F-127 for 15 min at 37°C. Next, the chamber was rinsed once with 1X PBS, and the myoblasts embedded in the hydrogel were seeded avoiding the formation of bubbles. After 10 min inside the incubator, 150 μL of myoblast proliferation media were added to the chamber (Day 1). After 24 h, myoblasts were rinsed once with 1X PBS and 150 μL of NMJ medium were added to initiate myoblast differentiation (Day 1). A full-medium change with NMJ medium was performed on Days 2, 4, and 6 in the skeletal muscle micro-tissue chamber. From Day 8 onward, a half-medium change was conducted every other day. Regarding the MN spheroid chamber, a full-medium change of MN induction and maturation medium was performed once a week.

Immunostaining of 3D NMJs

Fixation and immunocytochemistry were performed inside the microfluidic devices. For fixation, 150 μL of 4% formaldehyde (FA; # 28908, Thermo Fisher Scientific) in 1X PBS were added to the MN spheroid chamber and the skeletal micro-tissue chamber. After 20 min incubation at room temperature (RT), 4% FA was removed followed by three 20 min washes of 150 μL 1X PBS. Next, the sample was blocked overnight at 4°C in a blocking solution containing 5% normal donkey serum (NDS; #S30 Normal donkey, Millipore), 0.6% bovine serum albumin (BSA; #800-095-CG, Wisent Bioproducts), and 0.2% Triton X-100 (#TRX506, Bioshop) in 1X PBS. After blocking, samples were incubated with primary antibodies diluted in blocking solution for 48 h at 4°C. A primary antibody co-staining of NFH (1:1000; #ab4680, Abcam) and SV2 (3 μg/μL; DSHB) was applied to the 3D structures in both chambers, while the skeletal muscle micro-tissue was also incubated with MyHC (1:50; # 15-967, ProSci). Primary antibodies were washed out by performing three 20 min washes of 1X PBS. Then, samples were incubated with secondary

antibodies and Hoechst33342 diluted in blocking solution for 48 h at 4°C. NFH/SV2 co-staining was labeled with secondary antibodies against different species, both coupled to the same fluorophore (1:250; Chicken IgY-Alexa488, #703-545-155, Jackson Immunoresearch/Mouse IgG-Dylight 488, #ab96875, Abcam). In addition to secondary labeling (1:250; Rabbit IgG-Dylight 550, #ab96892, Abcam) of MyHC in skeletal muscle micro-tissue, α -bungarotoxin conjugated to Alexa Fluor 647 (1:50; #B35450, Thermo Fisher Scientific) was also applied to visualize AChRs. Finally, secondary antibodies and Hoechst33342 were washed out by performing three 20 min washes of 1X PBS. Samples were left on 1X PBS for imaging. Images were acquired with the Opera Phenix High-Content Screening System using the 20X/0.4 objective. Image size 5400 × 2160 × 70. Voxel size 0.29 μ m × 0.29 μ m × 5 μ m.

Morphological analysis of 3D NMJs

To analyze the images, we use the IMARIS software (version 10.2.0). First, images were converted into IMARIS files with the IMARIS File Converter (version 10.2.0). Then, images were stitched using IMARIS Stitcher (version 10.2.0) with an overlap of 5%. Finally, we developed a pipeline to analyze the 3D-reconstructed images. Briefly, NFH/SV2C co-staining was primarily filtered by an intensity threshold, while α -BTX staining was filtered by both intensity and size thresholds. To minimize the selection of background signals, each IMARIS module includes an AI training step to further refine and filter the staining. Using the objects-to-objects statistics feature, IMARIS calculates the shortest distance from each α -BTX cluster to an MN presynaptic terminal. The data was exported as a .xls file and plotted as a frequency histogram for analysis.

3. Results

Human primary myoblasts and iPSC-derived myoblasts form 3D skeletal muscle microtissues

To ensure the reproducibility of our protocol to generate 3D skeletal muscle micro-tissues, two sources of healthy control human myoblasts were used to generate skeletal muscle micro-tissues: primary myoblasts (SKB-F line) and iPSC-derived myoblasts (AIW002-02 iPSC line). Desmin⁺ SKB-F myoblasts (**Supplementary Figure 2A-C**) were used between passages 6–8 to generate skeletal muscle micro-tissues. RT-qPCR analyses showed that the myogenic regulatory factors *MYOD1* and *MYOG*, which are associated with early myogenic stages, were expressed at similar levels up to passage 8. In turn, the muscle structural gene *MYHC*, characteristic of terminal differentiation, was significantly upregulated at passage 9 (**Supplementary Figure 2D**). Importantly, SKB-F myoblasts differentiated in 2D into MyHC-expressing myotubes with sarcomeres cannot remain in culture for more than 10 days, as they begin detaching from the culture surface (**Supplementary Figure 2E**).

Following their embedding in the hydrogel, SKB-F myoblasts successfully rearranged around the anchoring pillars within the devices (**Figure 1A**), forming skeletal muscle micro-tissues expressing *MYHC* and *ACTN2* at both the transcriptional (**Figure 1B**) and protein levels (**Figure 1C**).

Additionally, a protocol originally designed to produce 2D iPSC-derived myotubes (26) was successfully optimized to generate iPSC-derived skeletal muscle micro-tissues. Starting from the AIW002-02 iPSC line (28), we generated AIW002-02 iMyoblasts (**Figure 2A**) that expressed *PAX3* and *MYOD1*, myogenic regulatory factors crucial for initiating myogenesis (**Figure 2B**). As

reported by Guo et al., AIW002-02 iMyoblasts exposed to prednisolone differentiation medium fused to form multinucleated Desmin⁺ and MyHC⁺ iMyotubes (**Figure 2C/D**) with a fusion index of 20–40% (**Figure 2E**). Furthermore, after 10 days of differentiation, iMyotubes exhibited sarcomeres (**Figure 2C/D**), and upregulated genes associated with later stages of differentiation including *MYOD1*, *MYOG*, *MYHC* and *ACTN2* (**Figure 2B**). Finally, AIW002-02 iMyoblasts, embedded in hydrogel, demonstrated their ability to develop into Desmin⁺ and MyHC⁺ skeletal muscle micro-tissues, which remained in culture for more than 10 days (**Figure 2F**).

In contrast to their 2D counterparts, which begin detaching around 10 days in culture, both primary and iPSC-derived skeletal muscle micro-tissues can remain in culture for extended periods exceeding 21 days while maintaining the expression of structural muscle markers.

Skeletal muscle micro-tissues exhibit subtetanic and tetanic calcium wave responses

To evaluate the functionality of our skeletal muscle micro-tissues, we optimized a tool to monitor changes in calcium activity. For this, primary and iPSC-derived skeletal muscle micro-tissues were loaded with the calcium dye reporter Fluo-4 AM and stimulated with electrical pulses at varying frequencies (Figure 3A). In skeletal muscle, low-frequency stimulation elicits individual twitches (subtetanic) that do not fuse into a fully sustained contraction (tetanic), which occurs with high-frequency stimulation (26). Consistently, stimulation of iPSC-derived skeletal muscle micro-tissues (Figure 3B) at 1 Hz and 500 Hz, elicited subtetanic (Figure 3C) and tetanic (Figure 3D) activity, respectively. Similarly, stimulation of primary skeletal muscle micro-tissues (Supplementary Figure 3A) at 1 Hz and 20 Hz, elicited subtetanic (Supplementary Figure 3B) and tetanic (Supplementary Figure 3C) activity.

Altogether, an image-based method was successfully established to assess calcium activity. Furthermore, tissues exhibited sub-tetanic and tetanic activity, characteristic of skeletal muscle. These findings suggest that skeletal muscle micro-tissues are functional and that, in a co-culture setting, a stimulus initiated by MNs can elicit a muscle response.

Fluorescent bead displacement correlates with changes in frequency of stimulation in skeletal muscle micro-tissues

In skeletal muscle, changes in calcium flux are typically linked to cell contractility. Therefore, we optimized a tool to assess the contractility of our skeletal muscle micro-tissues. For this, we incorporated 3 μ m fluorescent beads into the seeding protocol that (**Figure 4A**) evenly incorporated into the skeletal muscle micro-tissue (**Figure 4B**). Stimulation of iPSC-derived skeletal muscle micro-tissues at a low-frequency (1 Hz) elicited a subtetanic response, with an average bead displacement of 2.28 μ m \pm 1.07 μ m (**Figure 4C**). In contrast, stimulation at a high frequency (500Hz) induced a tetanic response, with a larger average bead displacement of 41.18 μ m \pm 14 μ m (**Figure 4D**). Altogether, our results confirm the successful establishment of an image-based method to assess muscle contractility, which correlates with the intensity of the stimuli.

iPSC-derived MN spheroids form 3D NMJs when co-cultured with human skeletal muscle micro-tissues

The timeline for 3D NMJ generation was established to ensure the earliest possible entry of iPSC-derived MNs into co-culture (**Figure 5A**). Seven days in ultra-low-attachment 96-well

plates were sufficient for iPSC-derived MN spheroids to assemble and remain cohesive during their transfer to the microfluidic device (Day -7). After 24 hours, MN spheroids began sprouting the first axons toward the periphery (Day -6). After seven days, the axons of MN spheroids reached the entrance of the skeletal muscle micro-tissue chamber, at which point the skeletal muscle micro-tissue was plated (Day 0). After two weeks of co-culture (Day 14), the axons sprouting from the MN spheroids had grown ~ 1 mm and made contact with the skeletal muscle micro-tissues (**Figure** 5B).

To investigate the formation of 3D NMJs, we performed confocal imaging and analyzed the images using IMARIS, a 3D analysis software. To reduce image acquisition and analysis times, we limited imaging and analysis to the region of the skeletal muscle micro-tissue that first comes into contact with the presynaptic MN axons (**Figure 5C**). After stitching, we developed an IMARIS pipeline to assess the number of α -BTX clusters (indicating AChRs) in the skeletal muscle membrane that co-localize with MN presynaptic terminals (**Figure 5D**). The pipeline uses the 3D-reconstructed image to define NFH/SV2-positive staining (Object 1) as well as α -BTX-positive staining (Object 2) (**Figure 5E**). Once the positive staining for all channels is defined, the two objects are superimposed, and object-to-object statistics are performed by the software (**Figure 5F**). Finally, a frequency histogram can be used to display the shortest distance to a presynaptic terminal for all α -BTX clusters within the analyzed volume (**Figure 5G**). Although present in reduced proportions, extrasynaptic AChRs are also found in skeletal muscle. Therefore, it is not surprising to find AChRs located far from the presynaptic terminals; nevertheless, the majority are located near them.

4. Discussion

In this study, we generated 3D skeletal micro-tissues from two human myoblast sources: primary and iPSC-derived myoblasts. Primary myoblasts were obtained from a commercial source and can be rapidly differentiated into skeletal muscle micro-tissues; however, despite achieving high fusion indices and rapid maturation, their limited self-renewal capacity restricts the production of skeletal muscle micro-tissues. In contrast, iPSC-derived myoblasts offer an unlimited source of stem cells to generate skeletal muscle micro-tissues, a critical factor for scalability and automation purposes. We reproduced a published protocol to obtain iPSC-derived iMyoblasts (26) from the AIW002-02 control line. These AIW002-02 iMyoblasts were a stably committed, expandable population of MYOD1+/PAX3+ stem cells that differentiated into multinucleated Desmin⁺ and MyHC⁺ iMyotubes with an average fusion index of ~22% under 2D conditions, approximately 14% higher than other reported protocols (26, 30, 31). Currently, only transgene-free protocols including a FACS purification step achieve high fusion indices (>80%), comparable to those of primary skeletal muscle micro-tissues (32, 33). However, FACS sorting is a complex technique that poses challenges for scalability. Advancing our understanding of myogenesis is essential for research groups to accurately replicate the factors driving skeletal muscle maturity and to facilitate the exclusive use of small molecules, which are more suitable for large-scale studies.

After optimizing the protocols for generating skeletal muscle micro-tissues, we developed two image-based techniques capable of reporting changes in intracellular calcium and the contractile capability of skeletal muscle micro-tissues. Importantly, these techniques are well-suited for high-content imaging systems, as they rely exclusively on the acquisition of time-lapse confocal fluorescent images. To measure intracellular calcium flux, we used a calcium indicator

dye Fluo-4 AM, which has been previously tested in 3D bioprinted skeletal muscle constructs exposed to ACh (34). Both primary and iPSC-derived skeletal muscle micro-tissues loaded with Fluo-4 AM responded to low and high-frequency stimuli, confirming the broad applicability of this assay. Alternatively, other groups have transduced myoblasts with a lentiviral vector encoding the fluorescent calcium indicator GCaMP6, driven by the muscle specific gene MHCK7, to assess calcium flux in skeletal muscle micro-tissues (17, 35, 36). However, such approaches present challenges for large-scale applications due to concerns related to viral yield, viral purification, cytotoxicity, and safety regulations.

To measure myotube contractile capacity, previous studies relied on the manual establishment of ROIs followed by the measurement of maximum movement distance (17), the quantification of pillar displacement (20, 35), or the manual attachment of the micro-tissue to a force transducer (36, 37). While these methods effectively assess absolute contraction force, they are challenging to scale, and their manual interventions may introduce observer biases. Here, we optimized the seeding protocol to incorporate fluorescent beads into skeletal muscle micro-tissues and use bead displacement as an indication of muscle contraction. To our knowledge, fluorescent bead displacement has never been implemented to assess 3D NMJs *in vitro*. Altogether, our results show that fluorescent bead movement can serve as an indirect measure of muscle force, as it positively correlates with changes in the frequency of stimulation.

Finally, we developed a timeline to co-culture human skeletal micro-tissues with iPSC-derived MN spheroids. This culture setting requires the independent generation of progenitors from both cell types prior to co-culture, unlike systems in which both cell types share the same progenitor and are differentiated simultaneously (13, 14). In the study of NMDs, this approach allows for the pairing of diseased MNs with healthy muscle, or vice versa, to investigate the

contribution of each cell type to disease progression. Additionally, using a microfluidic device to compartmentalize the MN soma enhances the physiological relevance of the model, as MNs are amongst the largest cells in the human body, with some reaching up to 1 m in length, making them more susceptible to certain stresses.

Our iPSC-derived MN spheroids successfully established contact with skeletal muscle micro-tissues to form NMJs, as confirmed by co-localization staining of NFH/SV2 with α-BTX. For the first time, we report the analysis of a human 3D NMJ *in vitro* as a fully reconstructed 3D structure, rather than analyzing it as independent 2D monolayers, which may lose valuable information. In the next phase of this research, we aim to further develop our transgene-free model by performing functional analyses of the NMJ, which will involve recording muscle responses to MN stimulation using our image-based tools.

A significant limitation in the development of 3D *in vitro* models is the availability of instruments and analysis software, which have largely designed for 2D models. While an increasing number of companies are working on systems for analyzing 3D cultures, these technologies remain in the early stages. The creation of straightforward, yet informative techniques and analysis pipelines will be crucial for advancing the translation of complex, physiologically relevant models into preclinical research.

Declarations

Ethics approval

The use of iPSCs in this research was approved by the McGill Research Ethics Board (IRB Study Number A03-M19-22A).

Consent for publication

Not applicable.

Availability of data and materials

All data generated or analyzed during this study are included in this published article.

Competing interests

The authors declare that they have no competing interests.

Funding

This study was supported Muscular Dystrophy Canada, the ALS Society of Canada, and the Quebec Consortium for Drug Discovery (CQDM) for project funding support.

Author's contributions

MJC-M contributed to the conceptualization, study design, data collection, result analysis, funding acquisition, and the writing, review, and editing of the manuscript. AKF-F collected a substantial portion of the data. MA contributed to the study design, result analysis and the review and editing of the manuscript. MC contributed to study design, and the review and editing of the manuscript. GH and SL generated and characterized AIW002-02 iPSC-derived MNPCs. CX-QC, TG, and NA performed quality control analyses for the AIW002-02 iPSC line. WR and AK contributed to image acquisition. TMD contributed to the study design, funding acquisition, and the reviewing and editing of the manuscript.

References

1. Sanes JR, Lichtman JW. Development of the vertebrate neuromuscular junction. *Annu Rev Neurosci.* **1999**;22:389-442.

- 2. Castellanos-Montiel MJ, Velasco I, Escobedo-Avila I. Modeling the neuromuscular junction in vitro: an approach to study neuromuscular junction disorders. *Ann N Y Acad Sci.* **2021**;1488(1):3-15.
- 3. Maury Y, Côme J, Piskorowski RA, Salah-Mohellibi N, Chevaleyre V, Peschanski M, Martinat C, Nedelec S. Combinatorial analysis of developmental cues efficiently converts human pluripotent stem cells into multiple neuronal subtypes. *Nat Biotechnol.* **2015**;33(1):89-96.
- 4. Du ZW, Chen H, Liu H, Lu J, Qian K, Huang CL, Zhong X, Fan F, Zhang SC. Generation and expansion of highly pure motor neuron progenitors from human pluripotent stem cells. *Nat Commun.* **2015**;6:6626.
- 5. Chal J, Al Tanoury Z, Hestin M, Gobert B, Aivio S, Hick A, Cherrier T, Nesmith AP, Parker KK, Pourquié O. Generation of human muscle fibers and satellite-like cells from human pluripotent stem cells in vitro. *Nat Protoc.* **2016**;11(10):1833-50.
- 6. Shelton M, Kocharyan A, Liu J, Skerjanc IS, Stanford WL. Robust generation and expansion of skeletal muscle progenitors and myocytes from human pluripotent stem cells. *Methods.* **2016**;101:73-84.
- 7. Kim H, Kim GS, Hyun SH, Kim E. Advancements in 2D and 3D In Vitro Models for Studying Neuromuscular Diseases. *Int J Mol Sci.* **2023**;24(23).
- 8. Osaki T, Uzel SGM, Kamm RD. On-chip 3D neuromuscular model for drug screening and precision medicine in neuromuscular disease. *Nat Protoc.* **2020**;15(2):421-49.
- 9. Osaki T, Uzel SGM, Kamm RD. Microphysiological 3D model of amyotrophic lateral sclerosis (ALS) from human iPS-derived muscle cells and optogenetic motor neurons. *Sci Adv.* **2018**;4(10):eaat5847.
- 10. Vila OF, Uzel SGM, Ma SP, Williams D, Pak J, Kamm RD, Vunjak-Novakovic G. Quantification of human neuromuscular function through optogenetics. *Theranostics*. **2019**;9(5):1232-46.
- 11. Demestre M, Orth M, Föhr KJ, Achberger K, Ludolph AC, Liebau S, Boeckers TM. Formation and characterisation of neuromuscular junctions between hiPSC derived motoneurons and myotubes. *Stem Cell Res.* **2015**;15(2):328-36.
- 12. Andersen J, Revah O, Miura Y, Thom N, Amin ND, Kelley KW, Singh M, Chen X, Thete MV, Walczak EM, Vogel H, Fan HC, Paşca SP. Generation of functional human 3D cortico-motor assembloids. *Cell.* **2020**;183(7):1913-29.e26.
- 13. Faustino Martins JM, Fischer C, Urzi A, Vidal R, Kunz S, Ruffault PL, Kabuss L, Hube I, Gazzerro E, Birchmeier C, Spuler S, Sauer S, Gouti M. Self-organizing 3D human trunk neuromuscular organoids. *Cell Stem Cell*. **2020**;26(2):172-86.e6.
- 14. Urzi A, Lahmann I, Nguyen LVN, Rost BR, García-Pérez A, Lelievre N, Merritt-Garza ME, Phan HC, Bassell GJ, Rossoll W, Diecke S, Kunz S, Schmitz D, Gouti M. Efficient generation of a self-organizing neuromuscular junction model from human pluripotent stem cells. *Nat Commun.* **2023**;14(1):8043.
- 15. Mavrommatis L, Jeong HW, Kindler U, Gomez-Giro G, Kienitz MC, Stehling M, Psathaki OE, Zeuschner D, Bixel MG, Han D, Morosan-Puopolo G, Gerovska D, Yang JH, Kim JB, Arauzo-Bravo MJ, Schwamborn JC, Hahn SA, Adams RH, Schöler HR, Vorgerd M, Brand-Saberi B, Zaehres H. Human skeletal muscle organoids model fetal myogenesis and sustain uncommitted PAX7 myogenic progenitors. *Elife.* **2023**;12.
- 16. Rao L, Qian Y, Khodabukus A, Ribar T, Bursac N. Engineering human pluripotent stem cells into a functional skeletal muscle tissue. *Nat Commun.* **2018**;9(1):126.

- 17. Afshar Bakooshli M, Lippmann ES, Mulcahy B, Iyer N, Nguyen CT, Tung K, Stewart BA, van den Dorpel H, Fuehrmann T, Shoichet M, Bigot A, Pegoraro E, Ahn H, Ginsberg H, Zhen M, Ashton RS, Gilbert PM. A 3D culture model of innervated human skeletal muscle enables studies of the adult neuromuscular junction. *Elife*. **2019**;8.
- 18. Urciuolo A, Serena E, Ghua R, Zatti S, Giomo M, Mattei N, Vetralla M, Selmin G, Luni C, Vitulo N, Valle G, Vitiello L, Elvassore N. Engineering a 3D in vitro model of human skeletal muscle at the single fiber scale. *PLoS One.* **2020**;15(5):e0232081.
- 19. Thiry L, Clément JP, Haag R, Kennedy TE, Stifani S. Optimization of long-term human iPSC-derived spinal motor neuron culture using a dendritic polyglycerol amine-based substrate. *ASN Neuro*. **2022**;14:17590914211073381.
- 20. Yamamoto K, Yamaoka N, Imaizumi Y, Nagashima T, Furutani T, Ito T, Okada Y, Honda H, Shimizu K. Development of a human neuromuscular tissue-on-a-chip model on a 24-well-plate-format compartmentalized microfluidic device. *Lab Chip.* **2021**;21(10):1897-907.
- 21. Chen C, Abdian N, Maussion G, Thomas RA, Demirova I, Cai E, Tabatabaei M, K. BL, Karamchandani J, A. FE, M. DT. Standardized quality control workflow to evaluate the reproducibility and differentiation potential of human iPSCs into neurons. *bioRxiv*. **2021**.
- 22. Castellanos-Montiel MJ, Chaineau M, Franco-Flores AK, Haghi G, Carrillo-Valenzuela D, Reintsch WE, Chen CX-Q, Durcan TM. An optimized workflow to generate and characterize iPSC-derived motor neuron (MN) spheroids. *Cells*. **2023**;12, 545.
- 23. Maussion G, Thomas RA, Demirova I, Gu G, Cai E, Chen CX, Abdian N, Strauss TJP, Kelaï S, Nauleau-Javaudin A, Beitel LK, Ramoz N, Gorwood P, Durcan TM. Auto-qPCR; a python-based web app for automated and reproducible analysis of qPCR data. *Sci Rep.* **2021**;11(1):21293.
- 24. Deneault E, Chaineau M, Nicouleau M, Castellanos Montiel MJ, Franco Flores AK, Haghi G, Chen CX, Abdian N, Shlaifer I, Beitel LK, Durcan TM. A streamlined CRISPR workflow to introduce mutations and generate isogenic iPSCs for modeling amyotrophic lateral sclerosis. *Methods.* **2022**;203:297-310.
- 25. Lépine S, Nauleau-Javaudin A, Deneault E, Chen CX, Abdian N, Franco-Flores AK, Haghi G, Castellanos-Montiel MJ, Maussion G, Chaineau M, Durcan TM. Homozygous ALS-linked mutations in TARDBP/TDP-43 lead to hypoactivity and synaptic abnormalities in human iPSC-derived motor neurons. *iScience*. **2024**;27(3):109166.
- 26. Guo D, Daman K, Chen JJ, Shi MJ, Yan J, Matijasevic Z, Rickard AM, Bennett MH, Kiselyov A, Zhou H, Bang AG, Wagner KR, Maehr R, King OD, Hayward LJ, Emerson CP, Jr. iMyoblasts for ex vivo and in vivo investigations of human myogenesis and disease modeling. *Elife*. **2022**;11.
- 27. Al Tanoury Z, Zimmerman JF, Rao J, Sieiro D, McNamara HM, Cherrier T, Rodríguez-delaRosa A, Hick-Colin A, Bousson F, Fugier-Schmucker C, Marchiano F, Habermann B, Chal J, Nesmith AP, Gapon S, Wagner E, Gupta VA, Bassel-Duby R, Olson EN, Cohen AE, Parker KK, Pourquié O. Prednisolone rescues Duchenne muscular dystrophy phenotypes in human pluripotent stem cell-derived skeletal muscle in vitro. *Proc Natl Acad Sci U S A.* **2021**;118(28).
- 28. Chen CX, Abdian N, Maussion G, Thomas RA, Demirova I, Cai E, Tabatabaei M, Beitel LK, Karamchandani J, Fon EA, Durcan TM. A Multistep Workflow to Evaluate Newly Generated iPSCs and Their Ability to Generate Different Cell Types. *Methods Protoc.* **2021**;4(3).
- 29. Olesen JH, Herskind J, Pedersen KK, Overgaard K. Potassium-induced potentiation of subtetanic force in rat skeletal muscles: influences of $\beta(2)$ -activation, lactic acid, and temperature. *Am J Physiol Cell Physiol.* **2021**;321(5):C884-c96.

- 30. Caron L, Kher D, Lee KL, McKernan R, Dumevska B, Hidalgo A, Li J, Yang H, Main H, Ferri G, Petek LM, Poellinger L, Miller DG, Gabellini D, Schmidt U. A Human Pluripotent Stem Cell Model of Facioscapulohumeral Muscular Dystrophy-Affected Skeletal Muscles. *Stem Cells Transl Med.* **2016**;5(9):1145-61.
- 31. Choi IY, Lim H, Estrellas K, Mula J, Cohen TV, Zhang Y, Donnelly CJ, Richard JP, Kim YJ, Kim H, Kazuki Y, Oshimura M, Li HL, Hotta A, Rothstein J, Maragakis N, Wagner KR, Lee G. Concordant but Varied Phenotypes among Duchenne Muscular Dystrophy Patient-Specific Myoblasts Derived using a Human iPSC-Based Model. *Cell Rep.* **2016**;15(10):2301-12.
- 32. Borchin B, Chen J, Barberi T. Derivation and FACS-mediated purification of PAX3+/PAX7+ skeletal muscle precursors from human pluripotent stem cells. *Stem Cell Reports*. **2013**;1(6):620-31.
- 33. van der Wal E, Iuliano A, In 't Groen SLM, Bholasing AP, Priesmann D, Sharma P, den Hamer B, Saggiomo V, Krüger M, Pijnappel W, de Greef JC. Highly contractile 3D tissue engineered skeletal muscles from human iPSCs reveal similarities with primary myoblast-derived tissues. *Stem Cell Reports.* **2023**;18(10):1954-71.
- 34. Kim JH, Kim I, Seol YJ, Ko IK, Yoo JJ, Atala A, Lee SJ. Neural cell integration into 3D bioprinted skeletal muscle constructs accelerates restoration of muscle function. *Nat Commun.* **2020**;11(1):1025.
- 35. Afshar ME, Abraha HY, Bakooshli MA, Davoudi S, Thavandiran N, Tung K, Ahn H, Ginsberg HJ, Zandstra PW, Gilbert PM. A 96-well culture platform enables longitudinal analyses of engineered human skeletal muscle microtissue strength. *Sci Rep.* **2020**;10(1):6918.
- 36. Madden L, Juhas M, Kraus WE, Truskey GA, Bursac N. Bioengineered human myobundles mimic clinical responses of skeletal muscle to drugs. *Elife*. **2015**;4:e04885.
- 37. Davis BN, Santoso JW, Walker MJ, Cheng CS, Koves TR, Kraus WE, Truskey GA. Human, Tissue-Engineered, Skeletal Muscle Myobundles to Measure Oxygen Uptake and Assess Mitochondrial Toxicity. *Tissue Eng Part C Methods*. **2017**;23(4):189-99.

Figures

A.

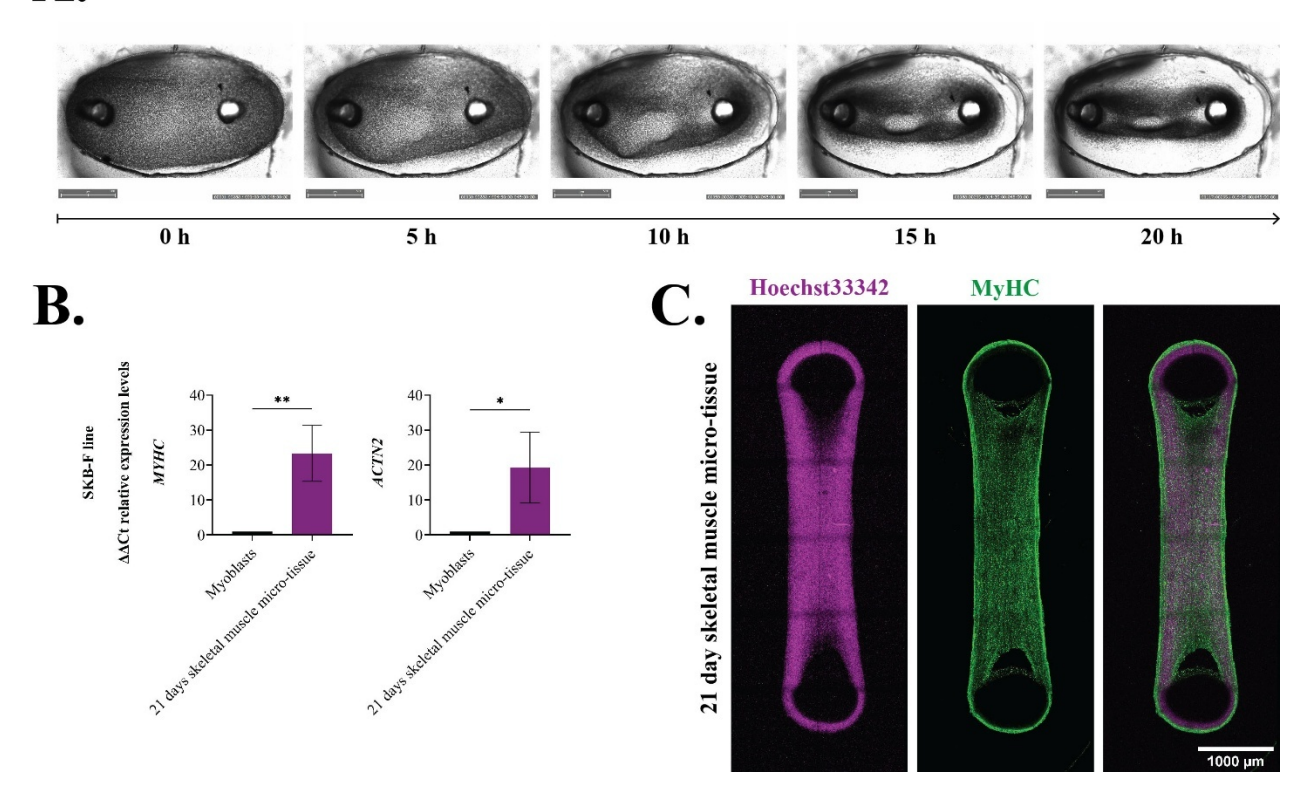


Figure 1. Generation of human primary skeletal muscle micro-tissues. A. Bright-field time-lapse showing the rearrangement of SKB-F myoblasts around the anchoring posts of the PDMS device. Scale bar, 500 μm. **B.** After 21 days in SKM-D medium, primary skeletal muscle micro-tissues expressed structural markers genes such as *MYHC* and *ACTN2*. Graph bars represent mean \pm SD; n=3. Significance was determined using Student's t-test. *, p ≤ 0.05; **, p ≤ 0.01. **C.** Similarly, MyHC is expressed by skeletal muscle micro-tissue at the protein level. Images represent the maximal projection of 20 optical slices acquired through confocal imaging. Scale bar, 1000 μm.

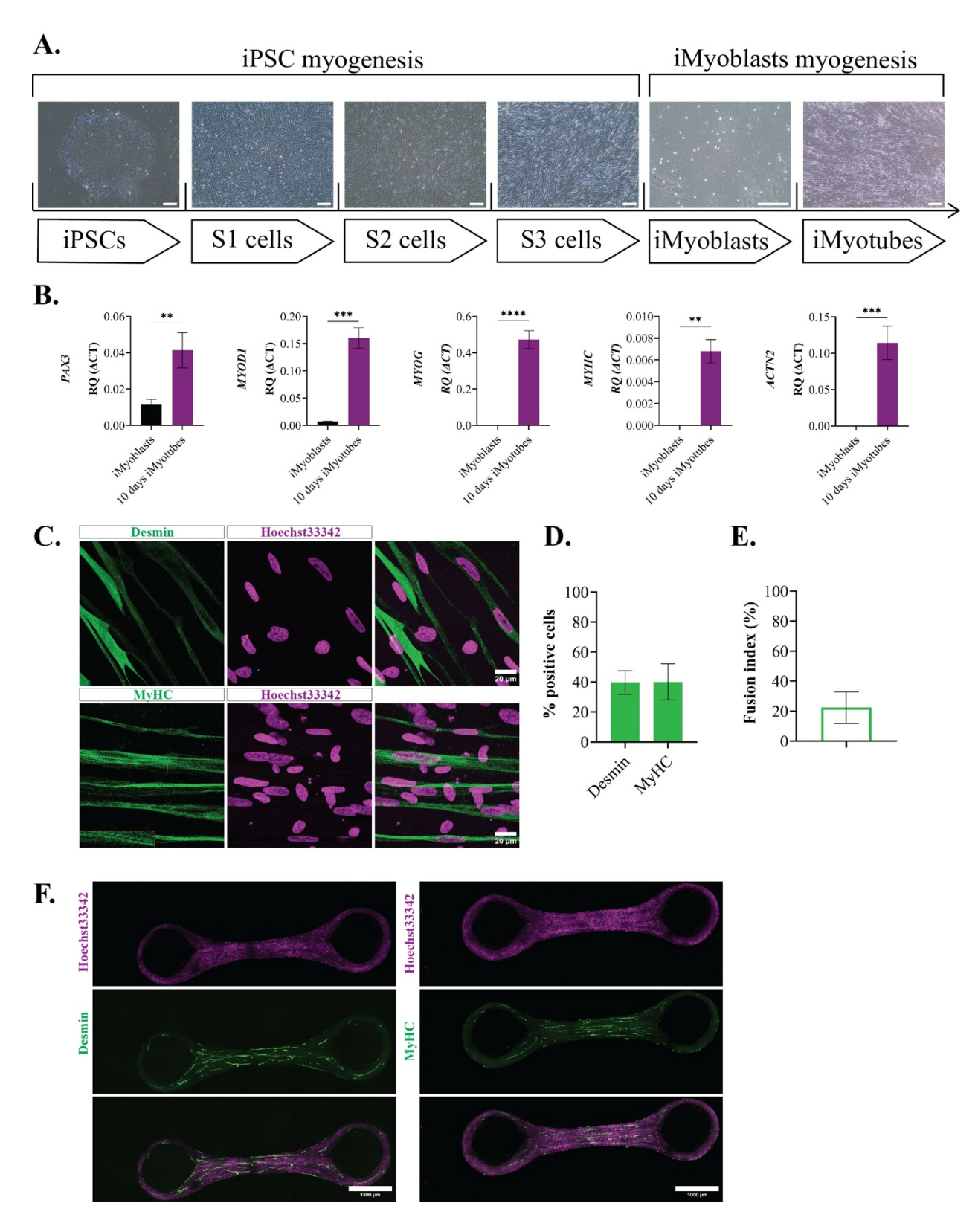


Figure 2. Generation of iPSC-derived skeletal muscle micro-tissues. A. Bright-field images illustrating the timeline for generating iPSC-derived AIW002-2 iMyoblasts and their subsequent

differentiation into iMyotubes. Scale bar, 100 μ m. **B.** RT-qPCR analysis showing the transcriptional expression of genes associated with different stages of myogenesis in AIW002-02 iMyoblasts and iMyotubes after 10 days of differentiation. Graph bars represent mean \pm SD; n=3. Significance was determined using Student's t-test. **, p \leq 0.01; ***, p \leq 0.001; ****, p \leq 0.0001. **C/D.** iPSC-derived AIW002-02 iMyoblasts differentiate into Desmin⁺/MyHC⁺ iMyotubes exhibiting sarcomeres. Scale bar, 20 μ m. Graph bars represent mean \pm SD; n=3. **E.** Quantification of the number of nuclei sharing plasma membrane (fusion index). **F.** iPSC-derived AIW002-02 iMyoblasts successfully differentiate into Desmin⁺ and MyHC⁺ skeletal muscle micro-tissues that remained in culture for over 10 days. Images represent the maximal intensity projection of 20 optical slices acquired through confocal imaging. Scale bar, 1000 μ m.

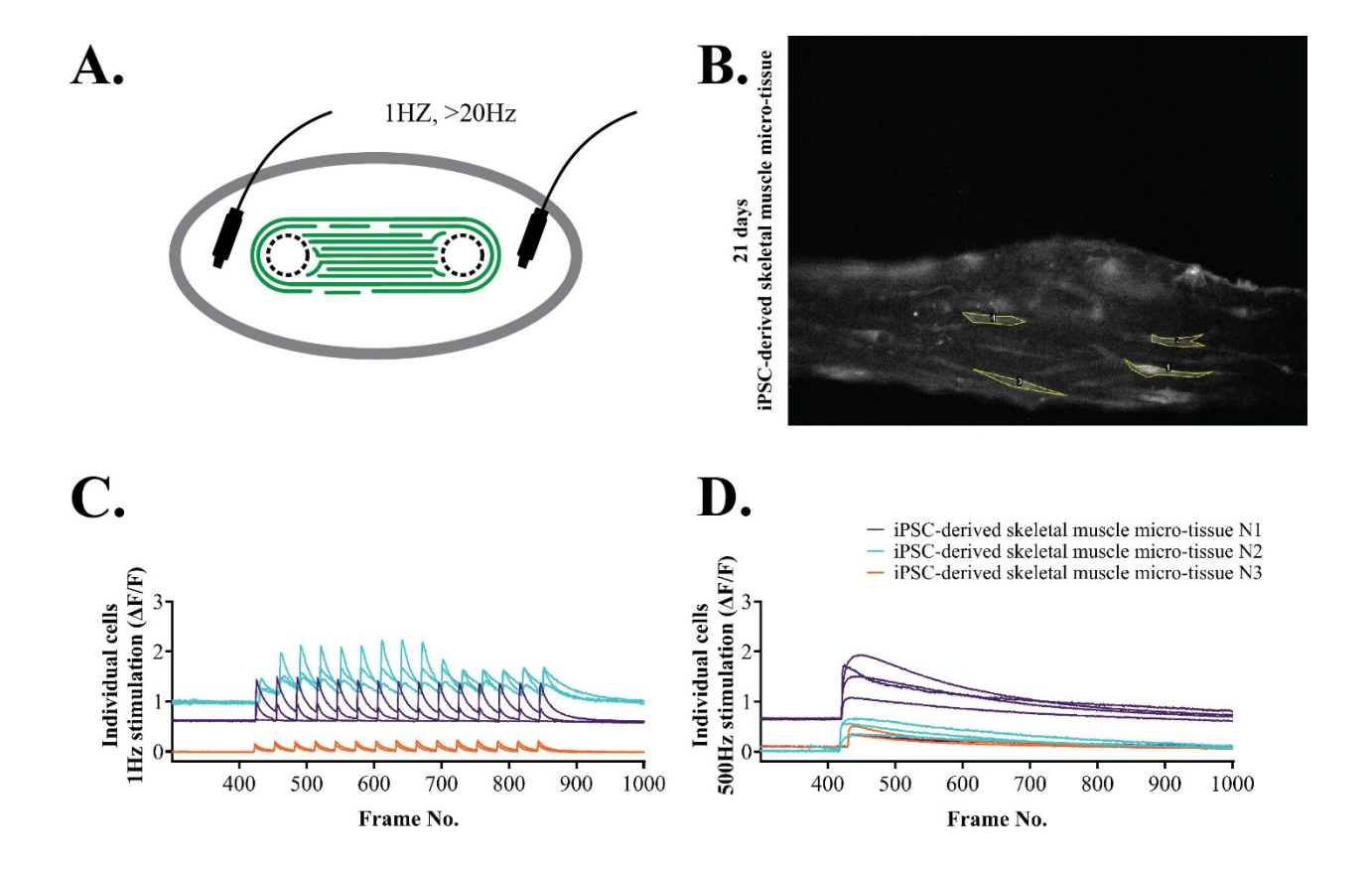


Figure 3. iPSC-derived skeletal muscle micro-tissues exhibited calcium waves associated with subtetanic and tetanic activity. A. Two electrodes were placed on either side of a skeletal muscle micro-tissue loaded with Fluo-4 AM. B. Epifluorescent image of an iPSC-derived skeletal muscle micro-tissue differentiated for 21 days and loaded with Fluo-4 AM, showing examples of myotubes selected as ROIs (yellow line) to measure changes in fluorescence intensity. C/D. Quantification of changes in fluorescence intensity following 1 Hz and 500 Hz stimulation of iPSC-derived skeletal muscle micro-tissues. Each line represents the response of an individual myotube within the tissue.

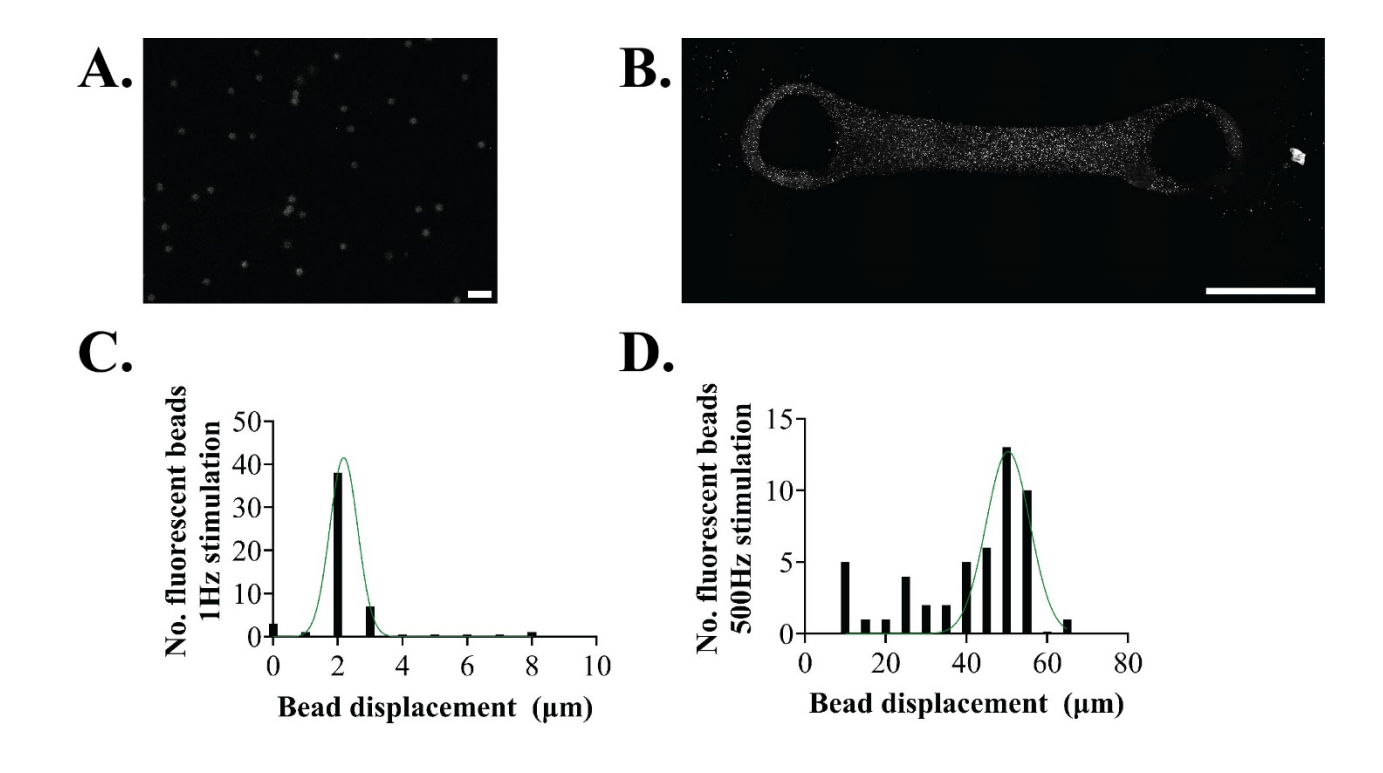


Figure 4. Fluorescent bead displacement correlates with stimulation frequency in iPSC-derived skeletal muscle micro-tissues. A. Representative epifluorescence image of 3 μm fluorescent beads. Scale bar, 10 μm. B. Fluorescent beads are incorporated and evenly distributed within iPSC-derived skeletal muscle micro-tissues. Image represents the maximal projection of 20 optical slices acquired through confocal imaging. Scale bar, 1000 μm. C. Frequency histogram of fluorescent bead displacement (μm) after 1 Hz stimulation, fitted with a Gaussian distribution. D. Frequency histogram of fluorescent bead displacement (μm) after 500 Hz stimulation, fitted with a Gaussian distribution.

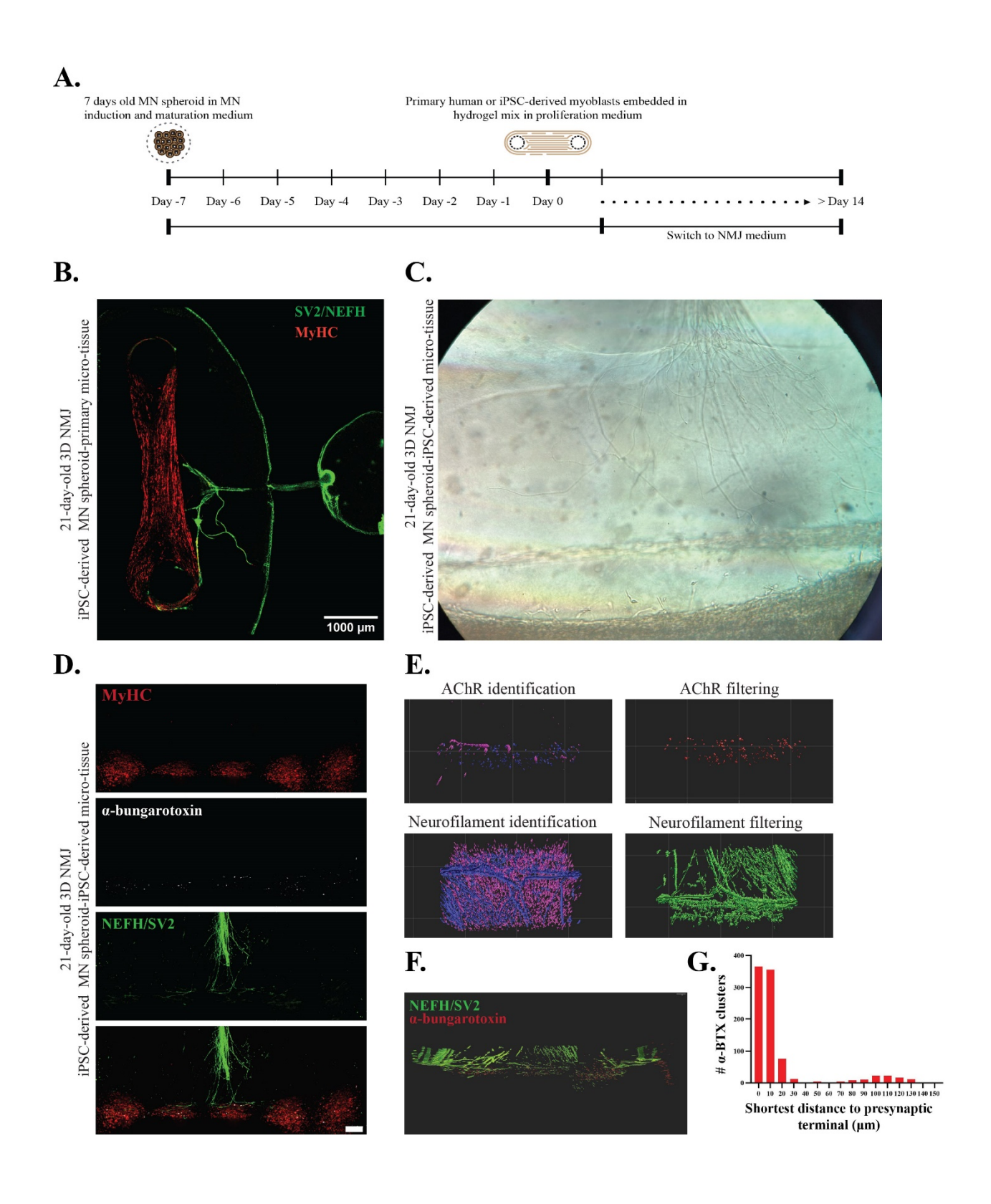


Figure 5. Co-localization of NFH/SV2 with α -BTX indicates 3D NMJ formation. A. Timeline for the establishment of a 3D NMJ in vitro. B. Representative stitched confocal image showing a

21-day-old co-culture of an AIW002-02 iPSC-derived MN spheroid and a primary skeletal muscle micro-tissue. Image represents the maximal projection of 20 optical slices acquired through confocal imaging. Scale bar, 1000 μ m. **C.** Representative bright-field image of the analysis area in a 21-day-old co-culture of an AIW002-02 iPSC-derived MN spheroid and an AIW002-02 iPSC-derived skeletal muscle micro-tissue. **D.** Representative stitched confocal image showing a 21-day-old co-culture stained with NFH/SV2 for presynaptic MN terminals, and MyHC and α -BTX for the skeletal muscle micro-tissue. Image represents the maximal projection of 20 optical slices acquired through confocal imaging. Scale bar, 100 μ m. **E.** A 3D analysis software was used to analyze the 3D-reconstructed image and define the positive staining for NFH/SV2 and α -BTX after the application of distinct filters. **F.** Representation of NFH/SV2-positive staining (Object 1) superimposed with α -BTX-positive staining (Object 2). **G.** Frequency histogram displaying the shortest distance from each α -BTX cluster to an axon.

Supplementary materials

Development of Image-Based Analysis Tools to Assess In Vitro 3D Neuromuscular Junction

morphology and function in a microfluidic device

María José Castellanos-Montiel, Anna Kristyna Franco-Flores, Mark Aurousseau, Mathilde

Chaineau, Ghazal Haghi, Sarah Lépine, Carol X.-Q. Chen, Taylor M. Goldsmith, Narges Abdian,

Wolfgang Reintsch, Andrea Krahn, Thomas M. Durcan.

Corresponding author e-mail: thomas.durcan@mcgill.ca (T.M.D)

207

Supplementary Table 1. qPCR Taqman probes

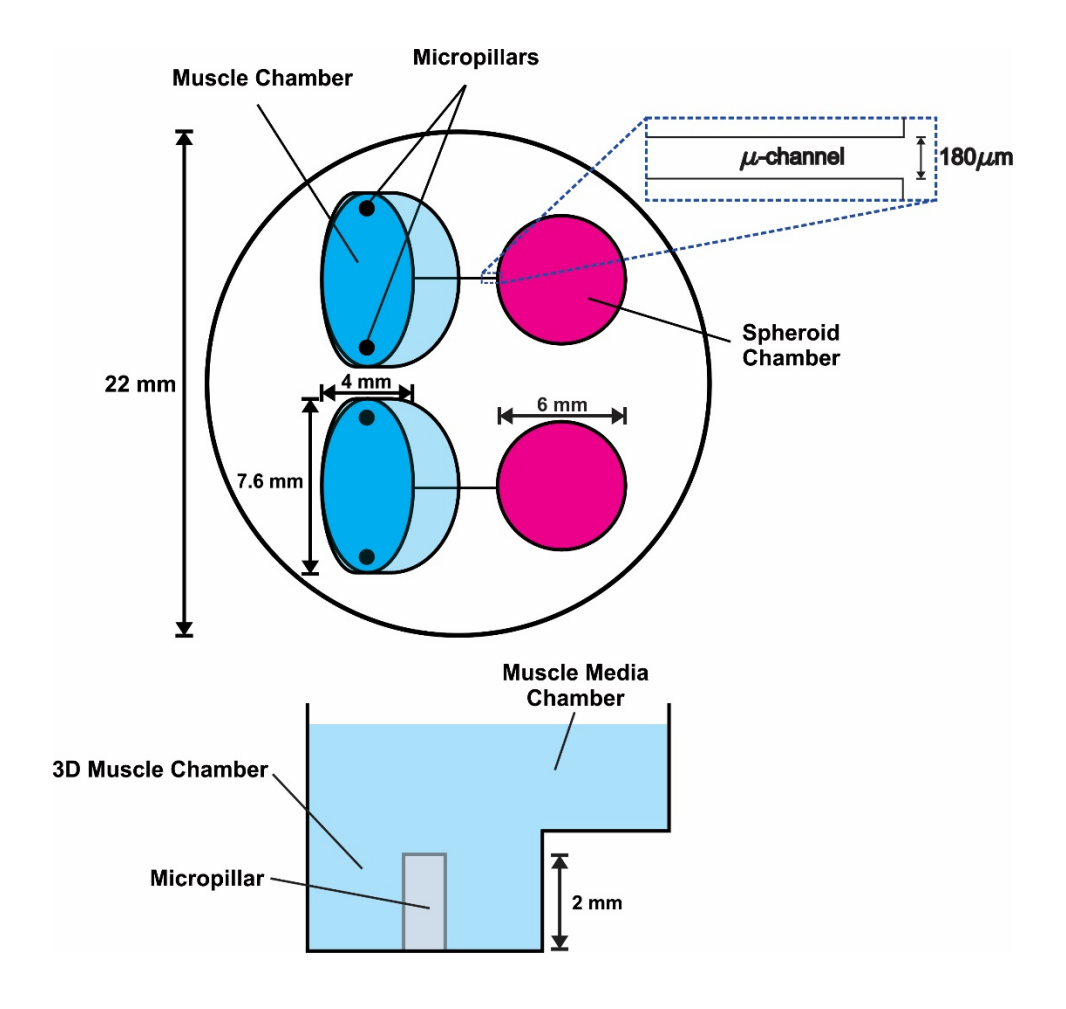
Gene	Reference
ACTN2	Hs00153809_m1
MYH2	Hs00430042_m1
MYOD1	Hs00159528_m1
MYOG	Hs01072232_m1
PAX3	Hs00240950_m1

Supplementary Table 2. Secondary antibodies

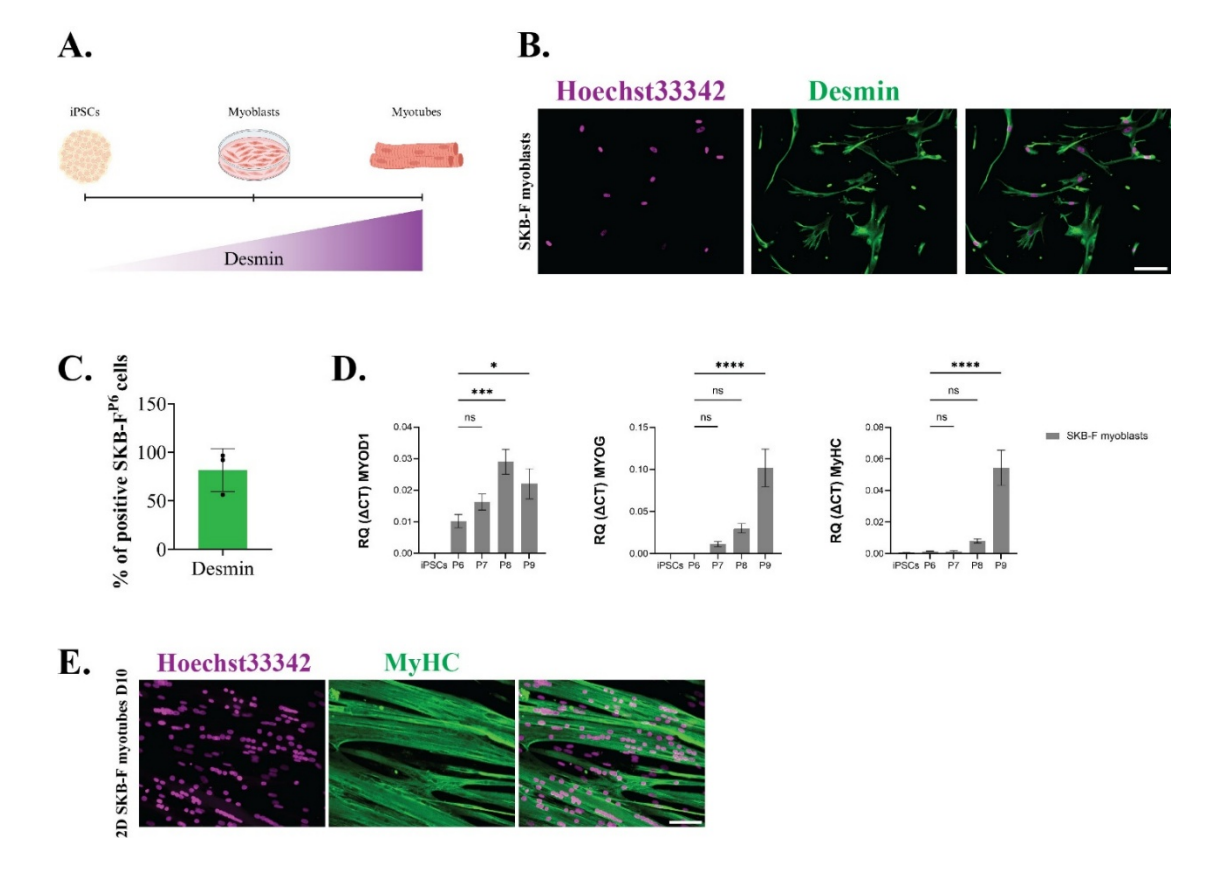
Antibody	Species	Working dilution	Reference
Desmin	Mouse	1:100	# M0760, DAKO
MyHC	Mouse	1:50	# ab51263, Abcam

Supplementary Table 3. Secondary antibodies

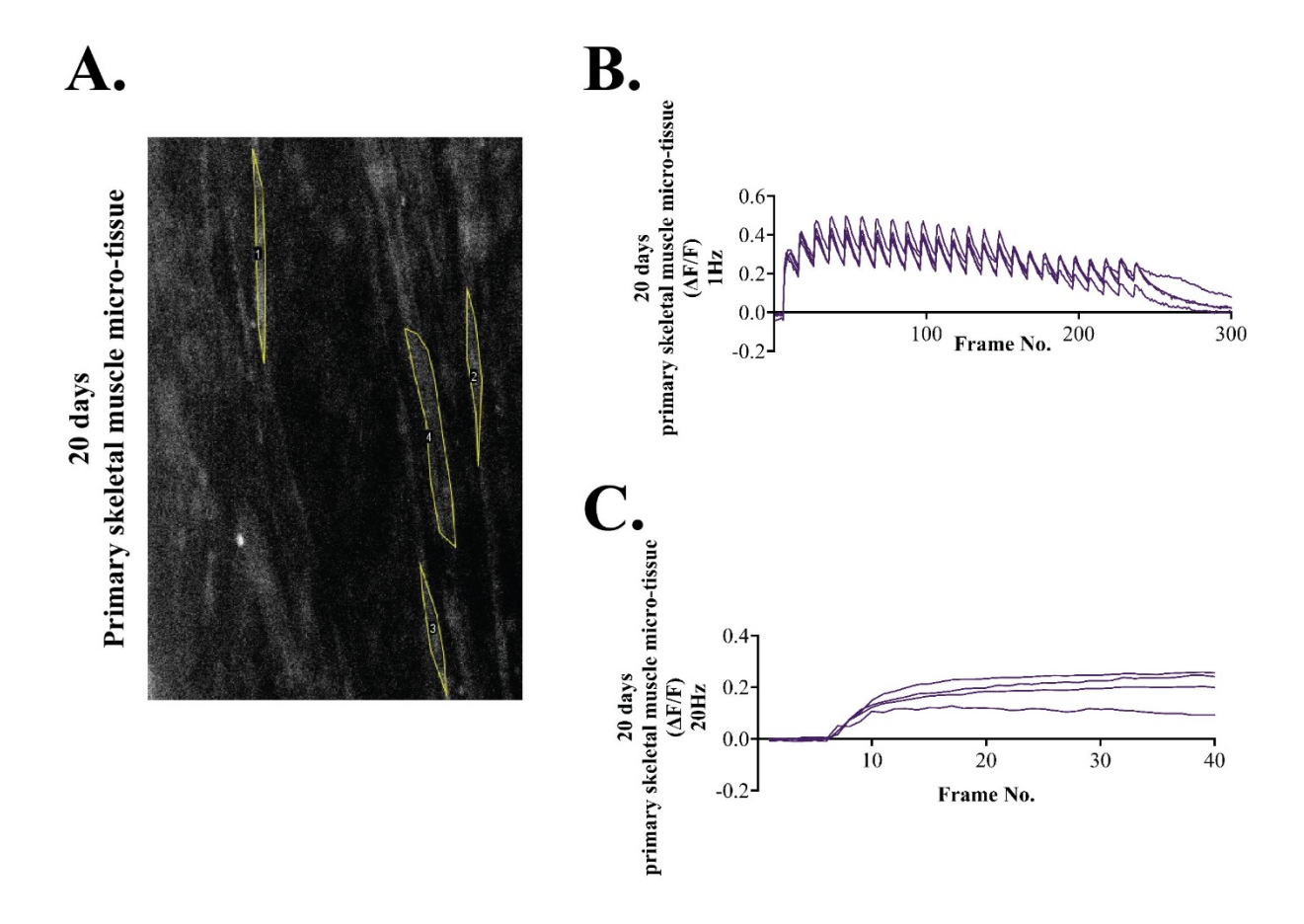
Host species	Target species-	Working dilution	Reference
	fluorophore		
Donkey	Mouse-Dylight488	1:250	#ab96875, Abcam
Hoechst33342	n/a	1:1000	# H3570, Thermo
			Fisher Scientic



Supplementary Figure 1. Schematic of NMJ^{3D} microfluidic device. Customized microfluidic devices for NMJ^{3D} co-cultures were fabricated and supplied by eNUVIO Inc. The device consists of two chambers: one designed to harbor the MN spheroid (pink chamber) and the other for the skeletal muscle micro-tissue (blue chamber). Both chambers are interconnected by a 180 μ m × 750 μ m microchannel channel that only permits the passage of axons.



Supplementary Figure 2. Characterization of a commercial cell line of human primary myoblasts. SKB-F, a commercial line of human primary myoblasts, was used to generate 3D skeletal muscle micro-tissues. **A.** The expression of desmin, a marker associated with myogenic differentiation was assessed by immunocytochemistry in three different lots supplied by the company. **B-C.** Approximately, 82 % of the SKB-F cells (81.4, SEM \pm 12.78) were desmin⁺ at passage 6 (P6). Scale bar, 100 μ m. **D.** Characterization of additional markers of myogenic differentiation (i.e. *MYOD1*, *MYOG*, *MYHC*) through qPCR showed that SKB-F myoblasts retain a similar expression profile until P8. Error bars represent \pm SEM, N=3, n=3. Significance was determined by one-way ANOVA, followed by Dunnett's post hoc test using P6 as the reference sample. ns = p > 0.05; *** = p < 0.05; **** = p < 0.001; ***** = p < 0.0001. **E.** SKB-F myoblasts differentiated in 2D fashion for 10 days in SKM-D medium expressed MyHC and exhibited sarcomeres. Scale bar, 100 μ m.



Supplementary Figure 3. Primary skeletal muscle micro-tissues exhibited calcium waves associated with subtetanic and tetanic activity. A. Epifluorescent image of a primary skeletal muscle micro-tissue differentiated for 20 days and loaded with Fluo-4 AM, showing examples of myotubes selected as ROIs (yellow line) to measure changes in fluorescence intensity. **B/C.** Quantification of changes in fluorescence intensity following 1 Hz and 20 Hz stimulation of primary skeletal muscle micro-tissues. Each line represents the response of an individual myotube within the tissue.

Discussion

Human *in vitro* 3D NMJ models using microfluidic devices have produced meaningful results in NMD modeling. However, the absence of a truly scalable model compatible with high-content approaches hinders their progression into preclinical research. The main goal of this project was to generate a human *in vitro* 3D NMJ within a microfluidic device with the potential to be scalable and suitable for high-content analysis.

The initial objective was to generate and characterize 3D MN spheroids from iPSCs of healthy donors, serving as the presynaptic component of the 3D NMJ model. In Chapter 1, iPSCderived MN spheroids were generated from two control lines (AIW002-02 and 3450) by modifying a pre-existing protocol to grow MNs as a 2D monolayer (1, 6). These spheroids were then characterized at the morphological, transcriptional, protein and functional levels at 14 and 28 days in final MN differentiation medium (1). A few groups had previously reported the generation of iPSC-derived MN spheroids (8, 10, 116, 126). In these studies, the characterization of MN spheroids primarily focused on the transcriptional and protein expression of MN markers, such as HB9, ISL1, and CHAT. Interestingly, the characterization of these markers at the protein level through immunocytochemistry revealed a dark hole in the center of the spheroids. This, along with the absence of PDK1 (a marker for cell survival, growth, and metabolism), was initially attributed to the presence of a necrotic core (10). However, by optimizing a tissue clearing protocol followed by immunocytochemistry in MN spheroids, we discovered that MN markers were evenly expressed throughout the core of the structures. This indicated that poor antibody penetration was a significant issue, suggesting that the previous interpretations of cell death may have resulted

from this limitation. Moreover, our technique allowed us to mount sixty spheroids on a 96-well plate for image acquisition and analysis using a high-content approach.

Since small-molecule MN differentiation protocols often generate a mixture of MNs, spinal INs, and glial cells (111, 127, 128), previous studies have also assessed markers associated with astrocytes and oligodendrocytes in MN spheroids (8, 10, 126). Surprisingly, the analysis of INs was not included. V2 and V3 IN domains flank the pMN domain in the ventral region of the spinal cord (35). Consequently, INs represent the major unintended cell type in these differentiation protocols (127, 128). Through transcriptional analysis via RT-qPCR and using our clearing and immunostaining protocol, we confirmed the presence of INs and oligodendrocytes in our MN spheroids (1). Interestingly, unlike the other methods (8, 10, 126), we did not detect the presence of astrocytes, which could result from the use of different compounds in the differentiation protocol.

We used a microelectrode array (MEA) approach to characterize the distinct functional properties of the MN spheroids. Through this analysis, we confirmed that the MN spheroids were capable of protruding neurites over time and empirically determined that neurite outgrowth was more pronounced at earlier differentiation time points (7-14 days). This was important for defining how long MN spheroids would remain in the round-bottom 96-well plates before co-culturing them with skeletal muscle micro-tissues. However, we acknowledge that the MEA method is not compatible with high-content data acquisition and analysis, as it relies on meticulous plating of the spheroids followed by extensive manual analysis. An alternative method is the use of high-density MEAs (HD-MEAs), which consist of thousands of electrodes with minimal space between them (129, 130, 131). These HD-MEAs increase spatiotemporal resolution and facilitate the

seeding process of 3D structures. Nonetheless, an important disadvantage of current HD-MEAs is that they lack a clear bottom for closely monitoring the culture's state over time.

Apart from their use in co-culture with muscle cells, MN spheroids can be utilized to study cell-autonomous mechanisms of diseases, particularly NMDs that selectively affect MNs. Thus, the second objective of this project was to use iPSC-derived 3D MN spheroids with fALS-linked mutations to investigate disease-related phenotypes and emphasize their utility in modeling NMDs.

In Chapter2, iPSCs harboring knock-in homozygous mutations in *SOD1* (SOD1^{D90A-KI}, SOD1^{G93A-KI}, and SOD1^{D90A/G93A-KI}), the second most common cause of fALS (78), were used to generate iPSC-derived MN spheroids. The AIW002-02 iPSC-line was engineered using CRISPR/Cas9 to introduce the mutations, serving as the isogenic control for precise phenotypic comparisons. Unlike in Chapter 1, in this chapter, MN spheroids were characterized for up to 56 days in final MN differentiation medium to determine whether new phenotypes would appear or become more pronounced over longer culture periods. Five phenotypes previously associated with fALS (132, 133, 134, 135) were found in mutant *SOD1* MN spheroids: 1) altered SOD1 expression, 2) reduced cell viability, 3) downregulation of neurofilament (NF) subunit expression and 4) abnormal functional features.

Importantly, a thorough analysis was performed to confirm that the percentages of unintended cell populations in the MN spheroids were consistent across genotypes, ensuring that the phenotypes were not attributable to differences in cell composition. In particular, INs are known to either excite or inhibit MNs (136), so a major concern was that differences in IN proportions could lead to misinterpretation of functional measurements. As previously observed, the presence

of INs and oligodendrocytes was detected in MN spheroids from both the isogenic and mutant SOD1 lines. However, they were present in similar proportions. This extensive characterization is not always performed, yet it is important to avoid confounding outcomes and facilitate comparisons across studies differentiating MN spheroids using different protocols.

3D MN spheroids showed a considerable advantage over 2D MN monolayers by enabling long-term culture of the cells. Using our current workflows, 2D MNs do not grow and survive beyond 42 days in final MN differentiation medium, with a propensity to form clusters that ultimately detach from the culture surface by this time point (111, 118). Moreover, in a previous study from our group, we failed to detect changes in cell viability, which we attributed to the MNs not being sufficiently mature to exhibit the phenotype (118). In contrast, a reduction in cell viability was detected after 56 days in MN spheroids. Similarly, the functional abnormalities that we observed were not statistically significant until 56 days. It is important to note that we chose 56 days as the endpoint for analyses simply to double the characterization time from our previous experiments. Since the quality of the cultures was not compromised (using the isogenic line as a reference), extending the culture time even further could potentially lead to more pronounced phenotypes in mutant SOD1 MN spheroids.

One of the mutations included in our analysis was the G93A variant, which, when overexpressed in mice, led to the creation of the most widely used animal model for preclinical ALS research, the SOD1^{G93A} mouse model (137, 138). Interestingly, the SOD1^{G93A} mouse model showed early NMJ denervation at 47 days, preceding the appearance of motor symptoms and MN loss between 80 and 100 days (139). This suggests that molecular changes at the NMJ may influence MN degeneration, particularly affecting fast-twitch motor units (140). Since SOD1^{G93A}-

KI MN spheroids have now been thoroughly characterized, a future application of our model may involve evaluating the impact of this variant on NMJ formation and degeneration.

Even though this chapter focused on the study of MNs, the model can be used as a cellular jigsaw, allowing the integration of other iPSC-derived cell types to enhance the physiological relevance of the culture. For instance, our MN spheroid model and its associated tools provided the foundation for another study in which iPSC-derived astrocytes were incorporated to create a more advanced system to study non-cell autonomous mechanisms in fALS (141).

A final note on Chapter 2 is that, initially, we had planned to focus exclusively on the homozygous SOD1^{G93A-KI} iPSC line previously developed by our group (119). After a year of work, confounding results in Western Blot analysis prompted us to perform a quality control check via Sanger sequencing to reassess the presence of the homozygous mutation. Unfortunately, we discovered that due to a human error, the mutant iPSC line was harboring two homozygous ALSrelated mutations (D90A and G93A) instead of one. To our knowledge, double homozygous mutations in SOD1 have not been observed in patients. In contrast, there is only one case study reporting the compound effect of two SOD1 heterozygous mutations (D90A and D96N). While D90A represents a frequent SOD1 mutation associated with slow-progressing ALS, the D96N mutation was reported for the first time in this study (142). Given this, we viewed the discovery of two homozygous mutations in our iPSC model as an opportunity to expand our analysis to a second disease-related mutation (D90A), and for the first time, investigate the potential synergistic effects of two SOD1 ALS-related mutations (D90A/G93A). This offers valuable insights into how different SOD1 mutations might interact in ALS pathogenesis, even though such combinations have not been observed in clinical cases. Our results concluded that D90A and G93A do not promote synergistic deleterious effects when present simultaneously in SOD1, suggesting that the

conformational change induced by the two mutations may have resulted in a structure similar to that of either of the single SOD1 mutants.

Following the generation of iPSC-derived MN spheroids and the demonstration of their potential to model NMDs, the project progressed to its third objective. In Chapter 3, we described the optimization of a protocol for generating and characterizing human 3D skeletal muscle structures, referred to as skeletal muscle micro-tissues.

Initially, commercially available primary myoblasts (SKB-line) were used to develop the protocol for generating skeletal muscle micro-tissues, while efforts were made to produce iPSCderived myoblasts. Primary myoblasts are widely utilized due to their accessibility and capacity for rapid differentiation into myotubes with a high fusion index and well-developed contractile units (108, 143, 144, 145). However, unlike iPSC-derived cells, which can be produced in large quantities, primary myoblasts have limited expansion potential unless immortalized (146), posing a challenge for large-scale experiments. Furthermore, when co-cultured with iPSC-derived MNs, primary myoblasts do not share a common genetic background. A major challenge in the iPSC field remains the development of a reproducible, transgene-free method to generate highly differentiated myotubes. To our knowledge, only two recent studies culturing transgene-free iPSCderived cells in a 2D system have reported a fusion index ranging from 20% to 60% (125, 147). The inclusion of a FACS sorting step has been shown to enhance efficiency in transgene-free iPSC differentiation protocols, achieving results comparable to those observed with differentiated primary myoblasts (143). While both transgene-based (11, 148, 149) and FACS-dependent transgene-free (143, 150, 151, 152) approaches yield high myogenic differentiation, they are not scalable due to the complexity of the required techniques and the need for extensive quality control.

To generate iPSC-derived myoblasts, we explored two transgene-free methods that were the most successful at the time (5, 153). Unfortunately, we were unable to reproduce their findings. One of the protocols was highly cell line-dependent, requiring the testing of several reagent concentrations for each cell line to achieve the desired results. Additionally, critical protocol time points were influenced by subjective factors, such as cell confluency (153). Although the second protocol was more streamlined, with defined reagent concentrations and cell densities (5), we were incapable of reproducing their results after troubleshooting with two control lines (AIW002-02 and 3450) (120). Following the publication of a protocol by Guo et al. (2022), we adhered to the authors' instructions and successfully reproduced their findings (125), generating iPSC-derived iMyoblasts from the AIW002-02 iPSC line. A meaningful advantage of this protocol is that iMyoblasts can be frozen for storage or stably propagated for over 12 passages, demonstrating their utility for large-scale studies. Finally, the protocol we optimized for generating primary skeletal muscle micro-tissues proved successful for generating iPSC-derived skeletal muscle micro-tissues.

Before transitioning to NMJ modeling, we sought to evaluate the functionality of our human skeletal muscle micro-tissues by analyzing intracellular calcium dynamics using a calcium dynamics using

a cassette encoding a calcium reporter (MHCK7-GCaMP6) to assess calcium dynamics, a process that would be both time-consuming and technically challenging for large-scale studies involving multiple patient lines. Additionally, contractile forces were measured by tracking pillar deflection, a method that can be difficult to monitor, making it challenging for high-content imaging and analysis.

After developing human skeletal muscle micro-tissues and tools to assess their functionality, we shifted our focus to generating the 3D *in vitro* model of the NMJ within a custom compartmentalized device. This work, described in Chapter 3, was carried out in collaboration with eNUVIO Inc.—a company specializing in microfluidic culture technologies—through a Mitacs Accelerate award. Together, we designed a device that met the unitary dimensions required for scaling into a 96-well microplate. The device consists of two adjacent chambers, each designed to hold either the MN spheroid or the skeletal muscle micro-tissue. These chambers are connected by a channel, allowing axons to pass from one chamber to the other. Consequently, up to 48 experiments will be possible in the scaled microplate (**Figure 7**). To date, the most scalable system using a compartmentalization approach supports up to 24 NMJ co-cultures within the same plate (116). Although this system can be scaled, as well as others (8, 10), they do not have the appropriate measures to be compatible with high-content imaging systems.

After multiple iterations, we successfully established an optimal timeline for co-culturing iPSC-derived MN spheroids and human skeletal muscle micro-tissues, enabling us to observe contact between the two cell types. Notably, in contrast to 2D NMJ systems (11, 111, 155), our 3D model facilitates long-term co-culture of these cells (> 21 days). Additionally, unlike other 3D *in vitro* systems where MNs and skeletal muscle are either co-derived from a common progenitor, such as NMPs (7, 117), or differentiated independently but cultured within the same compartment

(108), our compartmentalized platform supports axonal outgrowth of at least 1mm—the distance between the MN spheroid compartment and the anchoring posts. *In vivo*, MNs reside in the ventral horn of the spinal cord and extend long axons into the periphery to innervate target muscles. Due to this extensive projection, MNs are particularly vulnerable to stress. Therefore, systems that fail to recapitulate long-range axonal outgrowth lack physiological relevance, potentially concealing important disease-related phenotypes. As well, our system offers distinct advantages for disease modeling due to its modular design. The individual components—MN spheroids and skeletal muscle micro-tissues—can be studied separately to investigate disease mechanisms specific to motor neuron disorders or myopathies, respectively, before exploring their interactions at the NMJ. Moreover, the model supports various combinatorial configurations (e.g., control MNs with control muscle, disease MNs with control muscle, control MNs with disease muscle, or both components diseased), enabling detailed studies of each cell type's contribution to disease onset and progression.

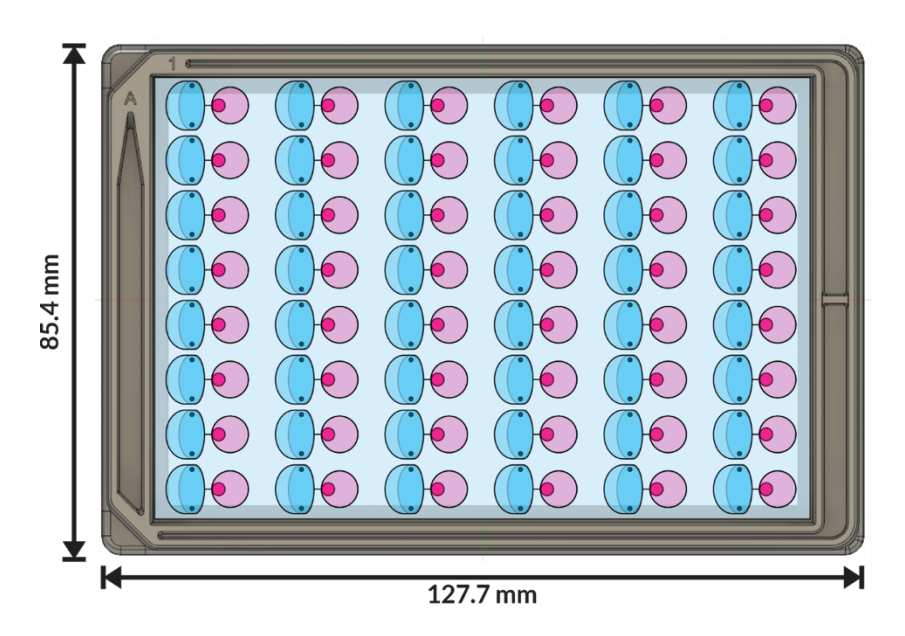


Figure 7. Scaled plate for 3D NMJ cultures. Figure provided by eNUVIO Inc., created using Inkscape version 1.4.

Our success building the model prompted the development of an additional image-based technique, described at the end of Chapter 3, to assess co-culture morphology in a manner compatible with high-content imaging systems. We used immunofluorescent staining to visualize the colocalization of presynaptic MN terminals and AChRs on the muscle membrane, confirming successful 3D NMJ formation through analysis of reconstructed 3D images. To date, comparable models have not reported such reconstruction for NMJ morphology analysis, relying instead on assessments derived from isolated 2D images (8, 10, 116). However, it is important to acknowledge that a limitation of imaging this system arises from its 3D nature, which requires the use of long-working distance objectives to visualize its full extent, thereby limiting the resolution of the structures.

As part of our future directions, we will assess NMJ function by utilizing our image-based approaches to assess muscle responses, with the only modification being that electrical stimulation must be applied to the MN spheroid while imaging is conducted in the skeletal muscle micro-tissue compartment to assess calcium flux and fluorescence bead displacement. Functional NMJ fidelity—defined as the percentage of MN-induced muscle contractions relative to the total number of NMJ stimulations—has been reported to reach at least 80% in other NMJ *in vitro* models, a benchmark we aim to replicate (8, 155). Furthermore, MN-induced contractions should cease upon the addition of d-tubocurarine, a pharmacological antagonist of AChRs, confirming the specificity of NMJ-mediated responses.

Additionally, we are interested in determining whether the reduction in MN spheroid firing observed in the SOD1 lines generated in Chapter 2 translates into decreased muscle function in our model. Demonstrating this link would support the use of the system as a phenotypic assay for the restoration of function in an *in vitro* ALS model.

Beyond the previously mentioned limitations—such as the challenges in skeletal muscle differentiation efficiency from iPSC sources and the resolution constraints when imaging NMJ morphology—another significant challenge lies in scaling our tools and fully leveraging the capabilities of the model in its larger format. Specifically, developing the necessary instruments to stimulate either the skeletal muscle micro-tissue or the MN spheroid while simultaneously imaging with the high-content screening system. This must be achieved without relying on optogenetics (156, 157, 158) as genetic engineering approaches are impractical for large-scale studies, as previously mentioned. Fortunately, the advancement of 3D models is driving companies to develop instruments for assessing these systems, fueled by a collective interest in integrating them into preclinical research.

Finally, the NMJ is a tripartite synapse that also includes PSCs, which play critical roles in NMJ maintenance and repair. Although a few studies have included PSCs in NMJ models (7, 105, 117), none have done so within compartmentalized systems—an approach that offers the advantage of spatially restricting PSC contact to the presynaptic MN terminal. Thus, the integration of PSCs into a 3D NMJ compartmentalized system would be a valuable step toward improving physiological relevance. We hypothesized that this could be achieved by adding Schwann cell progenitors to the skeletal muscle compartment, where axon-muscle contact can promote PSC differentiation and NMJ maturation, as demonstrated in 2D systems (105).

Conclusion

In conclusion, we successfully developed an iPSC-derived 3D MN model and the necessary analytical tools to characterize its key features, some of which are compatible with high-content approaches. Moreover, our 3D MN model has proven useful for studying cell-autonomous and non-cell-autonomous mechanisms in ALS, a NMD. Additionally, we demonstrated that a protocol originally designed to generate iPSC-derived 2D skeletal muscle can be reproduced and optimized to generate iPSC-derived skeletal muscle micro-tissues. We also developed two image-based techniques for assessing skeletal muscle micro-tissue function, which are suitable for high-content imaging systems. Upon co-culture with iPSC-derived MN spheroids, skeletal muscle micro-tissues form 3D NMJs within a microfluidic device as confirmed through another image-based technique that identifies co-localization between presynaptic MN terminals and AChRs on the muscle membrane. Taken together, we have developed a human *in vitro* 3D NMJ model, complemented by high-content compatible tools for analyzing its components both individually and in co-culture, which will facilitate the transition of these models into preclinical research.

References

- 1. Castellanos-Montiel MJ, Chaineau M, Franco-Flores AK, Haghi G, Carrillo-Valenzuela D, Reintsch WE, Chen CX-Q, Durcan TM. An optimized workflow to generate and characterize iPSC-derived motor neuron (MN) spheroids. *Cells*. 2023;12, 545.
- 2. Castellanos-Montiel MJ, Franco-Flores AK, Nicouleau M, Haghi G, Lépine S, Baeza B, Chen CX-Q, Goldsmith TM, Aprahamian N, Hua D, Chaineau M, Gursu L, Abdian N, Deneault E, Durcan TM. Mutations in SOD1 induce ALS-related phenotypes in 3D iPSC-derived motor neuron (MN) spheroids. *bioRxiv*. 2025:2025.01.28.635126.
- 3. Aubertin-Leheudre M, Pion CH, Vallée J, Marchand S, Morais JA, Bélanger M, Robitaille R. Improved Human Muscle Biopsy Method To Study Neuromuscular Junction Structure and Functions with Aging. *J Gerontol A Biol Sci Med Sci.* 2020;75(11):2098-102.
- 4. Jones RA, Harrison C, Eaton SL, Llavero Hurtado M, Graham LC, Alkhammash L, Oladiran OA, Gale A, Lamont DJ, Simpson H, Simmen MW, Soeller C, Wishart TM, Gillingwater TH. Cellular and Molecular Anatomy of the Human Neuromuscular Junction. *Cell Rep.* 2017;21(9):2348-56.
- 5. Chal J, Al Tanoury Z, Hestin M, Gobert B, Aivio S, Hick A, Cherrier T, Nesmith AP, Parker KK, Pourquié O. Generation of human muscle fibers and satellite-like cells from human pluripotent stem cells in vitro. *Nat Protoc*. 2016;11(10):1833-50.
- 6. Du ZW, Chen H, Liu H, Lu J, Qian K, Huang CL, Zhong X, Fan F, Zhang SC. Generation and expansion of highly pure motor neuron progenitors from human pluripotent stem cells. *Nat Commun*. 2015;6:6626.

- 7. Faustino Martins JM, Fischer C, Urzi A, Vidal R, Kunz S, Ruffault PL, Kabuss L, Hube I, Gazzerro E, Birchmeier C, Spuler S, Sauer S, Gouti M. Self-organizing 3D human trunk neuromuscular organoids. *Cell Stem Cell*. 2020;26(2):172-86.e6.
- 8. Osaki T, Uzel SGM, Kamm RD. On-chip 3D neuromuscular model for drug screening and precision medicine in neuromuscular disease. *Nat Protoc*. 2020;15(2):421-49.
- 9. Kim H, Kim GS, Hyun SH, Kim E. Advancements in 2D and 3D In Vitro Models for Studying Neuromuscular Diseases. *Int J Mol Sci.* 2023;24(23).
- 10. Osaki T, Uzel SGM, Kamm RD. Microphysiological 3D model of amyotrophic lateral sclerosis (ALS) from human iPS-derived muscle cells and optogenetic motor neurons. *Sci Adv*. 2018;4(10):eaat5847.
- 11. Rao L, Qian Y, Khodabukus A, Ribar T, Bursac N. Engineering human pluripotent stem cells into a functional skeletal muscle tissue. *Nat Commun*. 2018;9(1):126.
- 12. Vila OF, Uzel SGM, Ma SP, Williams D, Pak J, Kamm RD, Vunjak-Novakovic G. Quantification of human neuromuscular function through optogenetics. *Theranostics*. 2019;9(5):1232-46.
- 13. Welniarz Q, Dusart I, Roze E. The corticospinal tract: Evolution, development, and human disorders. *Dev Neurobiol*. 2017;77(7):810-29.
- 14. Seo JP, Jang SH. Different characteristics of the corticospinal tract according to the cerebral origin: DTI study. *AJNR Am J Neuroradiol*. 2013;34(7):1359-63.
- 15. Stifani N. Motor neurons and the generation of spinal motor neuron diversity. *Front Cell Neurosci*. 2014;8:293.

- 16. Jarrar W, Dias JM, Ericson J, Arnold HH, Holz A. Nkx2.2 and Nkx2.9 are the key regulators to determine cell fate of branchial and visceral motor neurons in caudal hindbrain. *PLoS One*. 2015;10(4):e0124408.
- 17. Murtazina A, Adameyko I. The peripheral nervous system. *Development*. 2023;150(9).
- 18. Chandrasekhar A. Turning heads: development of vertebrate branchiomotor neurons. *Dev Dyn.* 2004;229(1):143-61.
- 19. Rinaman L, & Koehnle, T. Development of Central Visceral Circuits. 2014. In: Oxford handbook of developmental behavioral neuroscience [Internet]. Available from: https://academic.oup.com/edited-volume/34498.
- 20. Friese A, Kaltschmidt JA, Ladle DR, Sigrist M, Jessell TM, Arber S. Gamma and alpha motor neurons distinguished by expression of transcription factor Err3. *Proc Natl Acad Sci U S A*. 2009;106(32):13588-93.
- 21. Bessou P, Emonet-Dénand F, Laporte Y. Motor fibres innervating extrafusal and intrafusal muscle fibres in the cat. *J Physiol*. 1965;180(3):649-72.
- 22. Ko CP, Robitaille R. Perisynaptic Schwann Cells at the Neuromuscular Synapse: Adaptable, Multitasking Glial Cells. *Cold Spring Harb Perspect Biol.* 2015;7(10):a020503.
- 23. Sanes JR, Lichtman JW. Development of the vertebrate neuromuscular junction. *Annu Rev Neurosci*. 1999;22:389-442.
- 24. Herrera AA, Grinnell AD, Wolowske B. Ultrastructural correlates of naturally occurring differences in transmitter release efficacy in frog motor nerve terminals. *J Neurocytol*. 1985;14(2):193-202.
- 25. Slater CR. The Structure of Human Neuromuscular Junctions: Some Unanswered Molecular Questions. *Int J Mol Sci.* 2017;18(10).

- 26. Heuser JE, Salpeter SR. Organization of acetylcholine receptors in quick-frozen, deepetched, and rotary-replicated Torpedo postsynaptic membrane. *J Cell Biol.* 1979;82(1):150-73.
- 27. Zou S, Pan BX. Post-synaptic specialization of the neuromuscular junction: junctional folds formation, function, and disorders. *Cell Biosci*. 2022;12(1):93.
- 28. Thowfeequ S, Srinivas S. Embryonic and extraembryonic tissues during mammalian development: shifting boundaries in time and space. *Philos Trans R Soc Lond B Biol Sci*. 2022;377(1865):20210255.
- 29. Sanes JR, Jessell T. M. Patterning the Nervous System. In: Kandel ER, Schwartz, J. H., Jessell, T. M., Siegelbaum, S. A., Hudspeth, A. J., editor. Principles of Neural Science. 5th edition ed: Mc Graw Hill Medical; 2013. p. 1165-865.
- 30. Wilson PA, Hemmati-Brivanlou A. Induction of epidermis and inhibition of neural fate by Bmp-4. *Nature*. 1995;376(6538):331-3.
- 31. Green D, Whitener AE, Mohanty S, Lekven AC. Vertebrate nervous system posteriorization: Grading the function of Wnt signaling. *Dev Dyn.* 2015;244(3):507-12.
- 32. Durston AJ, Timmermans JP, Hage WJ, Hendriks HF, de Vries NJ, Heideveld M, Nieuwkoop PD. Retinoic acid causes an anteroposterior transformation in the developing central nervous system. *Nature*. 1989;340(6229):140-4.
- 33. Placzek M, Jessell TM, Dodd J. Induction of floor plate differentiation by contact-dependent, homeogenetic signals. *Development*. 1993;117(1):205-18.
- 34. Kremnyov S, Henningfeld K, Viebahn C, Tsikolia N. Divergent axial morphogenesis and early shh expression in vertebrate prospective floor plate. *Evodevo*. 2018;9:4.

- 35. Ogura T, Sakaguchi H, Miyamoto S, Takahashi J. Three-dimensional induction of dorsal, intermediate and ventral spinal cord tissues from human pluripotent stem cells. *Development*. 2018;145(16).
- 36. Wilson L, Maden M. The mechanisms of dorsoventral patterning in the vertebrate neural tube. *Dev Biol.* 2005;282(1):1-13.
- 37. Thaler J, Harrison K, Sharma K, Lettieri K, Kehrl J, Pfaff SL. Active suppression of interneuron programs within developing motor neurons revealed by analysis of homeodomain factor HB9. *Neuron*. 1999;23(4):675-87.
- 38. Oda Y, Imai S, Nakanishi I, Ichikawa T, Deguchi T. Immunohistochemical study on choline acetyltransferase in the spinal cord of patients with amyotrophic lateral sclerosis. *Pathol Int*. 1995;45(12):933-9.
- 39. Arvidsson U, Riedl M, Elde R, Meister B. Vesicular acetylcholine transporter (VAChT) protein: a novel and unique marker for cholinergic neurons in the central and peripheral nervous systems. *J Comp Neurol*. 1997;378(4):454-67.
- 40. Carriedo SG, Yin HZ, Weiss JH. Motor neurons are selectively vulnerable to AMPA/kainate receptor-mediated injury in vitro. *J Neurosci*. 1996;16(13):4069-79.
- 41. Deries M, Gonçalves AB, Thorsteinsdóttir S. Skeletal Muscle Development: From Stem Cells to Body Movement. In: Rodrigues G, Roelen BAJ, editors. Concepts and Applications of Stem Cell Biology: A Guide for Students. Cham: Springer International Publishing; 2020. p. 159-85.
- 42. Tani S, Chung UI, Ohba S, Hojo H. Understanding paraxial mesoderm development and sclerotome specification for skeletal repair. *Exp Mol Med*. 2020;52(8):1166-77.

- 43. Aulehla A, Pourquié O. Signaling gradients during paraxial mesoderm development. *Cold Spring Harb Perspect Biol.* 2010;2(2):a000869.
- 44. Tzouanacou E, Wegener A, Wymeersch FJ, Wilson V, Nicolas JF. Redefining the progression of lineage segregations during mammalian embryogenesis by clonal analysis. *Dev Cell*. 2009;17(3):365-76.
- 45. Chal J, Pourquié O. Making muscle: skeletal myogenesis in vivo and in vitro. *Development*. 2017;144(12):2104-22.
- 46. Cairns DM, Sato ME, Lee PG, Lassar AB, Zeng L. A gradient of Shh establishes mutually repressing somitic cell fates induced by Nkx3.2 and Pax3. *Dev Biol.* 2008;323(2):152-65.
- 47. Buckingham M, Relaix F. The role of Pax genes in the development of tissues and organs: Pax3 and Pax7 regulate muscle progenitor cell functions. *Annu Rev Cell Dev Biol*. 2007;23:645-73.
- 48. Rudnicki MA, Schnegelsberg PN, Stead RH, Braun T, Arnold HH, Jaenisch R. MyoD or Myf-5 is required for the formation of skeletal muscle. *Cell*. 1993;75(7):1351-9.
- 49. Conerly ML, Yao Z, Zhong JW, Groudine M, Tapscott SJ. Distinct Activities of Myf5 and MyoD Indicate Separate Roles in Skeletal Muscle Lineage Specification and Differentiation. *Dev Cell*. 2016;36(4):375-85.
- 50. Venuti JM, Morris JH, Vivian JL, Olson EN, Klein WH. Myogenin is required for late but not early aspects of myogenesis during mouse development. *J Cell Biol.* 1995;128(4):563-76.
- 51. Ganassi M, Badodi S, Ortuste Quiroga HP, Zammit PS, Hinits Y, Hughes SM. Myogenin promotes myocyte fusion to balance fibre number and size. *Nat Commun.* 2018;9(1):4232.

- 52. Millay DP, O'Rourke JR, Sutherland LB, Bezprozvannaya S, Shelton JM, Bassel-Duby R, Olson EN. Myomaker is a membrane activator of myoblast fusion and muscle formation. *Nature*. 2013;499(7458):301-5.
- 53. Quinn ME, Goh Q, Kurosaka M, Gamage DG, Petrany MJ, Prasad V, Millay DP. Myomerger induces fusion of non-fusogenic cells and is required for skeletal muscle development. *Nat Commun.* 2017;8:15665.
- 54. Biressi S, Tagliafico E, Lamorte G, Monteverde S, Tenedini E, Roncaglia E, Ferrari S, Ferrari S, Cusella-De Angelis MG, Tajbakhsh S, Cossu G. Intrinsic phenotypic diversity of embryonic and fetal myoblasts is revealed by genome-wide gene expression analysis on purified cells. *Dev Biol.* 2007;304(2):633-51.
- 55. Cachaço AS, Pereira CS, Pardal RG, Bajanca F, Thorsteinsdóttir S. Integrin repertoire on myogenic cells changes during the course of primary myogenesis in the mouse. *Dev Dyn*. 2005;232(4):1069-78.
- 56. Bentzinger CF, Wang YX, Rudnicki MA. Building muscle: molecular regulation of myogenesis. *Cold Spring Harb Perspect Biol.* 2012;4(2).
- 57. Yoshida T, Delafontaine P. Mechanisms of IGF-1-mediated regulation of skeletal muscle hypertrophy and atrophy. *Cells*. 2020;9(9).
- 58. Wang Z, Grange M, Wagner T, Kho AL, Gautel M, Raunser S. The molecular basis for sarcomere organization in vertebrate skeletal muscle. *Cell*. 2021;184(8):2135-50.e13.
- 59. Ribeiro Ede A, Jr., Pinotsis N, Ghisleni A, Salmazo A, Konarev PV, Kostan J, Sjöblom B, Schreiner C, Polyansky AA, Gkougkoulia EA, Holt MR, Aachmann FL, Zagrović B, Bordignon E, Pirker KF, Svergun DI, Gautel M, Djinović-Carugo K. The structure and regulation of human muscle α-actinin. *Cell*. 2014;159(6):1447-60.

- 60. Lee YI. Differences in the constituent fiber types contribute to the intermuscular variation in the timing of the developmental synapse elimination. *Sci Rep.* 2019;9(1):8694.
- 61. Herbison GJ, Jaweed MM, Ditunno JF. Muscle fiber types. *Arch Phys Med Rehabil*. 1982;63(5):227-30.
- 62. Blemker SS, Brooks SV, Esser KA, Saul KR. Fiber-type traps: revisiting common misconceptions about skeletal muscle fiber types with application to motor control, biomechanics, physiology, and biology. *J Appl Physiol* (1985). 2024;136(1):109-21.
- 63. Moreno-Justicia R, Van der Stede T, Stocks B, Laitila J, Seaborne RA, Van de Loock A, Lievens E, Samodova D, Marín-Arraiza L, Dmytriyeva O, Browaeys R, Van Vossel K, Moesgaard L, Yigit N, Anckaert J, Weyns A, Van Thienen R, Sahl RE, Zanoteli E, Lawlor MW, Wierer M, Mestdagh P, Vandesompele J, Ochala J, Hostrup M, Derave W, Deshmukh AS. Human skeletal muscle fiber heterogeneity beyond myosin heavy chains. *Nat Commun.* 2025;16(1):1764.
- 64. Jessen KR, Mirsky R, Lloyd AC. Schwann Cells: Development and Role in Nerve Repair. *Cold Spring Harb Perspect Biol*. 2015;7(7):a020487.
- 65. Bezakova G, Ruegg MA. New insights into the roles of agrin. *Nat Rev Mol Cell Biol*. 2003;4(4):295-308.
- 66. Apel ED, Glass DJ, Moscoso LM, Yancopoulos GD, Sanes JR. Rapsyn is required for MuSK signaling and recruits synaptic components to a MuSK-containing scaffold. *Neuron*. 1997;18(4):623-35.
- 67. Tanowitz M, Si J, Yu DH, Feng GS, Mei L. Regulation of neuregulin-mediated acetylcholine receptor synthesis by protein tyrosine phosphatase SHP2. *J Neurosci*. 1999;19(21):9426-35.

- 68. Ferraro E, Molinari F, Berghella L. Molecular control of neuromuscular junction development. *J Cachexia Sarcopenia Muscle*. 2012;3(1):13-23.
- 69. Fox MA, Sanes JR, Borza DB, Eswarakumar VP, Fässler R, Hudson BG, John SW, Ninomiya Y, Pedchenko V, Pfaff SL, Rheault MN, Sado Y, Segal Y, Werle MJ, Umemori H. Distinct target-derived signals organize formation, maturation, and maintenance of motor nerve terminals. *Cell*. 2007;129(1):179-93.
- 70. Lichtman JW, Colman H. Synapse elimination and indelible memory. *Neuron*. 2000;25(2):269-78.
- 71. Castellanos-Montiel MJ, Velasco I, Escobedo-Avila I. Modeling the neuromuscular junction in vitro: an approach to study neuromuscular junction disorders. *Ann N Y Acad Sci*. 2021;1488(1):3-15.
- 72. Kuo IY, Ehrlich BE. Signaling in muscle contraction. *Cold Spring Harb Perspect Biol*. 2015;7(2):a006023.
- 73. Auld DS, Robitaille R. Perisynaptic Schwann cells at the neuromuscular junction: nerveand activity-dependent contributions to synaptic efficacy, plasticity, and reinnervation. *Neuroscientist*. 2003;9(2):144-57.
- 74. Robitaille R, Bourque MJ, Vandaele S. Localization of L-type Ca2+ channels at perisynaptic glial cells of the frog neuromuscular junction. *J Neurosci*. 1996;16(1):148-58.
- 75. Robitaille R, Jahromi BS, Charlton MP. Muscarinic Ca2+ responses resistant to muscarinic antagonists at perisynaptic Schwann cells of the frog neuromuscular junction. *J Physiol*. 1997;504 (Pt 2):337-47.

- 76. Descarries LM, Cai S, Robitaille R, Josephson EM, Morest DK. Localization and characterization of nitric oxide synthase at the frog neuromuscular junction. *J Neurocytol*. 1998;27(11):829-40.
- 77. Talbott EO, Malek AM, Lacomis D. The epidemiology of amyotrophic lateral sclerosis. *Handb Clin Neurol.* 2016;138:225-38.
- 78. Younger DS, Brown RH, Jr. Amyotrophic lateral sclerosis. *Handb Clin Neurol*. 2023;196:203-29.
- 79. Nijs M, Van Damme P. The genetics of amyotrophic lateral sclerosis. *Curr Opin Neurol*. 2024;37(5):560-9.
- 80. Mead RJ, Shan N, Reiser HJ, Marshall F, Shaw PJ. Amyotrophic lateral sclerosis: a neurodegenerative disorder poised for successful therapeutic translation. *Nat Rev Drug Discov*. 2023;22(3):185-212.
- 81. Newell ME, Adhikari S, Halden RU. Systematic and state-of the science review of the role of environmental factors in Amyotrophic Lateral Sclerosis (ALS) or Lou Gehrig's Disease. *Sci Total Environ*. 2022;817:152504.
- 82. Gilhus NE, Tzartos S, Evoli A, Palace J, Burns TM, Verschuuren J. Myasthenia gravis. *Nat Rev Dis Primers*. 2019;5(1):30.
- 83. Lazaridis K, Tzartos SJ. Autoantibody Specificities in Myasthenia Gravis; Implications for Improved Diagnostics and Therapeutics. *Front Immunol.* 2020;11:212.
- 84. Dresser L, Wlodarski R, Rezania K, Soliven B. Myasthenia Gravis: Epidemiology, Pathophysiology and Clinical Manifestations. *J Clin Med*. 2021;10(11).
- 85. Mantegazza R, Bonanno S, Camera G, Antozzi C. Current and emerging therapies for the treatment of myasthenia gravis. *Neuropsychiatr Dis Treat*. 2011;7:151-60.

- 86. Heydemann A, Siemionow M. A Brief Review of Duchenne Muscular Dystrophy Treatment Options, with an Emphasis on Two Novel Strategies. *Biomedicines*. 2023;11(3).
- 87. Ferizovic N, Summers J, de Zárate IBO, Werner C, Jiang J, Landfeldt E, Buesch K. Prognostic indicators of disease progression in Duchenne muscular dystrophy: A literature review and evidence synthesis. *PLoS One*. 2022;17(3):e0265879.
- 88. Duan D, Goemans N, Takeda S, Mercuri E, Aartsma-Rus A. Duchenne muscular dystrophy. *Nat Rev Dis Primers*. 2021;7(1):13.
- 89. Zakrzewski W, Dobrzyński M, Szymonowicz M, Rybak Z. Stem cells: past, present, and future. *Stem Cell Research & Therapy*. 2019;10(1):68.
- 90. Singh VK, Saini A, Kalsan M, Kumar N, Chandra R. Describing the Stem Cell Potency: The Various Methods of Functional Assessment and In silico Diagnostics. *Front Cell Dev Biol*. 2016;4:134.
- 91. Takahashi K, Yamanaka S. Induction of pluripotent stem cells from mouse embryonic and adult fibroblast cultures by defined factors. *Cell*. 2006;126(4):663-76.
- 92. Takahashi K, Tanabe K, Ohnuki M, Narita M, Ichisaka T, Tomoda K, Yamanaka S. Induction of pluripotent stem cells from adult human fibroblasts by defined factors. *Cell*. 2007;131(5):861-72.
- 93. Poetsch MS, Strano A, Guan K. Human Induced Pluripotent Stem Cells: From Cell Origin, Genomic Stability, and Epigenetic Memory to Translational Medicine. *Stem Cells*. 2022;40(6):546-55.
- 94. Sances S, Bruijn LI, Chandran S, Eggan K, Ho R, Klim JR, Livesey MR, Lowry E, Macklis JD, Rushton D, Sadegh C, Sareen D, Wichterle H, Zhang SC, Svendsen CN. Modeling ALS with

- motor neurons derived from human induced pluripotent stem cells. *Nat Neurosci*. 2016;19(4):542-53.
- 95. Maury Y, Côme J, Piskorowski RA, Salah-Mohellibi N, Chevaleyre V, Peschanski M, Martinat C, Nedelec S. Combinatorial analysis of developmental cues efficiently converts human pluripotent stem cells into multiple neuronal subtypes. *Nat Biotechnol*. 2015;33(1):89-96.
- 96. Ericson J, Morton S, Kawakami A, Roelink H, Jessell TM. Two critical periods of Sonic Hedgehog signaling required for the specification of motor neuron identity. *Cell.* 1996;87(4):661-73.
- 97. Jiwlawat N, Lynch E, Jeffrey J, Van Dyke JM, Suzuki M. Current Progress and Challenges for Skeletal Muscle Differentiation from Human Pluripotent Stem Cells Using Transgene-Free Approaches. *Stem Cells Int.* 2018;2018:6241681.
- 98. Zhao S, Chen J, Wu L, Tao X, Yaqub N, Chang J. Induced Pluripotent Stem Cells for Tissue-Engineered Skeletal Muscles. *Int J Mol Sci.* 2023;24(14).
- 99. Tajbakhsh S, Borello U, Vivarelli E, Kelly R, Papkoff J, Duprez D, Buckingham M, Cossu G. Differential activation of Myf5 and MyoD by different Wnts in explants of mouse paraxial mesoderm and the later activation of myogenesis in the absence of Myf5. *Development*. 1998;125(21):4155-62.
- 100. Ikeya M, Takada S. Wnt signaling from the dorsal neural tube is required for the formation of the medial dermomyotome. *Development*. 1998;125(24):4969-76.
- 101. Tortorella LL, Milasincic DJ, Pilch PF. Critical proliferation-independent window for basic fibroblast growth factor repression of myogenesis via the p42/p44 MAPK signaling pathway. *J Biol Chem.* 2001;276(17):13709-17.

- 102. Tureckova J, Wilson EM, Cappalonga JL, Rotwein P. Insulin-like growth factor-mediated muscle differentiation: collaboration between phosphatidylinositol 3-kinase-Akt-signaling pathways and myogenin. *J Biol Chem.* 2001;276(42):39264-70.
- 103. Pansters NA, Langen RC, Wouters EF, Schols AM. Synergistic stimulation of myogenesis by glucocorticoid and IGF-I signaling. *J Appl Physiol* (1985). 2013;114(9):1329-39.
- 104. Tooi N, Okama R, Sato H, Inose H, Ogasawara H, Senda H, Nakatsuji N, Kato K, Kiboku T, Igura K. Robust differentiation of human pluripotent stem cells into Schwann cells. *Biochem Biophys Res Commun.* 2024;729:150353.
- 105. Hörner SJ, Couturier N, Bruch R, Koch P, Hafner M, Rudolf R. hiPSC-Derived Schwann Cells Influence Myogenic Differentiation in Neuromuscular Cocultures. *Cells*. 2021;10(12).
- 106. Lin CY, Yoshida M, Li LT, Ikenaka A, Oshima S, Nakagawa K, Sakurai H, Matsui E, Nakahata T, Saito MK. iPSC-derived functional human neuromuscular junctions model the pathophysiology of neuromuscular diseases. *JCI Insight*. 2019;4(18).
- 107. Yoshida M, Kitaoka S, Egawa N, Yamane M, Ikeda R, Tsukita K, Amano N, Watanabe A, Morimoto M, Takahashi J, Hosoi H, Nakahata T, Inoue H, Saito MK. Modeling the early phenotype at the neuromuscular junction of spinal muscular atrophy using patient-derived iPSCs. *Stem Cell Reports*. 2015;4(4):561-8.
- 108. Afshar Bakooshli M, Lippmann ES, Mulcahy B, Iyer N, Nguyen CT, Tung K, Stewart BA, van den Dorpel H, Fuehrmann T, Shoichet M, Bigot A, Pegoraro E, Ahn H, Ginsberg H, Zhen M, Ashton RS, Gilbert PM. A 3D culture model of innervated human skeletal muscle enables studies of the adult neuromuscular junction. *Elife*. 2019;8.
- 109. Santhanam N, Kumanchik L, Guo X, Sommerhage F, Cai Y, Jackson M, Martin C, Saad G, McAleer CW, Wang Y, Lavado A, Long CJ, Hickman JJ. Stem cell derived phenotypic human

- neuromuscular junction model for dose response evaluation of therapeutics. *Biomaterials*. 2018;166:64-78.
- 110. Duc P, Vignes M, Hugon G, Sebban A, Carnac G, Malyshev E, Charlot B, Rage F. Human neuromuscular junction on micro-structured microfluidic devices implemented with a custom micro electrode array (MEA). *Lab Chip.* 2021;21(21):4223-36.
- 111. Thiry L, Clément JP, Haag R, Kennedy TE, Stifani S. Optimization of long-term human iPSC-derived spinal motor neuron culture using a dendritic polyglycerol amine-based substrate. *ASN Neuro*. 2022;14:17590914211073381.
- 112. Demestre M, Orth M, Föhr KJ, Achberger K, Ludolph AC, Liebau S, Boeckers TM. Formation and characterisation of neuromuscular junctions between hiPSC derived motoneurons and myotubes. *Stem Cell Res.* 2015;15(2):328-36.
- 113. Maffioletti SM, Sarcar S, Henderson ABH, Mannhardt I, Pinton L, Moyle LA, Steele-Stallard H, Cappellari O, Wells KE, Ferrari G, Mitchell JS, Tyzack GE, Kotiadis VN, Khedr M, Ragazzi M, Wang W, Duchen MR, Patani R, Zammit PS, Wells DJ, Eschenhagen T, Tedesco FS. Three-Dimensional Human iPSC-Derived Artificial Skeletal Muscles Model Muscular Dystrophies and Enable Multilineage Tissue Engineering. *Cell Rep.* 2018;23(3):899-908.
- 114. Andersen J, Revah O, Miura Y, Thom N, Amin ND, Kelley KW, Singh M, Chen X, Thete MV, Walczak EM, Vogel H, Fan HC, Paşca SP. Generation of functional human 3D cortico-motor assembloids. *Cell.* 2020;183(7):1913-29.e26.
- 115. Mavrommatis L, Jeong HW, Kindler U, Gomez-Giro G, Kienitz MC, Stehling M, Psathaki OE, Zeuschner D, Bixel MG, Han D, Morosan-Puopolo G, Gerovska D, Yang JH, Kim JB, Arauzo-Bravo MJ, Schwamborn JC, Hahn SA, Adams RH, Schöler HR, Vorgerd M, Brand-Saberi B,

- Zaehres H. Human skeletal muscle organoids model fetal myogenesis and sustain uncommitted PAX7 myogenic progenitors. *Elife*. 2023;12.
- 116. Yamamoto K, Yamaoka N, Imaizumi Y, Nagashima T, Furutani T, Ito T, Okada Y, Honda H, Shimizu K. Development of a human neuromuscular tissue-on-a-chip model on a 24-well-plate-format compartmentalized microfluidic device. *Lab Chip*. 2021;21(10):1897-907.
- 117. Urzi A, Lahmann I, Nguyen LVN, Rost BR, García-Pérez A, Lelievre N, Merritt-Garza ME, Phan HC, Bassell GJ, Rossoll W, Diecke S, Kunz S, Schmitz D, Gouti M. Efficient generation of a self-organizing neuromuscular junction model from human pluripotent stem cells. *Nat Commun*. 2023;14(1):8043.
- 118. Lépine S, Nauleau-Javaudin A, Deneault E, Chen CX, Abdian N, Franco-Flores AK, Haghi G, Castellanos-Montiel MJ, Maussion G, Chaineau M, Durcan TM. Homozygous ALS-linked mutations in TARDBP/TDP-43 lead to hypoactivity and synaptic abnormalities in human iPSC-derived motor neurons. *iScience*. 2024;27(3):109166.
- 119. Deneault E, Chaineau M, Nicouleau M, Castellanos Montiel MJ, Franco Flores AK, Haghi G, Chen CX, Abdian N, Shlaifer I, Beitel LK, Durcan TM. A streamlined CRISPR workflow to introduce mutations and generate isogenic iPSCs for modeling amyotrophic lateral sclerosis. *Methods*. 2022;203:297-310.
- 120. Chen CX, Abdian N, Maussion G, Thomas RA, Demirova I, Cai E, Tabatabaei M, Beitel LK, Karamchandani J, Fon EA, Durcan TM. A Multistep Workflow to Evaluate Newly Generated iPSCs and Their Ability to Generate Different Cell Types. *Methods Protoc*. 2021;4(3).
- 121. Rosen DR, Siddique T, Patterson D, Figlewicz DA, Sapp P, Hentati A, Donaldson D, Goto J, O'Regan JP, Deng HX, et al. Mutations in Cu/Zn superoxide dismutase gene are associated with familial amyotrophic lateral sclerosis. *Nature*. 1993;362(6415):59-62.

- 122. Nishiyama A, Niihori T, Suzuki N, Izumi R, Akiyama T, Kato M, Funayama R, Nakayama K, Warita H, Aoki Y, Aoki M. Updated Genetic Analysis of Japanese Familial ALS Patients Carrying SOD1 Variants Revealed Phenotypic Differences for Common Variants. *Neurol Genet*. 2024;10(6):e200196.
- 123. Bernard E, Pegat A, Svahn J, Bouhour F, Leblanc P, Millecamps S, Thobois S, Guissart C, Lumbroso S, Mouzat K. Clinical and Molecular Landscape of ALS Patients with SOD1 Mutations: Novel Pathogenic Variants and Novel Phenotypes. A Single ALS Center Study. *Int J Mol Sci.* 2020;21(18).
- 124. Cluskey S, Ramsden DB. Mechanisms of neurodegeneration in amyotrophic lateral sclerosis. *Mol Pathol*. 2001;54(6):386-92.
- 125. Guo D, Daman K, Chen JJ, Shi MJ, Yan J, Matijasevic Z, Rickard AM, Bennett MH, Kiselyov A, Zhou H, Bang AG, Wagner KR, Maehr R, King OD, Hayward LJ, Emerson CP, Jr. iMyoblasts for ex vivo and in vivo investigations of human myogenesis and disease modeling. *Elife*. 2022;11.
- 126. Kawada J, Kaneda S, Kirihara T, Maroof A, Levi T, Eggan K, Fujii T, Ikeuchi Y. Generation of a motor nerve organoid with human stem cell-derived neurons. *Stem Cell Reports*. 2017;9(5):1441-9.
- 127. Thiry L, Hamel R, Pluchino S, Durcan T, Stifani S. Characterization of human iPSC-derived spinal motor neurons by single-cell RNA sequencing. *Neuroscience*. 2020;450:57-70.
- 128. Namboori SC, Thomas P, Ames R, Hawkins S, Garrett LO, Willis CRG, Rosa A, Stanton LW, Bhinge A. Single-cell transcriptomics identifies master regulators of neurodegeneration in SOD1 ALS iPSC-derived motor neurons. *Stem Cell Reports*. 2021;16(12):3020-35.

- 129. Bertacchi M, Maharaux G, Loubat A, Jung M, Studer M. FGF8-mediated gene regulation affects regional identity in human cerebral organoids. *Elife*. 2024;13.
- 130. Wagenaar DA, Pine J, Potter SM. An extremely rich repertoire of bursting patterns during the development of cortical cultures. *BMC Neurosci*. 2006;7:11.
- 131. Sharf T, van der Molen T, Glasauer SMK, Guzman E, Buccino AP, Luna G, Cheng Z, Audouard M, Ranasinghe KG, Kudo K, Nagarajan SS, Tovar KR, Petzold LR, Hierlemann A, Hansma PK, Kosik KS. Functional neuronal circuitry and oscillatory dynamics in human brain organoids. *Nat Commun.* 2022;13(1):4403.
- 132. Huang M, Liu YU, Yao X, Qin D, Su H. Variability in SOD1-associated amyotrophic lateral sclerosis: geographic patterns, clinical heterogeneity, molecular alterations, and therapeutic implications. *Transl Neurodegener*. 2024;13(1):28.
- 133. Kim BW, Ryu J, Jeong YE, Kim J, Martin LJ. Human motor neurons with SOD1-G93A mutation generated from CRISPR/Cas9 gene-edited iPSCs develop pathological features of amyotrophic lateral sclerosis. *Front Cell Neurosci.* 2020;14:604171.
- 134. Chen H, Qian K, Du Z, Cao J, Petersen A, Liu H, Blackbourn LWt, Huang CL, Errigo A, Yin Y, Lu J, Ayala M, Zhang SC. Modeling ALS with iPSCs reveals that mutant SOD1 misregulates neurofilament balance in motor neurons. *Cell Stem Cell*. 2014;14(6):796-809.
- 135. Deng YC, Liu JW, Ting HC, Kuo TC, Chiang CH, Lin EY, Harn HJ, Lin SZ, Chang CY, Chiou TW. n-Butylidenephthalide recovered calcium homeostasis to ameliorate neurodegeneration of motor neurons derived from amyotrophic lateral sclerosis iPSCs. *PLoS One*. 2024;19(11):e0311573.

- 136. Lundfald L, Restrepo CE, Butt SJ, Peng CY, Droho S, Endo T, Zeilhofer HU, Sharma K, Kiehn O. Phenotype of V2-derived interneurons and their relationship to the axon guidance molecule EphA4 in the developing mouse spinal cord. *Eur J Neurosci*. 2007;26(11):2989-3002.
- 137. Gurney ME, Pu H, Chiu AY, Dal Canto MC, Polchow CY, Alexander DD, Caliendo J, Hentati A, Kwon YW, Deng HX, et al. Motor neuron degeneration in mice that express a human Cu,Zn superoxide dismutase mutation. *Science*. 1994;264(5166):1772-5.
- 138. Bonifacino T, Zerbo RA, Balbi M, Torazza C, Frumento G, Fedele E, Bonanno G, Milanese M. Nearly 30 Years of Animal Models to Study Amyotrophic Lateral Sclerosis: A Historical Overview and Future Perspectives. *Int J Mol Sci.* 2021;22(22).
- 139. Fischer LR, Culver DG, Tennant P, Davis AA, Wang M, Castellano-Sanchez A, Khan J, Polak MA, Glass JD. Amyotrophic lateral sclerosis is a distal axonopathy: evidence in mice and man. *Exp Neurol*. 2004;185(2):232-40.
- 140. Frey D, Schneider C, Xu L, Borg J, Spooren W, Caroni P. Early and selective loss of neuromuscular synapse subtypes with low sprouting competence in motoneuron diseases. *J Neurosci*. 2000;20(7):2534-42.
- 141. Soubannier V, Chaineau M, Gursu L, Lépine S, Kalaydjian D, Sirois J, Haghi G, Rouleau G, Durcan TM, Stifani S. Early nuclear phenotypes and reactive transformation in human iPSC-derived astrocytes from ALS patients with SOD1 mutations. *Glia*. 2024;72(11):2079-94.
- 142. Hand CK, Mayeux-Portas V, Khoris J, Briolotti V, Clavelou P, Camu W, Rouleau GA. Compound heterozygous D90A and D96N SOD1 mutations in a recessive amyotrophic lateral sclerosis family. *Ann Neurol*. 2001;49(2):267-71.
- 143. van der Wal E, Iuliano A, In 't Groen SLM, Bholasing AP, Priesmann D, Sharma P, den Hamer B, Saggiomo V, Krüger M, Pijnappel W, de Greef JC. Highly contractile 3D tissue

- engineered skeletal muscles from human iPSCs reveal similarities with primary myoblast-derived tissues. *Stem Cell Reports*. 2023;18(10):1954-71.
- 144. Madden L, Juhas M, Kraus WE, Truskey GA, Bursac N. Bioengineered human myobundles mimic clinical responses of skeletal muscle to drugs. *Elife*. 2015;4:e04885.
- 145. Wang J, Zhou CJ, Khodabukus A, Tran S, Han SO, Carlson AL, Madden L, Kishnani PS, Koeberl DD, Bursac N. Three-dimensional tissue-engineered human skeletal muscle model of Pompe disease. *Commun Biol.* 2021;4(1):524.
- 146. Ebrahimi M, Lad H, Fusto A, Tiper Y, Datye A, Nguyen CT, Jacques E, Moyle LA, Nguyen T, Musgrave B, Chávez-Madero C, Bigot A, Chen C, Turner S, Stewart BA, Pegoraro E, Vitiello L, Gilbert PM. De novo revertant fiber formation and therapy testing in a 3D culture model of Duchenne muscular dystrophy skeletal muscle. *Acta Biomater*. 2021;132:227-44.
- 147. Bou Akar R, Lama C, Aubin D, Maruotti J, Onteniente B, Esteves de Lima J, Relaix F. Generation of highly pure pluripotent stem cell-derived myogenic progenitor cells and myotubes. *Stem Cell Reports*. 2024;19(1):84-99.
- 148. Rashid MI, Ito T, Miya F, Shimojo D, Arimoto K, Onodera K, Okada R, Nagashima T, Yamamoto K, Khatun Z, Shimul RI, Niwa JI, Katsuno M, Sobue G, Okano H, Sakurai H, Shimizu K, Doyu M, Okada Y. Simple and efficient differentiation of human iPSCs into contractible skeletal muscles for muscular disease modeling. *Sci Rep.* 2023;13(1):8146.
- 149. Darabi R, Arpke RW, Irion S, Dimos JT, Grskovic M, Kyba M, Perlingeiro RC. Human ES- and iPS-derived myogenic progenitors restore DYSTROPHIN and improve contractility upon transplantation in dystrophic mice. *Cell Stem Cell*. 2012;10(5):610-9.

- 150. Borchin B, Chen J, Barberi T. Derivation and FACS-mediated purification of PAX3+/PAX7+ skeletal muscle precursors from human pluripotent stem cells. *Stem Cell Reports*. 2013;1(6):620-31.
- 151. Choi IY, Lim H, Estrellas K, Mula J, Cohen TV, Zhang Y, Donnelly CJ, Richard JP, Kim YJ, Kim H, Kazuki Y, Oshimura M, Li HL, Hotta A, Rothstein J, Maragakis N, Wagner KR, Lee G. Concordant but Varied Phenotypes among Duchenne Muscular Dystrophy Patient-Specific Myoblasts Derived using a Human iPSC-Based Model. *Cell Rep.* 2016;15(10):2301-12.
- 152. van der Wal E, Herrero-Hernandez P, Wan R, Broeders M, In 't Groen SLM, van Gestel TJM, van IWFJ, Cheung TH, van der Ploeg AT, Schaaf GJ, Pijnappel W. Large-Scale Expansion of Human iPSC-Derived Skeletal Muscle Cells for Disease Modeling and Cell-Based Therapeutic Strategies. *Stem Cell Reports*. 2018;10(6):1975-90.
- 153. Shelton M, Kocharyan A, Liu J, Skerjanc IS, Stanford WL. Robust generation and expansion of skeletal muscle progenitors and myocytes from human pluripotent stem cells. *Methods*. 2016;101:73-84.
- 154. Afshar ME, Abraha HY, Bakooshli MA, Davoudi S, Thavandiran N, Tung K, Ahn H, Ginsberg HJ, Zandstra PW, Gilbert PM. A 96-well culture platform enables longitudinal analyses of engineered human skeletal muscle microtissue strength. *Sci Rep.* 2020;10(1):6918.
- 155. Guo X, Smith V, Jackson M, Tran M, Thomas M, Patel A, Lorusso E, Nimbalkar S, Cai Y, McAleer CW, Wang Y, Long CJ, Hickman JJ. A Human-Based Functional NMJ System for Personalized ALS Modeling and Drug Testing. *Adv Ther (Weinh)*. 2020;3(11).
- 156. Sakar MS, Neal D, Boudou T, Borochin MA, Li Y, Weiss R, Kamm RD, Chen CS, Asada HH. Formation and optogenetic control of engineered 3D skeletal muscle bioactuators. *Lab Chip*. 2012;12(23):4976-85.

- 157. Raman R, Cvetkovic C, Uzel SG, Platt RJ, Sengupta P, Kamm RD, Bashir R. Optogenetic skeletal muscle-powered adaptive biological machines. *Proc Natl Acad Sci U S A*. 2016;113(13):3497-502.
- 158. Mills RJ, Parker BL, Monnot P, Needham EJ, Vivien CJ, Ferguson C, Parton RG, James DE, Porrello ER, Hudson JE. Development of a human skeletal micro muscle platform with pacing capabilities. *Biomaterials*. 2019;198:217-27.